Fisheries and Oceans Canada | Pêches et Océans Canada
Ecosystems and Oceans Science | Sciences des écosystèmes et des océans

Canadian Science Advisory Secretariat (CSAS)

Research Document 2026/004

National Capital Region

Assessment of Port Ocean Prediction System Developed Under Canada's Oceans Protection Plan: St. Lawrence Estuary

Simon St-Onge Drouin[1], Rachel Horwitz[2], Michael Dunphy[3], Maxim Krassovski[3], Stephanne Taylor[2], Adam Drozdowski[2], Hauke Blanken[3]

[1] Fisheries and Oceans Canada
Maurice Lamontagne Institute
850 route de la Mer
Mont-Joli, Quebec G5H 3Z4

[2] Fisheries and Oceans Canada
Bedford Institute of Oceanography
1 Challenger Drive
Dartmouth, Nova Scotia B2Y 4A2

[3] Fisheries and Oceans Canada
Institute of Ocean Sciences
9860 West Saanich Road
Sidney, British Columbia V8L 4B2

February 2026

Canada

Foreword

This series documents the scientific basis for the evaluation of aquatic resources and ecosystems in Canada. As such, it addresses the issues of the day in the time frames required and the documents it contains are not intended as definitive statements on the subjects addressed but rather as progress reports on ongoing investigations.

Published by:

Fisheries and Oceans Canada
Canadian Science Advisory Secretariat
200 Kent Street
Ottawa ON K1A 0E6

http://www.dfo-mpo.gc.ca/csas-sccs/
DFO.CSAS-SCAS.MPO@dfo-mpo.gc.ca

ISSN 1919-5044
ISBN 978-0-660-97077-6 Cat. No. Fs70-5/2026-004E-PDF

Correct citation for this publication:

St-Onge Drouin, S., Horwitz, R., Dunphy, M., Krassovski, M., Taylor, S., Drozdowski, A., and Blanken, H. 2026. Assessment of Port Ocean Prediction System Developed Under Canada's Oceans Protection Plan: St. Lawrence Estuary. DFO Can. Sci. Advis. Sec. Res. Doc. 2026/004. xi + 128 p.

Aussi disponible en français :

St-Onge Drouin, S., Horwitz, R., Dunphy, M., Krassovski, M., Taylor, S., Drozdowski, A. et Blanken, H. 2026. Évaluation du système de prévisions océaniques portuaires élaboré dans le cadre du Plan de Protection des Océans - Estuaire du Saint-Laurent. Secr. can. des avis sci. du MPO. Doc. de rech. 2026/004. xiii + 134 p.

TABLE OF CONTENTS

ABSTRACT xi
1. INTRODUCTION 1
2. PORT MODEL DESIGN 1
2.1. MODEL SELECTION 1
2.2. DOWNSCALING STRATEGY 2
2.3. SIMULATION SEQUENCING 2
2.4. SURFACE FORCING 3
2.5. AUTOMATION SUITE 3
2.6. ROBUSTNESS AND LIMITATIONS 4
3. ST. LAWRENCE ESTUARY 4
3.1. OCEANOGRAPHY OF THE AREA 4
3.2. DOMAIN AND CONFIGURATION 5
3.3. INITIALIZATION 6
3.4. OPEN BOUNDARY FORCING 6
3.4.1. Vertical datum 6
3.4.2. One-dimensional model: r1d 7
3.5. FRESHWATER INPUT 7
3.6. ICE MODEL 7
3.7. MODELLING SYSTEM STABILITY, ROBUSTNESS AND LIMITATIONS 8
3.7.1. Stability and robustness 8
3.7.2. Limitations 8
4. EVALUATION METRICS 8
4.1. HINDCAST 9
4.1.1. Water level 10
4.1.2. Water velocity 11
4.1.3. Water properties 12
4.1.4. Drift 13
4.2. FORECAST 14
5. HINDCAST EVALUATION RESULTS 15
5.1. WATER LEVEL 15
5.1.1. Long term mean sea surface height 15
5.1.2. Tidal water level 15
5.1.3. Non-tidal water level 16
5.1.4. Overall scores 17
5.1.5. Storm surge water level 17
5.2. WATER VELOCITY 17
5.2.1. Horizontal ADCPs 17
5.2.2. Current meter 18

5.2.3. Moored ADCPs 18
5.2.4. ADCP transects 19
5.2.5. Surface currents 20
5.3. WATER PROPERTIES 21
5.3.1. Sea-surface temperature 21
5.3.2. Moored CTDs 21
5.3.3. CTD profiles 22
5.3.4. Ferries 23
5.4. DRIFT 23
6. FORECAST EVALUATION RESULTS 24
6.1. NON-TIDAL WATER LEVEL 24
7. SUMMARY 24
8. KEY FINDINGS 24
9. ACKNOWLEDGEMENTS 25
10. REFERENCES CITED 25
11. TABLES 29
12. FIGURES 46

LIST OF TABLES

Table 1. Main parameters of STLE200's and STLE500's configuration.....29
Table 2. Monthly climatological runoff (m^3/s). 30
Table 3. Water level active station ID, names and offset to shift water level to CGVD28.....30
Table 4. Water level historical stations ID and names. 30
Table 5. M2 constituent comparison for active tide gauges for year 2021.....31
Table 6. S2 constituent comparison for active tide gauges for year 2021. 31
Table 7. N2 constituent comparison for active tide gauges for year 2021. 33
Table 8. K1 constituent comparison for active tide gauges for year 2021. 33
Table 9. M4 constituent comparison for active tide gauges for year 2021.....34
Table 10. M2 constituent comparison for historical tide gauges. 34
Table 11. Tidal water level scores for year 2021. 36
Table 12. Non-tidal water level scores for year 2021.....37
Table 13. Total water level scores for year 2021. 37
Table 14. Storm names and dates.....38
Table 15. Non-tidal scores averaged for the 7 chosen storms. 38
Table 16. Total surface currents scores from comparison with HADCP in Québec and Lévis. ..39
Table 17. Non-tidal surface currents scores from comparison with HADCP in Québec and Lévis. 39
Table 18. Tidal surface currents scores from comparison with HADCP in Québec and Lévis. ..39
Table 19. Amplitude and phase of the major surface currents constituents from the HADCPs in Québec and Lévis; phase, amplitude and tidal error for both STLE500 and STLE200. 39
Table 20. Total velocity statistics for ADCP at buoy IML-4. 41
Table 21. Non-tidal velocity statistics for ADCP at buoy IML-4.....41
Table 22. Tidal velocity statistics for ADCP at buoy IML-4. 42
Table 23. Near surface salinity and temperature scores for 2017 from comparison with MCTD fixed on tide gauges.....42
Table 24. Near surface temperature scores for years 2016-2019 for station 3057 from comparison with MCTD fixed on tide gauges. 43
Table 25. Near surface salinity scores for years 2016-2019 for station 3057 from comparison with MCTD fixed on tide gauges.....43
Table 26. Near surface temperature scores for years 2016-2021 for station 3100 from comparison with MCTD fixed on tide gauges. 43
Table 27. Scores for ferry's temperature and salinity at ~8m depth. 44
Table 28. Scores for TReX experiment drifter's database in 2020. 44
Table 29. Scores for drifters deployed around Saint-François, Ile d'Orléans, in July 2019. 45

LIST OF FIGURES

Figure 1. Schematic of one timestamp's set of pseudo-analysis (PA, in red) and forecast (in blue) runs. Grey dashed lines are spaced six hours apart, and orange arrows indicate where a restart file is generated and used to launch the subsequent step. The PA for today+1 will start with the same restart used to start today's 00Z forecast, and the pattern will repeat. 46

Figure 2. Limits of the CIOPS-E, STLE500 and STLE200 domains. 46

Figure 3. Bathymetry and limits of the STLE500's and STLE200's domain. 47

Figure 4. STLE500's bathymetry, with **i** and **j** indices as vertical and horizontal axis. OTPS tidal components are applied at the eastern open boundary.....48

Figure 5. STLE200's bathymetry, with **i** and **j** indices as vertical and horizontal axis. OTPS tidal components are applied at the eastern open boundary.....49

Figure 6. Cyclone locations every six hours from 2010-2021. 50

Figure 7. Maximum St. Lawrence River runoff per year, for the period 1968-2021. 51

Figure 8. Tide gauges stations for the upstream part of the modeled area. Active real-time stations are in black, and historical ones are in blue. 52

Figure 9. Tide gauges stations for the downstream part of the modeled area. Active real-time stations are in black, and historical ones are in blue. 53

Figure 10. Long-term (6 years) mean ssh (m) map for the STLE200 domain. 54

Figure 11. Long-term (6 years) mean ssh (m) map for the STLE500 domain. 55

Figure 12. Long-term (6 years) mean ssh for the 3 models and observations (black dotted line). STLE200 in red, STLE500 is in blue, and CIOPS-E is in green. The approximate connection location with the r1d model is indicated by an arrow. 56

Figure 13. M2 tidal amplitude (panel 1 and 2) and phase (panel 3 and 4) of the three models compared to observations at the active tide gauge stations (see Figure 8 and Figure 9 for a map of tide gauge stations).....57

Figure 14. S2 tidal amplitude (panel 1 and 2) and phase (panel 3 and 4) of the three models compared to observations at the active tide gauge stations (see Figure 5 and Figure 6 for a map of tide gauge stations).....58

Figure 15. N2 tidal amplitude (panel 1 and 2) and phase (panel 3 and 4) of the three models compared to observations at the active tide gauge stations (see Figure 5 and Figure 6 for a map of tide gauge stations).....59

Figure 16. K1 tidal amplitude (panel 1 and 2) and phase (panel 3 and 4) of the three models compared to observations at the active tide gauge stations (see Figure 5 and Figure 6 for a map of tide gauge stations).....60

Figure 17. M4 tidal amplitude (panel 1 and 2) and phase (panel 3 and 4) of the three models compared to observations at the active tide gauge stations (see Figure 5 and Figure 6 for a map of tide gauge stations).....61

Figure 18. M2 tidal amplitude (panel 1 and 2) and phase (panel 3 and 4) of the three models compared to observations at the historical tide gauge stations (see Figure 5 and Figure 6 for a map of tide gauge stations).....62

Figure 19. N2 tidal amplitude (panel 1 and 2) and phase (panel 3 and 4) of the three models compared to observations at the historical tide gauge stations (see Figure 5 and Figure 6 for a map of tide gauge stations).....63

Figure 20. S2 tidal amplitude (panel 1 and 2) and phase (panel 3 and 4) of the three models compared to observations at the historical tide gauge stations (see Figure 5 and Figure 6 for a map of tide gauge stations).....64

Figure 21. K1 tidal amplitude (panel 1 and 2) and phase (panel 3 and 4) of the three models compared to observations at the historical tide gauge stations (see Figure 5 and Figure 6 for a map of tide gauge stations).....65

Figure 22. M4 tidal amplitude (panel 1 and 2) and phase (panel 3 and 4) of the three models compared to observations at the historical tide gauge stations (see Figure 5 and Figure 6 for a map of tide gauge stations).....66

Figure 23. Non-tidal water level at station 3345 for year 2021. 67

Figure 24. Non-tidal water level at station 3300 for year 2021. 68

Figure 25. Non-tidal water level at station 3248 for year 2021. 69

Figure 26. Non-tidal water level at station 3100 for year 2021. 70

Figure 27. Non-tidal water level spectrum (top panel) and error spectrum (bottom panel) for station 3057, for year 2021. 71

Figure 28. Non-tidal water level spectrum (top panel) and error spectrum (bottom panel) for station 3424, for year 2021. 72

Figure 29. Water level scores temporal stability summary for each station and each model. For total water level (left panels), bias is on the vertical axis and CRMSE is on the horizontal axis. Right panels show tidal CRMSE on the vertical axis and non-tidal CRMSE on the horizontal axis. Each dot represents a single year score. 73

Figure 30. Non-tidal water level for the 7 chosen storm for station 2985.....74

Figure 31. Non-tidal water level for the 7 chosen storm for station 3057.....75

Figure 32. Non-tidal water level for the 7 chosen storm for station 3100.....76

Figure 33. Non-tidal water level for the 7 chosen storm for station 3248.....77

Figure 34. Map of the position (beginning of the 2 arrows) and the coverage (blue arrow) of the 2 HADCPs deployed on each side of the St. Lawrence river, one at the Port of Québec and one at the Lévis wharf. 78

Figure 35. Map of the position (red dots) of the 2 HADCPs deployed on each side of the St. Lawrence river, one at the Port of Québec and one at the Lévis wharf. STLE200 's bathymetrys is also plotted on the figure. 78

Figure 36. Lévis scatterplots of currents and principal axis of variance for year 2021 for observations, STLE500 and STLE200.....79

Figure 37. Québec scatterplots of currents and principal axis of variance for year 2021 for observations, STLE500 and STLE200.....79

Figure 38. HADCP results in Lévis and model outputs for year 2020. Along-shore total velocity currents from observations and the 2 models in panel 1, along-shore residual velocity in panel 2, and along-shore total velocity error in panel 3. 80

Figure 39. HADCP results in Lévis and model outputs for year 2021. Along-shore total velocity currents from observations and the 2 models in panel 1, along-shore residual velocity in panel 2, and along-shore total velocity error in panel 3. 81

Figure 40. HADCP results in Québec and model outputs for year 2020. Along-shore total velocity currents from observations and the 2 models in panel 1, along-shore residual velocity in panel 2, and along-shore total velocity error in panel 3. 82

Figure 41. HADCP results in Lévis and model outputs for year 2020. Tidal ellipses from observations and the 2 models for tidal constituents M2, N2, S2, K2, K1, O1, Q1, P1 and M4. 83

Figure 42. HADCP results in Lévis and model outputs for year 2021. Tidal ellipses from observations and the 2 models for tidal constituents M2, N2, S2, K2, K1, O1, Q1, P1 and M4. 84

Figure 43. HADCP results in Québec and model outputs for year 2021. Tidal ellipses from observations and the 2 models for tidal constituents M2, N2, S2, K2, K1, O1, Q1, P1 and M4. 85

Figure 44. Tidal ellipses from ADCP at buoy IML-4 and for the 2 coarser models (CIOPS-E and STLE500) for tidal constituents M2, K1, N2, S2, O1, P1, Q1, and K2, at 1.5-meter depth. 86

Figure 45. Tidal ellipses from ADCP at buoy IML-4 and for the 2 coarser models (CIOPS-E and STLE500) for tidal constituents M2, K1, N2, S2, O1, P1, Q1, and K2, at 20-meter depth. 87

Figure 46. Tidal ellipses from ADCP at buoy IML-4 and for the 2 coarser models (CIOPS-E and STLE500) for tidal constituents M2, K1, N2, S2, O1, P1, Q1, and K2, at 50-meter depth. 88

Figure 47. Tidal ellipses from ADCP at buoy IML-4 and for the 2 coarser models (CIOPS-E and STLE500) for tidal constituents M2, K1, N2, S2, O1, P1, Q1, and K2, at 100-meter depth. 89

Figure 48. Tidal ellipses from surface water ADCP at buoy IML-4 in 2016 and for the 2 coarser models (CIOPS-E and STLE500) for tidal constituents M2. 90

Figure 49. Tidal ellipses from ADCP at buoy IML-4 in 2016 and for the 2 coarser models (CIOPS-E and STLE500) for tidal constituents M2. 91

Figure 50. Mean total speed and direction (column 1), vector correlation magnitude and angle for total currents (column 2), tidal currents (column 3) and non-tidal currents (column 4), from the higher frequency ADCP at buoy IML-4 in 2016 and for the 2 coarser models (CIOPS-E and STLE500). 92

Figure 51. Mean total speed and direction (column 1), vector correlation magnitude and angle for total currents (column 2), tidal currents (column 3) and non-tidal currents (column 4), from the lower frequency ADCP at buoy IML-4 in 2016 and for the 2 coarser models (CIOPS-E and STLE500). 93

Figure 52. Short time series (1 week) of total currents u and v at 1.5-meter depth from the higher frequency ADCP at buoy IML-4 in 2016 for the 2 coarser models (CIOPS-E and STLE500). 94

Figure 53. Total velocity (up) and velocity error (bottom) rotary spectrum for ADCP 11947 at 10 m. Clockwise (CW) rotation on left panels and counterclockwise (CCW) rotation on right panels. 95

Figure 54. Total velocity (up) and velocity error (bottom) rotary spectrum for ADCP 11947 at 50 m. Clockwise (CW) rotation on left panels and counterclockwise (CCW) rotation on right panels. 96

Figure 55. Snapshot of surface currents for CIOPS-E (left panel) and STLE200 (right panel) for date 2017-06-08, 13H00 (UTC), corresponding to ebb tide and low water. Surface current

amplitude is represented by the color scale on the background of the white arrows. All cells of CIOPS-E are displayed, but only 1 cell out of 25 are displayed for STLE200 arrows (for clarity). All cells are shown for surface current magnitude (color scale). 97

Figure 56. Snapshot of surface currents for CIOPS-E (left panel) and STLE200 (right panel) for date 2017-06-08, 19H00 (UTC), corresponding to flood tide and high water. Surface current amplitude is represented by the color scale on the background of the white arrows. All cells of CIOPS-E are displayed, but only 1 cell out of 25 are displayed for STLE200 arrows (for clarity). All cells are shown for surface current magnitude (color scale). 98

Figure 57. Snapshot of surface currents for CIOPS-E (top panel) and STLE200 (second panel) for date 2017-06-08, 13H00 (UTC), corresponding to ebb tide and low water for STLE200 and CIOPS-E. Surface current amplitude is represented by the length of the arrows and by the color scale of the arrows. CIOPS-E surface currents are interpolated on STLE200's grid, and one cell out of 49 is shown on the figure (for clarity). The bottom panel is the surface currents from the Atlas of Tidal Currents, for the period to 0 to 1 hour after low water. The color scale is common to the 3 panels, and knots are used instead of m/s to fit the color scale of the tidal atlas. 99

Figure 58. Snapshot of surface currents for CIOPS-E (top panel) and STLE200 (second panel) for date 2017-06-08, 19H00 (UTC), corresponding to flood tide and high water for STLE200 and CIOPS-E. Surface current amplitude is represented by the length of the arrows and by the color scale of the arrows. CIOPS-E surface currents are interpolated on STLE200's grid, and one cell out of 49 is shown on the figure (for clarity). The bottom panel is the surface currents from the Atlas of Tidal Currents, for the period to 0 to 1 hour after low water. The color scale is common to the 3 panels, and knots are used instead of m/s to fit the color scale of the tidal atlas. 100

Figure 59. Near surface temperature and salinity for the 3 models and observations coming from MCTD fixed on tide gauges stations for years 2017, for station 2985 (see Figure 5 and Figure 6 for a map of tide gauge stations). 101

Figure 60. Near surface temperature and salinity for the 3 models and observations coming from MCTD fixed on tide gauges stations for years 2017, for station 3057 (see Figure 5 and Figure 6 for a map of tide gauge stations). 102

Figure 61. Near surface temperature and salinity for the 3 models and observations coming from MCTD fixed on tide gauges stations for years 2017, for station 3100 (see Figure 5 and Figure 6 for a map of tide gauge stations). 103

Figure 62. Near surface temperature and salinity for the 3 models and observations coming from MCTD fixed on tide gauges stations for years 2017, for station 3248 (see Figure 5 and Figure 6 for a map of tide gauge stations). 104

Figure 63. Near surface temperature and salinity for the 3 models and observations coming from MCTD fixed on tide gauges stations for years 2017, for station 3300 (see Figure 5 and Figure 6 for a map of tide gauge stations). 105

Figure 64. Near surface temperature and salinity for the 3 models and observations coming from MCTD fixed on tide gauges stations for years 2017, for station 3335 (see Figure 5 and Figure 6 for a map of tide gauge stations). 106

Figure 65. Near surface temperature and salinity for the 3 models and observations coming from MCTD fixed on tide gauges stations for years 2017, for station 3353 (see Figure 5 and Figure 6 for a map of tide gauge stations). 107

Figure 66. Near surface temperature and salinity for the 3 models and observations coming from MCTD fixed on tide gauges stations for years 2017, for station 3360 (see Figure 5 and Figure 6 for a map of tide gauge stations). 108

Figure 67. CTD cast and definition of the polygons over the 200m config domain. 109

Figure 68. CTD cast and definition of the polygons over the 500m config domain not covered by the 200m domain. 110

Figure 69. CTD cast comparison for the whole 200m domain. See Figure 67 for the definition of All_200 region. Note the log y-axes to show the differences in the first 10 meters..... 111

Figure 70. CTD cast comparison for the Middle Estuary region. See Figure 30 for the definition of Middle region. 112

Figure 71. CTD cast comparison for the Saguenay Fjord region. See Figure 30 for the definition of Sag region..... 113

Figure 72. CTD cast for the Saguenay Fjord region, just for STLE200. See Figure 30 for the definition of Sag region. 114

Figure 73. CTD cast comparison for the Maritime Estuary region. See Figure 30 for the definition of Maritim region. 115

Figure 74. Ship tracks of the Oceanex Connaigra for year 2018. Timing of the ship position is represented by the color scale. Red dotted rectangle represents the limits of STLE200 domain. 116

Figure 75. 8m salinity as collected by the ferry over the common section to the 3 models in the Middle Estuary. The horizontal axis is longitude with Ile-aux-Coudres and the city of Tadoussac marked as a landmark (see Figure 74). Vertical axis is the month of the year 2018. Row 1 are observations, row 2 to 4 are model results in column1, and differences with observations are in column 2. 117

Figure 76. 8m temperature as collected by the ferry over the common section to the 3 models in the Middle Estuary. The horizontal axis is longitude with Ile-aux-Coudres and the city of Tadoussac marked as a landmark (see Figure 74). Vertical axis is the month of the year 2018. Row 1 are observations, row 2 to 4 are model results in column1, and differences with o observations are in column 2. 118

Figure 77. Map of the drifter's path for the TReX experiment, 2020. Blue dotted rectangle is STLE500 domain. 119

Figure 78. Map of the drifter's path near Saint-François, Ile d'Orléans. Deployment is marked by a black cross. 119

Figure 79. Mean Molcard skill for TReX experiment drifter's database in 2020. 120

Figure 80. Mean separation distance for TReX experiment drifter's database in 2020. 121

Figure 81. Mean Molcard skill for drifters deployed in the area of Saint-François, Ile d'Orléans, in July 2019. 122

Figure 82. Mean separation distances for drifters deployed in the area of Saint-François, Ile d'Orléans, in July 2019. 123

Figure 83. Non-tidal water level bias and CRMSE for station 2985. 124

Figure 84. Non-tidal water level bias and CRMSE for station 3424. 125

Figure 85. Non-tidal water level bias and CRMSE for station 3057. 126

Figure 86. Non-tidal water level bias and CRMSE for station 3100. 127

Figure 87. Non-tidal water level bias and CRMSE for station 3248. 128

ABSTRACT

Canada's Oceans Protection Plan (OPP) was launched in 2016 to support initiatives aimed at protecting our marine environment from anthropogenic pressures. To this end, the Improving Drift Prediction and Nearshore Modelling sub-initiative of OPP developed six high-resolution port-scale hydrodynamic models, to improve safe navigation, and provide operational emergency response to events such as marine oil spills. The models were downscaled from the Coastal Ice-Ocean Prediction Systems East and West (CIOPS-E, CIOPS-W). Atmospheric forcing was provided by the High-Resolution Deterministic Prediction System (HRDPS). Model performance is assessed against available observational data and contrasted with the parent model using a multi-year hindcast. Evaluations of 48-hour forecasts are performed during a two-month period.

This document reports on the performance assessment for St. Lawrence Estuary’s ocean prediction system. Details about the system development and configuration are presented. Comparison of model results with data on water levels, currents, water properties and drift are also presented, and this comparison includes CIOPS-E where possible. Results show that performances of the high-resolution models for this region are improved for all observations used when compared to CIOPS-E in the Middle Estuary.

1. INTRODUCTION

Under the Improving Drift Prediction and Nearshore Modelling (DPNM) sub-initiative of Canada's Oceans Protection Plan (OPP), high-resolution models were developed for six Canadian ports and their approaches to enhance the Government of Canada's ocean modelling capabilities in support of environmental protection and marine safety applications (e.g., drift prediction for oil spills) and safety for navigation via a hydrographic e-navigation application. The six ports (three on the east coast and three on the west coast) were selected as at-risk for environmental incidents owing to their high tanker traffic and complex navigational needs. Models have been developed for the west coast ports of Kitimat, Lower Fraser River and Vancouver Harbour, and for the east coast ports of Saint John, the Strait of Canso, and the St. Lawrence estuary.

The models have been developed with both hindcast and forecast capabilities. For each port, a multi-year hindcast is presented with model validation against observations of water levels, velocities, temperature and salinity, as well as a drift experiment conducted using available drifters. Forecast performance is assessed over a two-month period.

The purpose of this document is to review the performance of the model for the St. Lawrence estuary and its approach. The design is common to all port models and is presented in Section 2, while Section 3 describes the specifics of the St. Lawrence estuary model. The evaluation parameters used to evaluate all models are detailed in Section 4, and Sections 5 and 6 respectively analyze the long hindcast evaluation results and the forecasts evaluation results for the St. Lawrence estuary. The performance of the St. Lawrence estuary model is summarized in Section 7, and the main key findings are listed in Section 8.

2. PORT MODEL DESIGN

The port models ("port ocean prediction systems," or POPS) follow a common structure designed to constrain system complexity. We use the same ocean general circulation model and code version, downscaling strategy, preprocessing tools, surface forcing product, and automation suite for all six POPS. The model grids, configuration/tuning, open boundary forcing, and freshwater input sources differ between POPS configurations.

2.1. MODEL SELECTION

The precursor to much of the OPP port modelling effort was conducted using the Finite Volume Community Ocean Model (FVCOM) (Chen et al. 2003) under the World Class Tanker Safety System (WCTSS) program, yielding prototype models for ports of Canso, Kitimat, and Vancouver Harbour. Even earlier, there have been modelling efforts based on Backhaus (Backhaus 1983; 1985) yielding models for the St. Lawrence estuary (Saucier and Chassé 2000) and the Gulf of St. Lawrence (Saucier 2003). These were then followed by implementation of an equivalent NEMO model by Environment and Climate Change Canada (ECCC), the Regional Marine Prediction System (RMPS) GSL. The RMPS was operational from 2011 to 2021, though none of these earlier models were considered for use in OPP. The WCTSS FVCOM prototypes used unstructured model meshes to resolve the coastal regions to within tens of metres or less, with resolution gradually decreasing to kilometres to match the parent model grid on the open boundary.

FVCOM has no history of operational deployment in Canada, while NEMO 3.6 (Nucleus of European Modelling of the Ocean) is used operationally by the Canadian Operational Network for Coupled Environmental PredicTion Systems (CONCEPTS). In the early part of OPP, a

comparison exercise between FVCOM 4.1 and NEMO 3.6 (Nudds et al. 2020) informed the decision-making process to select which codebase to use for the POPS models. Both codebases were used to construct models of the Bay of Fundy and the Port of Saint John (Paquin et al. 2020), which was chosen due to the large tides and complex circulation. NEMO 3.6's most significant deficiency in this context is the lack of wetting and drying, so if NEMO 3.6 could provide satisfactory results in the Bay of Fundy, then it would likely be suitable for use in the other regions. The two models were evaluated on how well they matched observations, as well as on computational efficiency, stability, and robustness. Both models were found to be skillful at reproducing observed data: neither model was significantly superior, and the choice of model to use going forward rested more heavily on the other factors.

Ultimately the decision was taken to proceed with NEMO 3.6, despite its structured grid, a somewhat coarser nearshore resolution, and higher demand for computational resources, to facilitate operationalization and align with modelling efforts at ECCC. Additional advantages of NEMO include active development that delivers regular code updates and bug fixes, an international NEMO Consortium group where members steer code development, and a well-established international operational modelling community.

Thus the ocean model used for all port ocean prediction systems is the CONCEPTS code: a fork of NEMO 3.6 (Madec 2016) that has been customized to meet the operational needs of CONCEPTS, for example (Dupont et al. 2015).

2.2. DOWNSCALING STRATEGY

The port models are downscaled solutions driven by larger-scale coastal ocean models currently operational at ECCC: the Coastal Ice-Ocean Prediction Systems East (CIOPS-E; Paquin et al. 2021a) and West (CIOPS-W; Paquin et al. 2021b) have 2-2.5 km resolution, and Salish Sea 500 (~500 m resolution) which is part of the CIOPS-W system. Output from these models forms the boundary conditions for our higher-resolution, smaller-area models. We use two levels of nesting to achieve a resolution fine enough to reach port scale. The nesting is one-way (coarse to fine), so no information is fed back to the larger scale models, allowing the models to run sequentially but otherwise independently of each other. This one-way nesting strategy also enables systematic errors to be corrected at the open boundaries.

We do not employ a dynamic ice model. Instead, we use a NEMO feature called "ice if", which uses input ice fields and the local freezing point to assess where ice cover exists, and in those locations it restores the sea surface temperature to the local freezing point and sets heat fluxes to -4 Wm^{-2} (Madec 2016).

We do not employ data assimilation or spectral nudging; all model runs are free runs.

River discharge data is used where available to supply the most realistic freshwater input to the model, and climatology is used when this is not available. Gauge data is also used in some cases to construct water level boundary conditions.

2.3. SIMULATION SEQUENCING

The port models operate in three configurations: hindcast, pseudo-analysis and forecast. Hindcasts are the most straightforward, using larger-scale model forcing and quality-controlled gauge data to drive the models. The model begins in the past from a cold-start (temperature and salinity interpolated as initial conditions, water at rest) or a hot-start (temperature, salinity, velocity, and sea-surface height interpolated as initial conditions) and reaches a spun-up state after a period of adjustment to the forcing. The model output is considered usable once spun up, and the model can run nearly up to the present in this configuration, provided that forcing data is

available. Pseudo-analysis runs are daily runs that keep the model state caught up to near-real-time, and do not include a direct data-assimilation component. Rather, the state is indirectly driven by data via boundary and surface forcing terms. These runs are used to initialize the first forecast of each day and may use different input than hindcasts depending on what data is available in real-time.

The pseudo-analysis and forecast schedule is chosen to match the schedule of the parent models that we use for forcing. Shortly after 00Z each day, a 24-hour pseudo-analysis simulation runs to catch up the model state to 00Z. This process uses restart files (so no spin up needed) and, where possible, uses gauge data drawn from a near-real-time data feed which receives limited quality control. Following the pseudo-analysis, the POPS generates four forecasts per day, each 48 hours long, which start from 00Z, 06Z, 12Z and 18Z. The daily 00Z forecast starts using the restart file from the daily pseudo-analysis and runs for 48 hours, saving a restart file six hours into the simulation. The 06Z forecast starts from this restart file, also saving a restart file six hours in, and similarly for the 12Z and 18Z forecasts. A schematic of this setup is shown in Figure 1. We focus only on the 00Z forecasts in this evaluation.

While the 00Z forecast simulation is nominally started at 00Z each day, in practice, the initialization of the simulation is delayed as it can not begin until all inputs are available from the larger scale models and the pseudo-analysis completes. At time of writing, this delay is approximately 5 hours, such that upon completion, each forecast simulation has about 43 hours of output that is in the future.

2.4. SURFACE FORCING

Surface forcing is derived from the High-Resolution Deterministic Prediction System (HRDPS) (Milbrandt et al. 2016) that runs operationally at ECCC and provides atmospheric weather forecasts four times per day at 2.5 km resolution. This is the highest-resolution operational atmospheric product available and is chosen to be consistent with the forcing used in CIOPS-E/W. In hindcast and pseudo-analysis mode, we use a time-blended form of the HRDPS forecasts, where hours 06–17 from successive forecasts are combined using weighted averaging to form temporally continuous fields with the same blending schedule as CIOPS-E/W. Additional details are given in the technical documentation for CIOPS-W version 1.5 (Paquin et al. 2022). Time blending is not used for forecasts.

The surface forcing is applied to the NEMO model using the CORE algorithms (Large and Yeager 2004) with modifications by ECCC to (a) read input data from the in-house RPN file format and (b) use the lowest diagnostic level of the atmospheric model rather than the conventional 2 m and 10 m data. Precipitation and sea-level pressure variations are also applied to the surface of the model.

2.5. AUTOMATION SUITE

The hindcast, pseudo-analysis and forecast simulations are all managed using ECCC's Maestro sequencing software. We have constructed a Maestro suite that is based on ECCC's CIOPS-E/W suites, where we use some of ECCC's functionality for the atmospheric forcing preparation and the mechanics of running the NEMO model, including managing restart files and outputs. We augment this baseline with functionality to prepare boundary forcing, extract data from the real-time data feed, generate the runoff forcing and prepare ice-concentration input files for the "ice-if" feature. Fallback strategies for missing data and persistence strategies for forecasts using gauge data are also implemented here.

2.6. ROBUSTNESS AND LIMITATIONS

For an operational model to be useful, it must be robust and not prone to failure. We have not assessed the models exhaustively in this regard; such testing is an ongoing process. However, some aspects have been explored:

- Where gauge data is needed as a model input, fallback mechanisms are implemented to mitigate missing or bad gauge data. Typically, this means we prepare a climatology for each gauge to stand in when the gauge data is unavailable. With these prepared ahead of time and with appropriate tooling to automate the switchover, the models can run despite missing gauge data and experience a graceful degradation through forcing with lower-quality data rather than a failure. Measuring the severity of the degradation under data-loss scenarios is reserved for future work.
- A long hindcast is conducted for model performance assessment. This long simulation demonstrates that the model is stable subject to a multi-year sample of weather/forcing conditions. In some cases, the hindcast period samples some extreme events, which helps bolster the case for model stability.
- Daily demonstration simulations (pseudo-analysis and four forecasts) have run for order one year on the General-Purpose Science Cluster (GPSC) on a best-effort basis, to show that the automation suite can run the models routinely and reveal edge cases that can be fixed to improve robustness further. The purpose of running these pre-operational, best-effort simulations is to demonstrate the functionality/stability of the NEMO-based numerical model and the driving automation suite and identify issues that would impact operational deployment. The dominant source of issues experienced that impede on-schedule daily forecasts are (a) GPSC compute system downtime, both planned and unplanned, and (b) lack of availability of the forcing data from the larger-scale models that are nominally mirrored on schedule from ECCC's systems. These issues are deemed an expected consequence of using a research cluster and would be mitigated using an operational cluster.

The models will have some limitations:

- Intrinsic variability is expected in each model, and this has not been characterized.
- The lack of wetting and drying capability in NEMO 3.6 requires artificial bathymetry deepening in intertidal regions.

3. ST. LAWRENCE ESTUARY

3.1. OCEANOGRAPHY OF THE AREA

The St. Lawrence estuary is a coastal area characterized by a complex bathymetry, strong tides and important runoffs from the St. Lawrence River, the second largest river in North America. The main source of energy dissipation arises from the action of the tides, as 94% of the energy in the Middle Estuary is contained in the tidal frequencies (Muir 1981).

In this report, the labels Riverine, Middle and Maritime Estuary will be used. The Riverine Estuary extends from Trois-Rivières to the western point of Ile d'Orléans; the Middle Estuary reaches the mouth of the Saguenay Fjord, and the Maritime Estuary ends at Pointe-des-Monts. This labeling is motivated by bathymetric features (Maritime/Middle Estuary), the limit of salt intrusion (Middle/Riverine Estuary) and the limit of significant tidal influence (Riverine Estuary/St. Lawrence River).

Surface currents over the whole estuary are affected by runoff from the St. Lawrence river, which averages 11400 m^3/s (Saucier et al. 2009). In the riverine part, this runoff creates a hydraulic slope. The mean water level is at 4 m higher than mean sea level (CGVD28) at Trois-Rivières and reaches sea level in the Middle Estuary between Ile d'Orléans and Saint-Joseph-de-la-Rive (Saucier and Chassé 2000).

The Middle Estuary is divided into a northern and southern part by a series of shoals. The northern part is generally deeper (more than 150m depth in the Bassin de Charlevoix) and covered by an almost-continuous channel. The South Channel and Middle Channel on the southern part are shallower than 40 m (El-Sabh 1988). Lateral salinity gradients between the north and south shores can reach up to 8 (Neu 1970), and salinity ranges from 0 to 30 over the whole Middle Estuary (Silverberg and El-Sabh 1990). Buoyancy effects impact residual currents over the whole water column up to the upstream part of the Middle Estuary, between Saint-Joseph-de-la-Rive and Ile d'Orléans (Simons et al. 2006).

At the limit of the Middle and Maritime Estuary, tidal buoyancy effects are of significant importance particularly at the head of the Laurentian Channel, near Tadoussac, where 75 meter depth isopycnals are lifted near the surface over the different sills (Saucier and Chassé 2000), generating important mixing processes.

The Maritime Estuary is deeper and wider, characterized by multiple cyclonic and anti-cyclonic gyres and an intense buoyant jet called the Gaspé Current, which is attached to the southern bottom slope. Multiple density fronts are also an important feature of this area (El-Sabh and Murty 1990, Saucier 2003).

3.2. DOMAIN AND CONFIGURATION

The St. Lawrence port model was initially planned to be nested into the 500m resolution Gulf of St. Lawrence model (GSL500) developed at ECCC. When the implementation of GSL500 was not supported by ECCC, a 500 m resolution downscaling model was added to the St. Lawrence port modelling system. Consequently, the grids of STLE500 and STLE200 are based on the GSL500 grid instead of the CIOPS-E grid. These grids are built with the tools used at ECCC to produce the GEM-LAM (Global Environmental Multiscale - Local Area Model) grids, like HRDPS at 2.5 km (Milbrandt et al. 2016). The center of this geographical projection is set at the center of the Gulf of St. Lawrence, and the grids are rotated counterclockwise by an angle of 37 degrees.

The whole St. Lawrence modelling system described here is illustrated in Figure 2. There are two levels of offline one-way nesting in this system: from CIOPS-E to STLE500 and from STLE500 to STLE200.

STLE500 (blue dashed box on Figure 3) extends from Pointe-des-Monts to Québec, just east of Québec's bridge. STLE200 (red dashed box on Figure 3) extends from Les Escoumins to Trois-Rivières, where the tide amplitude is much smaller (~15 cm): this makes it easier to connect with the one-dimensional model. The Saguenay Fjord (Figure 3) is included in STLE200 for 2 reasons: the water mass exchanges with the estuary at Tadoussac are important to correctly reproduce the water masses elsewhere in the estuary, and there are two ports in the Saguenay with possible other developments.

A short summary of the main parameters of both models are compiled in Table 1. The vertical resolution was reduced from 1m at the surface to 3m for STLE200 for numerical stability issues. The hypothesis for this instability is the existence of internal waves, resulting in higher vertical speed at higher resolution.

Bottom friction tuning was performed over the 200 m St. Lawrence Estuary domain (not on the Saguenay Fjord). This tuning was done accounting for the amplitude and phase of the M2 tidal constituent, as well as the hydraulic slope in the upstream estuary.

3.3. INITIALIZATION

The STLE500 hindcast begins on 2016-02-10, and we considered STLE500 output from 2016-04-20 for the hindcast evaluation, the remaining period being considered as a spin-up. The STLE200 hindcast begins on 2016-02-20, and we considered STLE200 output from 2016-04-20 for the hindcast evaluation, the remaining period being considered as a spin-up. The initial condition in the Saguenay Fjord, which is not part of the CIOPS-E domain, was initially taken from STLE400, another St. Lawrence estuary model (Saucier and Chassé 2000), for both STLE500 and STLE200. Upstream of the western limit of CIOPS-E, in the St. Lawrence Riverine Estuary, temperature and salinity (~0) are extrapolated from CIOPS-E western values.

3.4. OPEN BOUNDARY FORCING

The temperature, salinity, horizontal velocity and sea surface height (ssh) at the eastern boundary of the STLE500 at 500m horizontal resolution (blue box on Figure 2) are computed from the results of CIOPS-E (green box on Figure 2) results. In the same way, STLE500 provides the eastern boundary conditions to the 200m horizontal resolution model, STLE200 (red box on Figure 2).

There is a phase lag in tides propagated by CIOPS-E at the position of the eastern open boundary of STLE500. As a consequence, to improve the tides, currents and ssh are de-tided before being used at the eastern boundary of STLE500. Tidal components computed by the Oregon State University Tidal Prediction Software (OTPS) are then used at the boundary to reconstruct the tides, reducing the phase lag, as illustrated by the pale grey band on the bottom right of Figure 4. The tidal constituents used are: M2, N2, S2, K2, K1, O1, Q1, P1, M4, Mf, Mm, Mn4 and Ms4. The same treatment is done at the eastern open boundary of STLE200 (pale grey band on the bottom right of Figure 5), because STLE500 is also showing a phase lag at this position. Work has been done to get rid of OTPS tidal constituents at the boundary of STLE200 by adjusting the bottom friction in STLE500, with no concluding results yet.

3.4.1. Vertical datum

STLE500 and STLE200 bathymetric grids are referenced to the same vertical datum: CGVD28. CIOPS-E bathymetric grid is not referenced to the same vertical datum. The vertical datum used by CIOPS-E was unknown at the moment of writing this report. However, the mean sea level in CIOPS-E is approximately 32 cm below the mean sea-level observed at Rimouski, when this observation is referenced to the CGVD28. An attempt has been made to correct this offset at the eastern open boundary of STLE500, by adding the offset in the port model's sea-surface height open boundary condition, but change in the mean ssh modified the tidal propagation upstream, requiring a new tunning of bottom friction, which was not possible due to time constraints. As a consequence, there is no offset correction for the ssh at the eastern open boundary of STLE500. Further work on this issue is planned for the next model development phase. In order to remove these offsets in the figures presented in this report, a mean sea level offset of +37 cm is applied to all water level results from all 3 models, corresponding to an average of the offset at Rimouski (station 2985, offset = -32 cm) and at Baie Ste-Catherine (station 3424, offset = -42 cm).

3.4.2. One-dimensional model: r1d

Surface currents resulting from the St. Lawrence runoff are locally modulated by the tides. In order to propagate the tidal wave upstream of the western boundary, the NEMO model has to be coupled to a one-dimensional model, r1d, for the upstream part of the St. Lawrence River (from Montréal to Trois-Rivières), in a 2-way coupling mode.

This one dimensional model is based on a publication by Dronkers (Dronkers 1969). It uses the third implicit scheme and the application of this scheme to a system of river branches, described at pages 53-54 and 61-62 of the paper.

One constraint to this coupling scheme is that there is no momentum flux between r1d and NEMO. The runoff computed by r1d is added to the water column as if it were rain. Kinetic energy is then transferred to potential energy, possibly creating an artificial elevation bias. It is not clear how the tidal wave can propagate correctly from NEMO to r1d under these conditions. However, some tests have been done treating the St. Lawrence runoff as a normal river, resulting in a clear degradation of the mean sea level. Moreover, in the case of STLE200, the NEMO model is connected to r1d in the upstream part of the Riverine Estuary, at Trois-Rivières, where the tidal amplitude is only around 15 cm. The lack of momentum transfer at Trois-Rivières will not make a significant change in the Québec area where the tidal amplitude (~ 2m) is large compared to Trois-Rivières. The purpose of connecting NEMO to r1d at the upstream part of the Riverine Estuary, more than 130 km western of Québec, was mainly to minimize the effect of this coupling on Québec's area. In STLE500, r1d is connected east of Québec's bridge. This coupling area affects the water level in Quebec's region, but the usefulness of this configuration is to provide boundary conditions to STLE200 near Les Escoumins, much further east.

This r1d model propagates the tides upstream. This model also needs the St. Lawrence's River discharge as an upstream boundary condition. This discharge is provided by another one-dimensional model, STLT1061 (Lefaivre et al. 2016), operated on a DFO Quebec Region server. STLT1061 provides a tidally filtered runoff at Québec. The climatological values of the tributaries between Québec and the upstream section of r1d are subtracted from this runoff value, and the result is applied at the upstream end of r1d, around Montréal. Climatological runoffs of the tributaries are then reintroduced at the appropriate r1d section or NEMO grid cell. This method makes it possible to take advantage of the fact that STLT1061 assimilates the flow in real time for the major rivers.

3.5. FRESHWATER INPUT

Monthly climatologies are used for all river runoff, except for the St. Lawrence River, where we use a one-dimensional model (see section 3.4.2 above). Climatological values are presented in Table 2. Those runoff climatologies are taken from previous modelling works on the area (Saucier 2003; Saucier and Chassé 2000).

Forecast of the St. Lawrence's River discharge are provided by the STLT1061 model in order to feed the western boundary condition to perform the 48h forecast.

3.6. ICE MODEL

There is no explicit ice model yet in either of the two domains. Both models are using the NEMO ice-if model substitute, with CIOPS-E ice concentration.

3.7. MODELLING SYSTEM STABILITY, ROBUSTNESS AND LIMITATIONS

3.7.1. Stability and robustness

The hindcast of STLE500 and STLE200 was run successfully for 6 years and 4 months (2016/02 to 2022/06) and for a set of 67 forecast under the ports model's maestro suite. During this period, the highest freshet flows in 60 years were observed in 2017 and 2019 (Figure 7), and the model was stable and produced satisfactory results. Multiple storms also occurred over St. Lawrence domains during this period, some of which are presented in Figure 30 to Figure 33, in Table 14 and Table 15, and described in section 5.1.5. The models remained stable during those storms and water levels were correctly reproduced.

The DEMO pseudo-analysis and forecast was online for one year (2021/08/25 to 2022/08/14), on the General Purpose Science Cluster (GPSC), for both STLE500 and STLE200. The purpose of this was to identify issues that would impact operational deployment and to test the stability of the system. Most issues were related to a lack of data from the larger scale model or from a source of inputs for the different forcing (runoff, atmosphere), and to GPSC different system upgrade.

Fallbacks are in place for St. Lawrence runoff inputs provided by STLT1061: STLT1061 provides a 30-day forecast daily. In case of failure to provide the 48h runoff forecast, the last 30-day forecast will be used, which gives 30 days of security. In the event that no new forecast is provided for 30 days, a climatology of the St. Lawrence's runoff is used.

3.7.2. Limitations

As mentioned above, there is no explicit ice model yet in either of the two domains. The impact of this gap on surface currents is possibly more important for the Riverine Estuary and the Saguenay Fjord from January until March, the ice being mainly mobile for the rest of the area. However, this limitation must be taken in considerations for the whole area if the model is to be used during winter from January until March.

No bottom friction tuning was done in the Saguenay Fjord. As a result, tidal error is higher in this region (stations 3424 and 2460) than in surrounding areas.

The coarse resolution of the atmospheric model (HRDPS 2.5 km) is a limitation in areas with narrow channels, where higher resolution wind values would be needed to correctly resolve those channels. This is the case in the region of Québec (including Ile d'Orléans) and upstream, and also in the Saguenay Fjord. These areas would also benefit of a higher ocean grid resolution, which the HADCP results tend to support (see section 5.2.1) for the region of Québec.

As mentioned before (section 3.4.1), different vertical datums were used between port models and CIOPS-E. The consequence of not correcting this offset at the boundary is to subtract ~37 cm of water. Wave speed propagation in shallower area should be more impacted by this fact than in deeper areas.

4. EVALUATION METRICS

The model performance is assessed through the analysis of a multi-year hindcast and a shorter set of forecasts, where the dates considered are constrained by available surface and boundary forcing from larger scale models. The hindcast evaluation uses a wide set of observations to analyze the model's representation of ocean conditions, including tidal analysis and model drift that would be difficult to assess on a short model run. Meanwhile, the forecast evaluation

focuses on measuring the degradation of model skill as a function of forecast lead time for a smaller set of observations available during the forecast period.

Quality controlled data sources were preferred where possible. We performed additional quality control to some data as needed, including visual inspection, thresholding and automatic de-spiking to eliminate suspect data.

4.1. HINDCAST

Hindcast performance is assessed through comparison with available observational data. For each observation, we extract the corresponding virtual observation from the model. The error is defined as

$$\text{ERROR} = \mathcal{X}_m - \mathcal{X}_o ,$$

where $\mathcal{X}_o$ and $\mathcal{X}_m$ are the observed and modelled values such that a positive/negative value indicates a model over/underestimate. For currents, $\mathcal{X}_o$ and $\mathcal{X}_m$ are taken as complex numbers with the real part representing the eastward and imaginary the northward components of velocity.

We use several scores, the bias, the centered root mean square error (hereafter CRMSE) and the root mean square error (hereafter RMSE),

$$\text{bias} = \frac{1}{N}\sum \text{ERROR} = \frac{1}{N}\sum \mathcal{X}_m - \frac{1}{N}\sum \mathcal{X}_o = \overline{\mathcal{X}_m} - \overline{\mathcal{X}_o} ,$$

$$\text{CRMSE} = \sqrt{\frac{1}{N}\sum (ERROR\text{-}bias)^2},$$

$$\text{RMSE} = \sqrt{\frac{1}{N}\sum ERROR^2} = \sqrt{bias^2 + CRMSE^2},$$

and these measures retain the units of $\mathcal{X}$.

We also use the unitless gamma squared score,

$$\gamma^2 = \frac{CRMSE^2}{\sum (x_o - \overline{x_o})^2},$$

which is the ratio of error variance to observed variance, such that zero indicates perfect agreement between model and observation variance, and unity indicates error variance is as large as the signal variance. A value of unity or larger indicates no skill.

For scalar quantities, we use the unitless sample Pearson correlation coefficient score,

$$\text{PEARSONR} = \frac{\sum (x_m - \overline{x_m})(x_o - \overline{x_o})}{\sqrt{\sum (x_m - \overline{x_m})^2 \sum (x_o - \overline{x_o})^2}},$$

where zero indicates no correlation and unity indicates perfect correlation. For vector quantities (currents) we have the vector correlation coefficient (Kundu 1976; Röhrs and Christensen 2015),

$$\text{VECTORR} = \frac{\sum (x_m - \overline{x_m})^* (x_o - \overline{x_o})}{\sqrt{\sum (x_m - \overline{x_m})^2 \sum (x_o - \overline{x_o})^2}} ,$$

where the asterisk represents complex conjugation, which is also implied for squaring of complex numbers. This quantity is a complex number, where the magnitude measures the overall correlation and the angle is a measure of the average angle of the modelled current with respect to the observation. Here we compute the angle as positive clockwise to be consistent

with the convention of representing the velocity direction as positive clockwise from North. Lastly, the vector correlation angle is only considered meaningful when the correlation magnitude is large (Kundu 1976).

4.1.1. Water level

Water level observations from the Canadian Hydrographic Service (CHS) are transformed from CHS Chart Datum to Canadian Geodetic Vertical Datum of 1928 (CGVD28) by subtracting a station-specific offset. CHS provides these offsets are based on measurements from a GNSS (Global Navigation Satellite System) occupation at each station. Pacific US stations are shifted from the US datum to CGVD28 via NOAA's VDatum and NRCan Vertical Datum Transformations online tools. Atlantic US stations were gathered with a mean low-low water datum and converted to CGVD28 using conversion surfaces provided by CHS. Water level observations from the Water Survey of Canada (WSC) are shifted to CGVD28 using offsets provided by WSC.

Tidal analysis is performed using T_TIDE on one-year segments at an hourly sampling interval. Where data is available at a higher frequency, it is interpolated/subsampled to hourly frequency. Observations missing more than 10% of the data points are not detided. The tidal analysis enables the decomposition of the total water level into tidal and non-tidal parts as,

$$H_{total} = H_{tidal} + H_{nontidal}$$

The annual (SA) and semi-annual (SSA) constituents are excluded from the tidal analysis; these constituents are subsumed into the non-tidal component. For the present purpose this is adequate as the same process is applied to both model and observations, and the extent to which the models do not reproduce SA or SSA is captured in the non-tidal error scores. Constituents with signal-to-noise ratios below 2 are also subsumed into the non-tidal part. Water level bias is included in the non-tidal component. Scores are reported for the total, tidal and non-tidal components. Owing to a negligible cross-correlation between tidal and non-tidal water levels, to a good approximation, we have

$$\mathrm{CRMSE}^2_{total\,wl} \cong \mathrm{CRMSE}^2_{tidal\,wl} + \mathrm{CRMSE}^2_{nontidal\,wl},$$

which shows how these two errors contribute to the total. Amplitude and phase errors are reported for the significant constituents, as is the tidal error,

$$\text{TIDAL ERROR} = \left[\frac{1}{2}({h_o}^2 + {h_m}^2) - h_o h_m \cos(\phi_o - \phi_m)\right]^{\frac{1}{2}},$$

where h_o and ϕ_o are the observed (subscript *o*) amplitude and Greenwich phase lag for a given tidal constituent, while h_m and ϕ_m are the modeled (subscript *m*) amplitude and phase (Cummins and Oey 1997).

4.1.1.1. Storm surge evaluation

To evaluate the port models' performance during storms, a handful of stormy periods are selected for each port. The cyclone database of (Zhang et al. 2019), which provides global storm tracks from 1958 to 2021 (Figure 6 shows a zoom of North America), guides the selection. The database was queried for storms passing within a few hundred kilometres of each port model domain, and it provides a comprehensive list of storm events during the hindcast period. However, this list is quite extensive for some ports (particularly Canso and Saint John), so longer lists are narrowed down by considering minimum central pressure, examining water level gauges, and local media reports of storm impacts. The evaluation follows the residual water level hindcast evaluation in terms of performance scores and plots, but is limited to the storm periods.

Storm surge detiding is done using a 40-day window around the storm's peak, i.e., 20 days before to 20 days after. This differs from the typical water level analysis, which is done in yearly spans and as such can include more constituents. However, using a shorter window does a better job removing the tides during each storm, particularly in areas with non-stationary tides.

We note that storm surges may interact non-linearly with tides to impact water levels, but we do not investigate this phenomenon here.

4.1.2. Water velocity

Velocity data is available from ADCPs and some current metres in one of four configurations: mounted on a mooring, buoy mounted (i.e., floating), in a float towed by a ship, or horizontally mounted on a shore structure (HADCP). Only horizontal (east-west / north-south, u/v) velocities are considered here. The horizontal velocity's u/v and speed/direction decompositions are both considered, and directions are calculated as positive clockwise from north.

Model data is extracted to match the observed data's time span and spatial location. Time series longer than 29 days and with less than 10% of data points missing are detided using T_TIDE; hourly data is used for detiding, and where more frequent data is available, it is first down sampled. As with water level, the SA and SSA constituents are excluded from fitting, a Rayleigh value of 2 is used, and the observations and model data are processed the same way.

Currents are noisier, tend to have more missing data, are less stationary, and are impacted by more non-linear processes than water level observations, and these factors make the detiding process less robust. Owing to nonlinear processes such as bottom friction, some tidal (kinetic) energy will spread into adjacent frequencies, so fitting to tidal harmonics does not capture all variability induced by the tides, and some near-tidal variability remains in the residual velocities. We do not apply low-pass or band-stop filters to the residual to reduce the noise. While doing so would provide a more completely de-tided residual time series, some of the total signal would be unaccounted for by either the tidal or non-tidal evaluation. Given these caveats, the tidal component may be more accurately described as "the component of the currents that T_TIDE is able to fit." Currents are evaluated using similar metrics to water level, using complex formulations. Tidal constituents are evaluated using the ellipse error (Cummins and Thupaki 2018)

$$D_u = \left[\frac{1}{2}(A_o^2 + B_o^2 + A_m^2 + B_m^2) - \cos(g_o - g_m)\cos(\theta_o - \theta_m)(A_o A_m + B_o B_m) - \sin(g_o - g_m)\sin(\theta_o - \theta_m)\,(A_o B_m + A_m B_o)\right]^{1/2},$$

where A and B are semi-major and semi-minor axes, respectively, the subscripts *o* and *m* correspond to observed and modelled, g is phase, and θ is angle of inclination. For the non-tidal and total time series, complex formulations of the metrics listed at the beginning of the section are used, including bias, CRMSE, γ^2, and vector correlation.

We note that for single-location instruments, in particular moored current meters and moored and horizontally mounted ADCPs, we expect the scoring to be sensitive to the details of the model run under evaluation. Small errors in bathymetry can adjust the location of deterministic features (eddies, jets, meanders, etc.) and this can lead to large errors in the scoring. Meanwhile, chaotic internal variability can also affect the location of such features. An ensemble of model runs could help mitigate the latter but is beyond the scope of the current effort.

4.1.2.1. Horizontal ADCPs

HADCP data is decomposed into along- and cross-channel components, and evaluation is done primarily with mid-beam data to avoid edge effects. When a long enough time series is available, a tidal analysis is done as with moored instruments. Time series of the first week of data are plotted, regardless of how long the total time series is, to show the daily variability in the signal and how well the model captures it. Scatter plots are used to show the distribution of speed and direction of the total velocity, and the semi-major axis for the tidal ellipses are compared when feasible.

4.1.2.2. Current meters and moored ADCPs

Current meters report velocity at a single depth, so those velocities are evaluated at instrument-specific depths. For ADCPs on moorings or buoys, a standard set of depths at which to evaluate the velocities is selected on a per-port basis, considering local bathymetry and data availability; for brevity, statistics may be reported only at some depths for each instrument considered. These levels are defined relative to either a nominal surface (i.e., one with no sea-surface height variation) or the time varying sea surface. For regions with ADCPs in relatively deep water without a large tidal range, using the nominal surface is sufficient. For shallow regions and/or those with large tidal ranges, the evaluation is done relative to the time-varying sea surface, using the observed total water depth to process the observations and modelled sea surface to process the modelled currents.

The observations are preprocessed to remove any spurious data points: values larger than 10 m/s are discarded and the data points are resampled if needed to be evenly spaced.

Tidal analysis is done on all timeseries of at least 29 days at depths with less than 10% of the data missing. Tidal ellipses are plotted for the largest tidal constituents, including depth profiles of tidal ellipses for the largest constituents. Time series and histograms are plotted for both the non-tidal and total velocities. Analysis of total velocities only is done for shorter time series or time series with missing data. We note that if data is missing at consistent phases of the tide, then the analyzed results may be aliased, and so time series with substantive regular gaps are not analyzed or presented.

4.1.2.3. ADCP transects

ADCP transects are too short for tidal analysis, so only the total velocities are considered. An along-transect / cross-transect decomposition is used, with a constant angle used for decomposition for the entire transect; this is sufficient as the transects are typically short and straight. Along-transect plots of velocities at depth are used for evaluation. Scatter plots of bias vs CRMSE are also plotted, with the statistics calculated at each physical point and integrated over the transect.

4.1.3. Water properties

Conductivity-Temperature-Depth (CTD) profiles are grouped into manually defined subregions based on the geography of each port domain. This enables an aggregate assessment over areas, including bias and CRMSE as a function of depth for each area. Model results are taken from the nearest point to the data location and nearest to the observation time. Vertical profiles are interpolated to the model z-levels to bring all data to consistent depths.

Sea surface temperature buoy and moored CTD measurements are evaluated using the bias, CRMSE, χ^2 and Pearson's *r* scores over the evaluation period. Model values are linearly interpolated to observation locations in the horizontal and vertical dimensions. The observed and modelled time series are interpolated to the largest common data interval.

Ferry thermosalinographs are vessel-mounted temperature and conductivity sensors. They provide a measure of near-surface water temperature and salinity by collecting data through one of the vessel's seawater circuits. Model results for comparison with these data are taken from the point nearest to the observed locations both horizontally and vertically and then linearly interpolated to the observation times. Hovmöller plots of observations, model results and differences, plus basic statistics, are used to assess the model performances relating to near-surface water.

4.1.4. Drift

The models' performance in drift trajectory prediction is assessed by comparing the observed tracks of ocean surface drifters with analogous trajectories modelled using the surface currents output by the port models, in combination with wind forcing from the National HRDPS atmospheric forecast. This comparison is done using the drift evaluation tool developed as part of the DPNM sub-initiative, in the OpenDrift configuration (Soontiens and Holden 2024).

Windage on the surface drifters is applied by computing the wind drag coefficient based on the drifters' drag area ratio (Niiler et al. 1995; Daniel et al. 2002; Röhrs et al. 2012; Hourston 2021; Blanken et al. 2021). This coefficient parameterizes the effect of direct wind drag on the parts of the drifter exposed above the water surface and varies with drifter geometry. To account for wave-induced Stokes' drift, an additional 1% of the wind speed is added (Sutherland et al. 2020), and this sum is applied as the windage in the trajectory prediction.

This method of applying windage assumes that currents over the draft of the drifter are known exactly, as are winds directly at the ocean surface. However, in reality, neither of these assumptions is true, since:

1. The representation of surface currents in NEMO is limited by stability restrictions on near-surface vertical resolution and model uncertainty in general; and
2. Wind speed from the HRDPS model is also subject to model uncertainty and given at 10 m where winds are usually ~30% larger than at 1 m but could be as much as five times larger depending on wind speed and atmospheric stability (Smith 1988).

The representation of Stokes' drift as 1% of the wind speed represents a further assumption, as this value was derived by comparing tracks from various types of surface drifters to currents from the Regional Ice-Ocean Prediction System (RIOPS) ocean model and Canadian Arctic Prediction System (CAPS) atmospheric model (Sutherland et al. 2020). As noted in the discussion section of (Sutherland et al. 2020) and references therein, this value can vary widely depending on the combination of ocean and atmospheric forcing, which implies that model uncertainty contributes significantly to the appropriate value here. The authors also note that explicitly including Stokes drift based on a wave prediction system is preferable over parameterization based on wind velocity.

The windage term used here could be optimized by deriving it for each ocean/atmospheric model combination using the procedure in (Sutherland et al. 2020). However, this is beyond the scope of this report: the focus is on improvements to the current forcing for drift simulations without evaluating the suitability of wind predictions in the port model domains for drift prediction or commenting on the potential utility of a port-scale wave prediction system. The windage parameterization used here is merely intended to provide a consistent, deterministic linkage between modelled currents, winds, and the motion of various drifter types. As considerable uncertainty is associated with this windage term, evaluation of surface currents against observations from ADCPs and current meters is deemed the primary determinant of model suitability for drift prediction, rather than analysis of observed and modelled drifter tracks.

Periods where drifters were active in the model domain are identified, and modelled trajectories are started every hour along the drift tracks. The benefits of starting drift tracks in this manner are to reduce the sensitivity to initial conditions and increase the number of tracks available. However, it means that some drift tracks are not independent and thus the errors may be correlated. Modelled trajectories were computed for a user-specified period of 24 hours or more, where possible. However, in some regions, the majority of the observed drifter tracks were less than 24 hours long, and here a shorter modelled trajectory length was chosen.

Observed drifter tracks were truncated to areas covered by the 'wet' cells of the port model domains to avoid launching virtual drifters in 'dry' parts of the domain where observed drifters are near the shoreline, which may not be precisely resolved. In addition, to facilitate interpolation of starting locations for virtual drifters, observed trajectories were split where time gaps between position records exceeded two hours. In the remaining portions, position records were interpolated to a consistent time interval ranging from five minutes to one hour.

For each model – observation pair of trajectories, two statistics are computed to assess the model performance. First is the separation distance, D, which is given by,

$$D(t) = |\dot{x_o}(t) - \dot{x_m}(t)|$$

Here $\dot{x_o}$ and $\dot{x_m}$ are the positions of the observed and modelled drifter, and || denotes the magnitude of the vector difference, i.e., the distance, between them.

Second is the instantaneous skill score, S, following (Molcard et al. 2009), which is given by

$$S(t) = \max\left(0, 1 - \frac{D(t)}{d_o(t)}\right)$$

Here $d_o(t)$ is the displacement of the observed drifter from the starting point of the pair. The rationale for the normalization by $d_o(t)$ is to increase the skill assigned to a trajectory prediction as the trajectory length increases, even if the separation distance remains constant. A separation distance of, for example, 500 m represents a less grievous error in a trajectory that is 10 km long than in one that is 500 m long. A value of S=1 indicates a perfect prediction.

4.2. FORECAST

The forecast evaluation involves running a set of forecasts (here 48 hours long, each starting at 00Z) and evaluating the performance over the independent forecasts as a function of lead time. Forecast evaluation was performed for a set of order 60 consecutive forecasts by comparing the model values with tide gauge, sea surface temperature and horizontal ADCP records. The set of forecasts were taken from winter 2021/22 for logistical reasons. Forecast performance was evaluated as the discrepancy (bias and CRMSE) with observed values as a function of forecast lead time. The error growth curves represent the discrepancy averaged over the set of evaluated forecasts, and we include 95% confidence intervals computed with a bootstrap method.

To detide the forecast and the corresponding hindcast water level series we subtract the tidal signal precalculated based on the hindcast covering the forecast evaluation period. The tidal signal is obtained with a T_TIDE fit with a Rayleigh number as low as 0.1 (overfitting) to ensure maximal energy removal at tidal frequencies. Such strong suppression of tidal energy was implemented to clear the error growth curves of any tidal residual, which otherwise would dominate the curve.

5. HINDCAST EVALUATION RESULTS

In this section, we evaluate the performances of the port ocean prediction systems STLE200 and STLE500 for the period 2016-04-20 to 2022-06-01. Comparison with CIOPS-E is included where possible. All model results used are hourly and instantaneous.

5.1. WATER LEVEL

Positions of the tide gauges used are plotted in Figure 8 for the Riverine and upstream part of the Middle Estuary area and in Figure 9 for the downstream part of the Middle Estuary and Maritime Estuary. Active real-time stations (in black) are used in subsection 5.1.1 to subsection 5.1.5 and historical ones (in blue) will be added in subsection 5.1.2.2. Table 3 lists the station IDs, names and offset used to shift water level data from chart datum to CGVD28 for active stations and Table 4 lists station ID and names of historical tide gauges.

5.1.1. Long term mean sea surface height

Long-term (6 years) mean ssh maps for both St. Lawrence's domains are presented in Figure 10 for STLE200 and Figure 11 for STLE500. As mentioned in section 3.4.1, a mean sea level offset of +37 cm is applied to all water level results from all 3 models. Modeled and observed long-term mean ssh are also compared in Figure 12, after adding the 37 cm offset. The 3 models show similar long-term mean ssh differences for stations 2985 (only STLE500 and CIOPS-E) and 3424. For CIOPS-E, the long-term mean ssh differences increase at station 3057 (+26.9 cm) and at station 3100 (+30.8 cm) (Table 13). For STLE500, the long-term mean ssh differences is similar to STLE200 until it reaches station 3248 (+32.6 cm). This increase in the mean ssh for both CIOPS-E and STLE500 corresponds in space with the places where both models are connected with the r1d model, which are illustrated by colored arrows in Figure 12. The possible reasons for this error are discussed in section 3.3. For STLE200, connecting to the 1D model has the opposite effect: the average water level decreases (around -30 cm). One possible explanation for this is that water at the western boundary of STLE200 do not experience a comparable acceleration as the western boundaries of STLE500 and CIOPS-E: tidal amplitude is only around 15 cm (compared to more than 2m) and St. Lawrence runoff is the main driver for surface currents, which are always in the same direction (downstream).

5.1.2. Tidal water level

5.1.2.1. Active real-time tide gauges station

For this subsection, year 2021 was chosen because data are available for stations 3424 and 3460, which is not the case for previous years. Only tidal constituents with amplitude > 25 cm are presented.

M2 tidal constituent amplitude and phase of the three models are compared to observations for the active tide gauge stations (see Figure 8 and Figure 9 for a map of tide gauge stations), for year 2021, in Figure 13. Those numbers are also in Table 5, plus the tidal error. With the exception of tidal amplitude for station 3424, results for phase and amplitude error are equivalent or improved for all the active tide gauges where STLE200 is not the only model covering the station (3428, 3100, 3057 and 3424). When including the tidal phase and looking at the tidal error (Table 5), tides are clearly improved in STLE200 at these four stations. These four stations are covering a significant part of STLE200's domain where stratification exist, which means that having a 3D model is an advantage over a 2D model. Station 3424 is located at Baie Ste-Catherine, at the entrance of the Saguenay Fjord, just upstream of an important sill. Bottom friction tuning works has been focused on the Middle Estuary itself, not in the Saguenay Fjord, and results at this station might be improved in the next development iteration. The same

reasoning applies to station 3460, which is further upstream in the Saguenay Fjord (Figure 9). Station 2895 (Rimouski) shows that downstream of the domain, M2 tide in STLE500 is improved compared to CIOPS-E. In the western part, for stations 3300, 3335, 3345, 3353 and 3360, tidal error is increased for STLE200 (STLE500 and CIOPS-E domain do not extend to these western stations). For 3300, this error is caused principally by a weaker modeled amplitude (~10cm), while the four upstream stations are also showing a significant phase lag (up to -17.5 degrees). It was decided that the model extends that far west to move the connection with the r1d model away from Québec, and to a place where the tidal amplitude is minimum (~15 cm in Trois-Rivières). Bottom friction tuning has been minimum in this western area, and in the next development iteration, greater attention will be paid to these stations.

S2, N2 and K1 tidal constituent amplitude and phase of the three models are compared to observations in Table 6, Table 7 and Table 8 and on Figure 14, Figure 15 and Figure 16, respectively. STLE200's tidal errors are smaller than 2 cm for all stations except for constituent S2 at stations 3424 and 3460 in the Saguenay Fjord.

The quarter-diurnals M4 tidal constituent amplitude and phase of the three models are compared to observations in Table 9 and Figure 17. This constituent becomes significant between stations 3100 and 3335 (> 15cm and up to 31 cm, see Table 9). It accounts for up to ~5cm of the tidal error. It will therefore be important to take this into account when doing the recalibration of the tides for the Riverine Estuary.

5.1.2.2. Historical tide gauges stations

M2 tidal constituent amplitude and phase of the three models are compared to observations for historical tide gauges (hereafter HTG) stations (see Figure 8 and Figure 9 for a map of tide gauge stations), in Figure 18. Those numbers are also in Table 10, plus the tidal error. Those comparison are not as reliable as active tide gages (section 5.1.2), as some of the constituents were computed using only 14 days of water level data. However, they are presented here as they give a more global spatial picture of the modeled tidal constituents, with 52 stations along the St. Lawrence estuary.

In the eastern region, from station 2955 to station 3030 (from east to west, or right to left on the figure), STLE500 is generally better than CIOPS-E and STLE200 in amplitude and phase. From station 3160 until western boundary, STLE200's tidal error is generally smaller than STLE500, and STLE500's tidal error is generally smaller than CIOPS-E. Exceptions are station 3075, where STLE500 is better than STLE200, due to a phase lag error, and station 3080, where STLE500's tidal error is smaller by ~1cm compared to STLE200.

Figure 19 to Figure 22 shows tidal constituent amplitude and phase comparison with HTG for the other main constituents (N2, S2, K1 and M4). Amplitude and phase are generally improved in STLE200 and STLE500 compared to CIOPS-E. The quarter-diurnals M4 tidal constituent amplitude becomes significant (> 15cm) between stations 3190 and 3300.

5.1.3. Non-tidal water level

Figures 23 to 25 are showing non-tidal water level for 3 stations in the Riverine Estuary. For station 3345 (Figure 23), there is a negative bias, which is reported in Table 13 as -14.2 cm, and the non-tidal water level is smaller in the model at the maximum of the freshet (beginning of April) by up to ~1 m. This bias might be removed by increasing the bottom friction in that area, which will also be needed to improve the M2 tidal amplitude (which is too big by 7.9 cm, see Table 5). A new bottom friction tuning will be done in the next development phase. However, the modeled temporal variability is in good agreement with the observations. Modeled temporal variability is also in good agreement with observations at stations 3300, 3248 and 3100 for

STLE200 and STLE500 (Figure 24, Figure 25 and Figure 26). At station 3100 (Figure 25), CIOPS-E error is increased from May until November.

Figure 27 and Figure 28 are showing non-tidal water level spectrum. The 3 models produce spectrum similar to observations, but higher frequencies (over 6 cpd) are underrepresented in all 3 models.

5.1.4. Overall scores

All tidal water level scores for 2021 presented in Table 11 are improved with increased resolution, for all stations common to 2 or 3 model domains. CRMSE is averaging to 7.3 cm in the Middle Estuary (stations 3100, 3057 and 3424) for STLE200, compared to 32.6 cm for CIOPS-E.

Non-tidal water level scores for 2021 presented in Table 12 are generally improved with increased resolution. Exceptions are that STLE500 shows slightly better scores than STLE200 for stations 3057 (CRMSE, χ^2 and pearson) and 3424 (χ^2). For station 3057, CRMSE is increased by 1.5% for STLE200 compared to STLE500, χ^2 is increased by 0.3% for STLE200 compared to STLE500 and pearson is decreased by 0.5% for STLE200 compared to STLE500.

Table 13 presents scores for total water level. All scores (bias, CRMSE, χ^2 and pearson) for 2021 are improved everywhere with increased resolution, for all stations common to 2 or 3 model domains. CRMSE in the Middle Estuary (stations 3100, 3057 and 3424) averages to 14.7 cm for STLE200, 21.5 cm for STLE500 and 35.4 cm for CIOPS-E.

Figure 29 presents water level scores temporal stability summary for each station and each model. For total water level (left panels), bias is on the vertical axis and CRMSE is on the horizontal axis. The right panels show tidal CRMSE on the vertical axis and non-tidal CRMSE on the horizontal axis. Each dot represents a single year score. No score or station shows significant differences from year to year.

5.1.5. Storm surge water level

Seven storms were chosen, according to their impact (minimum atmospheric pressure) on the St. Lawrence models' area. The chosen storms are listed on Table 14. On Table 15, we see that all three scores (CRMSE, χ^2 and pearson) are improved with increased resolution at all stations common to 2 or 3 models. A four-day non-tidal water level time series is shown for the seven storms for station 2985 in Figure 30, for station 3057 in Figure 31, for station 3100 in Figure 32 and for station 3248 in Figure 33. The storm surge is clearly visible in all 3 models. The upstream stations (3300 to 3360) show lower scores. This is particularly true for stations 3345 to 3360. It coincides with a strong tidal phase lag at these stations for M2 constituent (Table 5). The storm surge influence is not propagated as well as other stations, just like the tidal wave. This might be improved when bottom friction and bathymetry of this upstream area are revisited to improve the tides. Wet and dry scheme could also improve those scores.

5.2. WATER VELOCITY

5.2.1. Horizontal ADCPs

Two horizontal ADCP (HADCP) were deployed on each side of the St. Lawrence river, one at Lévis and one at Québec, for a ~2-month period in 2020 and in 2021 (Figure 34 and Figure 35). Québec's data for 2020 is unusable because of device problems.

Figure 36 (Lévis) and Figure 37 (Québec) show scatterplots of currents and principal axis of variance for year 2021 for observations, STLE500 and STLE200. As the principal axis contains

99.7% (Lévis) and 99.1% (Québec) of the variance, only currents on this axis are presented here. This axis corresponds to along-shore current, and positive is approximately northward current (downstream direction). Lévis along-shore total and residual velocity results are shown in Figure 38 (2020) and Figure 39 (2021). There is a clear improvement of the along-shore total velocity with increased resolution from 500 m to 200 m, which is visible on panel 1 and 3. This is corroborated by all total surface current scores (CRMSE, χ^2 and pearson) in Table 16. CRMSE is reduced by 54% (2020) and 59% (2021) from 500m to 200m. The amplitude of the signal is too weak for STLE500 and STLE200 on panel 1 of Figure 38. However, this error is smaller for STLE200, which is corroborated in Table 19: the error on M2 amplitude, the principal tidal constituent, goes from -46.2 cm to -14.6 cm (2020) and from -41.9 cm to -11.8 cm when increasing resolution from 500 m to 200 m. Non-tidal surface currents scores (Table 17) are slightly decreased for STLE200 in 2020 compared to STLE500 (CRMSE increased by 3%) but increased in 2021 (CRMSE decreased by 1.9%).

Québec along-shore total and residual velocity results are shown in Figure 40. There is a clear improvement of the along-shore total velocity with increased resolution from 500 m to 200 m, which is visible on panel 1 and 3. This is corroborated by all total surface current scores (CRMSE, χ^2 and pearson) in Table 16. CRMSE is reduced by 54.7% from 500m to 200m. The amplitude of the signal is too strong for both models, unlike the results in Lévis. However, this error is smaller for STLE200, which is corroborated in Table 19: the error on M2 amplitude goes from +31 cm to +12 cm when increasing resolution from 500 m to 200 m. Averaged CRMSE over the 2 stations and the 2 years gives 43.8 cm/s for STLE500 and 19.4 cm/s for STLE200.

Concerning strictly tides, all the scores are improved (Table 18), and all the tidal errors are reduced with increased resolution (Table 19), with the exception of N2 and Q1 for year 2021. Tidal ellipses in Figure 41, Figure 42 and Figure 43 shows that M2 is the most important constituent and is well aligned at Lévis, but the major axis of the M2 ellipse at Québec has an angle compared to observations.

Along-shore residual currents in Lévis are too weak (Figure 38 and Figure 39, panel 2) and they are too strong in Québec (Figure 40, panel 2). This asymmetry is accentuated in STLE500. One hypothesis is that the horizontal resolution is insufficient to correctly resolve this asymmetry. This hypothesis will need more investigation.

One particularity observed in both Lévis and Québec in the along-shore total velocity currents (modeled and observed) is that signals are truncated during ebbtide. This tidal asymmetry is reported in literature for shallow water and estuarine system when the M4 quarter-diurnal tidal constituent amplitude is significant. The signal observed from Québec and Lévis HADCP is similar to the signal of figure 1 in Aubrey and Speer (1985), for ebb-dominated tide.

5.2.2. Current meter

No current meter was available inside the domains of the St. Lawrence model. Some can perhaps be found, and investigations will be done on this in the future.

5.2.3. Moored ADCPs

The only available ADCP data for the St. Lawrence models were the ones at the IML-4 buoy, outside STLE200 domain. After looking at multi-year data, significant discrepancies were observed between years. Discussion with technicians responsible for device operation at IML-4 revealed that compass problems were reported for post 2016 years and that some of these years had not taken magnetic declination into account. For these reasons, only year 2016 is presented here. In 2016, two RDI brand ADCPs were attached to IML-4 buoy: one at 300kHz (named 11947) and one at 1200kHz (named 10749) for the top 10 meters.

Figure 44 to Figure 47 shows tidal ellipses for M2, K1, N2, S2, O1, P1, Q1, and K2 constituents at 1.5m, 20m, 50m and 100m respectively. At 1.5-meter depth (Figure 44), tidal ellipses of STLE500 are closer to observations for M2 and S2, and both models are similar for the other constituents. At 20 meters depth (Figure 45), STLE500 is closer to observations for N2, and both models are similar for the other constituents, with different ellipse major axis angle for M2 and S2. At 50 meters depth (Figure 46), CIOPS-E ellipse amplitude is too big for M2, N2 and S2, and STLE500 ellipse's shape are closer to observations for these constituents. At 100 meters depth, both models are similar, CIOPS-E is better aligned for S2 and STLE500 amplitude is closer to observations for N2. As M2 is the most significant constituents at all depth, only this constituent's tidal ellipses for the whole vertical coverage of the instrument are shown on Figure 48 and Figure 49.

Figure 48 shows the tidal ellipses for the first 10 meters as observed by the higher frequency ADCP (10749). CIOPS-E ellipses amplitude are too small, and the direction of rotation is reversed compared to observations and STLE500.

Figure 49 shows the tidal ellipses for the first 100 meters as observed by the lower frequency ADCP (11947). STLE500 ellipses are more similar to observations than CIOPS-E: CIOPS-E are too small and rotate in the inverse direction for the first 20 m, and too big from ~30m to 80 m.

In Figure 50, we see that mean speed, total and tidal vector correlation magnitude for the top 10 meters are improved with STLE500 for device 10749. Indeed, all scores (bias, RMSE, $\chi 2$ and vector correlation magnitude) except vector correlation degrees in Table 20 and Table 22 for station 10749 are improved. Non-tidal currents show a better vector correlation magnitude for STLE500 from surface to 7.5m, and CIOPS-E is better from 7.5m to 10m. The same thing is true for all non-tidal scores on Table 21, with 2 exceptions: vector correlation degrees is improved for CIOPS-E and RMSE is improved for STLE500 at all depth (1.5m to 10m).

In Figure 51, we see that vector correlation magnitude for the top 30 meters concerning total currents and for the top 50m concerning tidal currents are improved for STLE500 for device 11947, which is reflected in RMSE, χ^2 and vector correlation magnitude scores of Table 20 (total currents) and χ^2 and RMSE scores in Table 22 (tidal currents). Non-tidal vector correlation magnitude is better in CIOPS-E, except at the surface (7.5m) where vector correlation magnitude and RMSE are improved in STLE500 (Table 21), which is consistent with instrument 10749.

Figure 52 is showing a short time series (1 week) of total currents u and v at 1.5-meter depth from the higher frequency ADCP at buoy IML-4 in 2016 for the 2 coarser models (CIOPS-E and STLE500). The general shape of the signal is better reproduced by STLE500 for this time series.

Total velocity rotary spectra are shown in Figure 53 at 10 m. Both models compare similarly at lower frequency to observations, and STLE500 is closer to observations at frequencies higher than semi-diurnal, for both clockwise and counterclockwise rotation. The same rotary spectra but at 50 m is shown on Figure 54. At this depth, STLE500 is closer to observations at almost all frequencies.

In general, STLE500 shows better performances for the first 30m for total currents, and CIOPS-E is showing better performances from 30m to bottom for total currents at IML-4 buoy station.

5.2.4. ADCP transects

No ship mounted ADCP transect were available inside the domains of the St. Lawrence model. Some can perhaps be found, and investigations will be done on this in the future.

5.2.5. Surface currents

Snapshots of surface currents at ebb and flood tide are shown on Figure 55 and Figure 56, respectively, for CIOPS-E and STLE200, corresponding to low water and high water. Surface current amplitude is represented by the color scale on the background of the white arrows. Greater current structure is apparent in STLE200. Some of these added structures can certainly be attributed to the higher resolution bathymetry, for example the absence of some islands in CIOPS-E. The contribution of the Saguenay Fjord is clearly visible on the right panel (STLE200) of Figure 55. In addition, an eddy forming to the right of the current coming from the Saguenay Fjord is present in STLE200, but not in CIOPS-E. The baroclinic tidal currents resulting from the stratification of the Middle St. Lawrence Estuary, which is almost inexistent in CIOPS-E, might also explain some differences, but more investigations would be needed to confirm this hypothesis.

Figure 57 and Figure 58 shows the same snapshot of surface currents for CIOPS-E and STLE200 on panel 1 and 2 as Figure 55 and Figure 56, but this time on the native STLE200 grid. CIOPS-E surface currents are rotated and interpolated on STLE200 native grid, and only one cell out of 49 is shown on the figure. On panel 3 the tidal currents are displayed from a validated 3D prognostic model STLE400 (Saucier et al. 1999; Saucier and Chassé 2000). This model has been calibrated and validated for surface currents with 51 ADCP and more than 600 surface drifters. More recently, a new set of surface drifters (St-Onge-Drouin et al. 2014) has been used for surface drift validation. This tidal atlas has been used by mariners for the last 20 years in the Middle and Riverine St. Lawrence Estuary. It is not observations, but it is the best estimate of the tidal surface currents in this region at the moment. However, it is important to keep in mind that this tidal atlas only takes tides into account, with no atmospheric forcings and under the influence of averaged July runoff. In order to enable comparison with the tidal atlas figures, the color scale associated with the amplitude of the modeled surface currents is the same as the one used in the tidal atlas (from 0 to 7 knots) and the color is directly on the arrow. The tidal atlas surface currents are grouped by 3 arrows, each arrow corresponding to a 20-minute slice of the hour. The first (the furthest to the left) is the one that matches the timing of the model results.

A general remark on Figure 57 and Figure 58 is that STLE200 and CIOPS-E modeled surface currents amplitude are stronger than the atlas. This can be attributed to multiple factors: firstly, surface layer thickness (the tidal atlas first layer thickness is 5 m, compared to 3 m and 1 m for STLE200 and CIOPS-E), secondly different baroclinic circulation intensity due to different freshwater inputs (2017 is the second highest maximum freshet St. Lawrence runoff in the last 60 years), thirdly winds are not taken into account in the tidal atlas, and finally different tidal results between models (amplitude and phase of the different constituents). On Figure 57 (ebb tide), the main differences between STLE200 and CIOPS-E are, firstly, the impact of Ile Rouge (in the middle of the estuary, below the Saguenay Fjord's mouth) dividing the ebbing current in two and creating a recirculation downstream of the island and secondly, the impact of Saguenay Fjord surface currents. Both of these structures are similar between STLE200 and the tidal atlas. On Figure 58 (flood tide), we see that the fine structures of surface currents are better represented in STLE200 than in CIOPS-E.

In general, during both ebb and flood tide, surface current patterns of STLE200 agree better with the tidal atlas than CIOPS-E.

5.3. WATER PROPERTIES

5.3.1. Sea-surface temperature

No sea-surface temperature data were available inside the domains of the St. Lawrence model. Some can perhaps be found (at IML-4, for example), and considered in the future. However, multiple near-surface moored CTDs are presented in the next section.

5.3.2. Moored CTDs

Temperature and salinity sensors are fixed to all active tide gauges described at section 5.1. However, salinity data is unusable for most of the upstream stations in the Riverine Estuary. Due to the quantity of stations and years available, only figures and tables for year 2017 will be presented here. Year 2017 is chosen because all stations had data for this year, which is not always the case. Station 3057, for which temperature and salinity are present for years 2016-2019, and station 3100, are presented for each available year (only in tables, Table 24 to Table 26). These 2 stations are the only ones with multi-year data common to all 3 models.

The easternmost station, 2985 (Figure 59) is common to only CIOPS-E and STLE500. CIOPS-E shows better scores (bias, CRMSE, χ^2 and Pearson) for both salinity and temperature (Table 23).

Station 3057 (Figure 60) is common to the 3 models. CIOPS-E is too warm from April until July, and STLE200 is showing 3 warm spikes between August and October. A fresh salinity bias in CIOPS-E is persistent throughout the year, with values between -20 and -5 psu. All temperature scores are significantly improved in STLE500 and STLE200 compared to CIOPS-E for this station (Table 23). Salinity bias and Pearson scores are also improved, but CRMSE and χ^2 are better for CIOPS-E (χ^2 exceeds 1 for STLE500 and STLE200, meaning that variance of error exceeds that of observations). The reason for this is due to the low variability in the CIOPS-E salinity signal. Indeed, looking at panel 2 of Figure 60, we see that the variability of the salinity signal in CIOPS-E is smaller, compared to STLE500 and STLE200, which is expected because mixing is increased in this area in CIOPS-E. The water masses are mostly uniform and non-stratified in the Middle Estuary area in CIOPS-E, and consequently, the tidal effect on salinity variation at station 3057 is minimized. This low variability induced by CIOPS-E increased mixing in the Middle Estuary gives better results for salinity CRMSE and χ^2 compared to STLE200 and STLE500. These high CRMSE values for STLE200 and STLE500 at station 3057 probably mean that horizontal salinity gradient is too high in this area. Indeed, looking at salinity from ferry data in Figure 75, the landmark of Ile-aux-Coudres (within ~10 km of station 3057) shows a stronger temporal variation in salinity for STLE200 and STLE500 compared to observations. In observations, the region of high salinity variation is downstream of Ile-aux-Coudres (and station 3057).

Station 3100 (Figure 61) is also common to the 3 models. Here STLE500 and STLE200 are giving similar results, and CIOPS-E shows a warm bias between March and June, and a cold bias between June and December. This bias is due to a wrong temperature climatology used in the r1d model couple to CIOPS-E, which is connected close to this station. Also, this climatology is not interpolated in time, which gives the staircase look to the CIOPS-E temperature signal. All the scores are improved in STLE500 and STLE200, and STLE200 is slightly improved compared to STLE500 for CRMSE, χ^2 and Pearson (Table 23).

Station 3248 (Figure 62) is common to STLE500 and STLE200, and scores are similar between both models. CRMSE is slightly better for STLE200 (Table 23).

Stations 3300, 3335, 3353 and 3600 are presented on Figure 62 to Figure 66. They all show a stronger cold bias in October and December (~-2.5 degrees). This is possibly due to the use of a climatology for St. Lawrence temperature.

Looking at yearly temperature scores for station 3057 (Table 24), all scores are improved in STLE500 and STLE200 compared to CIOPS-E, and no trends in bias from year to year are observed in any model. Salinity bias (Table 25) is improved in both higher resolution models for every year, and no trends are observed. CRMSE and χ^2 scores are better in CIOPS-E for reasons detailed above (low variability in CIOPS-E salinity signal at this station). χ^2 exceeds 1 for STLE500 and STLE200, meaning that variance of error exceeds that of observations.

All temperature scores for station 3100 are improved for all years with increased resolution, with two exceptions (bias in year 2020 is smaller in STLE500 compared to STLE200). No trends are observed in bias from year to year.

5.3.3. CTD profiles

Maps of the CTD casts and defined polygons are shown in Figure 67 and Figure 68. Only the profiles common to all 3 domains were used for analysis, and no outlier profiles were removed. The initial default threshold value of 3 x standard deviation in a specific polygon was removing all CTD casts in the Middle Estuary because of the large CIOPS-E standard deviation.

Over the area named All_200 (Figure 69), which includes all CTDs in the STLE200 domain common to the 3 domains, STLE500 has the smaller temperature bias over the whole water column. Surface temperatures (0 – 10m) are colder in CIOPS-E. Salinity are comparable between STLE500 and STLE200.

Over the area named Middle (Figure 70), which includes all CTDs in the Middle Estuary common to the 3 domains, STLE500 is showing smaller bias over the whole water column, and CIOPS-E is showing colder bias for the top 10 m and a warmer bias from 10m to bottom. Both higher resolution models perform similarly for salinity, but STLE200 shows a saltier bias from 10m to bottom. CIOPS-E results have a strong fresh bias at all depths in this area, due to the increased mixing west of Tadoussac.

Over the area named Sag (Figure 71), which includes all CTDs in the Saguenay Fjord common to the 3 domains, STLE500 is also showing smaller bias in temperature and the top 10 m are too cold in CIOPS-E. For surface salinity, STLE200 presents the smaller bias, CIOPS-E is too salty and STLE500 is too fresh. Figure 72 shows the bias and standard deviation PDFs for only STLE200, which is the only domain covering entirely the Saguenay Fjord. Note that the number of CTD casts is higher (approximately six times more), because the preceding figure includes only CTDs common to the 3 models, and CIOPS-E has just a small part of the Saguenay Fjord. There is a positive salinity bias of approximately 2 psu and a positive temperature bias over the whole water column, apart from the first few meters for temperature.

Over the area named Maritim (Figure 73), which includes all CTDs in the Maritime Estuary common to CIOPS-E and STLE500, bias is generally smaller in CIOPS-E compared to STLE500 for salinity and temperature. This, again, might be explained by the increased mixing in CIOPS-E upstream of Tadoussac: the objective of this increase was to better reproduce the water masses downstream of Tadoussac, in the Maritime Estuary.

A general comment about all CTD figures: the increased mixing west of Tadoussac in CIOPS-E was added when CIOPS-E migrated from version 1 to version 2. The salinity bias seen in the STLE200 and STLE500 PDFs increased by a value around 1 over the whole water column when using CIOPS-E v2 instead of CIOPS-E v1. The change in CIOPS-E explains at least part of the salinity bias for STLE500 and STLE200 that is seen on CTD cast PDF figures.

5.3.4. Ferries

The Oceanex Connaigra is a ferry going from Montréal to St. John's Newfoundland multiple times during the year. Ship tracks are shown on Figure 74. There is a salinity and temperature sensor on it, at an average depth of 8m. Only year 2018 is shown in the figures, but all years (2016 to 2022) are compiled in the scores table.

Figure 75 shows the observed and modeled salinity on the first column, and the difference between model and observations on the second column. If we look at the 3 different models, we see that the seasonal cycle and the spatial variation is quite well reproduced by the 200m and the 500m models, but CIOPS-E is missing all of it because of the increased vertical mixing upstream of Tadoussac. Both STLE200 and STLE500 are showing a fresh bias upstream of Ile-aux-Coudres, and a saltier bias between Ile-aux-Coudres and Tadoussac. All scores (bias, CRMSE and RMSE) are improved in STLE200 and STLE500 compared to CIOPS-E for salinity (Table 27), for every year. Bias is smaller in STLE500 (-0.455 to 0.675, and 0.106 for 2016-2022 period) compared to STLE200 (0.382 to 1.493, and 0.959 for 2016-2022 period). This is possibly due to the higher vertical resolution (~1m) in STLE500 compared to STLE200 (~3m). Bias in CIOPS-E is -5.759 psu for 2016-2022 period, but this bias is more asymmetric in space than the 2 higher resolution models, being negative western of Tadoussac and positive eastern of Tadoussac. A bias computed separately for these two regions would give higher bias values for CIOPS-E, as seen on the figure.

Figure 76 shows the observed and modeled temperature on the first column, and the differences on the second column. Differences are more important in CIOPS-E: a warm bias exists upstream of Ile-aux-Coudres from March until July, and it changes to a cold bias from July until the end of October (when the data ends). Generally, a warm bias exists between Ile-aux-Coudres and Tadoussac, and STLE500 is giving better overall results. Temperature bias in Table 27 are reduced in STLE500 compared to STLE200. This might be due again to the vertical resolution of the surface layers (~1m for STLE500 and ~3 for STLE200). Temperature biases are smaller in CIOPS-E for period 2016-2022 compared to STLE200, however Figure 76 shows that this bias is asymmetric in time and space in CIOPS-E, as mentioned above. CRMSE and RMSE are improved for STLE500 and STLE200 compared to CIOPS-E for all years.

5.4. DRIFT

Two sets of data were available inside the St. Lawrence model domains. The first dataset comes from year 2020 of the Gulf of St. Lawrence Tracer Release eXperiment (TReX), where drifters were released in the Maritime Estuary (not in STLE200's domain). A total of 232 drifter paths from this experiment were used to assess the models drift capacity in this area. These observed paths are shown on Figure 77. Mean Molcard skill are similar for both STLE500 and CIOPS-E models (Figure 79 and Table 28). The first 6 hours shows higher Molcard skill for STLE500, and CIOPS-E values are higher for the rest of the 24h. The same thing is reflected in the mean separation distance (Figure 80).

The second drifter's dataset counts only 4 observed paths near Saint-François, at the eastern end of Ile d'Orléans (Figure 78) and were collected by ECRC-SIMEC (Eastern Canada Response Corporation, Société d'Intervention Maritime, Est du Canada). Duration of the drift are shorter, and only the first 4 hours of Molcard skill and mean separation distance were computed. We can see on Figure 81 and Figure 82 that Molcard skill and mean separation distance are significantly improved for STLE500 and STLE200 compared to CIOPS-E: +35% after 4 hours for Molcard from CIOPS-E to STLE200, and mean separation distance reduced by 42.4% (4.03 km to 2.32 km) (Table 29). STLE500 and STLE200 shows similar results.

6. FORECAST EVALUATION RESULTS

Forecast evaluation was made for the period from December 1, 2021, to February 1, 2022. 48 hours forecast were made every day starting at 0h00 during this period.

6.1. NON-TIDAL WATER LEVEL

Water level stations common to 2 or more models are presented, which makes five stations (Figure 83 to Figure 87), on we see which bias and CRMSE between models and observations. For station 2985 (Figure 83), only common to STLE500 and CIOPS-E, bias is slightly smaller for STLE500 compared to CIOPS-E, and no trends are visible over the 48h periods. CRMSE is slightly smaller for STLE500, and a small increasing trend is seen through the 48h. The main factor to explain this trend (and the one in the following figures) is the atmospheric forecast inaccuracy (winds, and to a lesser extent pressure). For station 3424 in Figure 84, bias is stronger in CIOPS-E: approximately -4 cm compared to around -2 cm for STLE500 and STLE200. CRMSE is similar for the 3 models, STLE200 being slightly smaller than the 2 coarser models. For station 3057 (Figure 85), bias is similar between STLE500 and STLE200 (around -3 cm), and bigger for CIOPS-E (around +25 cm). CRMSE is comparable for the 3 models. We see similar results for bias at station 3100 (Figure 86): STLE500 and STLE200 are similar (around -5 cm) and bigger for CIOPS-E (around +23 cm). CRMSE is also similar for STLE200 and STLE500 (~12cm), and bigger for CIOPS-E (~15cm). For station 3248, bias is around zero for STLE200, and around +35 cm for STLE500. CRMSE is smaller for STLE200 (~13cm) compared to STLE500 (~15 cm).

7. SUMMARY

Model results from CIOPS-E, STLE500 and STLE200 were compared to water level gauges (including during storm surge), horizontal and multi-level ADCP, the Atlas of Tidal Currents, moored CTDs, CTD profiles, ferry thermosalinographs and drifter's path. Model results comparison with observations shows that STLE200's modeling performances are generally improved for all observations used compared to CIOPS-E in the Middle Estuary. We also see improvements from 500m resolution to 200m, except for water masses, where STLE500 shows smaller temperature and salinity bias. Forecast evaluation was performed for non-tidal water-level, which shows no trends in bias over 48h forecast results.

8. KEY FINDINGS

- The connection with the r1d model result in an increase in mean water level for both CIOPS-E and STLE500 (around +31cm). It's the opposite for STLE200 near Trois-Rivières (around -30 cm).
- Tidal water level scores are improved at all common stations in STLE200 and M2 tidal error is reduced in STLE200 at all common stations. CRMSE is 7.3 cm in the Middle Estuary for STLE200, compared to 32.6 cm for CIOPS-E.
- All total water level scores are improved everywhere with increased resolution. CRMSE in the Middle Estuary is 14.7 cm for STLE200, 21.5 cm for STLE500 and 35.4 cm for CIOPS-E.
- Storm surges are clearly visible in all three models, and scores are improved for higher resolution models.

- When surface currents are compared with HADCPs in Québec and Lévis, CRMSE is averaging to 43.8 cm/s for STLE500 and 19.4 cm/s for STLE200. The signal is tidally asymmetric (in obs. and results), probably due to a significant contribution of M4.
- STLE500 shows better performances for the first 30m for total currents, and CIOPS-E is showing better performances from 30m to bottom for total currents at IML-4 buoy station.
- Comparison with MCTDs, ferry thermosalinograph and CTD casts highlights the strong improvement of STLE200 and STLE500 over CIOPS-E in the Middle Estuary, due in part to the increased mixing upstream of Tadoussac in CIOPS-E.
- Forecast eval shows that no trends are visible over the 48h periods for bias, and a small increasing trend is seen in CRMSE over the 48h.

9. ACKNOWLEDGEMENTS

Thanks to Denis Lefaivre for his continuous support and all the interesting discussions. Thanks to all the OPP port leads group: Rachel Horwitz, Michael Dunphy, Stephanne Taylor, Adam Drozdowski, Maxim Krassovski and Hauke Blanken. Thanks to François Roy, Greg Smith, Jean-Philippe Paquin and Frederic Dupont at ECCC for their support on the model development. Thanks to Nancy Soontiens for the drift evaluation tool and for her help with St. Lawrence drift data. Thanks to Ji Lei for her help with the maestro suite. Thanks to Caroline Lafleur, Félix St-Pierre and Michel Rousseau for collecting and researching ocean data. Thanks to Simon Senneville for numerous interesting exchanges about St. Lawrence numerical modelling. Thanks also to Pascal Matte, Pierre Levasseur (SIMEC drifter's data), Peter Galbraith (Ferry data), Alain D'Astous (STLT1061 outputs), André Godin (meaningful discussions about vertical datum) and all the colleagues that collected data in the St. Lawrence estuary.

10. REFERENCES CITED

Aubrey, D.G., and P.E. Speer. 1985. "A Study of Non-Linear Tidal Propagation in Shallow Inlet/Estuarine Systems Part I: Observations." *Estuarine, Coastal and Shelf Science* 21 (2): 185–205. https://doi.org/10.1016/0272-7714(85)90096-4.

Backhaus, Jan O. 1983. "A Semi-Implicit Scheme for the Shallow Water Equations for Application to Shelf Sea Modelling." *Continental Shelf Research* 2 (4): 243–54. https://doi.org/10.1016/0278-4343(82)90020-6.

———. 1985. "A Three-Dimensional Model for the Simulation of Shelf Sea Dynamics." *Deutsche Hydrographische Zeitschrift* 38 (4): 165–87. https://doi.org/10.1007/BF02328975.

Blanken, Hauke, Caterina Valeo, Charles Hannah, Usman T. Khan, and Tamás Juhász. 2021. "A Fuzzy-Based Framework for Assessing Uncertainty in Drift Prediction Using Observed Currents and Winds." *Frontiers in Marine Science* 8 (November):618094. https://doi.org/10.3389/fmars.2021.618094.

Chen, Changsheng, Hedong Liu, and Robert C. Beardsley. 2003. "An Unstructured Grid, Finite-Volume, Three-Dimensional, Primitive Equations Ocean Model: Application to Coastal Ocean and Estuaries." *Journal of Atmospheric and Oceanic Technology* 20 (1): 159–86. https://doi.org/10.1175/1520-0426(2003)020<0159:AUGFVT>2.0.CO;2.

Cummins, Patrick F., and Lie-Yauw Oey. 1997. "Simulation of Barotropic and Baroclinic Tides off Northern British Columbia." *Journal of Physical Oceanography* 27 (5): 762–81. https://doi.org/10.1175/1520-0485(1997)027<0762:SOBABT>2.0.CO;2.

Cummins, Patrick F., and Pramod Thupaki. 2018. “A Note on Evaluating Model Tidal Currents against Observations.” *Continental Shelf Research* 152 (January):35–37. https://doi.org/10.1016/j.csr.2017.10.007.

Daniel, Pierre, Gwénaële Jan, Fanch Cabioc’h, Yves Landau, and Erwann Loiseau. 2002. “Drift Modeling of Cargo Containers.” *Spill Science & Technology Bulletin* 7 (5–6): 279–88. https://doi.org/10.1016/S1353-2561(02)00075-0.

Dronkers, J. J. 1969. “Tidal Computations for Rivers, Coastal Areas, and Sea.” *Journal of the Hydraulics Division* 95 (1): 29–78. https://doi.org/10.1061/JYCEAJ.0001941.

Dupont, F., S. Higginson, R. Bourdallé-Badie, Y. Lu, F. Roy, G. C. Smith, J.-F. Lemieux, G. Garric, and F. Davidson. 2015. “A High-Resolution Ocean and Sea-Ice Modelling System for the Arctic and North Atlantic Oceans.” *Geoscientific Model Development* 8 (5): 1577–94. https://doi.org/10.5194/gmd-8-1577-2015.

El-Sabh, Mohammed. 1988. “Physical Oceanography of the St. Lawrence Estuary.” *Hydrodynamics of Estuaries, Vol. II, Estuarine Case Studies.*, 1988, CRC Press edition.

El-Sabh, Mohammed I., and Tad. S. Murty. 1990. “Mathematical Modelling of Tides in the St. Lawrence Estuary.” In *Oceanography of a Large-Scale Estuarine System*, edited by Mohammed I. El-Sabh and Norman Silverberg, 10–50. New York, NY: Springer New York. https://doi.org/10.1007/978-1-4615-7534-4_2.

Hourston, Roy A.S. 2021. *Surface Ocean Circulation Tracking Drifter Data from the Northeastern Pacific and Western Arctic Oceans, 2014-2020*. Sidney, B.C.: Fisheries and Oceans Canada = Pêches et Océans Canada.

Kundu, Pijush K. 1976. “Ekman Veering Observed near the Ocean Bottom.” *Journal of Physical Oceanography* 6 (2): 238–42. https://doi.org/10.1175/1520-0485(1976)006<0238:EVONTO>2.0.CO;2.

Large, WIlliam George, and Stephen G. Yeager. 2004. “Diurnal to Decadal Global Forcing for Ocean and Sea-Ice Models: The Data Sets and Flux Climatologies.” NCAR Technical Note NCAR/TN-460+STR. Boulder, CO: Climate and Global Dynamics Division: National Center for Atmospheric Research.

Lefaivre, Denis, Alain D’Astous, and Pascal Matte. 2016. “Hindcast of Water Level and Flow in the St. Lawrence River Over the 2005–2012 Period.” *Atmosphere-Ocean* 54 (3): 264–77. https://doi.org/10.1080/07055900.2016.1168281.

Madec, Gurvan. 2016. *NEMO Ocean Engine*. Note Du Pole de Modelisation de l’Institut Pierre-Simon Laplace 27. NEMO European Consortium.

Milbrandt, Jason A., Stéphane Bélair, Manon Faucher, Marcel Vallée, Marco L. Carrera, and Anna Glazer. 2016. “The Pan-Canadian High Resolution (2.5 Km) Deterministic Prediction System.” *Weather and Forecasting* 31 (6): 1791–1816. https://doi.org/10.1175/WAF-D-16-0035.1.

Molcard, A., P.M. Poulain, P. Forget, A. Griffa, Y. Barbin, J. Gaggelli, J.C. De Maistre, and M. Rixen. 2009. “Comparison between VHF Radar Observations and Data from Drifter Clusters in the Gulf of La Spezia (Mediterranean Sea).” *Journal of Marine Systems* 78 (November):S79–89. https://doi.org/10.1016/j.jmarsys.2009.01.012.

Muir, Langley Russel. 1981. “Internal tides in a partially mixed estuary.” Phd Thesis, University of Southampton. https://waves-vagues.dfo-mpo.gc.ca/library-bibliotheque/57080.pdf.

Neu, H. J. A. 1970. “A Study on Mixing and Circulation in the St. Lawrence Estuary up to 1964.” *AOL REPORT 1970-9*, 1970.

Niiler, Pearn P., Andrew S. Sybrandy, Kenong Bi, Pierre M. Poulain, and David Bitterman. 1995. “Measurements of the Water-Following Capability of Holey-Sock and TRISTAR Drifters.” *Deep Sea Research Part I: Oceanographic Research Papers* 42 (11–12): 1951–64. https://doi.org/10.1016/0967-0637(95)00076-3.

Nudds, Shannon, Youyu Lu, Simon Higginson, Susan P. Haigh, Jean-Philippe Paquin, Mitchell O’Flaherty-Sproul, Stephanne Taylor, et al. 2020. “Evaluation of Structured and Unstructured Models for Application in Operational Ocean Forecasting in Nearshore Waters.” *Journal of Marine Science and Engineering* 8 (7): 484. https://doi.org/10.3390/jmse8070484.

Paquin, Jean-Philippe, Youyu Lu, Stephanne Taylor, Hauke Blanken, Guillaume Marcotte, Xianmin Hu, Li Zhai, et al. 2020. “High-Resolution Modelling of a Coastal Harbour in the Presence of Strong Tides and Significant River Runoff.” *Ocean Dynamics* 70 (3): 365–85. https://doi.org/10.1007/s10236-019-01334-7.

Paquin, Jean-Philippe, François Roy, Gregory C. Smith, Frédéric Dupont, Sarah MacDermid, Yukie Hata, Oleksandr Huizy, et al. 2021a. “Coastal Ice Ocean Prediction System for the East Coast of Canada (CIOPS-E): Update from Version 1.5.0 to 2.0.0” Canadian Centre for Meteorological and Environmental Prediction Tech. Note. https://collaboration.cmc.ec.gc.ca/cmc/cmoi/product_guide/docs/tech_notes/technote_ciops-west-200_e.pdf.

Paquin, Jean-Philippe, Gregory C. Smith, Frédéric Dupont, Sarah MacDermid, Yukie Hata, Oleksandr Huizy, Ji Lei, et al. 2021b. “Coastal Ice Ocean Prediction System for the West Coast of Canada (CIOPS-W), Update from Version 1.5.0 to 2.0.0.” Canadian Centre for Meteorological and Environmental Prediction Tech. Note. https://collaboration.cmc.ec.gc.ca/cmc/cmoi/product_guide/docs/tech_notes/technote_ciops-west-200_e.pdf.

Paquin, Jean-Phillipe, Gregory C. Smith, Francois Roy, Frederic Dupont, Sarah MacDermid, Ji Lei, Youyu Lu, Stephanne Taylor, Hauke Blanken, and Li Zhai. 2022. “Coastal Ice Ocean Prediction System for the West Coast of Canada (CIOPS-W): System Description for Versions 1.0.0 and 1.5.0.” Canadian Centre for Meteorological and Environmental Prediction Tech. Note. https://collaboration.cmc.ec.gc.ca/cmc/cmoi/product_guide/docs/tech_notes/technote_ciops-west-100_e.pdf.

Röhrs, Johannes, and Kai H. Christensen. 2015. “Drift in the Uppermost Part of the Ocean.” *Geophysical Research Letters* 42 (23). https://doi.org/10.1002/2015GL066733.

Röhrs, Johannes, Kai Håkon Christensen, Lars Robert Hole, Göran Broström, Magnus Drivdal, and Svein Sundby. 2012. “Observation-Based Evaluation of Surface Wave Effects on Currents and Trajectory Forecasts.” *Ocean Dynamics* 62 (10–12): 1519–33. https://doi.org/10.1007/s10236-012-0576-y.

Saucier, FJ, J Chassé, M Couture, R Dorais, A D’astous, D Lefaivre, and A Gosselin. 1999. “The Making of a Surface Current Atlas of the St. Lawrence Estuary, Canada.” *WIT Transactions on the Built Environment* 43.

Saucier, François J. 2003. “Modeling the Formation and Circulation Processes of Water Masses and Sea Ice in the Gulf of St. Lawrence, Canada.” *Journal of Geophysical Research* 108 (C8): 3269. https://doi.org/10.1029/2000JC000686.

Saucier, François J., and Joël Chassé. 2000. “Tidal Circulation and Buoyancy Effects in the St. Lawrence Estuary.” *Atmosphere-Ocean* 38 (4): 505–56. https://doi.org/10.1080/07055900.2000.9649658.

Saucier, François J., François Roy, Simon Senneville, Gregory Smith, Denis Lefaivre, Bruno Zakardjian, and Jean-François Dumais. 2009. “Modélisation de la circulation dans l’estuaire et le golfe du Saint-Laurent en réponse aux variations du débit d’eau douce et des vents.” *Revue des sciences de l’eau* 22 (2): 159–76. https://doi.org/10.7202/037480ar.

Silverberg, Norman, and Mohammed I. El-Sabh. 1990. “The St. Lawrence Estuary: Concluding Remarks.” In *Oceanography of a Large-Scale Estuarine System*, edited by Mohammed I. El-Sabh and Norman Silverberg, 421–29. New York, NY: Springer New York. https://doi.org/10.1007/978-1-4615-7534-4_18.

Simons, Rachel D., Stephen G. Monismith, Ladd E. Johnson, Gesche Winkler, and François J. Saucier. 2006. “Zooplankton Retention in the Estuarine Transition Zone of the St. Lawrence Estuary.” *Limnology and Oceanography* 51 (6): 2621–31. https://doi.org/10.4319/lo.2006.51.6.2621.

Smith, Stuart D. 1988. “Coefficients for Sea Surface Wind Stress, Heat Flux, and Wind Profiles as a Function of Wind Speed and Temperature.” *Journal of Geophysical Research* 93 (C12): 15467. https://doi.org/10.1029/JC093iC12p15467.

St-Onge-Drouin, Simon, Gesche Winkler, Jean-François Dumais, and Simon Senneville. 2014. “Hydrodynamics and Spatial Separation between Two Clades of a Copepod Species Complex.” *Journal of Marine Systems* 129 (January):334–42. https://doi.org/10.1016/j.jmarsys.2013.07.014.

Soontiens, Nancy, and Jennifer Holden J. 2024. “A framework for evaluation and characterization of drift prediction in the marine environment.” Can. Tech. Rep. Hydrogr. Ocean Sci. 383: ix + 45 p. https://waves-vagues.dfo-mpo.gc.ca/library-bibliotheque/41252287.pdf.

Sutherland, Graig, Nancy Soontiens, Fraser Davidson, Gregory C. Smith, Natacha Bernier, Hauke Blanken, Douglas Schillinger, et al. 2020. “Evaluating the Leeway Coefficient of Ocean Drifters Using Operational Marine Environmental Prediction Systems.” *Journal of Atmospheric and Oceanic Technology* 37 (11): 1943–54. https://doi.org/10.1175/JTECH-D-20-0013.1.

Zhang, Minghong, William Perrie, and Zhenxia Long. 2019. “Springtime North Pacific Oscillation and Summer Sea Ice in the Beaufort Sea.” *Climate Dynamics* 53 (1–2): 671–86. https://doi.org/10.1007/s00382-019-04627-1.

11. TABLES

Table 1. Main parameters of STLE200's and STLE500's configuration.

Parameter	Outer grid (STLE500)	Inner grid (STLE200)
Grid dimensions, NX × NY × NZ	290 × 813 × 75	670 × 1640 × 36
Horizontal resolution, ΔX × ΔY	Approx. 500 m	Approx. 200 m
Vertical resolution	1 m surface, 26 m bottom	3 m surface, 20 m bottom
Baroclinic / barotropic time step	30 s / 4.3 s	8 s / 1.6 s
Open boundary update frequency	1 h	1 h
Open boundary SSH offset	0 cm	0 cm
Open boundary barotropic/baroclinic/tracers	Flather/specified/specified	Flather/specified/specified
Source of tidal forcing	OTPS	OTPS
Tidal constituents forced	M2, S2, N2, K2, K1, O1, Q1, P1, M4, Mf, Mm, Mn4, Ms4	M2, S2, N2, K2, K1, O1, Q1, P1, M4, Mf, Mm, Mn4, Ms4
Equation of state	EOS-80	EOS-80
Free surface	Variable volume	Variable volume
Light penetration	Two band	Two band
Lateral boundary condition	Partial slip (shlat=1.2)	Partial slip (shlat=0.6)
Momentum advection	Vector form, 20 sub-steps for vertical advection	Vector form, 20 sub-steps for vertical advection
Momentum lateral diffusion	Horizontal bilaplacian and Smagorinsky	Horizontal bilaplacian and Smagorinsky
Tracer advection	Total Variance Dissipation, 20 vertical advection sub-steps	Total Variance Dissipation, 20 vertical advection sub-steps
Tracer lateral diffusion	Iso-neutral Laplacian and Smagorinsky	Iso-neutral Laplacian and Smagorinsky
Vertical diffusion	k-ε (GLS)	k-ε (GLS)
Bottom friction	Log-layer	Log-layer, spatially varying
Bottom roughness length	0.0001	0.0002

Table 2. Monthly climatological runoff (m^3/s).

River name	Longitude	Latitude	Jan	Feb	Mar	Apr	May	Jun	Jul	Aug	Sep	Oct	Nov	Dec
Bécancour	-72,44	46,38	11	11	27	76	32	13	9	14	13	19	21	19
Batiscan	-72,23	46,52	37	36	47	231	265	105	72	67	61	95	94	63
Saint-Anne	-72,20	46,55	16	16	19	96	151	58	41	40	41	57	48	26
Portneuf	-71,87	46,68	5	3	3	29	11	7	5	6	10	8	11	4
Jacques-Cartier	-71,74	46,67	22	22	23	86	189	83	58	55	55	68	50	33
Chaudière	-71,27	46,74	52	53	137	173	228	85	55	76	72	105	120	92
Etchemin	-71,23	46,76	11	14	21	84	43	21	17	18	16	25	27	20
Saint-Charles	-71,21	46,82	2	0	3	30	14	8	2	4	9	8	9	3
Rivière du Sud	-70,52	47,02	6	10	22	104	138	15	13	0	0	0	101	0
Malbaie	-70,06	47,66	12	10	11	46	124	56	32	25	23	30	26	15
Saguenay	-69,64	48,12	1090	1120	1130	1220	1390	1290	1180	1160	1160	1200	1160	1080
Portneuf	-69,03	48,66	19	16	16	70	244	117	61	49	38	49	44	28
Betsiamite	-68,81	48,82	346	344	301	247	289	257	213	259	214	259	276	311
Rimouski	-68,58	48,46	10	7	9	51	143	46	23	18	16	19	25	18
Outardes	-68,36	49,03	194	167	148	201	868	833	478	395	370	400	324	247
Manicouagan	-68,04	49,20	646	632	571	513	1280	1830	1050	855	805	859	757	686
Godbout	-67,53	49,32	13	12	12	43	177	63	37	24	27	45	34	21
Matane	-67,53	48,85	8	5	4	16	177	83	36	21	20	33	37	26

Table 3. Water level active station ID, names and offset to shift water level to CGVD28.

Station ID	Station name	Offset (m)
2985	Rimouski	2.277
3057	Saint-Joseph-de-la-Rive	3.375
3075	Banc du Cap Brule	2.625
3100	Saint-Laurent I.O.	2.523
3110	Saint-Francois I.O.	2.116
3248	Vieux-Quebec	1.982
3280	Neuville	1.374
3300	Portneuf	1.122
3335	Deshaillons-sur-Saint-Laurent	0.702
3345	Batiscan	-1.89
3353	Becancour	-2.564
3360	Trois-Rivieres	-2.956
3424	Baie-Sainte-Catherine	2.405
3460	Port Alfred	2.648

Table 4. Water level historical stations ID and names.

Station ID	Station name	Station ID	Station name	Station ID	Station name
2826	Godbout	3052	Cap-aux-Oies	3130	Riviere-du-Loup
2840	Baie-Comeau	3058	St-Bernard-Ile-aux-Coudres	3140	Ile-aux-Lièvres

Station ID	Station name	Station ID	Station name	Station ID	Station name
2880	Forestville	3060	Cap-aux-Corbeaux	3160	Pointe-aux-Orignaux
2883	Sainte-Anne-de-Portneuf	3070	Sault-au-Cochon	3170	Saint-Jean-Port-Joli
2900	Les Escoumins	3071	Rocher Neptune	3175	L'islet-sur-Mer
2955	Matane	3075	Banc du Cap Brulé	3180	Ile aux Grues
2975	Institut Maurice-Lamontagne	3080	St-Joachim	3190	Grosse Ile
2980	Pointe-au-Père	3087	Ste-Anne-de-Beaupré	3200	Berthier
2995	Bic	3095	Montmorency	3246	Saint-Charles(bassin)
3000	Ile Bicquette	3105	St-Jean-Ile-d'Orléans	3250	Québec (Lauzon)
3005	Trois-Pistoles	3110	St-Laurent-Ile-d'Orléans	3251	Immigration Warf
3030	Saint-Simeon	3120	Ile Verte	3260	Saint-Romuald
3045	Pointe-au-Pic	3122	Ile Verte	3264	Quai Irving
3048	Saint-Irenée	3125	Gros Cacouna	3425	Tadoussac

Table 5. M2 constituent comparison for active tide gauges for year 2021.

	Observed		Amplitude Error (m)			Phase Error (deg)			Tidal Error (m)		
Station	Amplitude (m)	Phase (deg)	CIOPSE	STLE500	STLE200	CIOPSE	STLE500	STLE200	CIOPSE	STLE500	STLE200
3360	0.085 ± 0.002	135.4 ± 2.0	—	—	+0.055	—	—	-9.41	—	—	0.041
3353	0.192 ± 0.005	117.1 ± 1.5	—	—	+0.080	—	—	-16.80	—	—	0.074
3345	0.286 ± 0.006	100.1 ± 0.9	—	—	+0.079	—	—	-17.46	—	—	0.089
3335	0.619 ± 0.010	68.5 ± 0.8	—	—	-0.024	—	—	-7.71	—	—	0.060
3300	1.421 ± 0.011	28.7 ± 0.4	—	—	-0.098	—	—	+0.18	—	—	0.069
3280	1.536 ± 0.011	9.8 ± 0.4	—	—	-0.018	—	—	-1.02	—	—	0.023
3248	1.833 ± 0.012	331.3 ± 0.4	—	-0.618	-0.025	—	-0.67	-0.32	—	0.437	0.019
3100	2.047 ± 0.011	304.0 ± 0.3	-0.436	+0.065	+0.028	+4.51	-5.06	-0.06	0.325	0.138	0.020
3057	2.023 ± 0.010	257.5 ± 0.3	-0.009	+0.009	-0.011	-11.34	-6.17	-2.28	0.282	0.154	0.057
3424	1.532 ± 0.008	215.7 ± 0.3	+0.096	-0.024	-0.107	-15.40	-10.16	+1.71	0.306	0.191	0.082
3460	1.782 ± 0.010	219.4 ± 0.3	—	—	-0.121	—	—	+1.27	—	—	0.090
2985	1.254 ± 0.006	201.5 ± 0.2	+0.108	-0.009	—	-6.49	-2.86	—	0.130	0.045	—

Table 6. S2 constituent comparison for active tide gauges for year 2021.

	Observed		Amplitude Error (m)			Phase Error (deg)			Tidal Error (m)		
Station	Amplitude (m)	Phase (deg)	CIOPSE	STLE500	STLE200	CIOPSE	STLE500	STLE200	CIOPSE	STLE500	STLE200
3360	0.024 ± 0.003	174.8 ± 5.9	—	—	+0.014	—	—	-10.73	—	—	0.011
3353	0.052 ± 0.005	156.3 ± 5.3	—	—	+0.019	—	—	-14.50	—	—	0.017
3345	0.075 ± 0.007	140.1 ± 4.0	—	—	+0.015	—	—	-13.72	—	—	0.018
3335	0.135 ± 0.010	114.2 ± 4.2	—	—	-0.001	—	—	-5.44	—	—	0.009
3300	0.286 ± 0.009	79.7 ± 2.1	—	—	-0.015	—	—	+2.41	—	—	0.014

	Observed		Amplitude Error (m)			Phase Error (deg)			Tidal Error (m)		
Station	Amplitude (m)	Phase (deg)	CIOPSE	STLE500	STLE200	CIOPSE	STLE500	STLE200	CIOPSE	STLE500	STLE200
3280	0.314 ± 0.011	60.8 ± 1.5	—	—	+0.001	—	—	+1.32	—	—	0.005
3248	0.413 ± 0.011	19.9 ± 1.7	—	-0.148	-0.006	—	+1.04	+2.07	—	0.105	0.011
3100	0.488 ± 0.011	352.4 ± 1.4	-0.109	-0.004	+0.007	+3.45	-1.87	+2.07	0.079	0.012	0.014
3057	0.577 ± 0.009	297.6 ± 1.0	-0.011	-0.033	-0.006	-11.24	-4.89	-0.76	0.080	0.041	0.007
3424	0.484 ± 0.006	258.1 ± 1.1	+0.003	-0.033	-0.053	-18.93	-12.12	+1.66	0.113	0.074	0.038
3460	0.570 ± 0.009	262.4 ± 1.0	—	—	-0.056	—	—	+1.27	—	—	0.040
2985	0.397 ± 0.005	243.3 ± 0.8	+0.009	-0.019	—	-8.98	-3.15	—	0.045	0.020	—

Table 7. N2 constituent comparison for active tide gauges for year 2021.

	Observed		Amplitude Error (m)			Phase Error (deg)			Tidal Error (m)		
Station	Amplitude (m)	Phase (deg)	CIOPSE	STLE500	STLE200	CIOPSE	STLE500	STLE200	CIOPSE	STLE500	STLE200
3360	0.017 ± 0.003	102.5 ± 9.1	—	—	+0.008	—	—	-5.01	—	—	0.006
3353	0.036 ± 0.005	84.4 ± 8.4	—	—	+0.011	—	—	-14.38	—	—	0.011
3345	0.051 ± 0.005	68.8 ± 6.3	—	—	+0.010	—	—	-14.32	—	—	0.012
3335	0.102 ± 0.010	42.5 ± 4.9	—	—	-0.007	—	—	-6.44	—	—	0.009
3300	0.225 ± 0.011	5.9 ± 2.5	—	—	-0.025	—	—	+2.60	—	—	0.019
3280	0.247 ± 0.010	346.8 ± 2.5	—	—	-0.011	—	—	+1.80	—	—	0.009
3248	0.312 ± 0.012	307.1 ± 2.2	—	-0.124	-0.011	—	+2.67	+2.71	—	0.088	0.013
3100	0.363 ± 0.012	280.0 ± 2.0	-0.094	-0.017	-0.002	+3.12	-0.82	+2.68	0.067	0.013	0.012
3057	0.407 ± 0.009	227.6 ± 1.4	-0.012	-0.023	+0.004	-12.41	-4.82	-1.95	0.061	0.029	0.010
3424	0.336 ± 0.008	189.9 ± 1.4	+0.009	-0.015	-0.019	-18.88	-10.52	+2.02	0.078	0.043	0.016
3460	0.387 ± 0.010	193.3 ± 1.4	—	—	-0.019	—	—	+1.21	—	—	0.014
2985	0.279 ± 0.005	176.2 ± 1.1	+0.012	-0.008	—	-9.72	-2.59	—	0.035	0.010	—

Table 8. K1 constituent comparison for active tide gauges for year 2021.

	Observed		Amplitude Error (m)			Phase Error (deg)			Tidal Error (m)		
Station	Amplitude (m)	Phase (deg)	CIOPSE	STLE500	STLE200	CIOPSE	STLE500	STLE200	CIOPSE	STLE500	STLE200
3360	0.029 ± 0.002	102.5 ± 3.0	—	—	+0.019	—	—	-4.79	—	—	0.013
3353	0.051 ± 0.003	82.1 ± 2.4	—	—	+0.021	—	—	-9.16	—	—	0.016
3345	0.072 ± 0.004	72.7 ± 2.9	—	—	+0.016	—	—	-11.90	—	—	0.016
3335	0.115 ± 0.005	51.2 ± 2.4	—	—	+0.003	—	—	-5.73	—	—	0.009
3300	0.178 ± 0.007	21.5 ± 2.3	—	—	+0.010	—	—	-1.02	—	—	0.007
3280	0.193 ± 0.008	9.0 ± 2.5	—	—	+0.015	—	—	-1.27	—	—	0.011
3248	0.229 ± 0.009	344.8 ± 2.4	—	-0.052	+0.009	—	-344.73	-0.25	—	0.053	0.007
3100	0.252 ± 0.010	328.4 ± 2.1	-0.014	-0.004	+0.012	+11.82	+2.21	+0.25	0.037	0.007	0.009
3057	0.266 ± 0.011	298.3 ± 2.2	+0.001	-0.009	+0.003	-2.00	+2.46	-0.73	0.007	0.010	0.003
3424	0.242 ± 0.009	283.1 ± 2.5	+0.017	-0.006	-0.003	-7.05	+0.07	+3.35	0.025	0.004	0.010
3460	0.247 ± 0.011	284.6 ± 2.3	—	—	0	—	—	+3.62	—	—	0.011
2985	0.236 ± 0.009	278.1 ± 2.3	+0.018	-0.004	—	-1.57	+3.49	—	0.014	0.011	—

Table 9. M4 constituent comparison for active tide gauges for year 2021.

	Observed		Amplitude Error (m)			Phase Error (deg)			Tidal Error (m)		
Station	Amplitude (m)	Phase (deg)	CIOPSE	STLE500	STLE200	CIOPSE	STLE500	STLE200	CIOPSE	STLE500	STLE200
3360	0.033 ± 0.002	181.4 ± 3.6	—	—	+0.019	—	—	-16.59	—	—	0.016
3353	0.071 ± 0.003	158.4 ± 3.6	—	—	+0.040	—	—	-31.34	—	—	0.044
3345	0.088 ± 0.005	122.8 ± 3.1	—	—	+0.044	—	—	-27.99	—	—	0.048
3335	0.184 ± 0.011	57.7 ± 3.4	—	—	+0.010	—	—	-5.71	—	—	0.015
3300	0.310 ± 0.016	336.4 ± 3.0	—	—	+0.041	—	—	+7.26	—	—	0.041
3280	0.235 ± 0.012	297.6 ± 2.7	—	—	+0.034	—	—	+3.42	—	—	0.026
3248	0.274 ± 0.012	216.3 ± 2.5	—	+0.022	+0.033	—	+7.96	+1.71	—	0.032	0.024
3100	0.236 ± 0.010	180.6 ± 2.2	+0.030	+0.051	+0.045	+8.61	-2.87	+1.92	0.034	0.037	0.032
3057	0.100 ± 0.005	320.1 ± 2.7	-0.012	-0.004	-0.005	+31.56	-12.57	-11.48	0.037	0.015	0.014
3424	0.040 ± 0.003	50.3 ± 3.5	-0.005	+0.009	+0.019	+299.61	-34.24	+1.73	0.027	0.019	0.014
3460	0.092 ± 0.005	69.7 ± 3.1	—	—	+0.024	—	—	-0.11	—	—	0.017
2985	0.021 ± 0.002	13.1 ± 5.1	+0.007	+0.013	—	+332.09	+9.99	—	0.010	0.010	—

Table 10. M2 constituent comparison for historical tide gauges.

	Observed		Amplitude Error (m)			Phase Error (deg)			Tidal Error (m)		
Station	Amplitude (m)	Phase (deg)	CIOPSE	STLE500	STLE200	CIOPSE	STLE500	STLE200	CIOPSE	STLE500	STLE200
03360	0.072	142.06	—	—	+0.041	—	—	-16.45	—	—	0.034
03353	0.182	118.08	—	—	+0.054	—	—	-17.60	—	—	0.059
03345	0.293	101.53	—	—	+0.035	—	—	-18.43	—	—	0.074
03335	0.581	70.31	—	—	-0.030	—	—	-9.34	—	—	0.069
03300	1.384	28.90	—	—	-0.119	—	—	+0.14	—	—	0.084
03280	1.538	8.86	—	—	-0.068	—	—	+0.16	—	—	0.048
03264	1.728	338.49	—	-0.853	-0.021	—	+10.49	+0.59	—	0.624	0.020
03260	1.822	335.02	—	-0.881	-0.103	—	+9.21	+1.98	—	0.640	0.085
03251	1.737	330.82	—	-0.701	+0.009	—	+6.66	+3.02	—	0.508	0.065
03246	1.771	330.50	—	-0.570	+0.005	—	-0.98	-0.97	—	0.404	0.021
03250	1.825	328.92	—	-0.572	-0.044	—	-2.42	-1.22	—	0.407	0.042
03095	1.757	325.18	—	-0.443	+0.053	—	+1.36	+1.02	—	0.314	0.044
03110	1.934	318.77	—	-0.124	+0.048	—	-8.55	-3.31	—	0.216	0.087

	Observed		Amplitude Error (m)			Phase Error (deg)			Tidal Error (m)		
Station	Amplitude (m)	Phase (deg)	CIOPSE	STLE500	STLE200	CIOPSE	STLE500	STLE200	CIOPSE	STLE500	STLE200
03087	2.054	311.09	—	-0.343	-0.098	—	-1.18	+0.65	—	0.244	0.071
03105	2.022	310.20	—	-0.026	-0.003	—	-6.29	-1.07	—	0.157	0.027
03460	1.802	217.79	—	—	-0.149	—	—	+2.20	—	—	0.115
03080	2.043	301.98	-0.466	-0.035	-0.017	+2.27	-2.15	+2.81	0.333	0.059	0.071
03100	2.027	303.38	-0.460	+0.046	+0.004	+5.53	-4.67	+0.48	0.347	0.122	0.012
03200	1.908	305.09	-0.362	+0.137	+0.090	+5.00	-5.08	+0.24	0.277	0.157	0.064
03075	2.099	296.16	—	-0.099	-0.080	—	+7.66	+12.93	—	0.206	0.333
03190	2.045	300.76	-0.480	+0.003	-0.030	+2.49	-4.05	-0.12	0.344	0.102	0.021
03070	1.947	280.42	-0.260	+0.153	+0.159	+2.26	+1.11	+2.60	0.191	0.112	0.130
03071	2.104	287.36	-0.445	-0.014	-0.027	-1.27	-3.76	-1.16	0.316	0.098	0.035
03180	1.989	297.69	-0.450	+0.062	+0.033	+1.76	-5.87	-2.20	0.320	0.153	0.059
03060	1.996	259.20	-0.038	-0.099	-0.051	-8.47	+1.40	+1.90	0.208	0.077	0.059
03058	1.930	263.42	+0.059	+0.020	+0.049	-16.30	-8.11	-6.09	0.395	0.195	0.151
03175	1.824	292.15	-0.174	+0.170	+0.155	-13.08	-8.18	-5.03	0.305	0.227	0.161
03057	2.021	255.52	-0.020	0	-0.025	-9.97	-4.91	-1.10	0.247	0.122	0.032
03170	1.853	281.32	-0.189	+0.083	+0.057	-9.93	-4.64	-1.28	0.253	0.123	0.050
03052	1.940	248.66	+0.052	+0.040	-0.041	-10.28	-4.62	+0.66	0.252	0.115	0.033
03048	1.918	244.68	+0.061	+0.046	-0.032	-10.51	-5.36	-0.24	0.256	0.132	0.023
03045	1.813	242.65	+0.111	+0.060	-0.023	-12.19	-5.99	-0.73	0.291	0.143	0.023
03160	1.731	251.23	+0.135	+0.077	+0.006	-15.33	-9.26	-4.01	0.352	0.209	0.086
03030	1.616	229.62	+0.134	+0.050	-0.026	-9.16	-1.49	+4.47	0.212	0.047	0.090
03140	1.629	226.49	+0.053	+0.020	-0.059	-3.94	-1.12	+4.02	0.089	0.027	0.090
03425	1.574	211.99	+0.048	-0.063	-0.149	-12.28	-7.71	+3.28	0.244	0.153	0.122
03130	1.536	224.58	+0.061	-0.030	-0.118	-6.91	-1.84	+3.38	0.140	0.040	0.104
03125	1.487	220.00	+0.040	-0.080	-0.154	-8.98	-2.28	+3.81	0.169	0.070	0.127
03120	1.363	209.63	+0.168	-0.033	-0.140	-8.83	-2.62	+4.46	0.197	0.049	0.122
03122	1.401	221.83	+0.132	-0.091	—	-20.78	-13.01	—	0.385	0.226	—
02900	1.415	203.19	+0.108	-0.011	-0.114	-6.09	-2.49	+4.60	0.134	0.044	0.112
03005	1.404	202.09	+0.098	-0.029	-0.140	-4.35	-1.00	+5.03	0.104	0.027	0.129
02883	1.338	203.52	+0.105	-0.011	—	-10.11	-6.12	—	0.188	0.101	—

	Observed		Amplitude Error (m)			Phase Error (deg)			Tidal Error (m)		
Station	Amplitude (m)	Phase (deg)	CIOPSE	STLE500	STLE200	CIOPSE	STLE500	STLE200	CIOPSE	STLE500	STLE200
02880	1.408	198.66	+0.018	-0.099	—	-5.91	-2.00	—	0.104	0.077	—
03000	1.345	204.10	+0.081	-0.028	—	-7.40	-2.46	—	0.139	0.045	—
02995	1.370	202.93	+0.032	-0.088	—	-6.38	-1.91	—	0.111	0.069	—
02985	1.279	200.61	+0.081	-0.037	—	-6.02	-2.46	—	0.114	0.046	—
02980	1.273	199.98	+0.083	-0.035	—	-5.76	-2.30	—	0.110	0.043	—
02975	1.212	199.09	+0.108	+0.006	—	-5.46	-1.41	—	0.114	0.022	—
02840	1.174	192.97	+0.076	-0.026	—	-4.79	-1.34	—	0.089	0.027	—
02826	1.050	193.22	+0.134	+0.037	—	-6.14	-2.87	—	0.127	0.046	—
02955	1.142	194.22	+0.053	-0.046	—	-2.80	+0.78	—	0.055	0.034	—

Table 11. Tidal water level scores for year 2021.

	CRMSE (m)			χ^2			Pearson		
Station	CIOPSE	STLE500	STLE200	CIOPSE	STLE500	STLE200	CIOPSE	STLE500	STLE200
3360	—	—	0.05	—	—	0.454	—	—	0.985
3353	—	—	0.09	—	—	0.315	—	—	0.951
3345	—	—	0.104	—	—	0.199	—	—	0.952
3335	—	—	0.064	—	—	0.017	—	—	0.991
3300	—	—	0.085	—	—	0.006	—	—	0.998
3280	—	—	0.043	—	—	0.001	—	—	0.999
3248	—	0.46	0.045	—	0.113	0.001	—	0.994	0.999
3100	0.343	0.143	0.055	0.05	0.009	0.001	0.995	0.996	1
3057	0.299	0.162	0.067	0.038	0.011	0.002	0.981	0.994	0.999
3424	0.336	0.209	0.097	0.082	0.031	0.007	0.963	0.984	0.999
3460	—	—	0.105	—	—	0.006	—	—	0.999
2985	0.142	0.055	—	0.021	0.003	—	0.993	0.998	—

Table 12. Non-tidal water level scores for year 2021.

	CRMSE (m)			χ^2			Pearson		
Station	CIOPSE	STLE500	STLE200	CIOPSE	STLE500	STLE200	CIOPSE	STLE500	STLE200
3360	—	—	0.158	—	—	0.155	—	—	0.92
3353	—	—	0.166	—	—	0.198	—	—	0.896
3345	—	—	0.147	—	—	0.17	—	—	0.911
3335	—	—	0.152	—	—	0.172	—	—	0.913
3300	—	—	0.174	—	—	0.203	—	—	0.893
3280	—	—	0.154	—	—	0.182	—	—	0.905
3248	—	0.181	0.153	—	0.246	0.176	—	0.872	0.908
3100	0.162	0.148	0.139	0.249	0.206	0.183	0.867	0.892	0.904
3057	0.138	0.128	0.13	0.331	0.286	0.294	0.818	0.845	0.841
3424	0.109	0.108	0.108	0.298	0.293	0.294	0.84	0.844	0.846
3460	—	—	0.126	—	—	0.289	—	—	0.848
2985	0.089	0.086	—	0.263	0.246	—	0.861	0.87	—

Table 13. Total water level scores for year 2021.

	bias (m)			CRMSE (m)			χ^2			Pearson		
Station	CIOPSE	STLE500	STLE200	CIOPSE	STLE500	STLE200	CIOPSE	STLE500	STLE200	CIOPSE	STLE500	STLE200
3360	—	—	-0.294	—	—	0.165	—	—	0.165	—	—	0.914
3353	—	—	-0.312	—	—	0.189	—	—	0.216	—	—	0.89
3345	—	—	-0.142	—	—	0.18	—	—	0.179	—	—	0.912
3335	—	—	0.007	—	—	0.165	—	—	0.074	—	—	0.963
3300	—	—	0.135	—	—	0.193	—	—	0.029	—	—	0.986
3280	—	—	0.076	—	—	0.16	—	—	0.018	—	—	0.991
3248	—	0.326	0.026	—	0.494	0.159	—	0.122	0.013	—	0.984	0.994
3100	0.308	-0.020	-0.003	0.379	0.205	0.15	0.059	0.017	0.009	0.988	0.992	0.996
3057	0.269	0.006	0.001	0.329	0.206	0.146	0.045	0.018	0.009	0.977	0.991	0.996
3424	-0.045	-0.002	0	0.353	0.235	0.145	0.088	0.039	0.015	0.96	0.98	0.994
3460	—	—	0.067	—	—	0.164	—	—	0.014	—	—	0.995
2985	0.053	0.043	—	0.167	0.101	—	0.029	0.01	—	0.989	0.995	—

Table 14. Storm names and dates.

Storm name	Date
nov18c	2018-11-28 12H00
jan21	2021-01-17 6H00
mar17	2017-03-15 6H00
oct10	2019-10-18 0H00
mar21	2021-03-29 6H00
Dorian	2019-09-08 0H00
Ida	2021-09-03 0H00

Table 15. Non-tidal scores averaged for the 7 chosen storms.

	CRMSE (m)			**χ^2**			**Pearson**		
Station	CIOPSE	STLE500	STLE200	CIOPSE	STLE500	STLE200	CIOPSE	STLE500	STLE200
03360	**—**	—	0.088	—	—	0.839	—	—	0.638
03353	**—**	—	0.091	—	—	0.625	—	—	0.721
03345	**—**	—	0.087	—	—	0.421	—	—	0.803
03335	**—**	—	0.101	—	—	0.254	—	—	0.881
03300	**—**	—	0.139	—	—	0.188	—	—	0.913
03280	**—**	—	0.120	—	—	0.139	—	—	0.940
03248	**—**	0.156	0.125	—	0.226	0.140	—	0.897	0.934
03100	0.133	0.118	0.115	0.194	0.142	0.135	0.913	0.930	0.936
03057	0.094	0.089	0.085	0.117	0.102	0.097	0.951	0.953	0.956
03424	0.059	0.057	0.052	0.100	0.093	0.087	0.950	0.955	0.959
03460	**—**	—	0.077	—	—	0.119	—	—	0.941
02985	0.052	0.050	—	0.094	0.090	—	0.952	0.955	—

Table 16. Total surface currents scores from comparison with HADCP in Québec and Lévis.

	CRMSE (m/s)		χ^2		Pearson	
Station	**STLE500**	**STLE200**	**STLE500**	**STLE200**	**STLE500**	**STLE200**
Lévis 2020	0.418	0.192	0.203	0.043	0.924	0.981
Lévis 2021	0.398	0.164	0.148	0.025	0.955	0.989
Québec 2021	0.497	0.225	0.397	0.081	0.88	0.968

Table 17. Non-tidal surface currents scores from comparison with HADCP in Québec and Lévis.

	CRMSE (m/s)		χ^2		Pearson	
Station	**STLE500**	**STLE200**	**STLE500**	**STLE200**	**STLE500**	**STLE200**
Lévis 2020	0.128	0.132	0.677	0.725	0.575	0.581
Lévis 2021	0.108	0.106	0.715	0.687	0.538	0.590
Québec 2021	0.125	0.109	0.836	0.633	0.488	0.609

Table 18. Tidal surface currents scores from comparison with HADCP in Québec and Lévis.

	CRMSE (m/s)		χ^2		Pearson	
Station	**STLE500**	**STLE200**	**STLE500**	**STLE200**	**STLE500**	**STLE200**
Lévis 2020	0.404	0.147	0.195	0.026	0.933	0.991
Lévis 2021	0.383	0.125	0.139	0.015	0.961	0.994
Québec 2021	0.481	0.197	0.383	0.064	0.889	0.977

Table 19. Amplitude and phase of the major surface currents constituents from the HADCPs in Québec and Lévis; phase, amplitude and tidal error for both STLE500 and STLE200.

		Observed		Amplitude Error (m/s)		Phase Error (deg)		Tidal Error (m/s)	
Station	**Const.**	**Amplitude (m/s)**	**Phase (deg)**	**STLE500**	**STLE200**	**STLE500**	**STLE200**	**STLE500**	**STLE200**
Lévis 2020	M2	1.356	113.06	-0.462	-0.146	+12.55	-0.83	0.368	0.104
	N2	0.275	93.50	-0.129	-0.072	+13.69	-0.88	0.098	0.051
	S2	0.365	160.55	-0.126	-0.029	+19.26	+7.42	0.113	0.038
	K1	0.084	110.32	-0.006	+0.007	+27.10	+13.12	0.027	0.015
	O1	0.093	86.24	-0.011	-0.014	+18.25	+2.82	0.021	0.010
	Q1	0.028	20.48	-0.016	-0.017	+32.19	-15.81	0.014	0.013
	M4	0.272	45.07	-0.030	+0.004	+26.50	+7.61	0.086	0.026
Lévis 2021	M2	1.366	111.40	-0.419	-0.118	+12.88	-0.63	0.347	0.084
	N2	0.145	102.58	-0.020	+0.031	+8.31	-8.47	0.020	0.027
	S2	0.341	166.65	-0.085	+0.011	+17.91	+6.33	0.089	0.028
	K1	0.086	119.47	-0.002	+0.011	+22.23	+14.34	0.023	0.018
	O1	0.095	79.62	-0.008	-0.010	+20.62	+7.31	0.024	0.011
	Q1	0.009	126.29	-0.001	-0.006	+7.75	+6.81	0.001	0.004
	M4	0.242	42.76	-0.011	+0.019	+27.29	+8.93	0.079	0.031
Québec 2021	M2	1.005	97.56	+0.308	+0.119	+26.91	+11.23	0.436	0.169
	N2	0.126	90.45	+0.048	+0.034	+19.10	+2.87	0.048	0.025
	S2	0.259	157.03	+0.095	+0.051	+27.94	+13.96	0.123	0.061
	K1	0.062	124.40	+0.058	+0.014	+16.20	-12.23	0.044	0.014

		Observed		Amplitude Error (m/s)		Phase Error (deg)		Tidal Error (m/s)	
Station	**Const.**	**Amplitude (m/s)**	**Phase (deg)**	**STLE500**	**STLE200**	**STLE500**	**STLE200**	**STLE500**	**STLE200**
	O1	0.068	93.77	+0.054	+0.004	+8.76	-3.24	0.039	0.004
	Q1	0.010	110.02	+0.002	-0.005	+21.13	+19.16	0.003	0.004
	M4	0.255	48.43	+0.065	-0.005	+22.63	+3.34	0.092	0.011

Table 20. Total velocity statistics for ADCP at buoy IML-4.

		Bias u (m/s)	Bias v (m/s)	Bias u (m/s)	Bias v (m/s)	RMSE (m/s)		vector correlation magnitude		vector correlation degrees	
Station	**Depth (m)**	**CIOPSE**	**CIOPSE**	**STLE500**	**STLE500**	**CIOPSE**	**STLE500**	**CIOPSE**	**STLE500**	**CIOPSE**	**STLE500**
10749 11m 2016-04 to 2016-11	**1,5**	0,082	0,039	0,021	-0,001	0,343	0,309	0,371	0,525	1,89	8,228
	5	0,075	0,043	0,016	0,007	0,312	0,282	0,369	0,518	1,395	8,352
	7,5	0,059	0,036	0,001	0,002	0,31	0,283	0,363	0,508	0,014	7,953
	10	0,05	0,037	-0,005	0,002	0,297	0,273	0,35	0,493	-2,262	6,313
11947 106m 2016-04_2016-11	**7,5**	0,089	0,058	0,032	0,023	0,269	0,248	0,358	0,499	3,804	12,198
	10	0,066	0,054	0,012	0,019	0,273	0,252	0,346	0,483	-0,655	9,911
	15	0,029	0,042	-0,016	0,009	0,273	0,26	0,314	0,432	-6,738	6,528
	20	0,013	0,028	-0,027	-0,002	0,264	0,259	0,276	0,365	-12,728	0,24
	50	-0,019	0,004	-0,04	-0,007	0,218	0,244	0,442	0,309	-6,074	1,617
	100	-0,036	0,002	-0,021	0,001	0,156	0,17	0,632	0,548	6,066	7,814

Table 21. Non-tidal velocity statistics for ADCP at buoy IML-4.

		RMSE (m/s)		vector correlation magnitude		vector correlation degrees	
Station	**Depth (m)**	**CIOPSE**	**STLE500**	**CIOPSE**	**STLE500**	**CIOPSE**	**STLE500**
10749 11m 2016-04 to 2016-11	**1,5**	0,29	0,268	0,299	0,348	-8,44	13,094
	5	0,263	0,247	0,299	0,317	-8,653	14,763
	7,5	0,251	0,245	0,293	0,289	-6,605	17,118
	10	0,237	0,234	0,27	0,256	-4,883	17,064
11947 106m 2016-04 to 2016-11	**7,5**	0,236	0,218	0,283	0,289	-3,272	19,923
	10	0,228	0,218	0,275	0,257	-6,248	17,631
	15	0,212	0,22	0,245	0,2	-4,105	15,811
	20	0,202	0,217	0,201	0,17	-0,089	15,281
	50	0,177	0,218	0,283	0,061	-4,018	24,681
	100	0,127	0,142	0,247	0,078	-6,331	32,581

Table 22. Tidal velocity statistics for ADCP at buoy IML-4.

		χ^2		RMSE (m/s)	
Station	**Depth (m)**	**CIOPSE**	**STLE500**	**CIOPSE**	**STLE500**
10749 11m 2016-04 to 2016-11	**1.5**	0.671	0.433	0.175	0.141
	5	0.676	0.423	0.159	0.126
	7.5	0.691	0.403	0.176	0.135
	10	0.705	0.411	0.174	0.133
11947 106m 2016-04 to 2016-11	**7.5**	0.716	0.619	0.121	0.113
	10	0.724	0.487	0.146	0.119
	15	0.817	0.514	0.167	0.132
	20	0.938	0.631	0.165	0.135
	50	0.983	0.697	0.123	0.104
	100	0.341	0.364	0.085	0.088

Table 23. Near surface salinity and temperature scores for 2017 from comparison with MCTD fixed on tide gauges.

		temperature			**salinity**		
Station name	**score**	**CIOPSE**	**STLE500**	**STLE200**	**CIOPSE**	**STLE500**	**STLE200**
2985	**bias (deg C | PSU)**	0.205	0.960	—	0.139	0.508	—
	CRMSE (deg C | PSU)	1.256	1.629	—	2.111	2.341	—
	χ^2	0.101	0.170	—	0.553	0.680	—
	Pearson	0.967	0.973	—	0.685	0.658	—
3057	**bias (deg C | PSU)**	1.634	0.829	1.097	-13.126	0.030	0.299
	CRMSE (deg C | PSU)	2.435	1.216	1.250	3.259	4.193	4.247
	χ^2	0.242	0.060	0.064	0.666	1.103	1.131
	Pearson	0.921	0.979	0.984	0.597	0.691	0.660
3100	**bias (deg C | PSU)**	-3.199	-0.152	-0.152	—	—	—
	CRMSE (deg C | PSU)	5.258	1.032	0.932	—	—	—
	χ^2	0.355	0.014	0.011	—	—	—
	Pearson	0.837	0.993	0.994	—	—	—
3248	**bias (deg C | PSU)**	—	-0.272	-0.292	—	—	—
	CRMSE (deg C | PSU)	—	1.201	1.068	—	—	—
	χ^2	—	0.019	0.015	—	—	—
	Pearson	—	0.991	0.993	—	—	—
3300	**bias (deg C | PSU)**	—	—	-0.144	—	—	—
	CRMSE (deg C | PSU)	—	—	1.278	—	—	—
	χ^2	—	—	0.021	—	—	—
	Pearson	—	—	0.990	—	—	—
3335	**bias (deg C | PSU)**	—	—	-0.268	—	—	—
	CRMSE (deg C | PSU)	—	—	1.538	—	—	—
	χ^2	—	—	0.028	—	—	—
	Pearson	—	—	0.986	—	—	—
3353	**bias (deg C | PSU)**	—	—	-0.584	—	—	—
	CRMSE (deg C | PSU)	—	—	1.369	—	—	—

		temperature			salinity		
Station name	**score**	**CIOPSE**	**STLE500**	**STLE200**	**CIOPSE**	**STLE500**	**STLE200**
	χ^2	—	—	0.024	—	—	—
	Pearson	—	—	0.988	—	—	—
3360	**bias (deg C | PSU)**	—	—	-0.649	—	—	—
	CRMSE (deg C | PSU)	—	—	1.624	—	—	—
	χ^2	—	—	0.032	—	—	—
	Pearson	—	—	0.989	—	—	—

Table 24. Near surface temperature scores for years 2016-2019 for station 3057 from comparison with MCTD fixed on tide gauges.

temperature. station 3057

year	**bias (deg C)**			**CRMSE (deg C)**			**χ^2**			**Pearson**		
	CIOPSE	**500**	**200**	**CIOPSE**	**500**	**200**	**CIOPSE**	**500**	**200**	**CIOPSE**	**500**	**200**
2016	2.645	1.119	1.518	2.602	1.692	1.652	0.547	0.231	0.221	0.892	0.924	0.932
2017	1.621	0.826	1.091	2.430	1.214	1.249	0.240	0.060	0.063	0.922	0.979	0.984
2018	2.214	1.040	1.255	2.409	1.114	1.098	0.229	0.049	0.048	0.935	0.982	0.989
2019	2.077	1.233	1.419	2.503	1.180	1.228	0.265	0.059	0.064	0.939	0.984	0.989

Table 25. Near surface salinity scores for years 2016-2019 for station 3057 from comparison with MCTD fixed on tide gauges.

salinity. station 3057

year	**bias (PSU)**			**CRMSE (PSU)**			**χ^2**			**Pearson**		
	CIOPSE	**500**	**200**	**CIOPSE**	**500**	**200**	**CIOPSE**	**500**	**200**	**CIOPSE**	**500**	**200**
2016	-12.030	1.286	1.520	2.817	4.240	4.371	0.772	1.749	1.859	0.533	0.610	0.581
2017	-13.166	0.004	0.274	3.283	4.205	4.263	0.664	1.089	1.119	0.600	0.689	0.659
2018	-11.785	0.808	1.151	2.941	4.373	4.450	0.671	1.484	1.536	0.574	0.639	0.594
2019	-12.745	-0.054	0.268	2.743	4.236	4.227	0.665	1.587	1.580	0.581	0.689	0.652

Table 26. Near surface temperature scores for years 2016-2021 for station 3100 from comparison with MCTD fixed on tide gauges.

temperature. station 3100

year	**bias (deg C)**			**CRMSE (deg C)**			**χ^2**			**Pearson**		
	CIOPSE	**500**	**200**	**CIOPSE**	**500**	**200**	**CIOPSE**	**500**	**200**	**CIOPSE**	**500**	**200**
2016	-5.364	-0.559	-0.548	5.171	0.894	0.816	0.447	0.013	0.011	0.756	0.993	0.994
2017	-3.175	-0.151	-0.151	5.245	1.028	0.928	0.352	0.014	0.011	0.839	0.993	0.994
2018	-2.897	0.113	0.056	5.689	1.254	1.098	0.364	0.018	0.014	0.844	0.993	0.995
2019	-2.596	0.390	0.326	5.354	0.838	0.728	0.362	0.009	0.007	0.830	0.996	0.997
2020	-3.217	-0.225	-0.234	5.062	1.055	0.890	0.329	0.014	0.010	0.855	0.993	0.995
2021	-3.759	-0.757	-0.680	5.000	1.243	1.104	0.315	0.019	0.015	0.868	0.990	0.992

Table 27. Scores for ferry's temperature and salinity at ~8m depth.

		Salinity			Temperature		
	period	**CIOPSE**	**STLE500**	**STLE200**	**CIOPSE**	**STLE500**	**STLE200**
bias (PSU | Deg C)	**2016**	-5.593	0.675	1.493	-0.317	-0.113	0.789
	2017	-6.095	0.251	1.182	0.056	0.181	0.707
	2018	-5.337	0.105	0.914	0.476	0.385	0.984
	2019	-5.627	-0.035	0.896	0.545	0.490	0.950
	2020	-6.055	-0.455	0.381	0.684	0.309	0.655
	2021	-5.792	0.303	1.086	0.220	0.428	0.960
	2022	-4.366	0.297	1.125	1.122	0.465	0.514
	2016-2022	-5.759	0.106	0.959	0.322	0.317	0.851
CRMSE (PSU | Deg C)	**2016**	6.250	2.587	3.004	2.640	1.266	1.464
	2017	6.629	3.186	3.242	2.443	1.139	1.240
	2018	6.445	3.247	3.312	2.692	1.146	1.296
	2019	6.622	3.494	3.559	2.466	1.106	1.295
	2020	6.316	3.331	3.497	2.229	0.992	1.170
	2021	6.441	3.039	3.219	2.443	1.039	1.306
	2022	7.283	4.930	4.776	1.686	0.863	0.782
	2016-2022	6.475	3.214	3.346	2.496	1.117	1.292
RMSE (PSU | Deg C)	**2016**	8.387	2.674	3.355	2.658	1.271	1.663
	2017	9.005	3.196	3.451	2.444	1.153	1.427
	2018	8.368	3.248	3.436	2.734	1.209	1.627
	2019	8.689	3.494	3.670	2.526	1.209	1.606
	2020	8.750	3.362	3.517	2.332	1.039	1.341
	2021	8.662	3.054	3.397	2.452	1.123	1.621
	2022	8.490	4.939	4.907	2.025	0.980	0.936
	2016-2022	8.665	3.216	3.480	2.517	1.161	1.547

Table 28. Scores for TReX experiment drifter's database in 2020.

	Molcard Skill		**Separation Distance (km)**	
Hour	**CIOPSE**	**STLE500**	**CIOPSE**	**STLE500**
1	0.23	0.24	1.12	1.10
2	0.23	0.24	2.22	2.17
3	0.22	0.24	3.29	3.22
4	0.22	0.23	4.33	4.26
5	0.22	0.23	5.32	5.27
6	0.22	0.22	6.27	6.27
7	0.22	0.22	7.17	7.26
8	0.23	0.22	8.02	8.22
9	0.24	0.22	8.82	9.17
10	0.24	0.23	9.58	10.09
11	0.25	0.23	10.31	11.02
12	0.26	0.23	11.01	11.95
13	0.27	0.23	11.70	12.87

	Molcard Skill		Separation Distance (km)	
Hour	**CIOPSE**	**STLE500**	**CIOPSE**	**STLE500**
14	0.28	0.23	12.38	13.78
15	0.29	0.24	13.04	14.67
16	0.29	0.24	13.67	15.54
17	0.30	0.24	14.32	16.37
18	0.30	0.24	14.96	17.17
19	0.31	0.25	15.59	17.93
20	0.31	0.25	16.21	18.65
21	0.31	0.25	16.83	19.32
22	0.32	0.26	17.39	19.93
23	0.32	0.26	17.94	20.53
24	0.32	0.27	18.48	21.13

Table 29. Scores for drifters deployed around Saint-François, Ile d'Orléans, in July 2019.

	Molcard Skill			Separation Distance (km)		
Hour	**CIOPSE**	**STLE500**	**STLE200**	**CIOPSE**	**STLE500**	**STLE200**
1	0.45	0.54	0.56	1.18	0.86	0.63
2	0.48	0.63	0.64	2.53	1.50	1.17
3	0.45	0.68	0.65	3.78	1.79	1.72
4	0.48	0.68	0.65	4.03	2.12	2.32

12. FIGURES

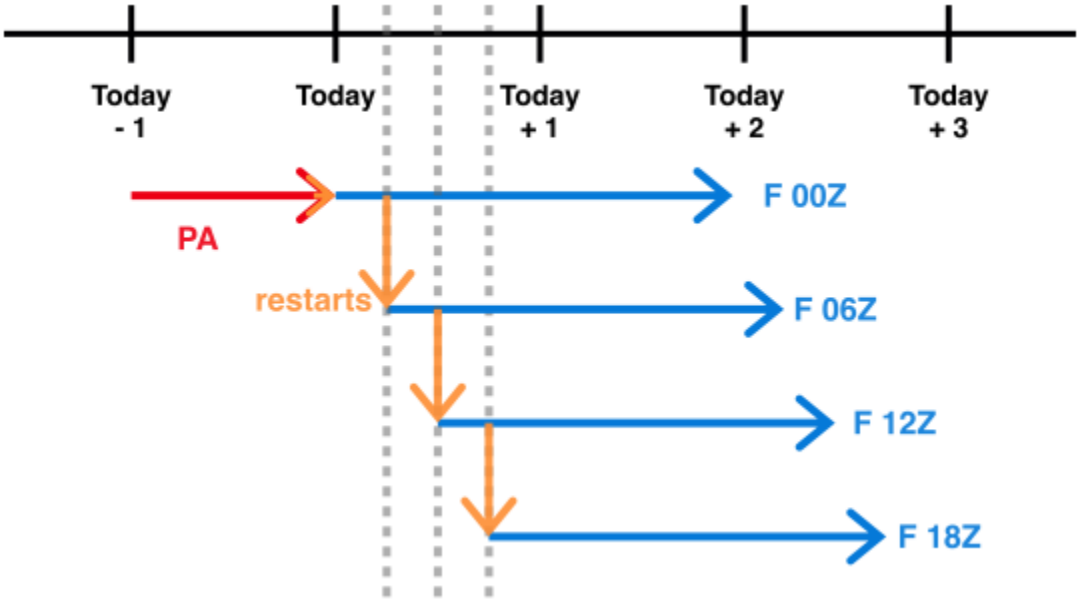

Figure 1. Schematic of one timestamp's set of pseudo-analysis (PA, in red) and forecast (in blue) runs. Grey dashed lines are spaced six hours apart, and orange arrows indicate where a restart file is generated and used to launch the subsequent step. The PA for today+1 will start with the same restart used to start today's 00Z forecast, and the pattern will repeat.

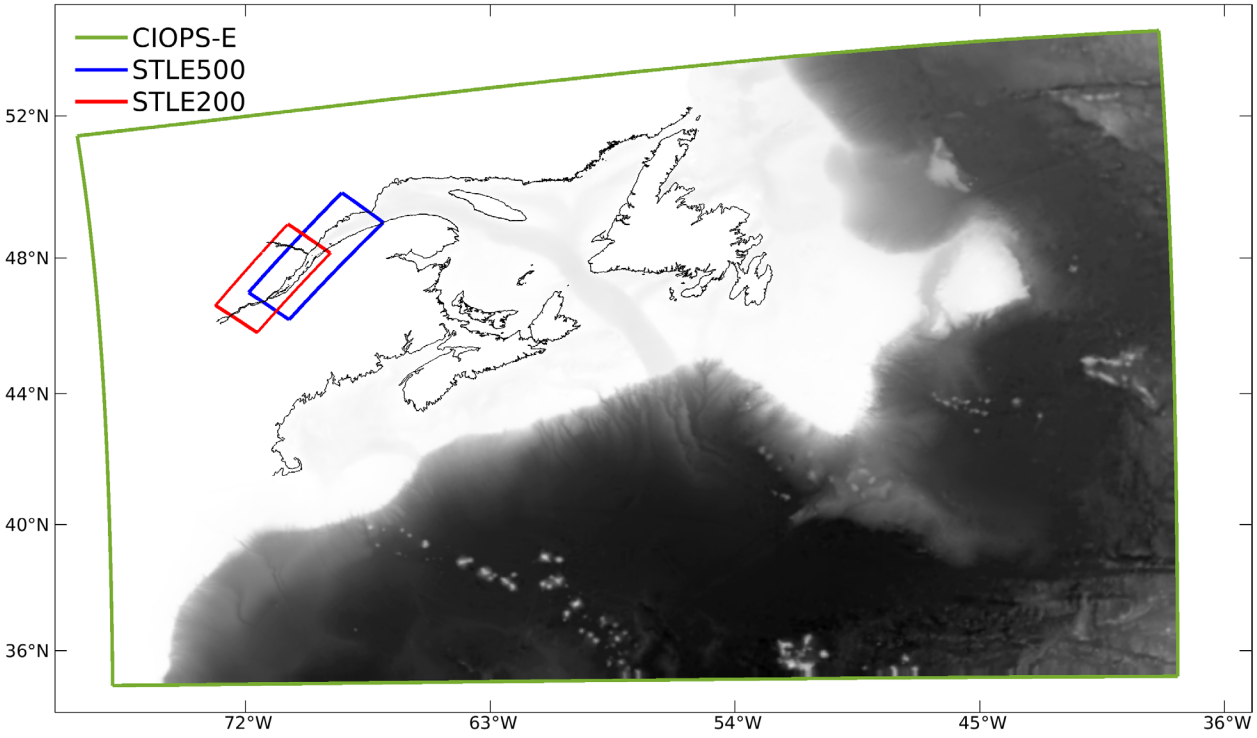

Figure 2. Limits of the CIOPS-E, STLE500 and STLE200 domains.

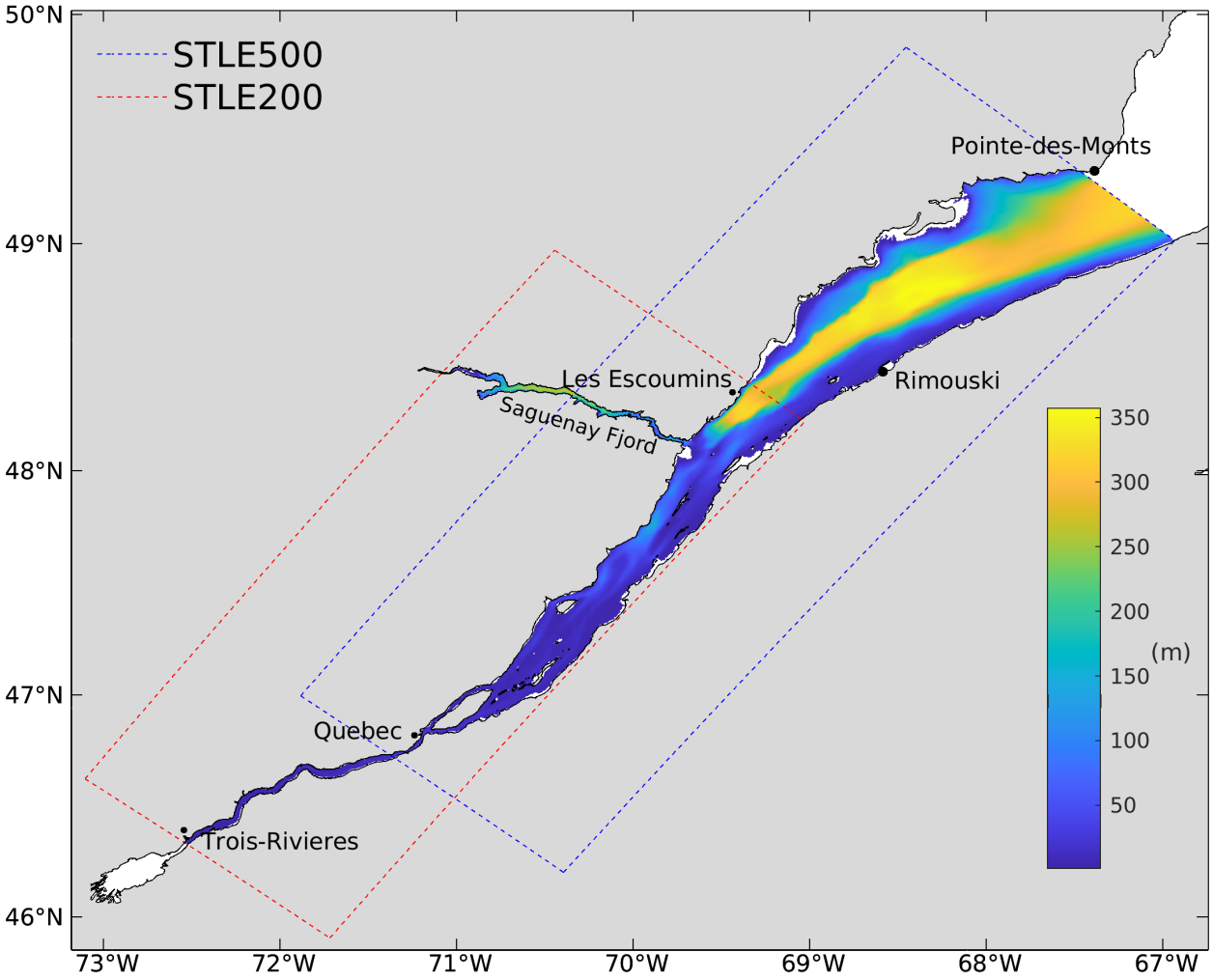

Figure 3. Bathymetry and limits of the STLE500's and STLE200's domain.

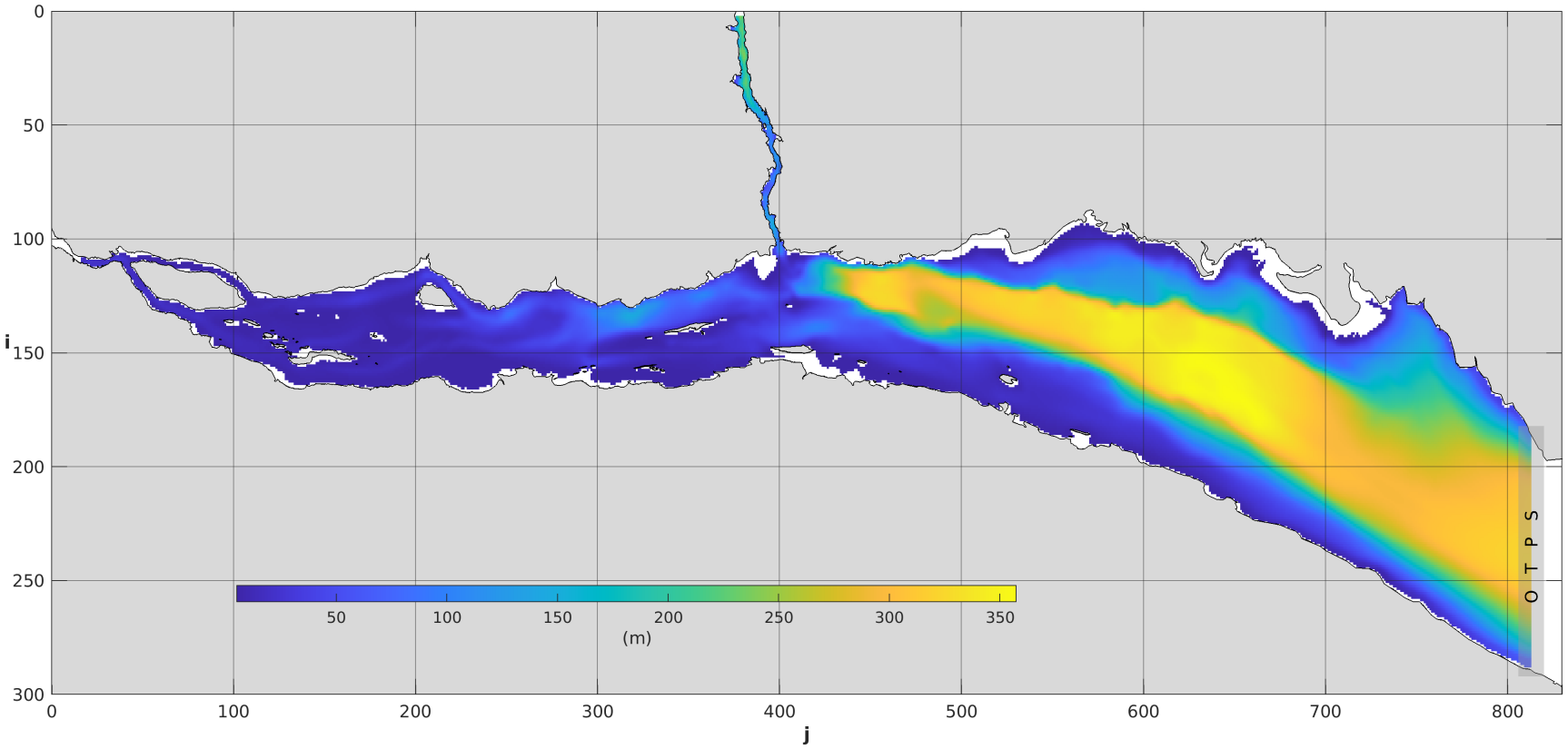

*Figure 4. STLE500's bathymetry, with **i** and **j** indices as vertical and horizontal axis. OTPS tidal components are applied at the eastern open boundary.*

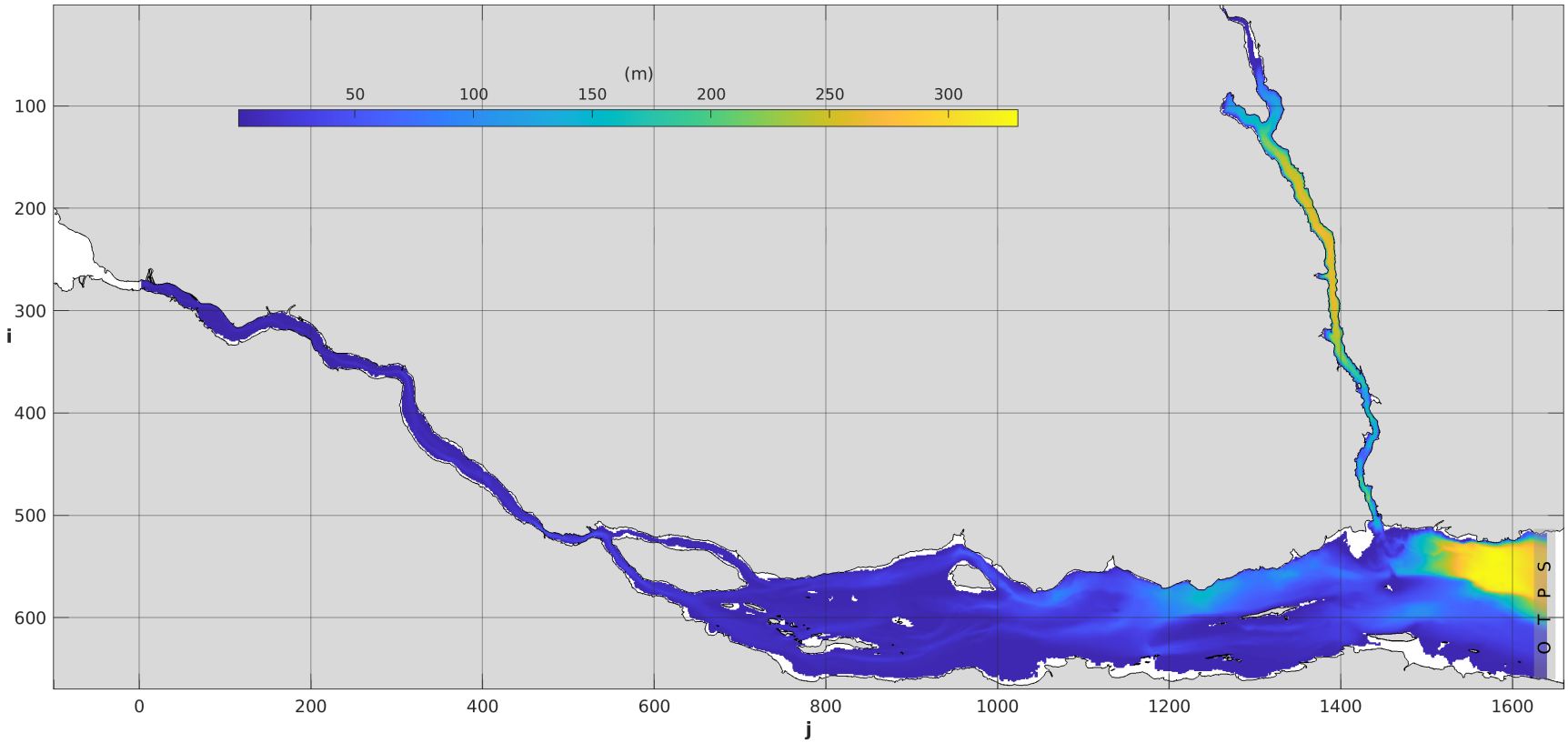

*Figure 5. STLE200's bathymetry, with **i** and **j** indices as vertical and horizontal axis. OTPS tidal components are applied at the eastern open boundary.*

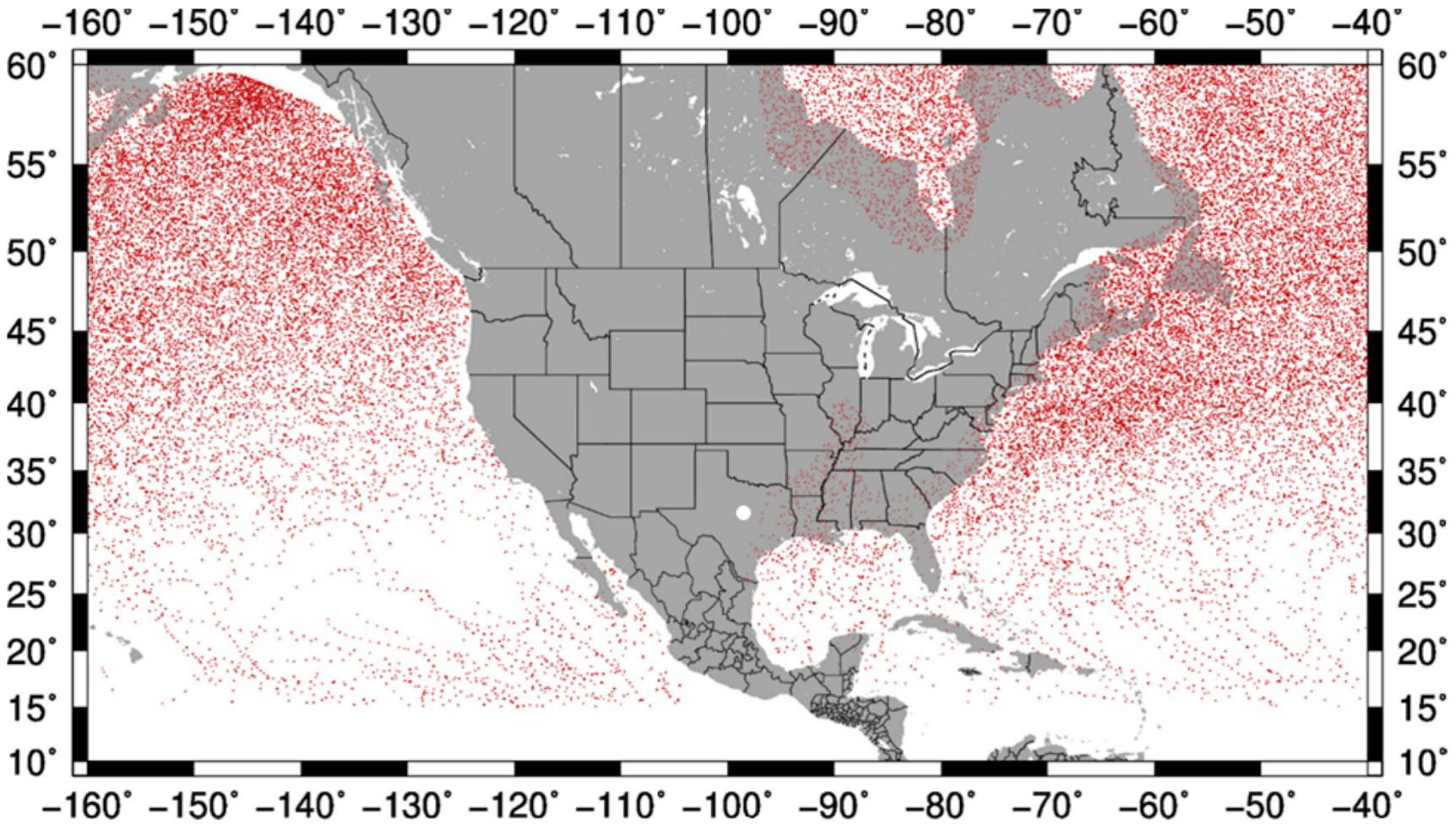

Figure 6. Cyclone locations every six hours from 2010-2021.

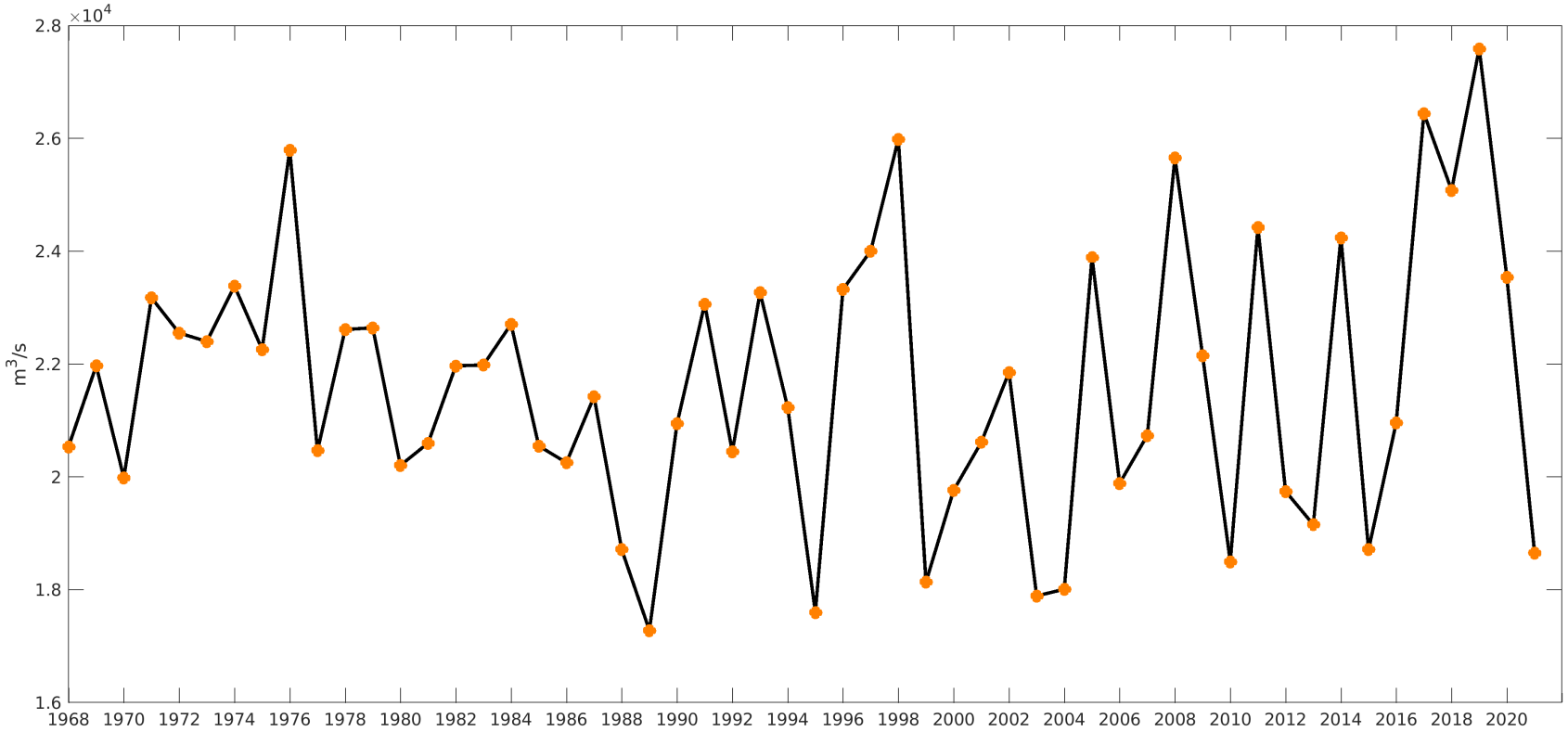

Figure 7. Maximum St. Lawrence River runoff per year, for the period 1968-2021.

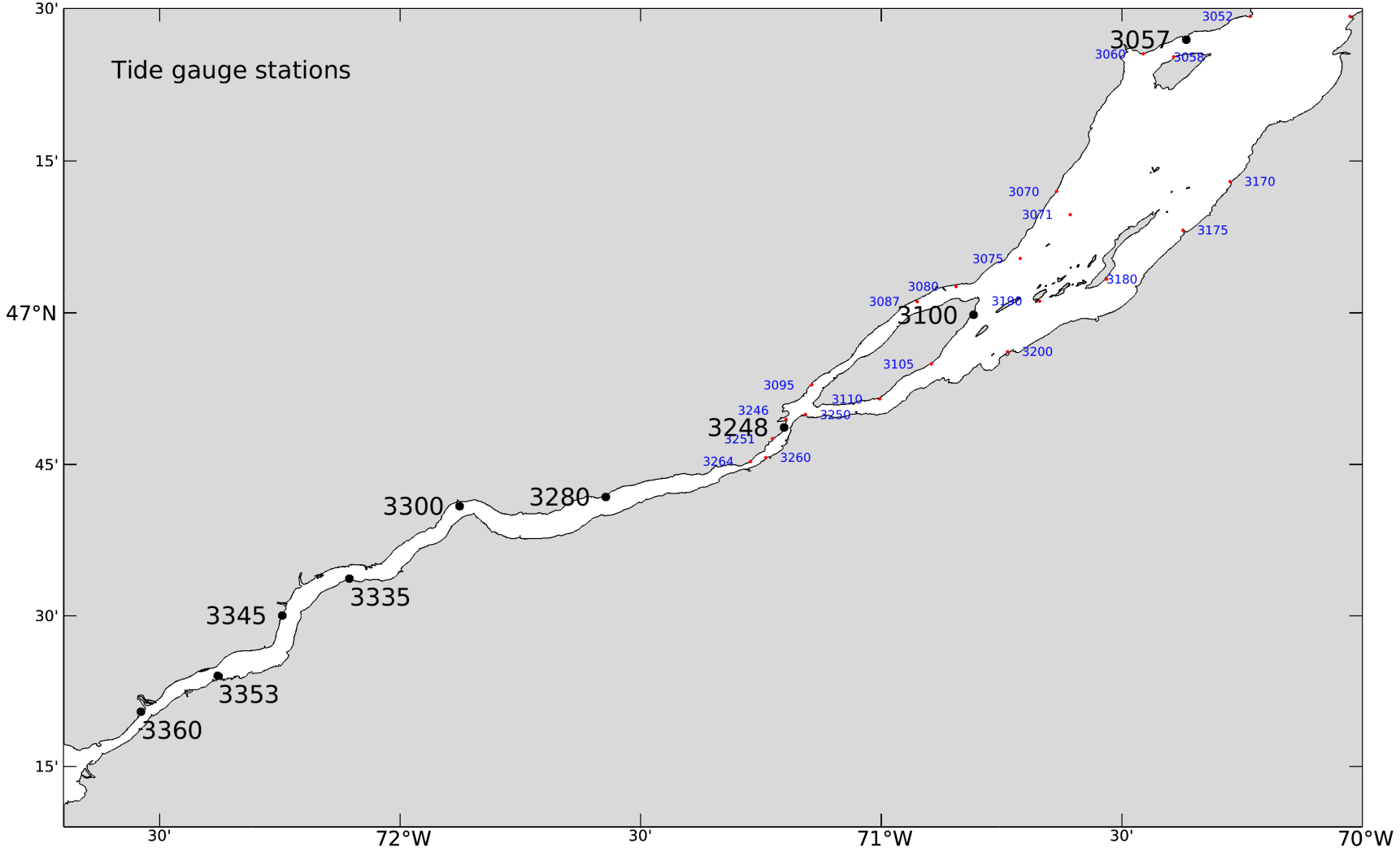

Figure 8. Tide gauges stations for the upstream part of the modeled area. Active real-time stations are in black, and historical ones are in blue.

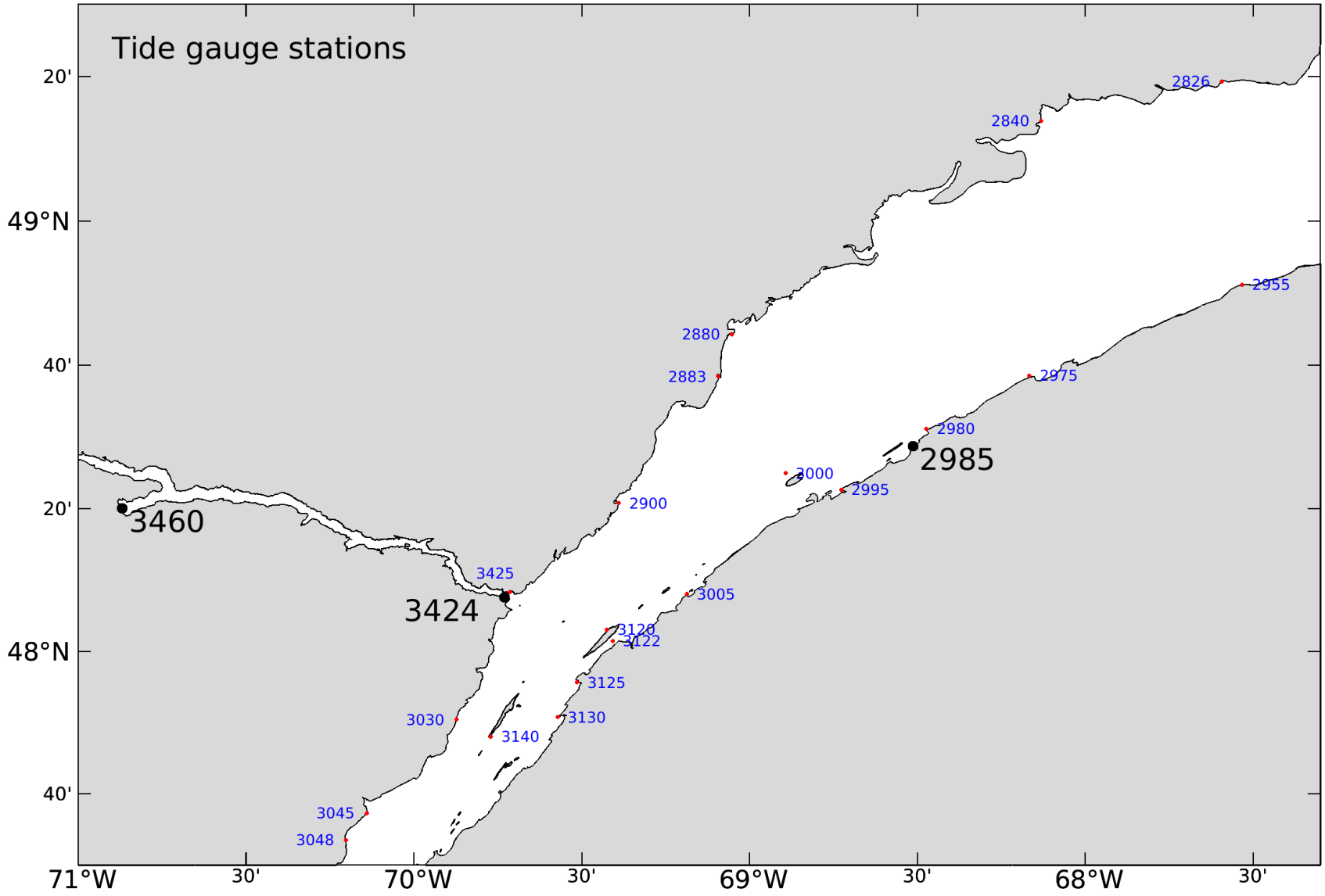

Figure 9. Tide gauges stations for the downstream part of the modeled area. Active real-time stations are in black, and historical ones are in blue.

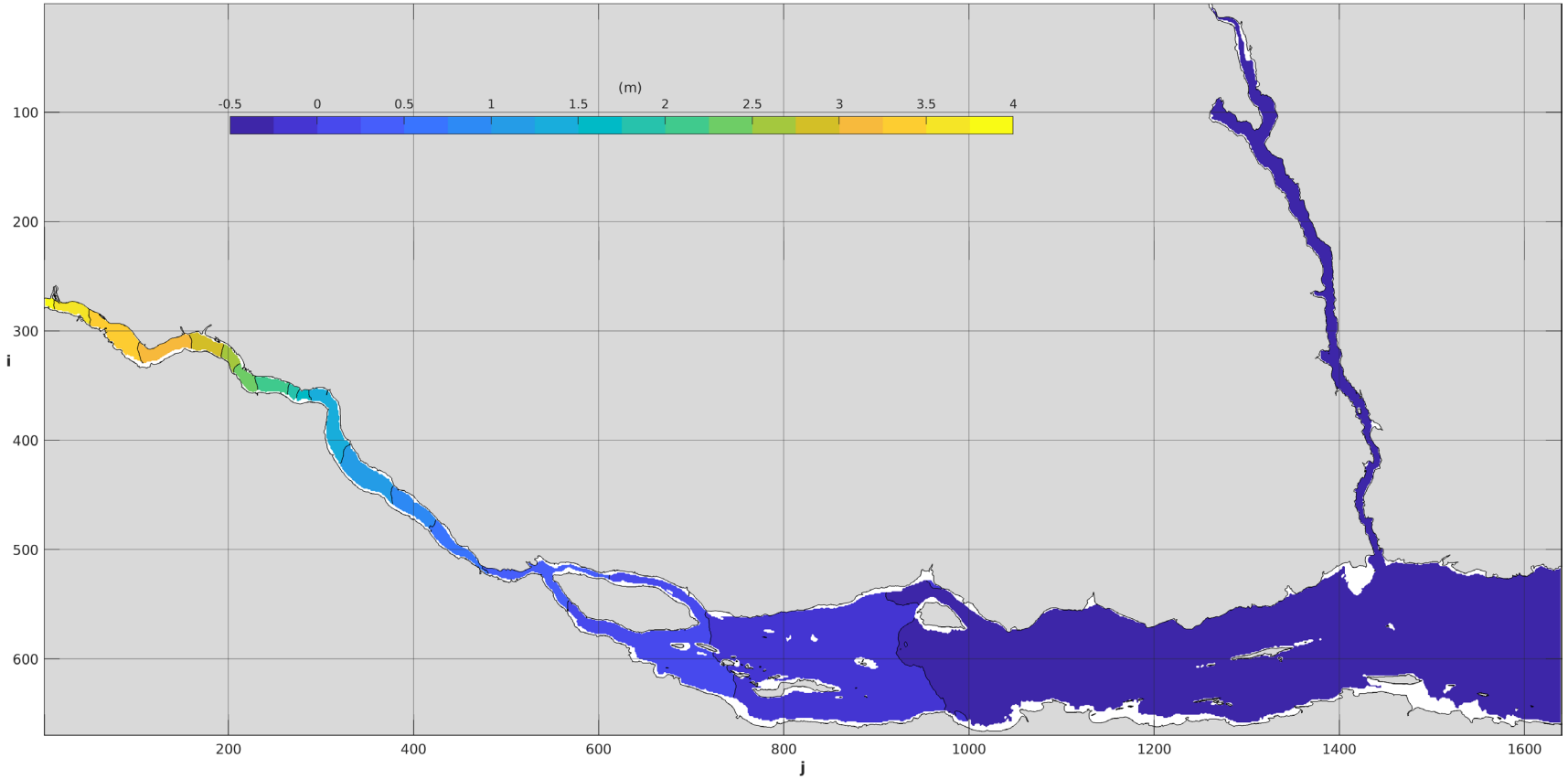

Figure 10. Long-term (6 years) mean ssh (m) map for the STLE200 domain.

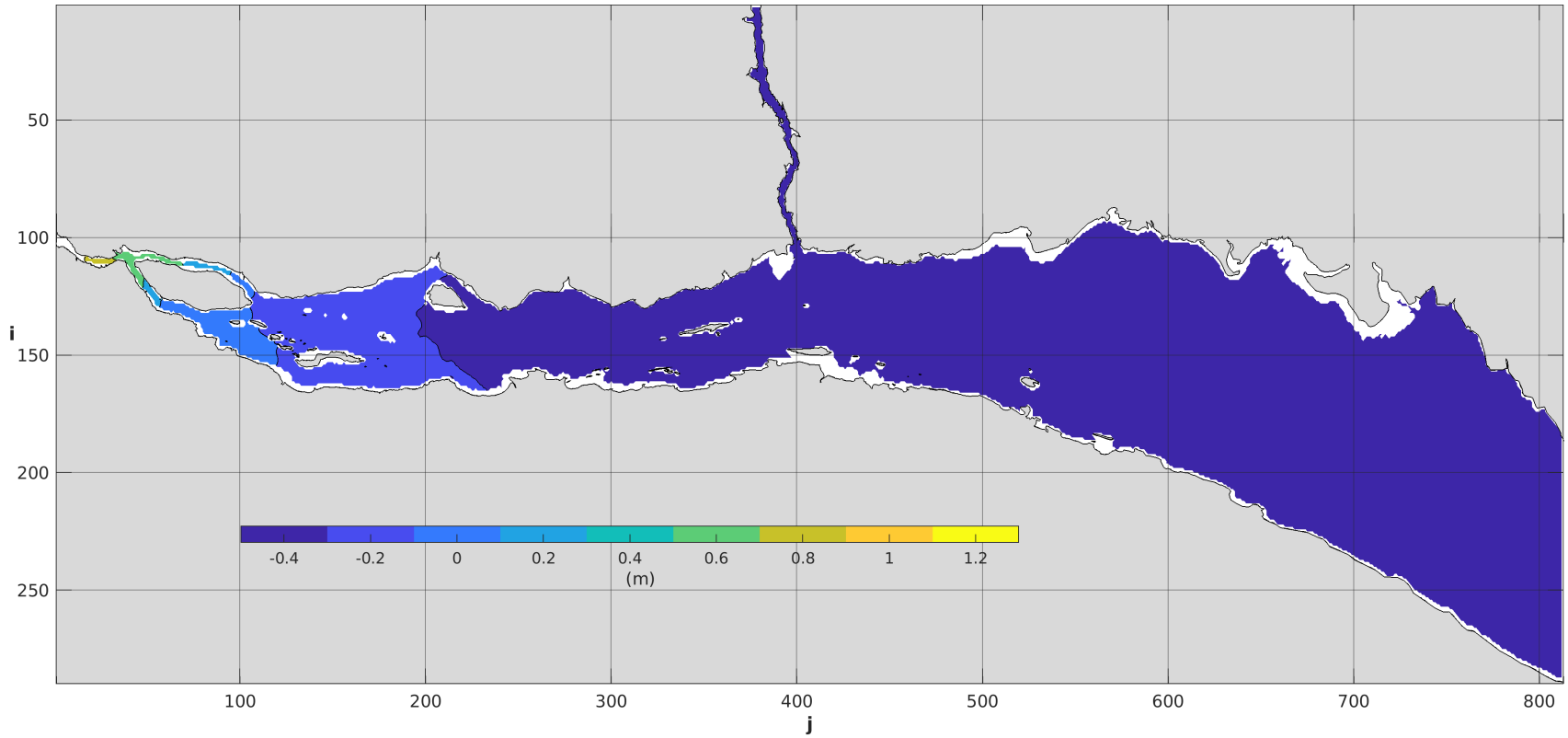

Figure 11. Long-term (6 years) mean ssh (m) map for the STLE500 domain.

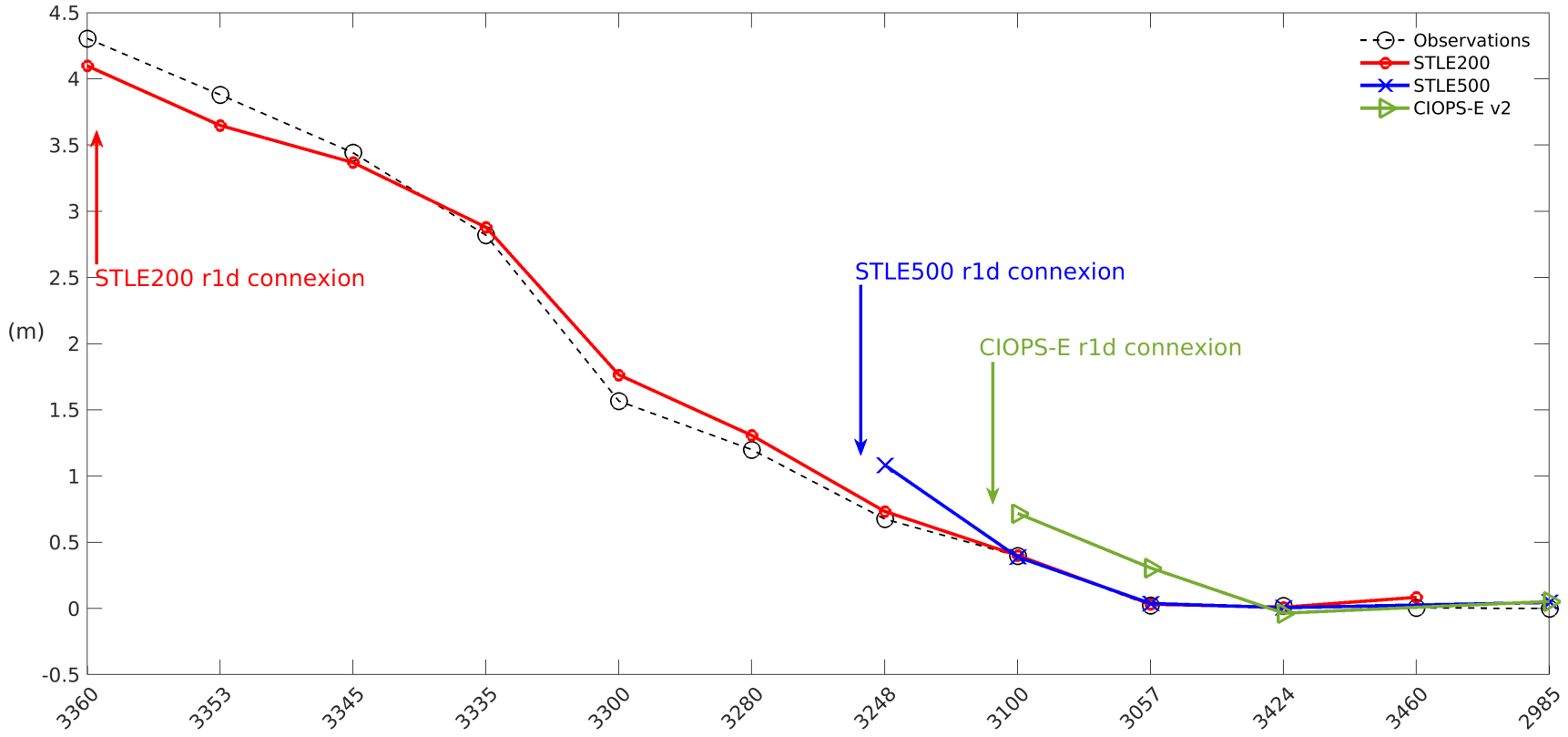

Figure 12. Long-term (6 years) mean ssh for the 3 models and observations (black dotted line). STLE200 in red, STLE500 is in blue, and CIOPS-E is in green. The approximate connection location with the r1d model is indicated by an arrow.

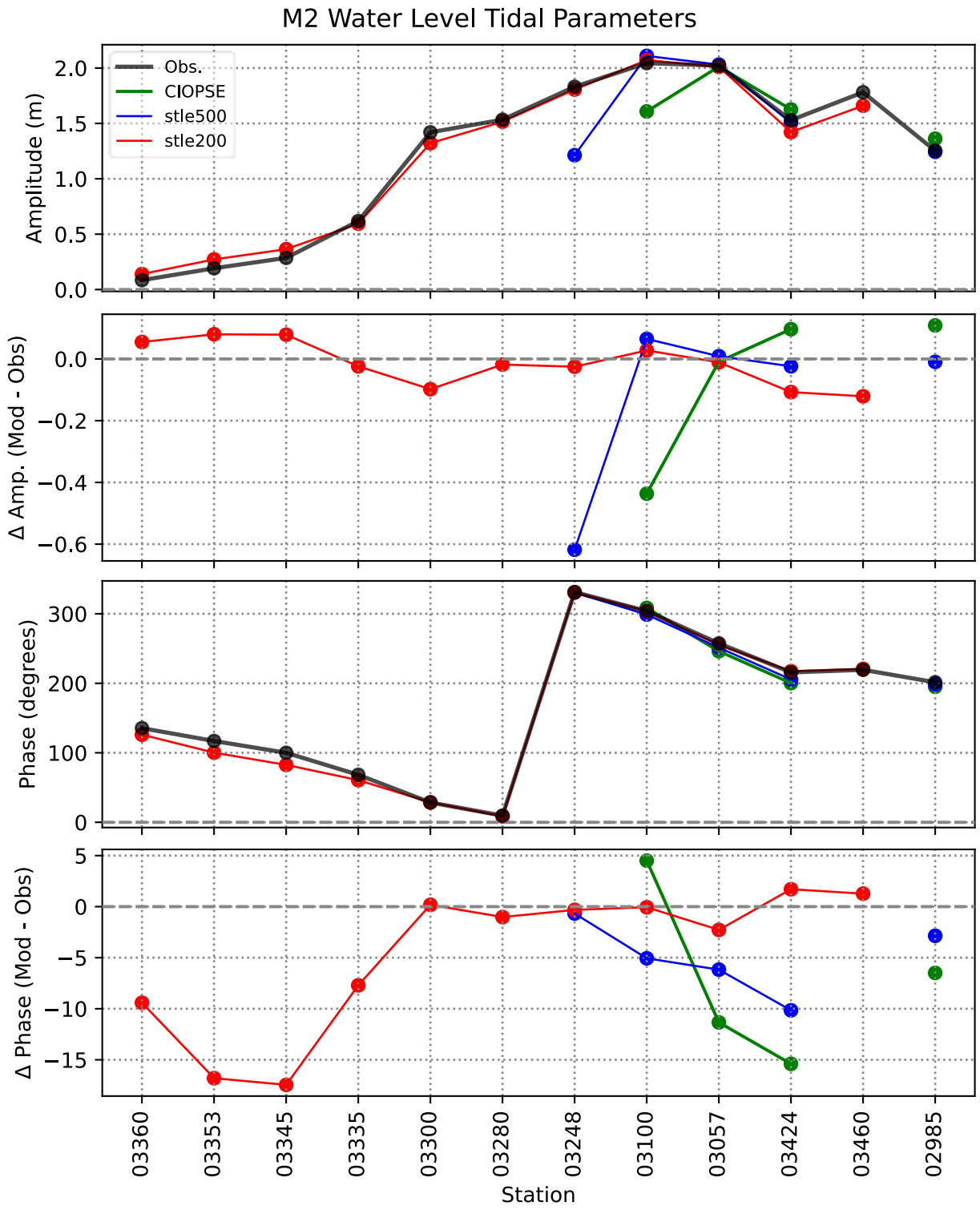

Figure 13. M2 tidal amplitude (panel 1 and 2) and phase (panel 3 and 4) of the three models compared to observations at the active tide gauge stations (see Figure 8 and Figure 9 for a map of tide gauge stations).

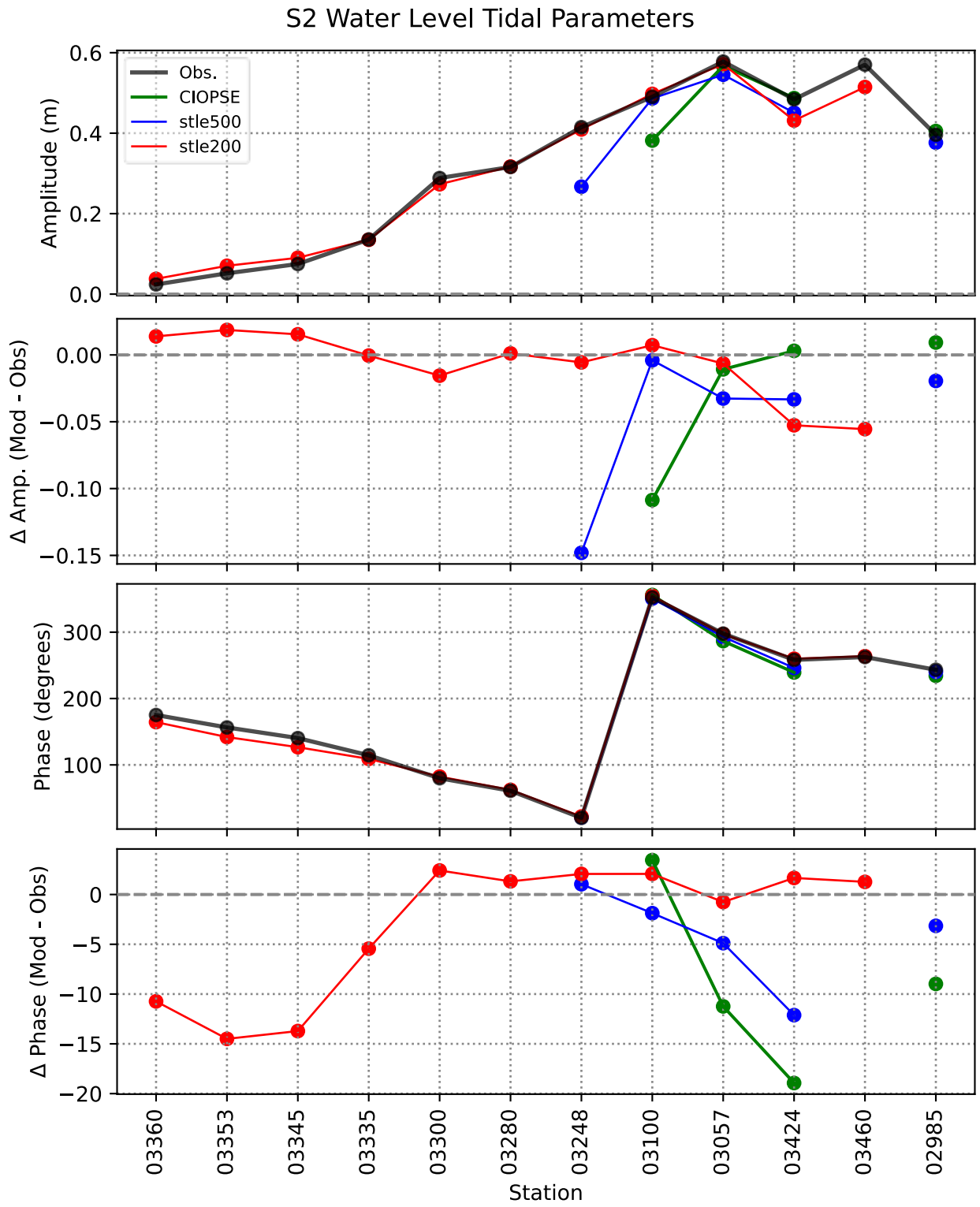

Figure 14. S2 tidal amplitude (panel 1 and 2) and phase (panel 3 and 4) of the three models compared to observations at the active tide gauge stations (see Figure 5 and Figure 6 for a map of tide gauge stations).

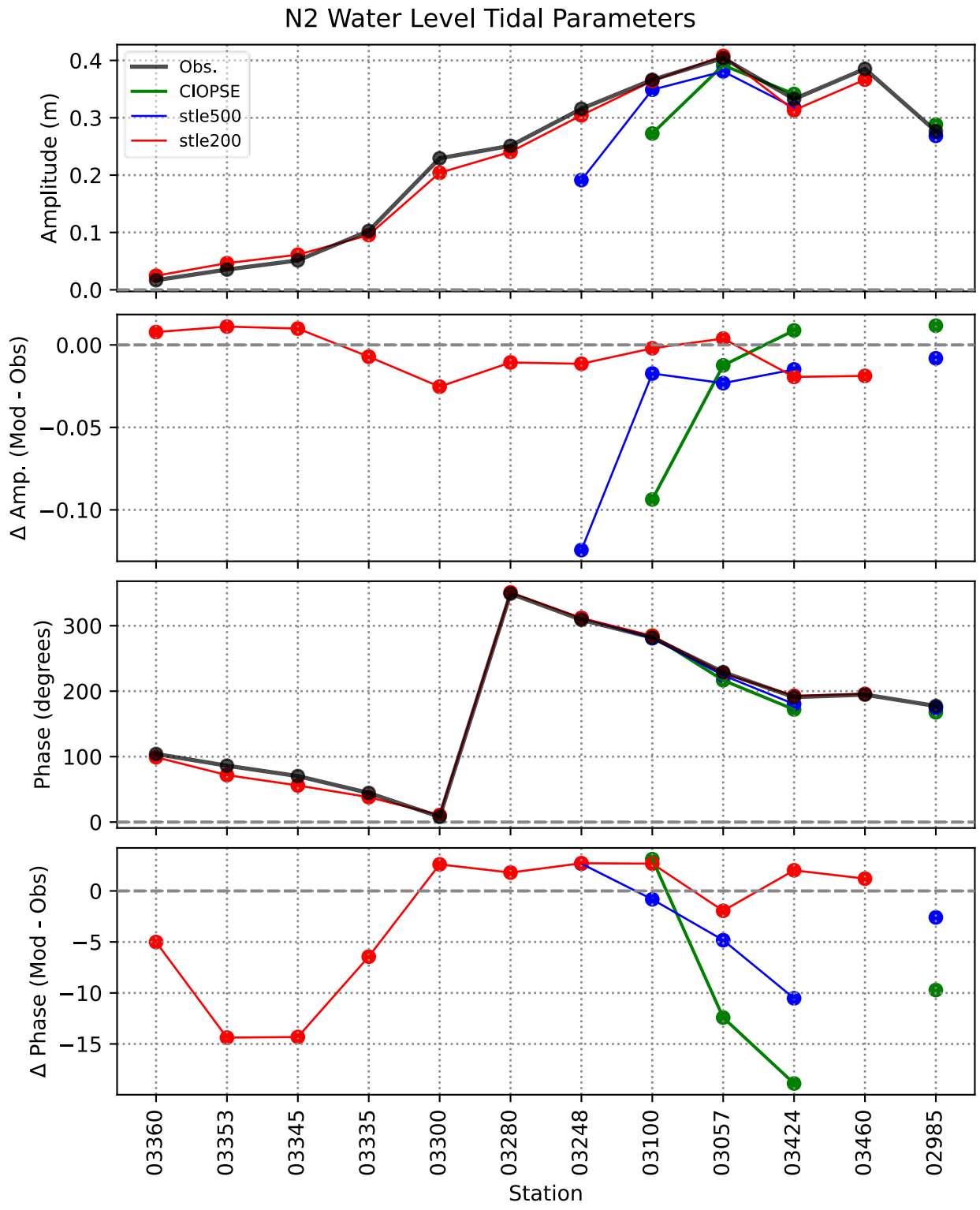

Figure 15. N2 tidal amplitude (panel 1 and 2) and phase (panel 3 and 4) of the three models compared to observations at the active tide gauge stations (see Figure 5 and Figure 6 for a map of tide gauge stations).

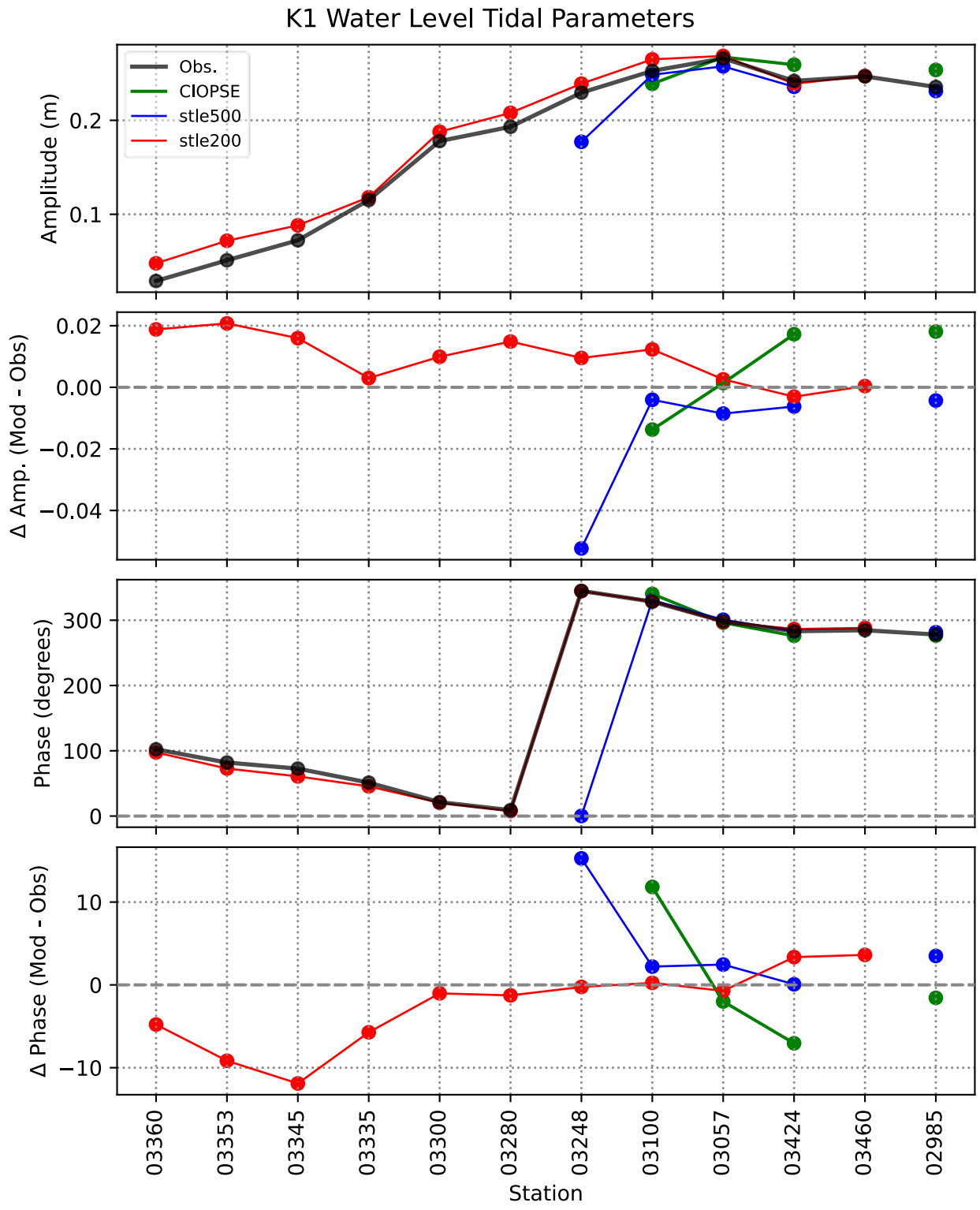

Figure 16. K1 tidal amplitude (panel 1 and 2) and phase (panel 3 and 4) of the three models compared to observations at the active tide gauge stations (see Figure 5 and Figure 6 for a map of tide gauge stations).

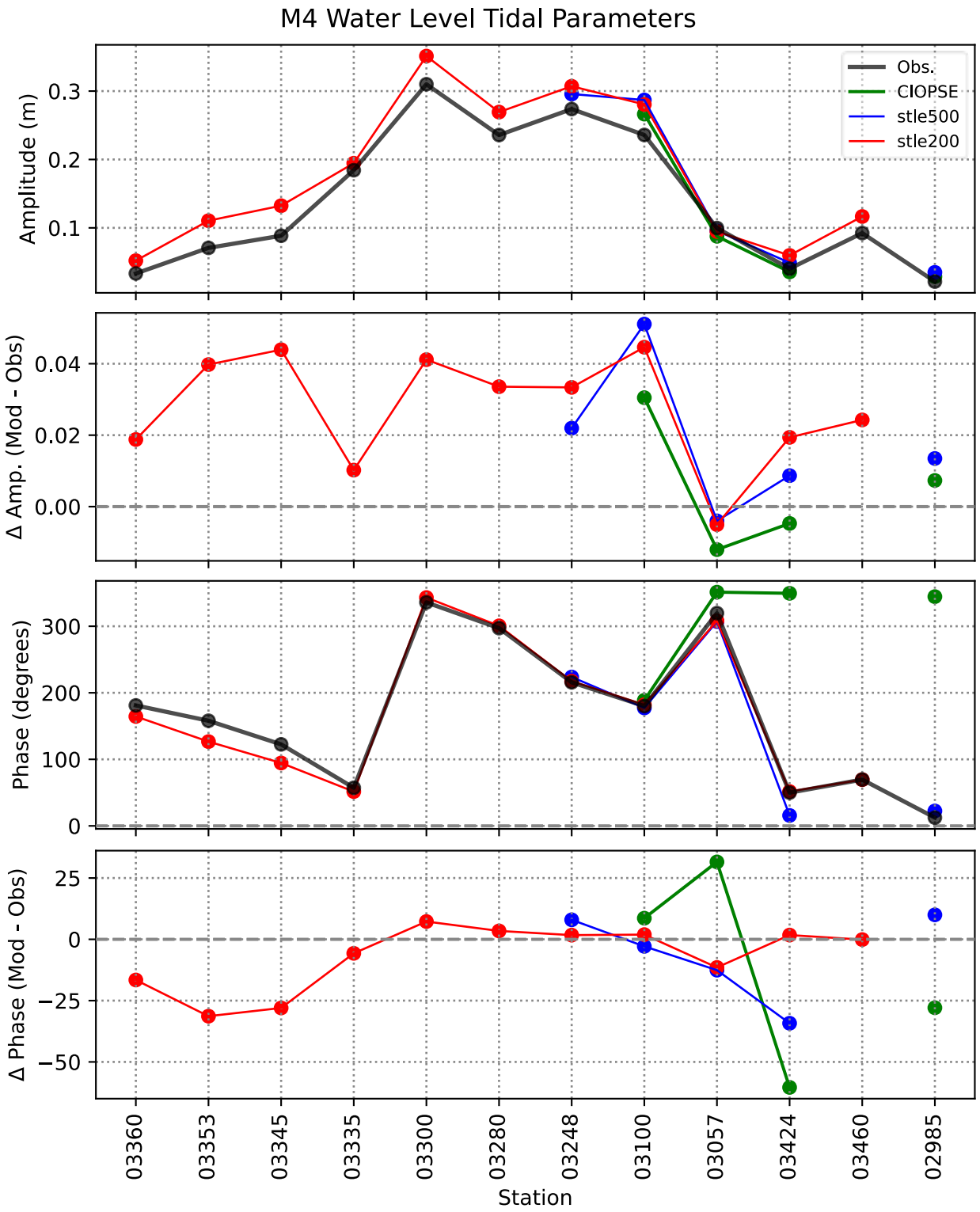

Figure 17. M4 tidal amplitude (panel 1 and 2) and phase (panel 3 and 4) of the three models compared to observations at the active tide gauge stations (see Figure 5 and Figure 6 for a map of tide gauge stations).

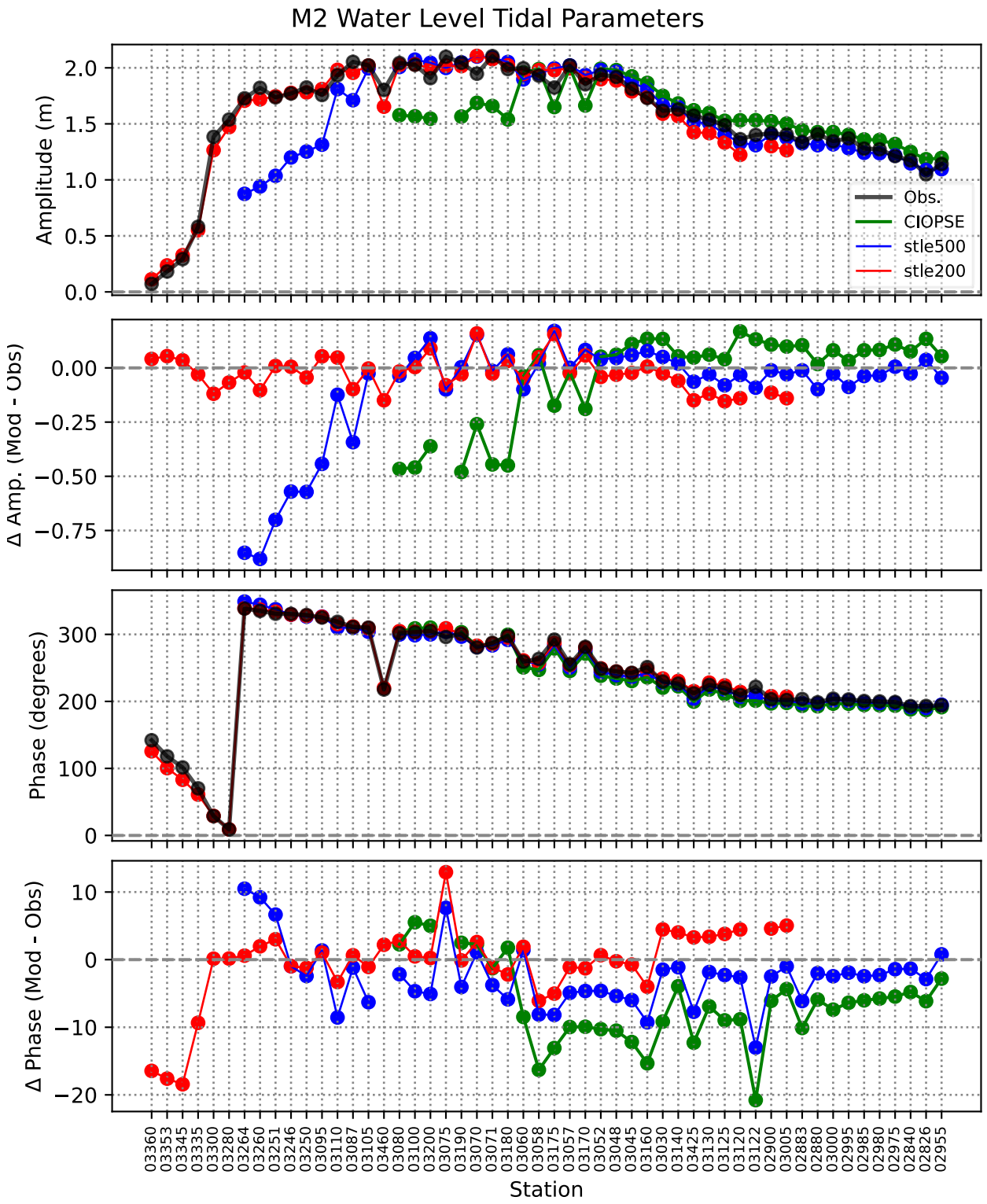

Figure 18. M2 tidal amplitude (panel 1 and 2) and phase (panel 3 and 4) of the three models compared to observations at the historical tide gauge stations (see Figure 5 and Figure 6 for a map of tide gauge stations).

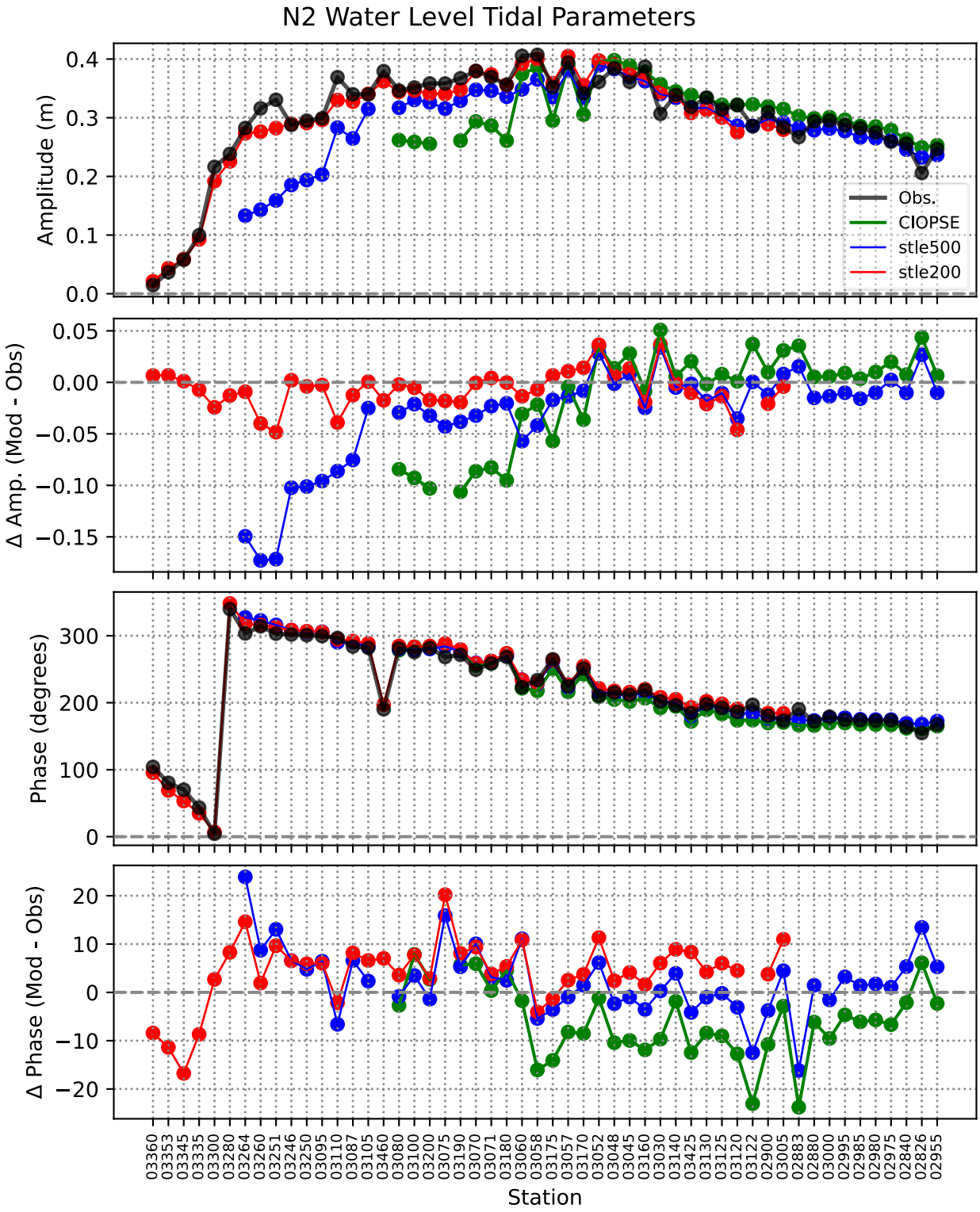

Figure 19. N2 tidal amplitude (panel 1 and 2) and phase (panel 3 and 4) of the three models compared to observations at the historical tide gauge stations (see Figure 5 and Figure 6 for a map of tide gauge stations).

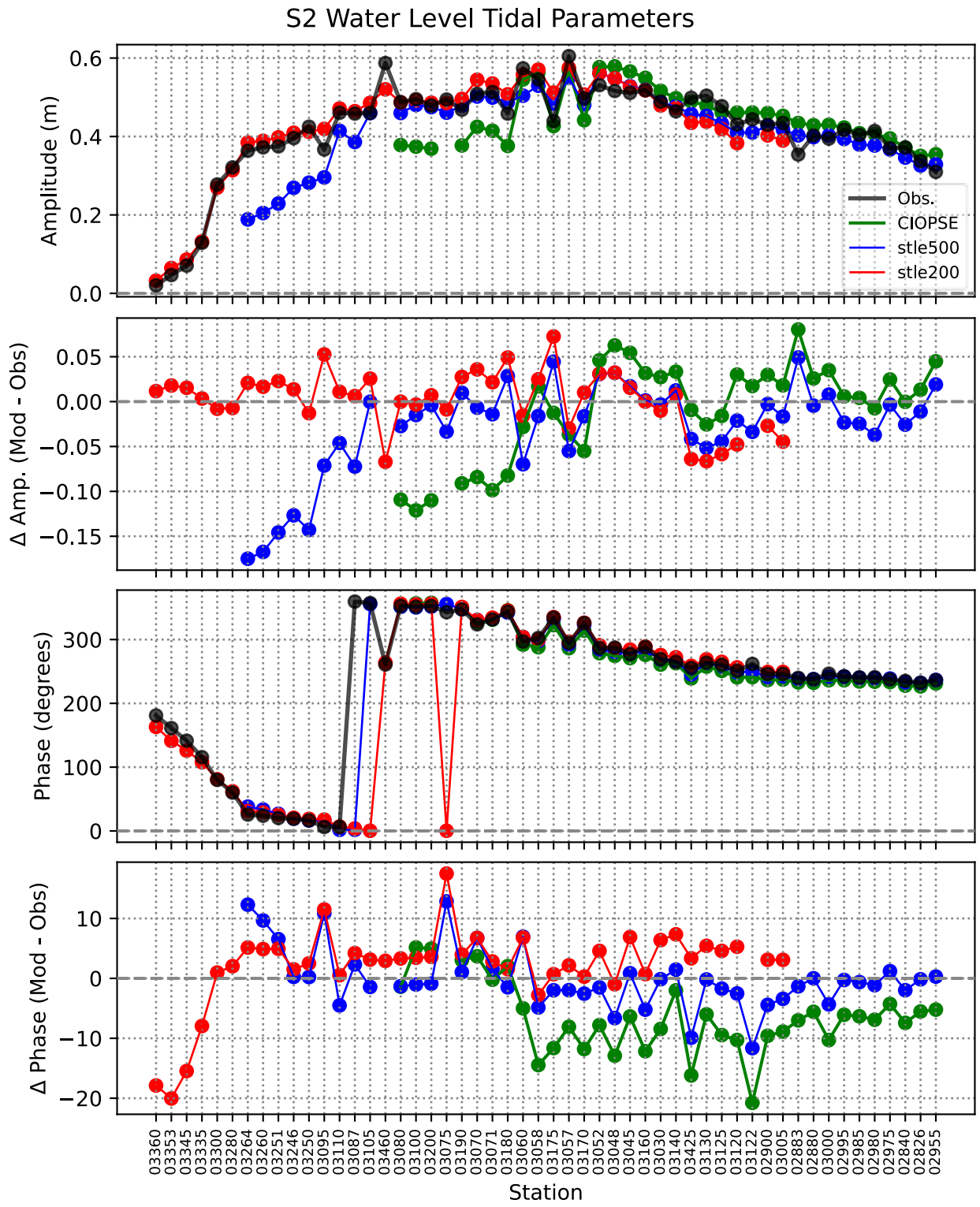

Figure 20. S2 tidal amplitude (panel 1 and 2) and phase (panel 3 and 4) of the three models compared to observations at the historical tide gauge stations (see Figure 5 and Figure 6 for a map of tide gauge stations).

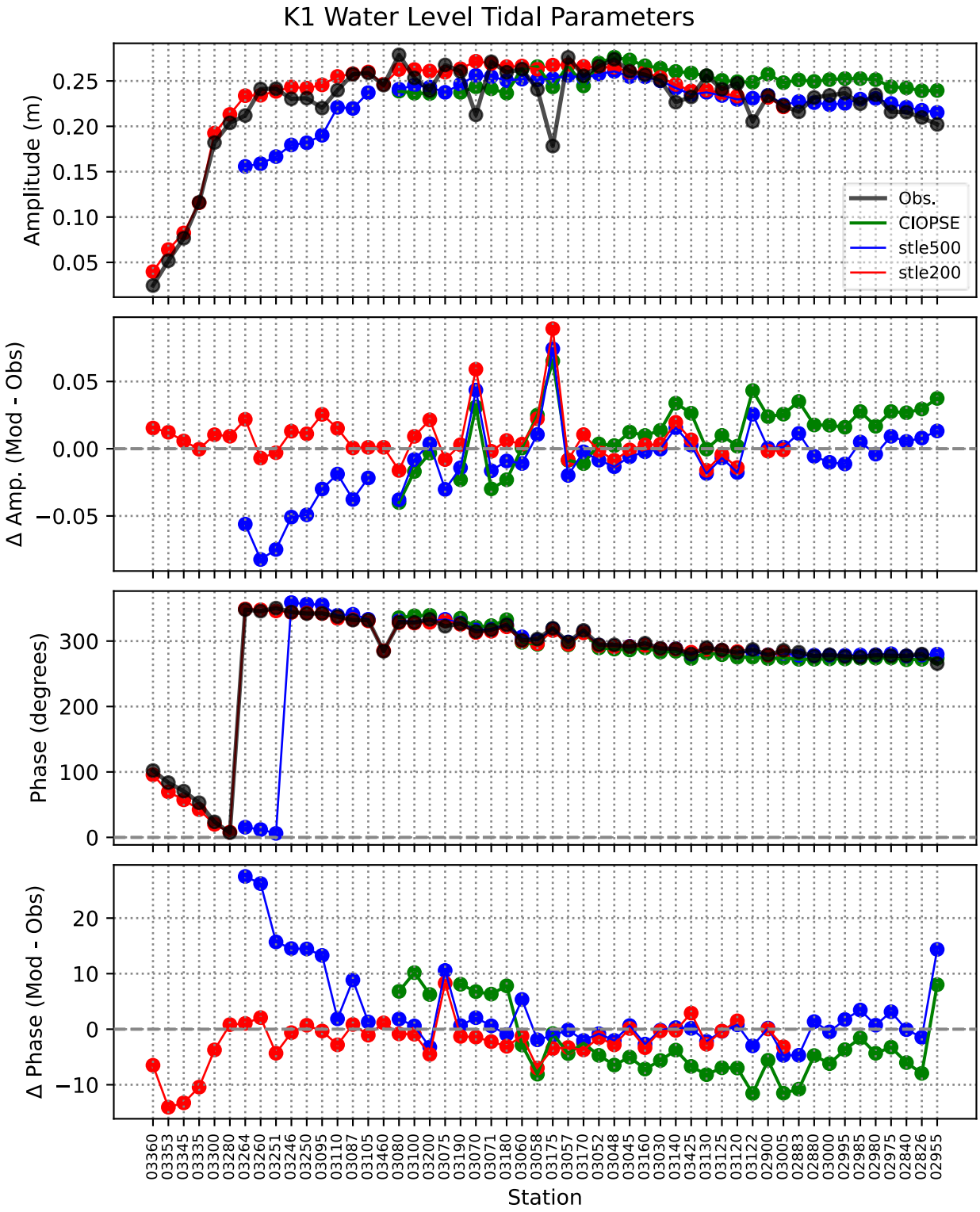

Figure 21. K1 tidal amplitude (panel 1 and 2) and phase (panel 3 and 4) of the three models compared to observations at the historical tide gauge stations (see Figure 5 and Figure 6 for a map of tide gauge stations).

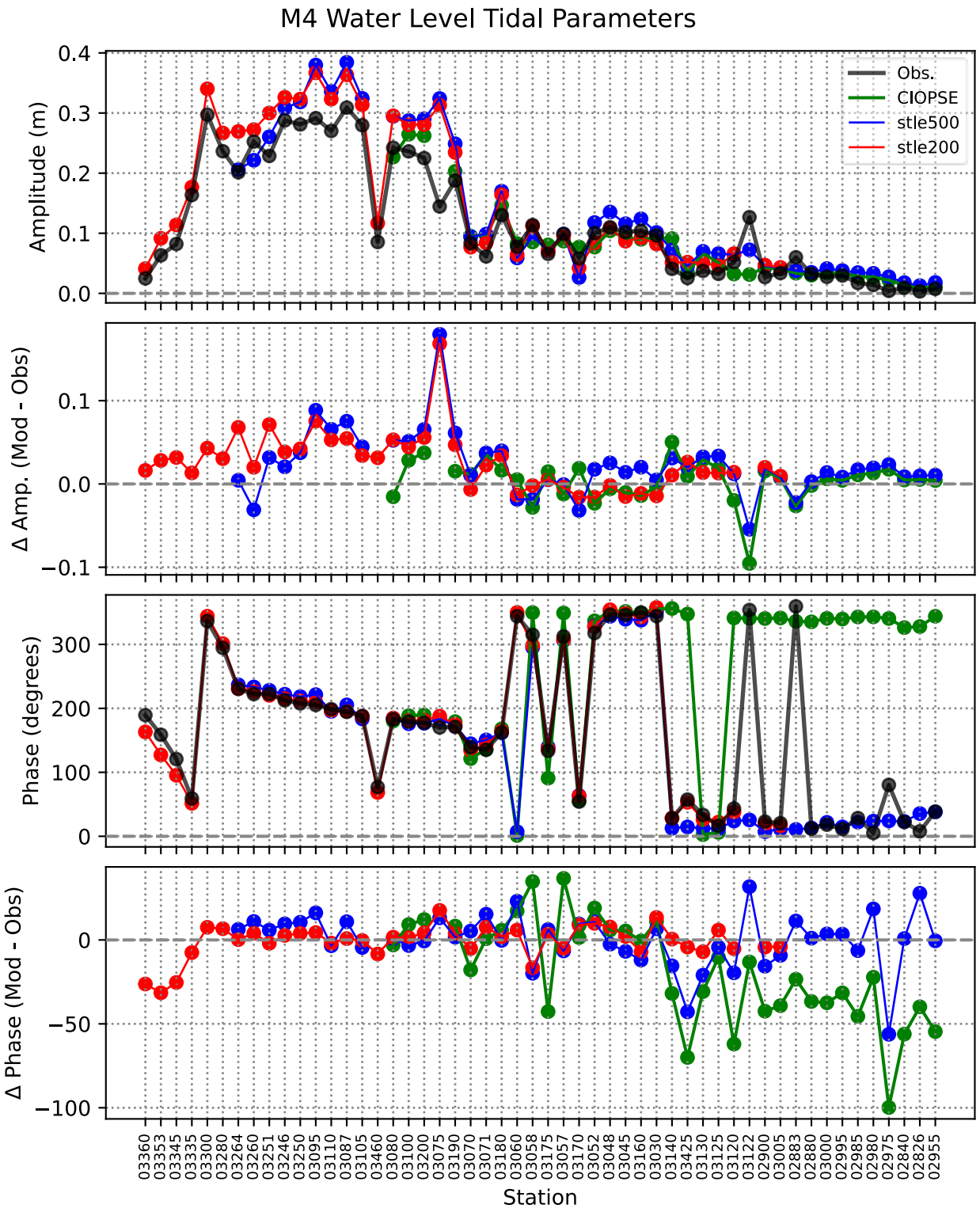

Figure 22. M4 tidal amplitude (panel 1 and 2) and phase (panel 3 and 4) of the three models compared to observations at the historical tide gauge stations (see Figure 5 and Figure 6 for a map of tide gauge stations).

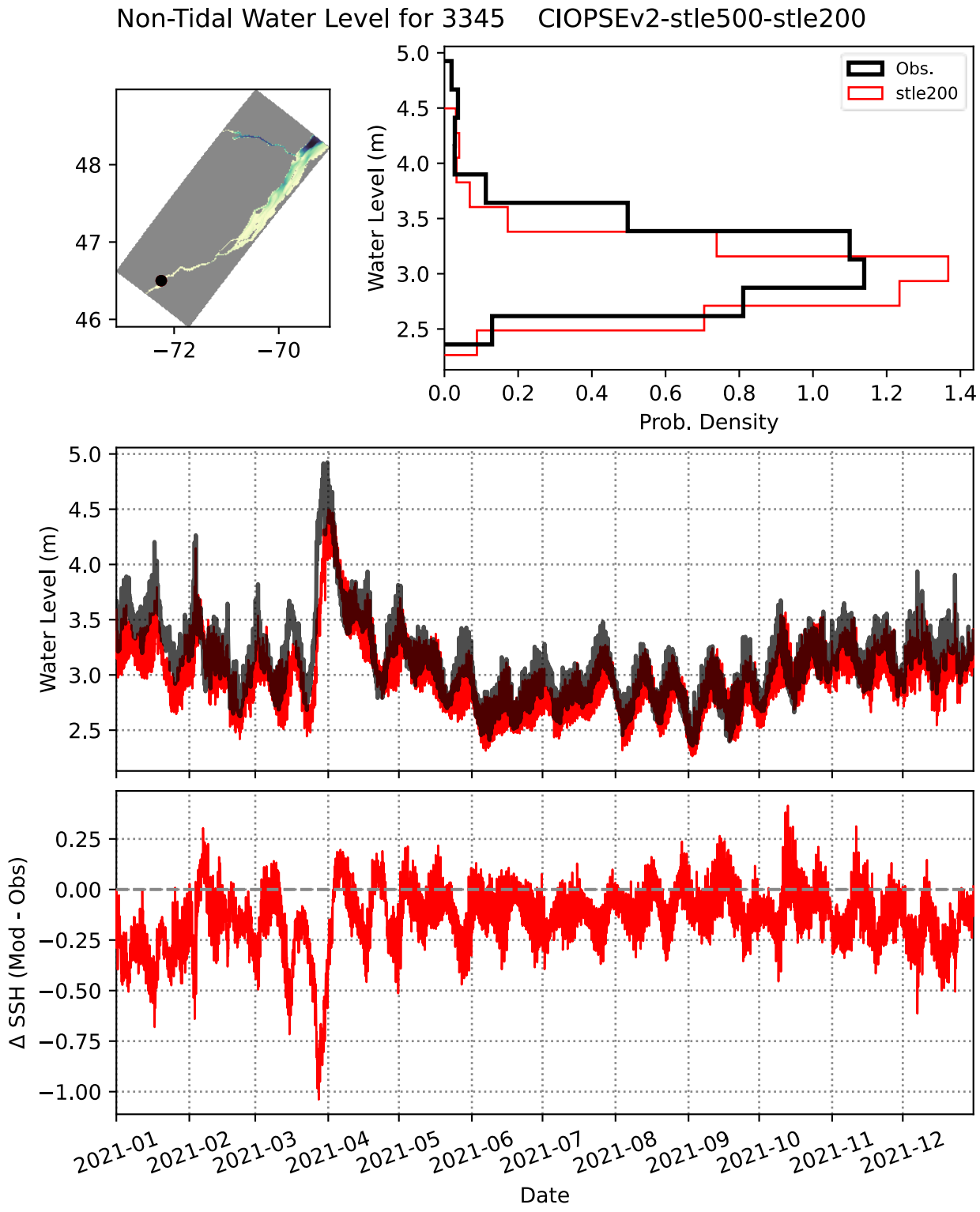

Figure 23. Non-tidal water level at station 3345 for year 2021.

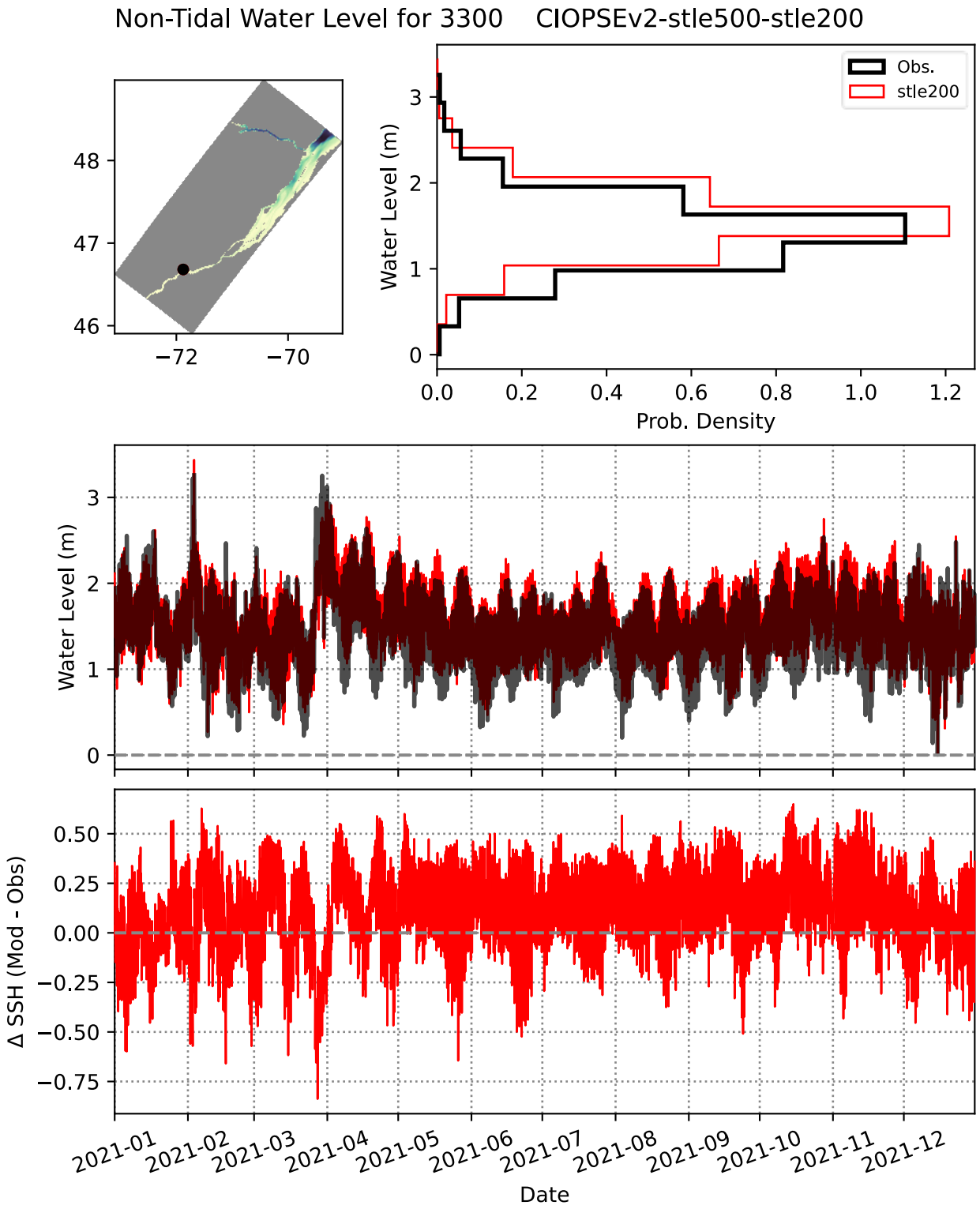

Figure 24. Non-tidal water level at station 3300 for year 2021.

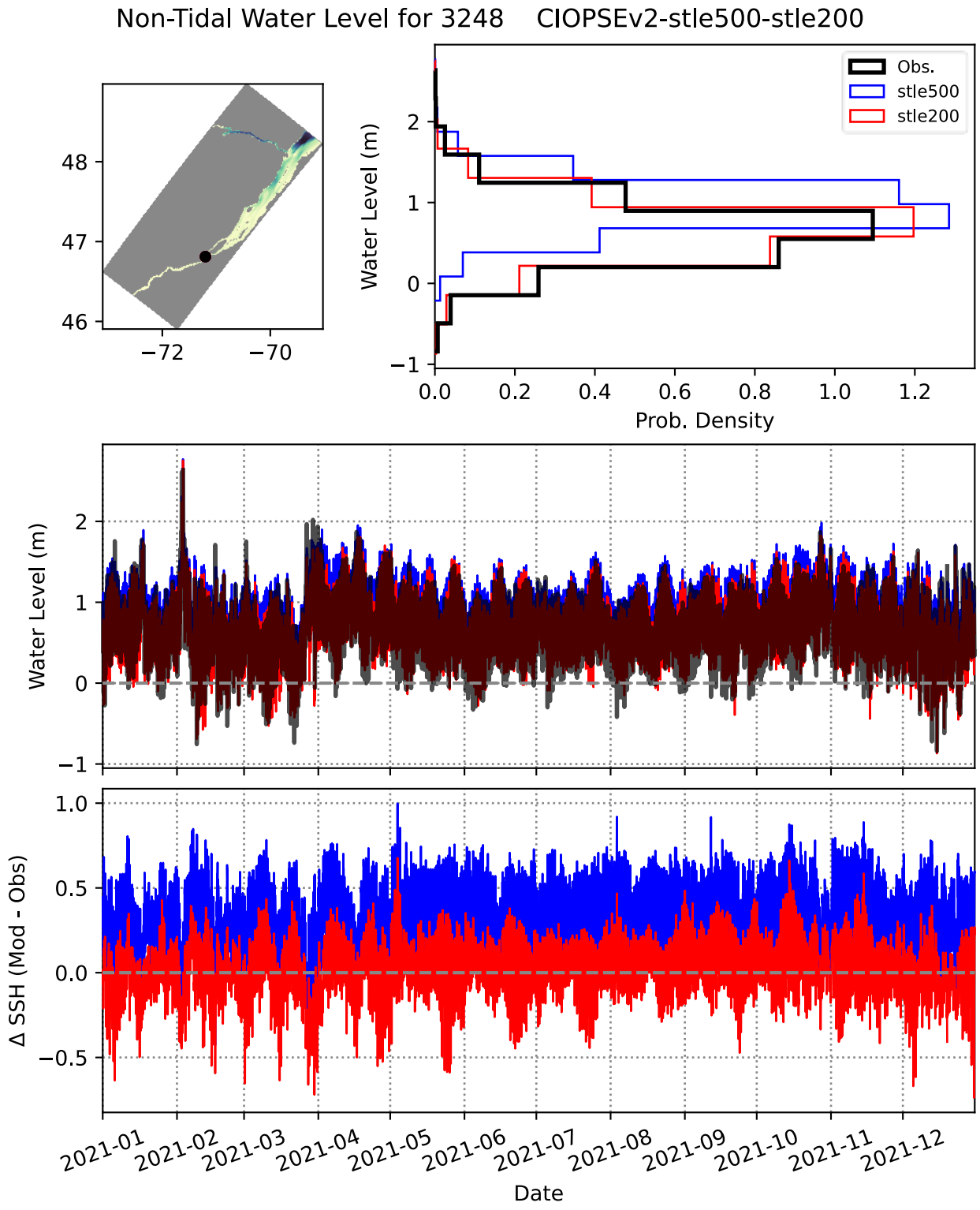

Figure 25. Non-tidal water level at station 3248 for year 2021.

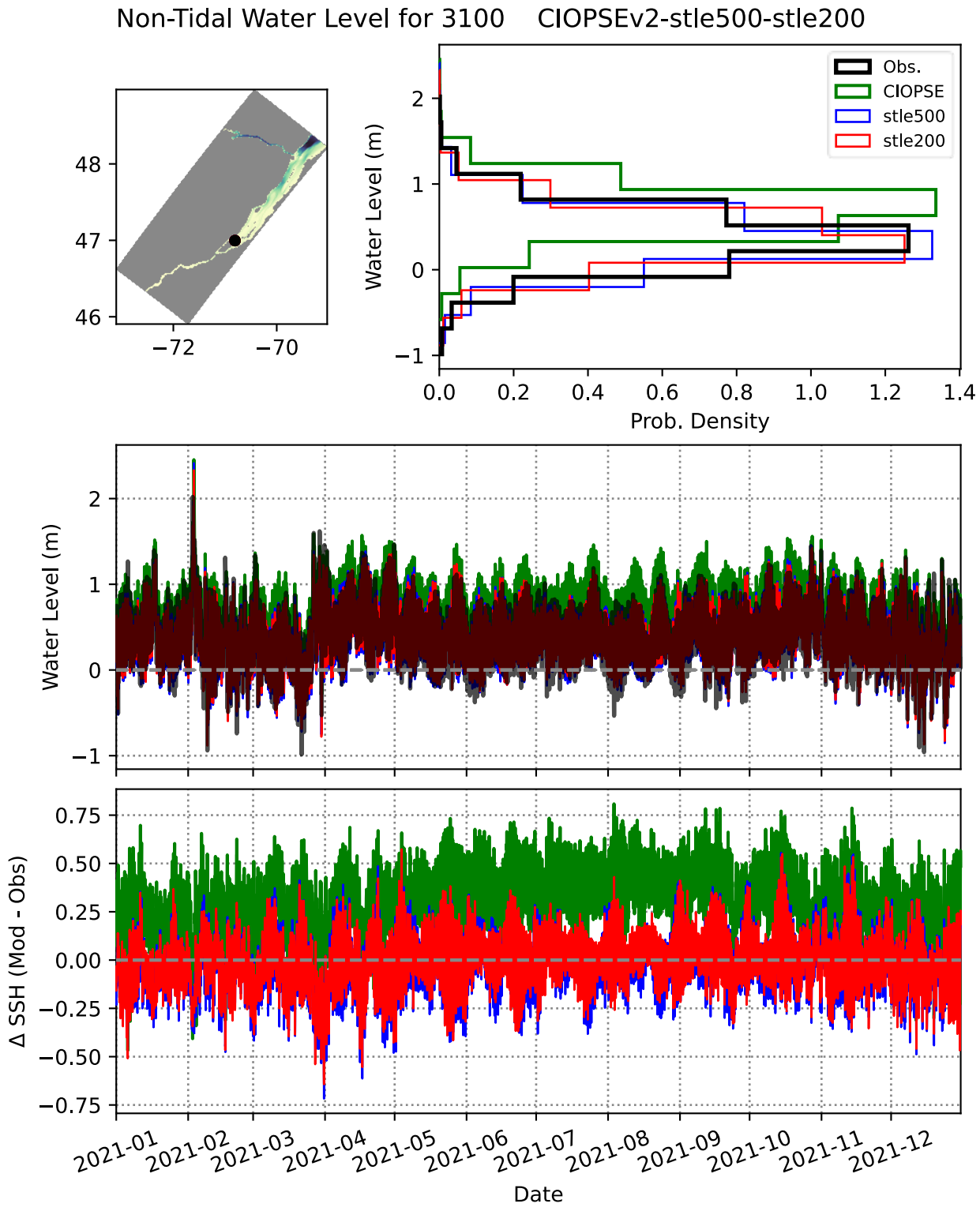

Figure 26. Non-tidal water level at station 3100 for year 2021.

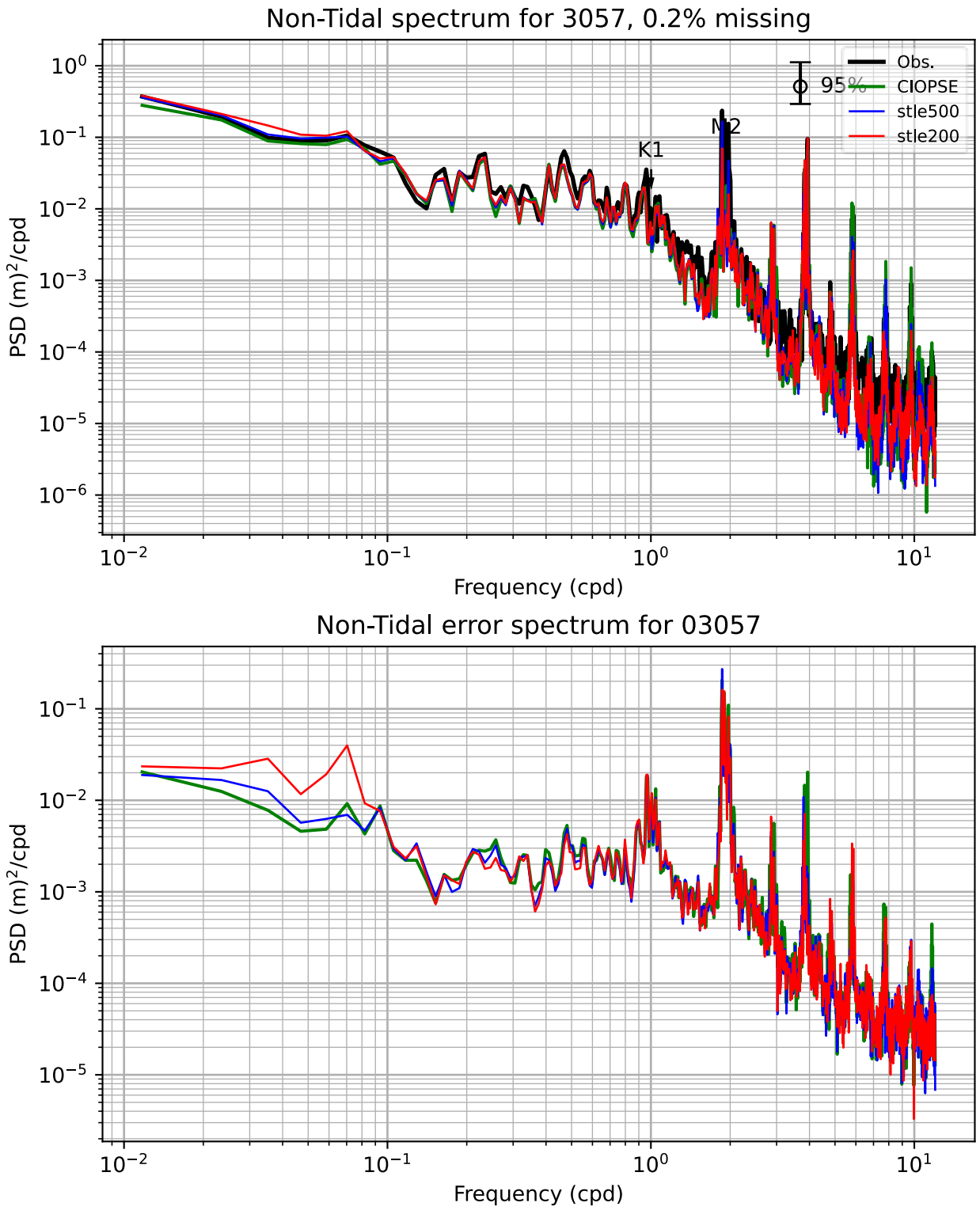

Figure 27. Non-tidal water level spectrum (top panel) and error spectrum (bottom panel) for station 3057, for year 2021.

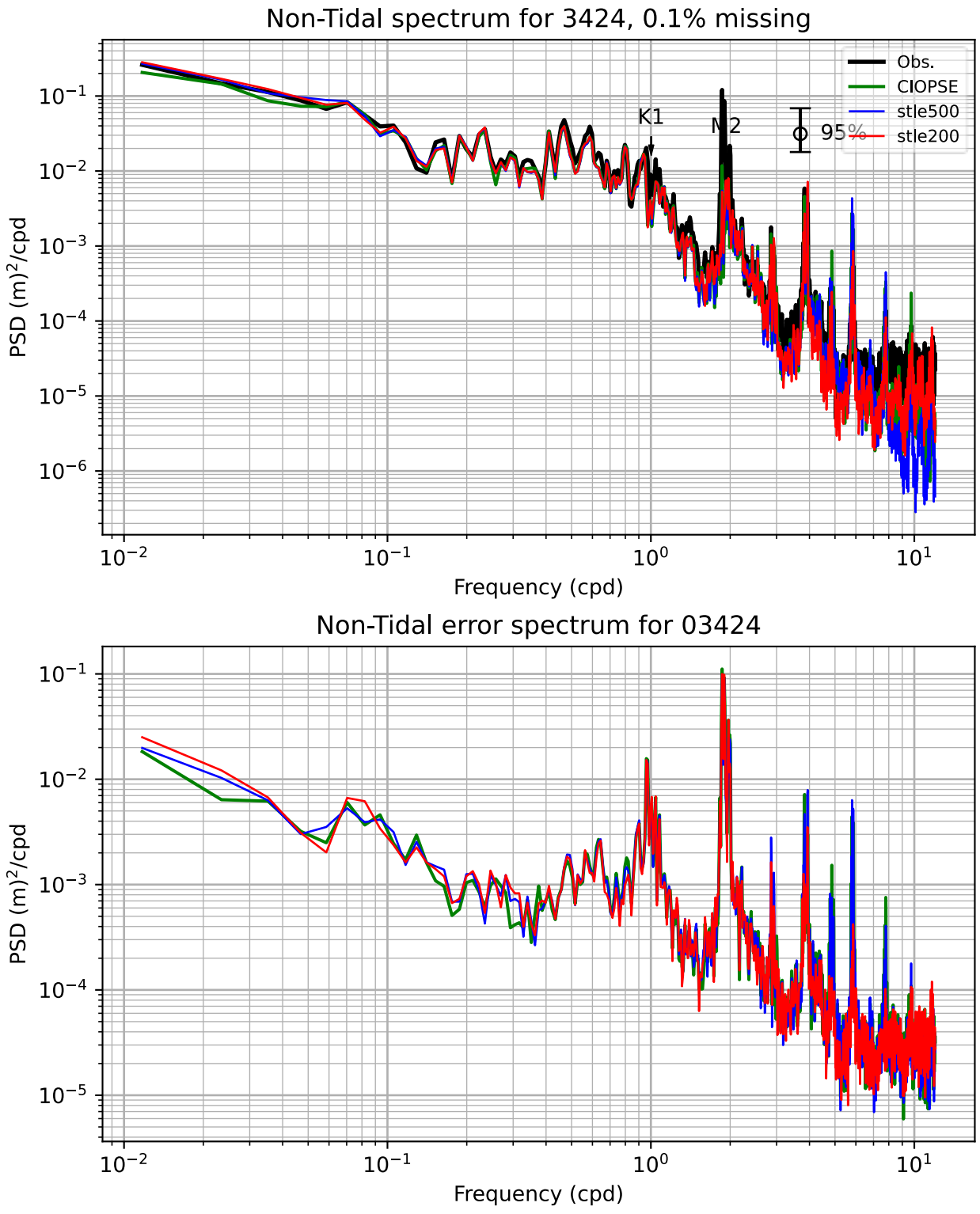

Figure 28. Non-tidal water level spectrum (top panel) and error spectrum (bottom panel) for station 3424, for year 2021.

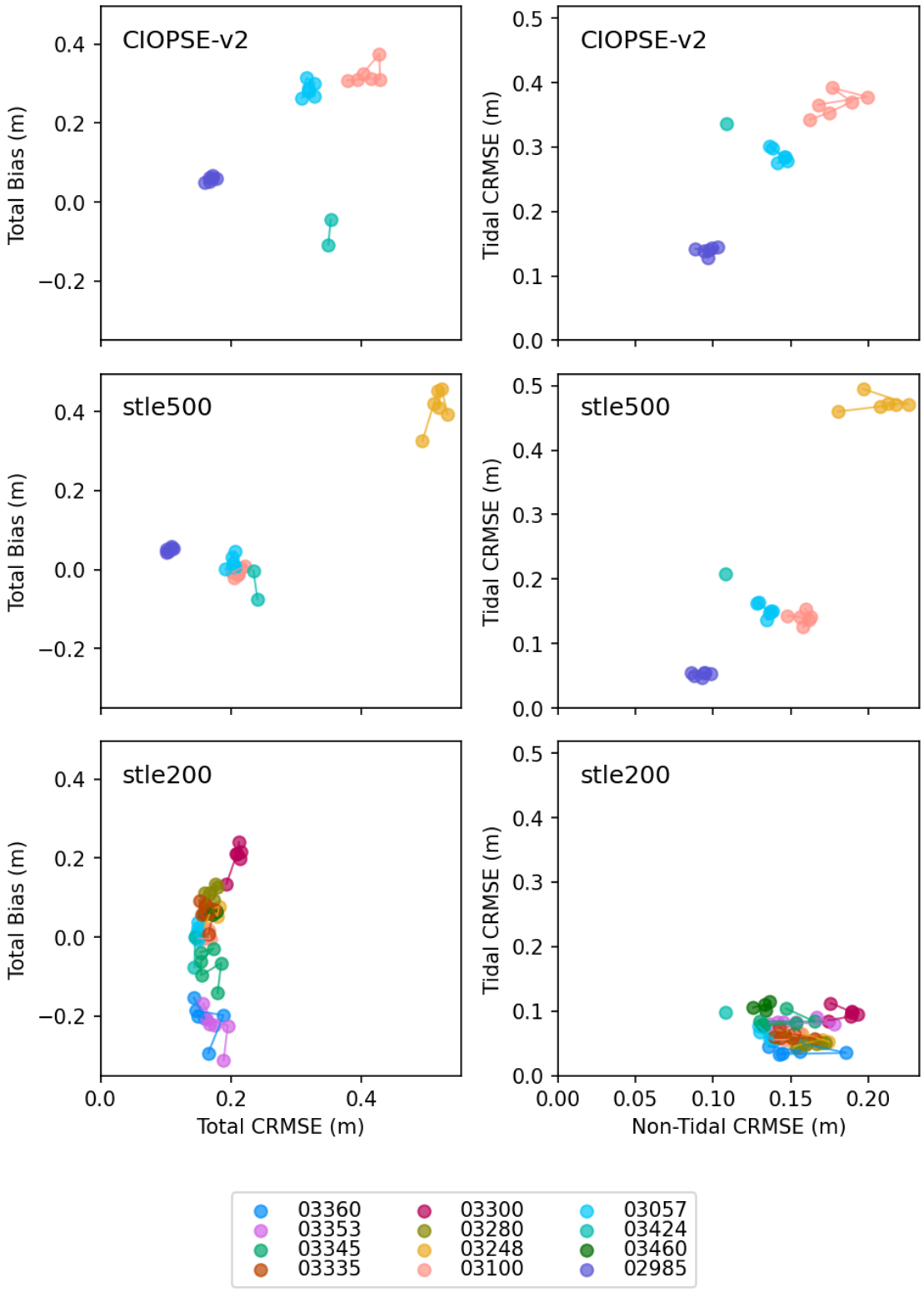

Figure 29. Water level scores temporal stability summary for each station and each model. For total water level (left panels), bias is on the vertical axis and CRMSE is on the horizontal axis. Right panels show tidal CRMSE on the vertical axis and non-tidal CRMSE on the horizontal axis. Each dot represents a single year score.

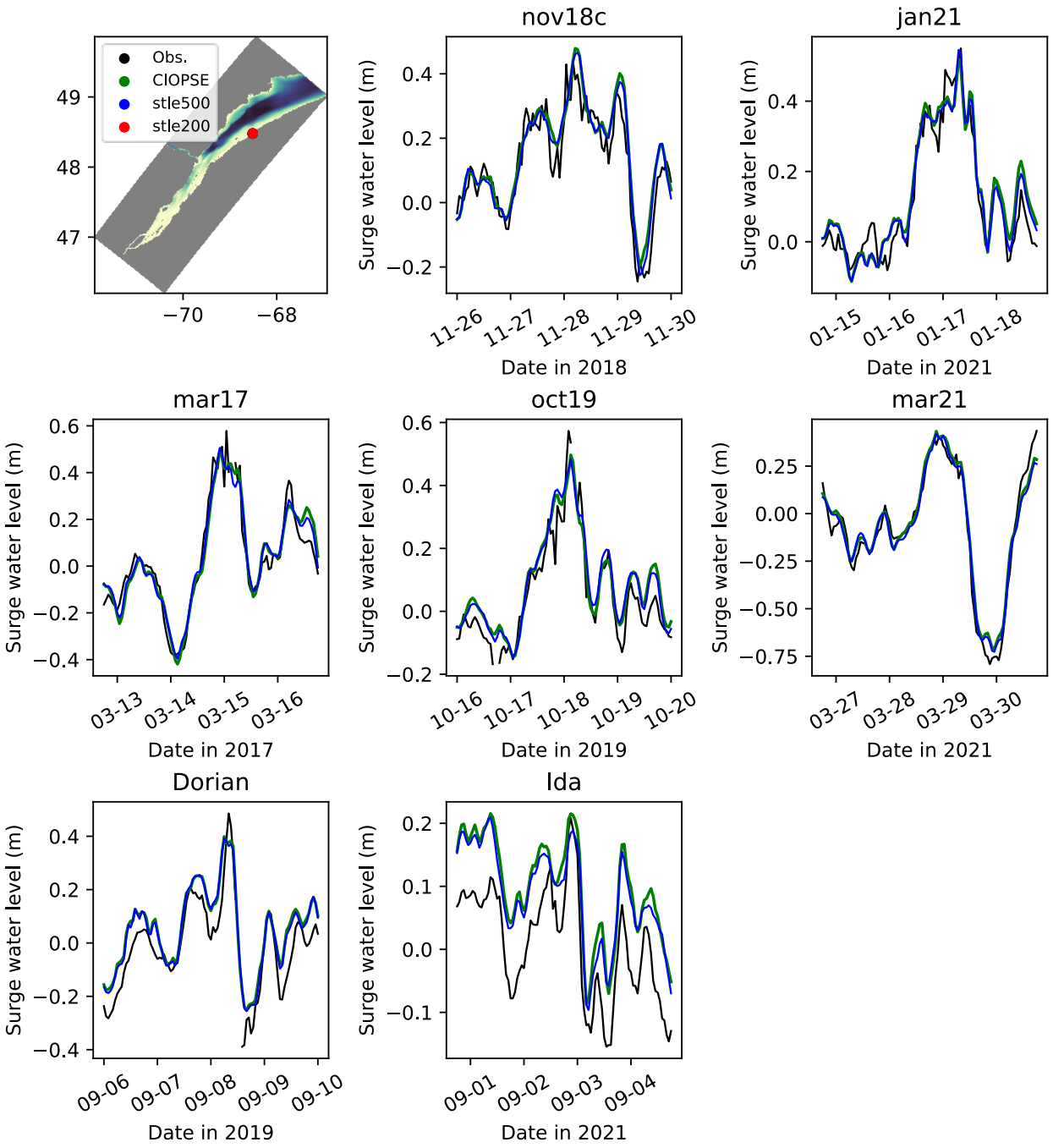

Figure 30. Non-tidal water level for the 7 chosen storm for station 2985.

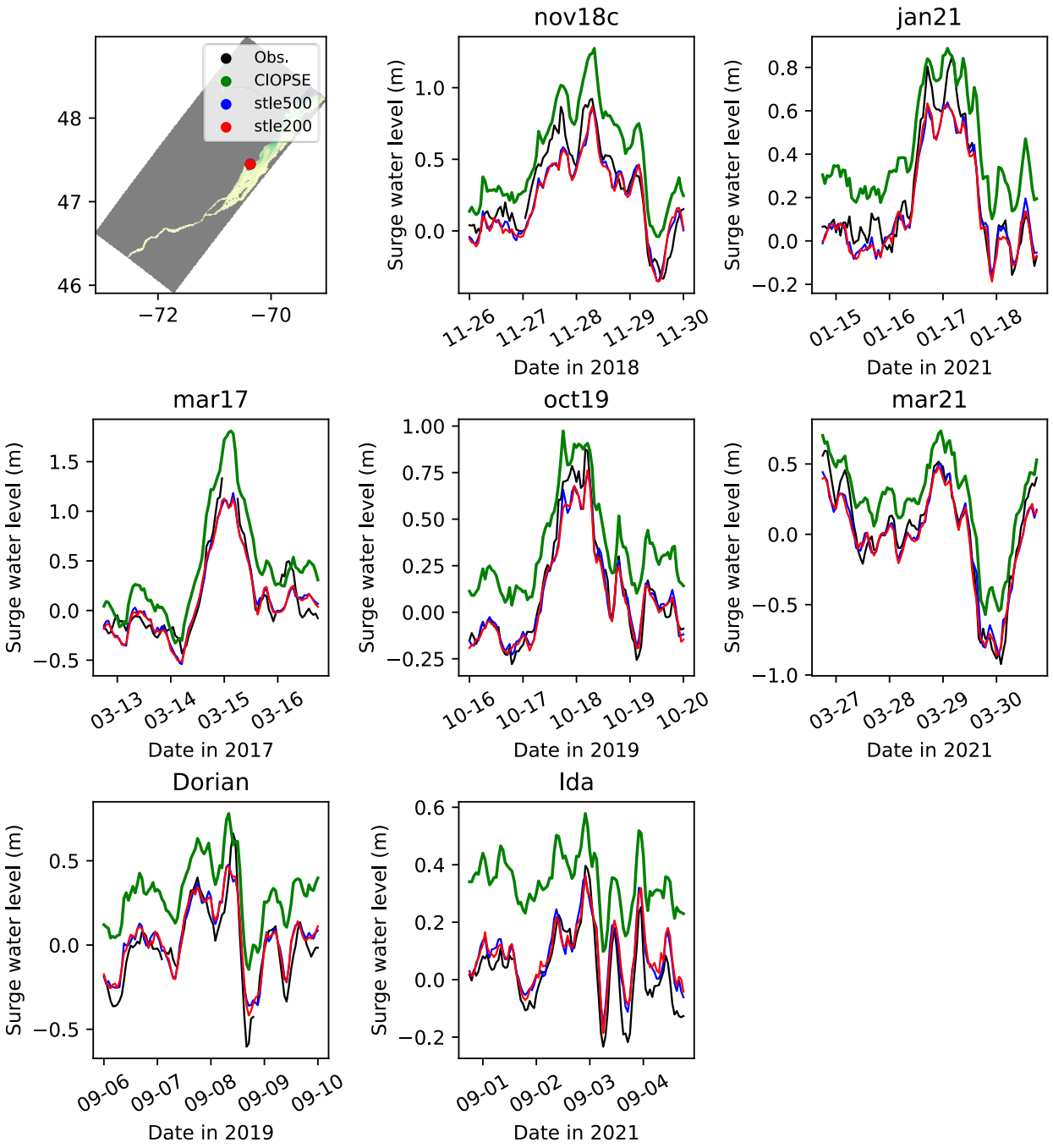

Figure 31. Non-tidal water level for the 7 chosen storm for station 3057.

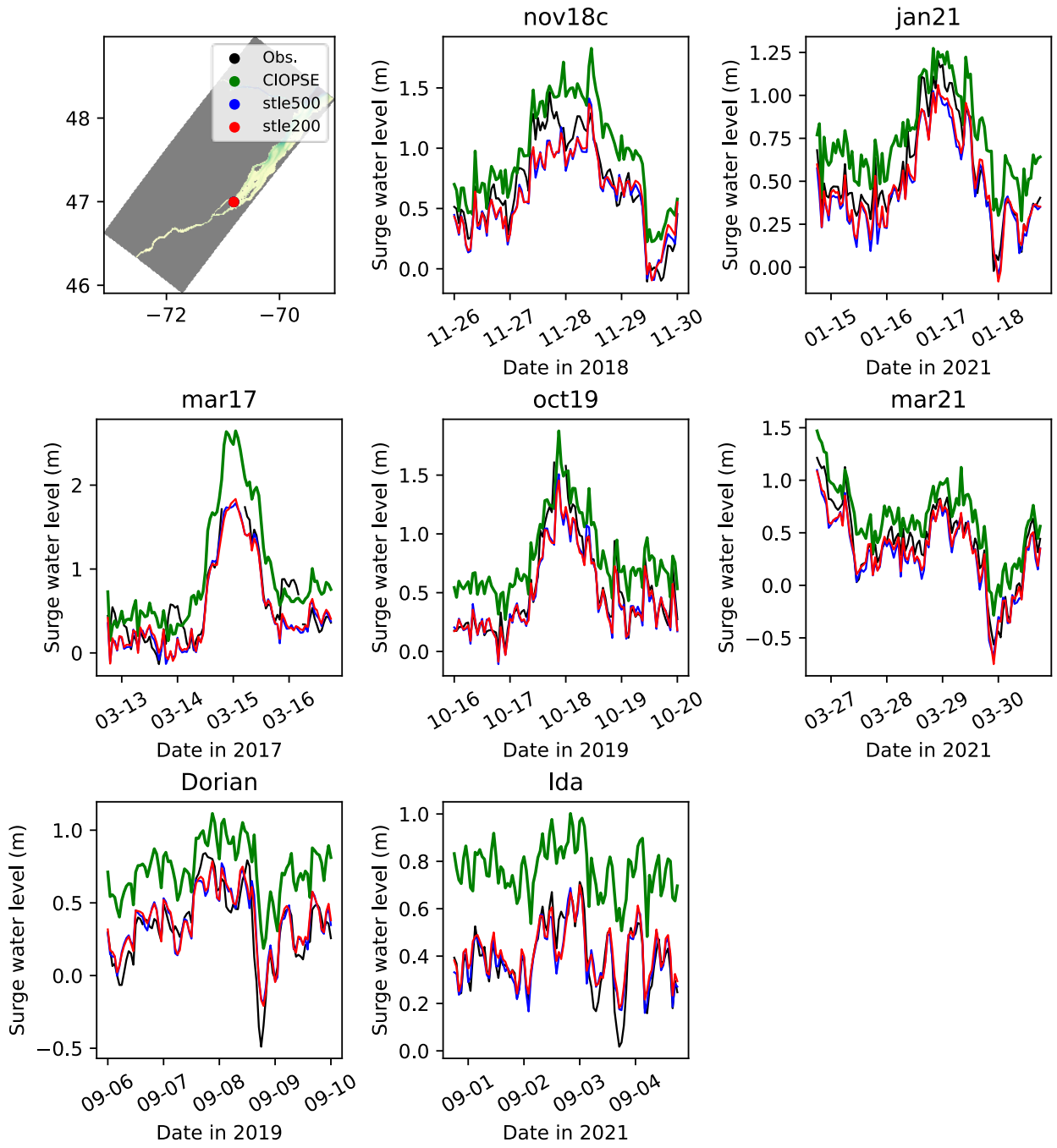

Figure 32. Non-tidal water level for the 7 chosen storm for station 3100.

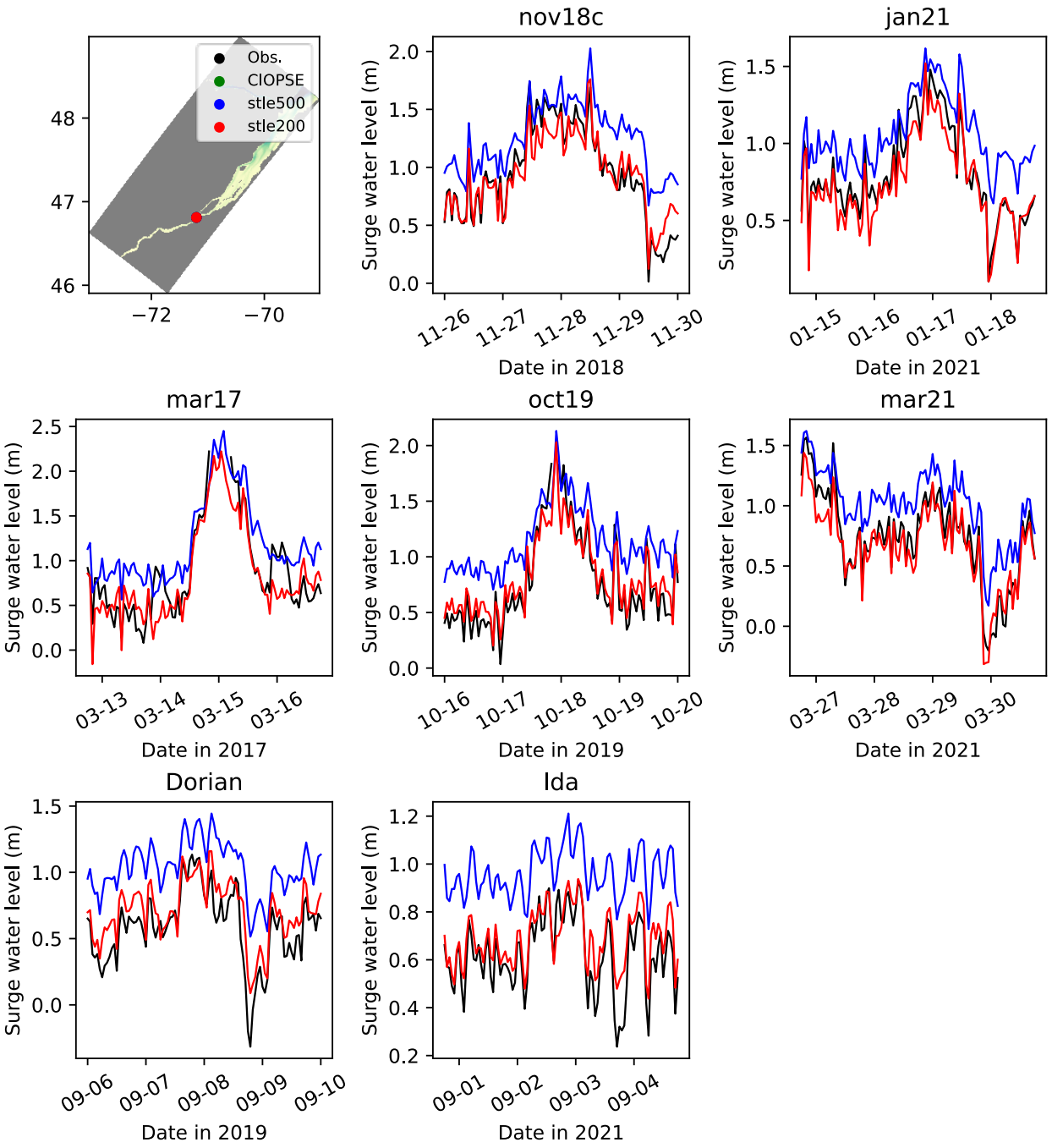

Figure 33. Non-tidal water level for the 7 chosen storm for station 3248.

Figure 34. Map of the position (beginning of the 2 arrows) and the coverage (blue arrow) of the 2 HADCPs deployed on each side of the St. Lawrence river, one at the Port of Québec and one at the Lévis wharf.

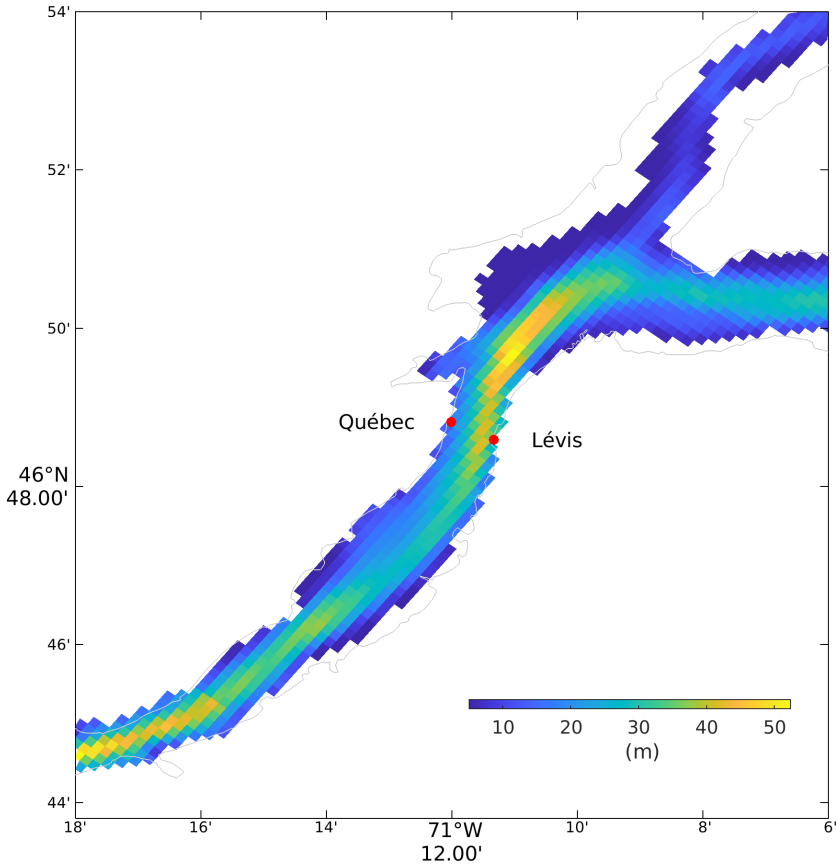

Figure 35. Map of the position (red dots) of the 2 HADCPs deployed on each side of the St. Lawrence river, one at the Port of Québec and one at the Lévis wharf. STLE200 's bathymetrys is also plotted on the figure.

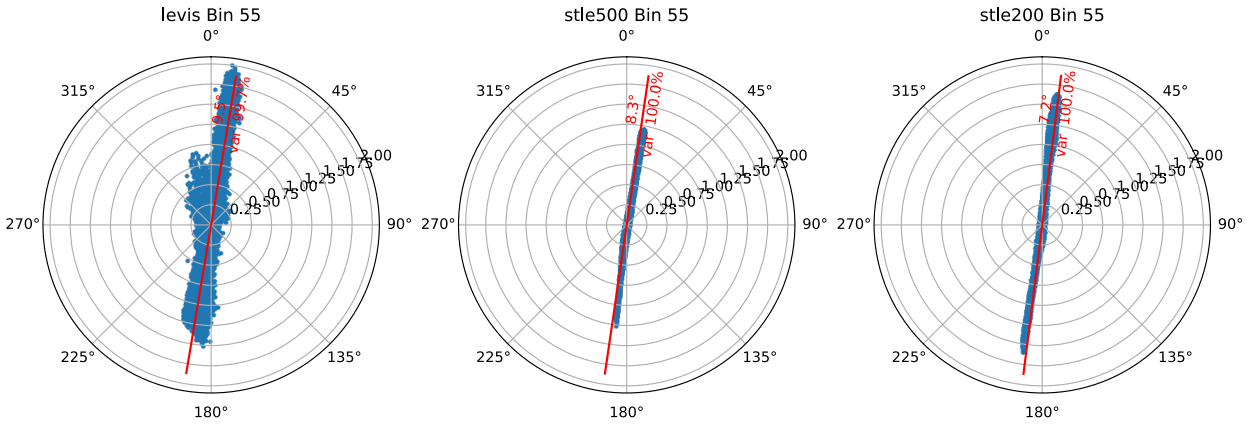

Figure 36. Lévis scatterplots of currents and principal axis of variance for year 2021 for observations, STLE500 and STLE200.

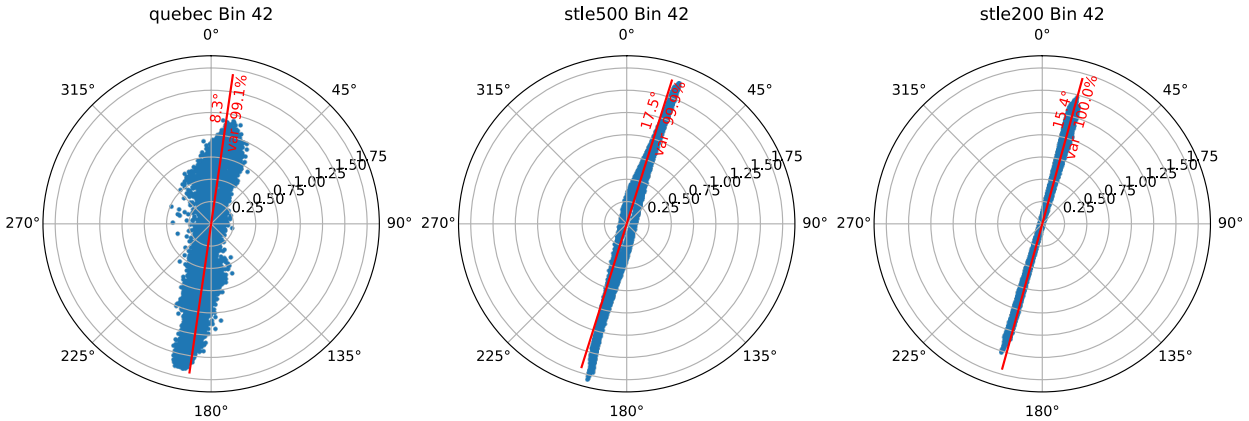

Figure 37. Québec scatterplots of currents and principal axis of variance for year 2021 for observations, STLE500 and STLE200.

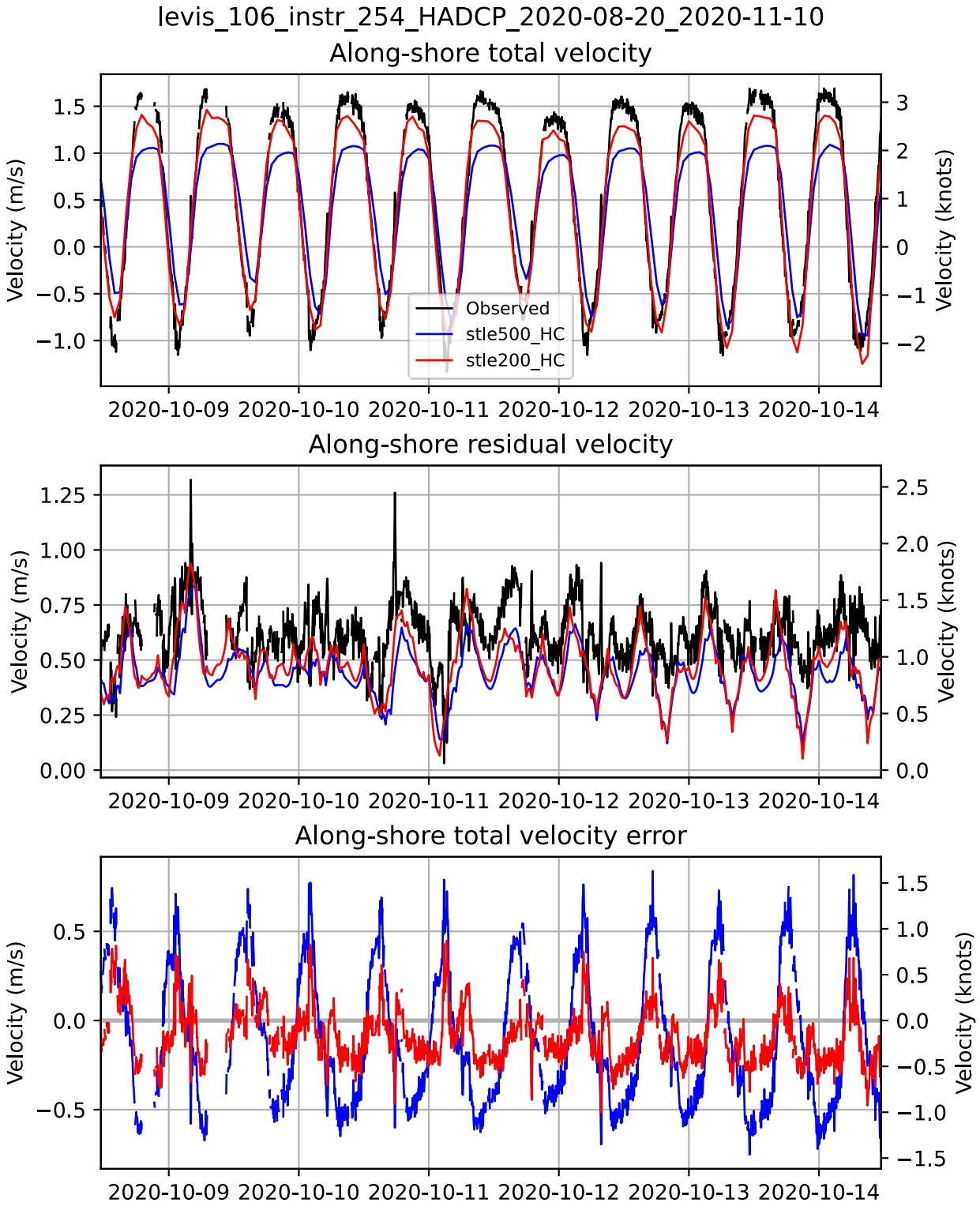

Figure 38. HADCP results in Lévis and model outputs for year 2020. Along-shore total velocity currents from observations and the 2 models in panel 1, along-shore residual velocity in panel 2, and along-shore total velocity error in panel 3.

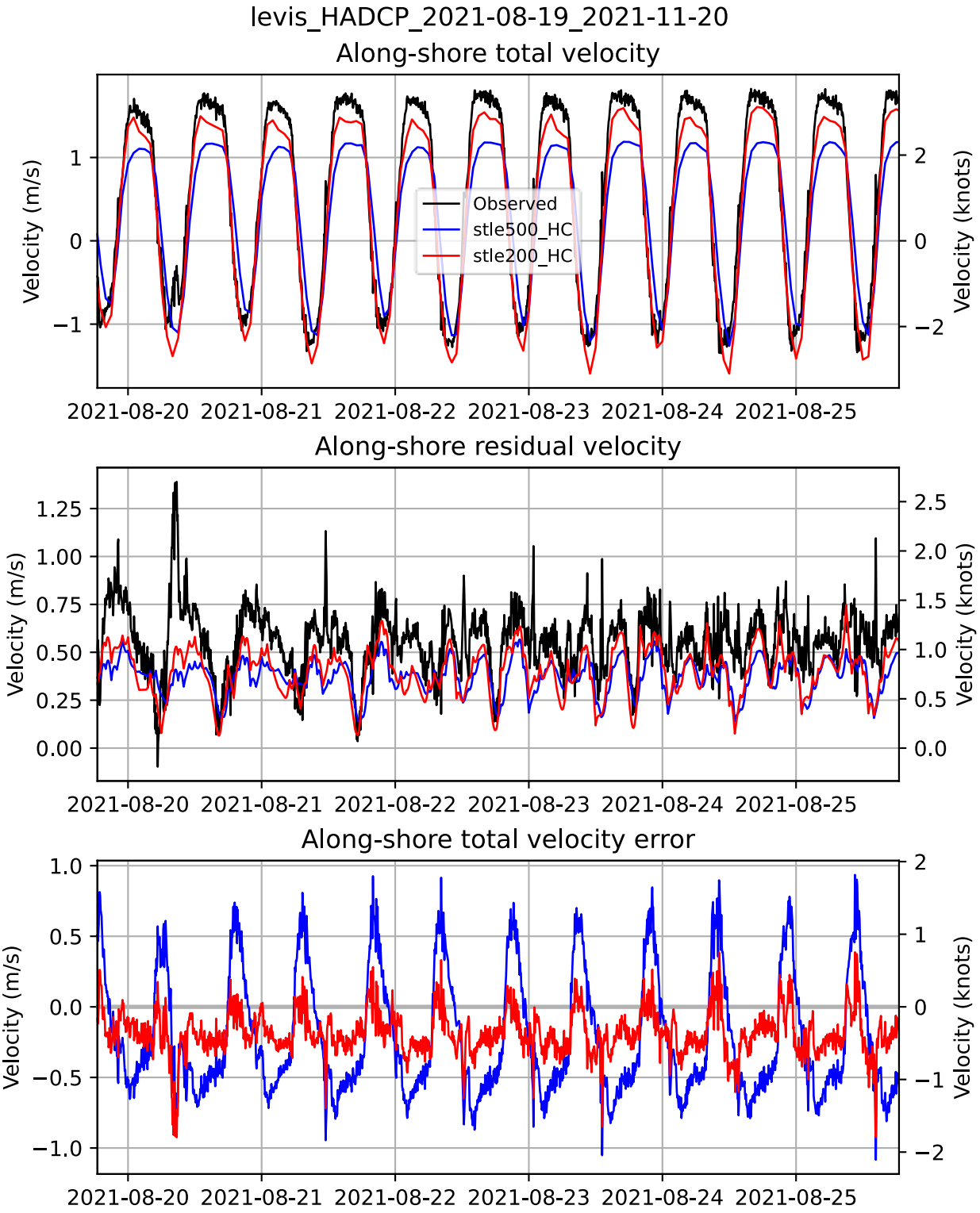

Figure 39. HADCP results in Lévis and model outputs for year 2021. Along-shore total velocity currents from observations and the 2 models in panel 1, along-shore residual velocity in panel 2, and along-shore total velocity error in panel 3.

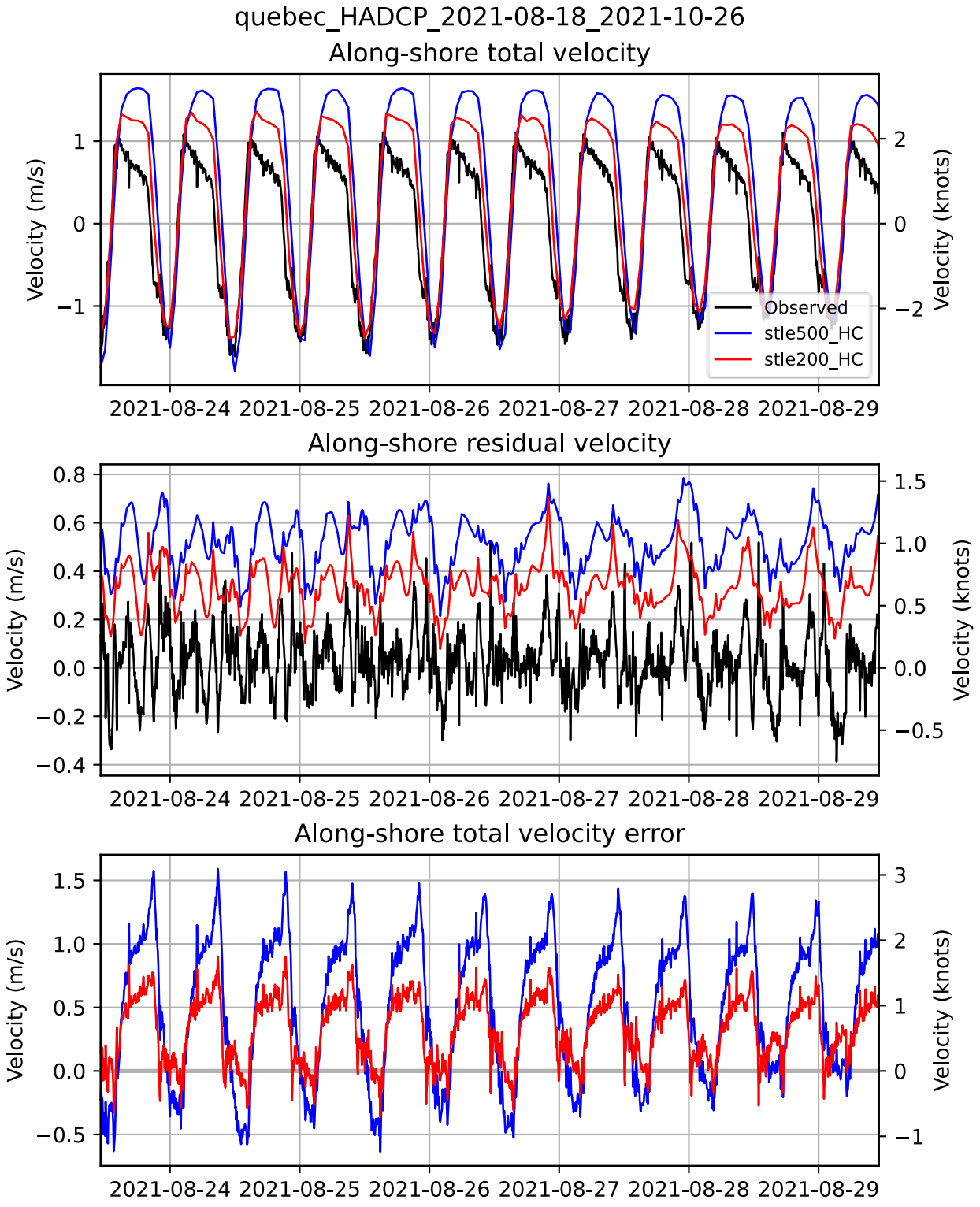

Figure 40. HADCP results in Québec and model outputs for year 2020. Along-shore total velocity currents from observations and the 2 models in panel 1, along-shore residual velocity in panel 2, and along-shore total velocity error in panel 3.

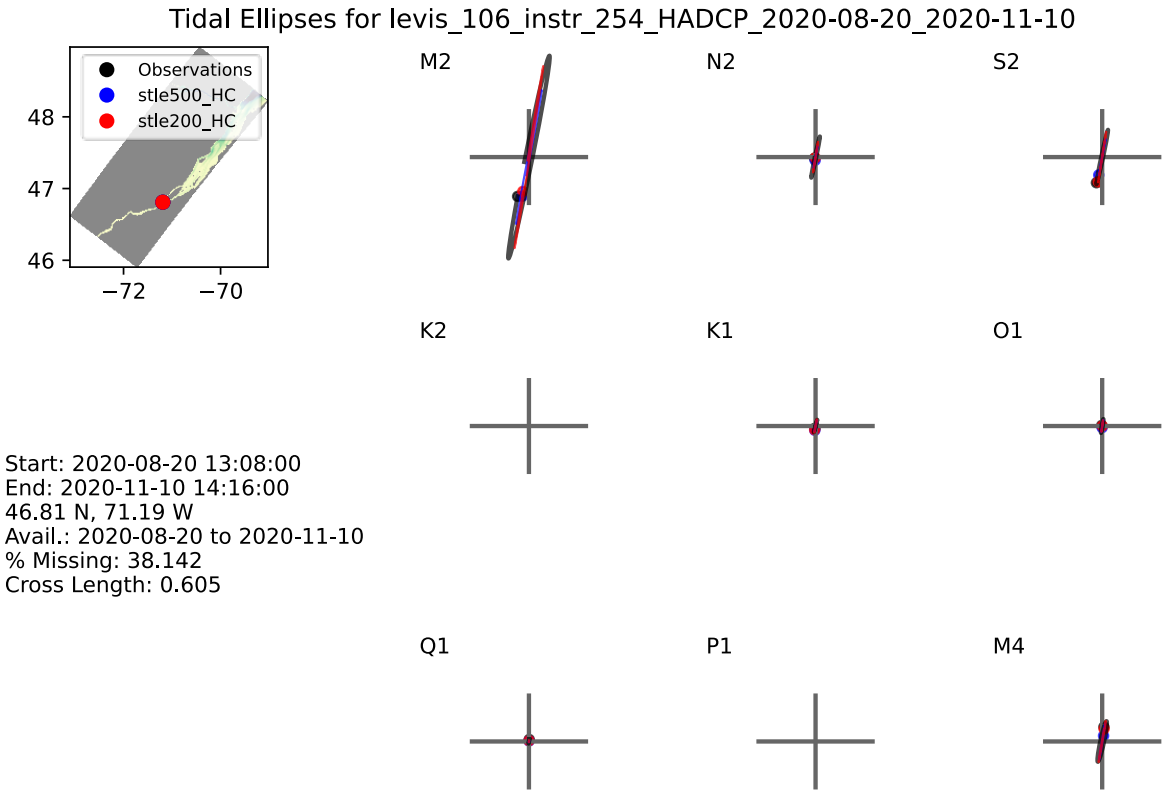

Figure 41. HADCP results in Lévis and model outputs for year 2020. Tidal ellipses from observations and the 2 models for tidal constituents M2, N2, S2, K2, K1, O1, Q1, P1 and M4.

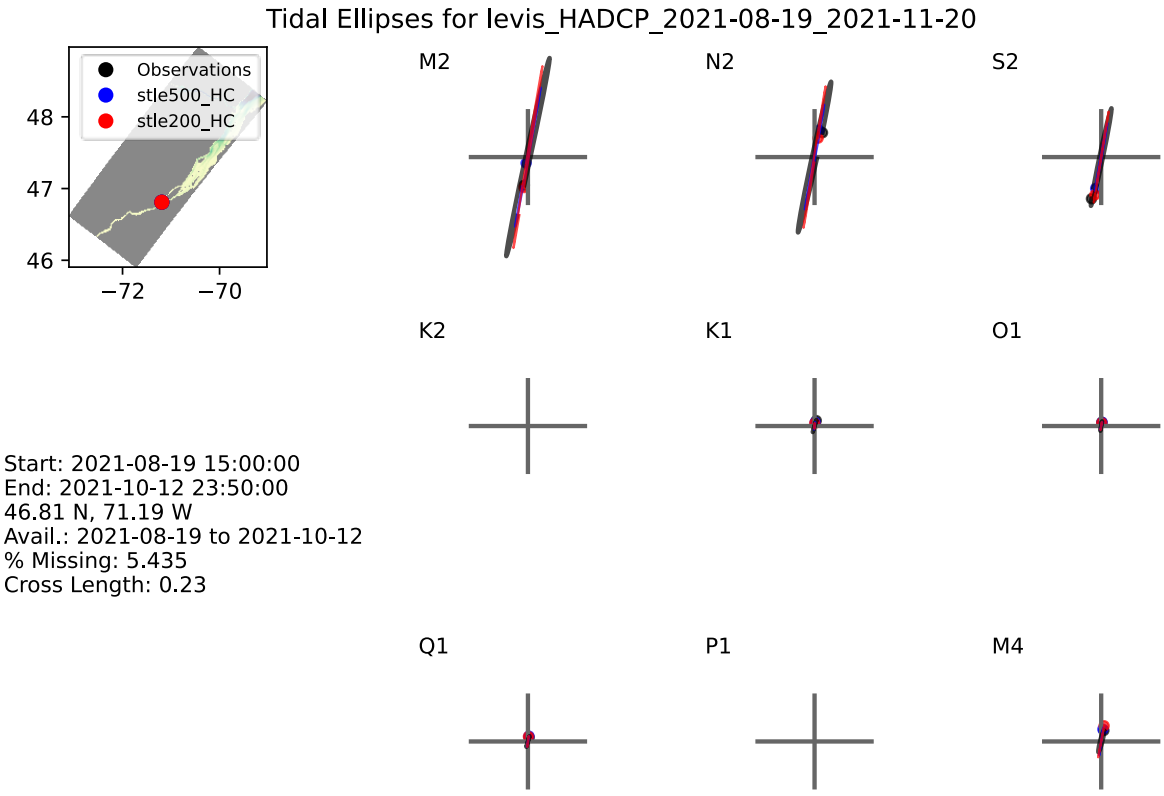

Figure 42. HADCP results in Lévis and model outputs for year 2021. Tidal ellipses from observations and the 2 models for tidal constituents M2, N2, S2, K2, K1, O1, Q1, P1 and M4.

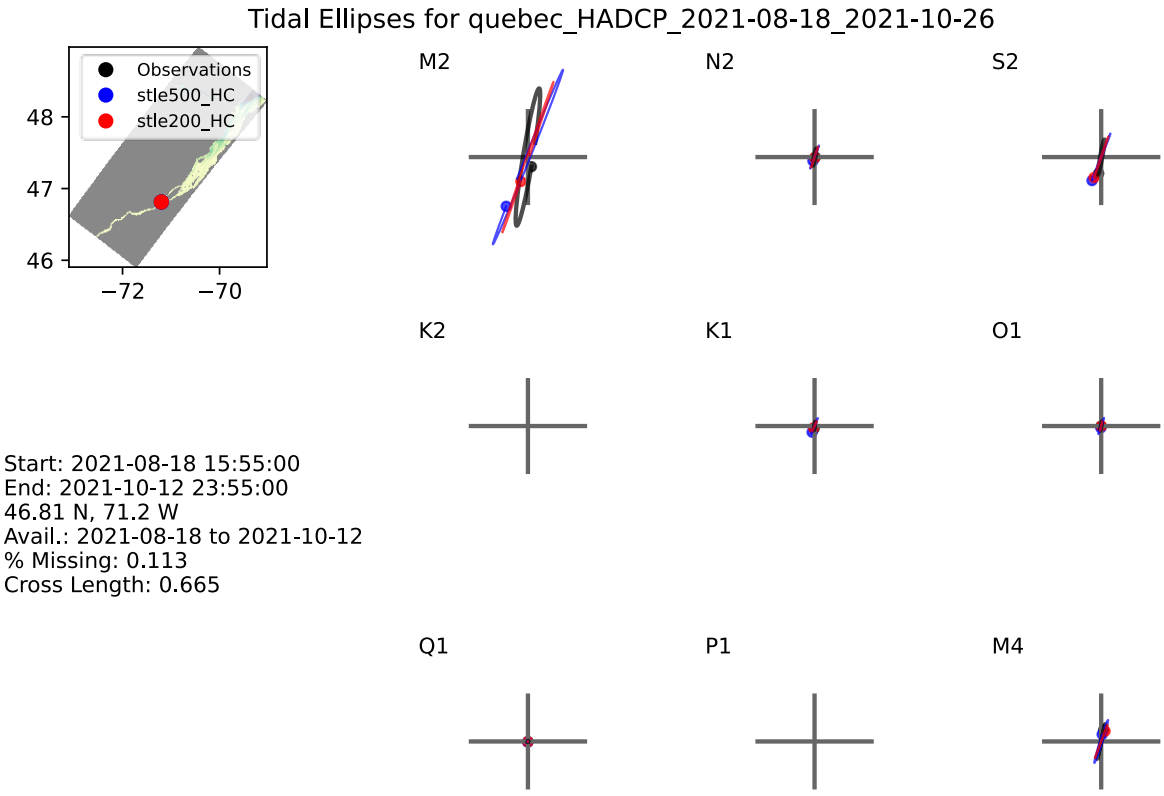

Figure 43. HADCP results in Québec and model outputs for year 2021. Tidal ellipses from observations and the 2 models for tidal constituents M2, N2, S2, K2, K1, O1, Q1, P1 and M4.

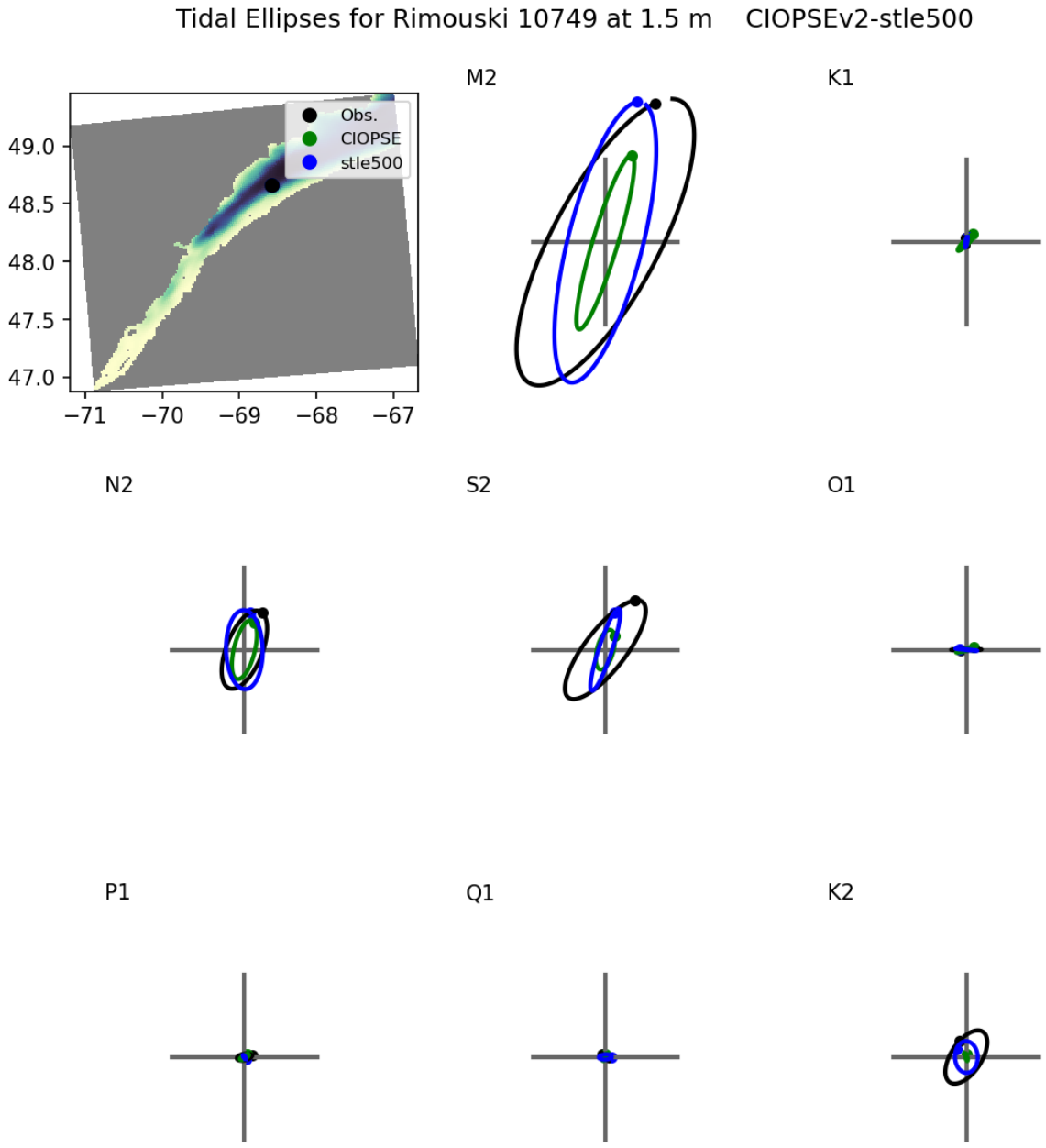

Figure 44. Tidal ellipses from ADCP at buoy IML-4 and for the 2 coarser models (CIOPS-E and STLE500) for tidal constituents M2, K1, N2, S2, O1, P1, Q1, and K2, at 1.5-meter depth.

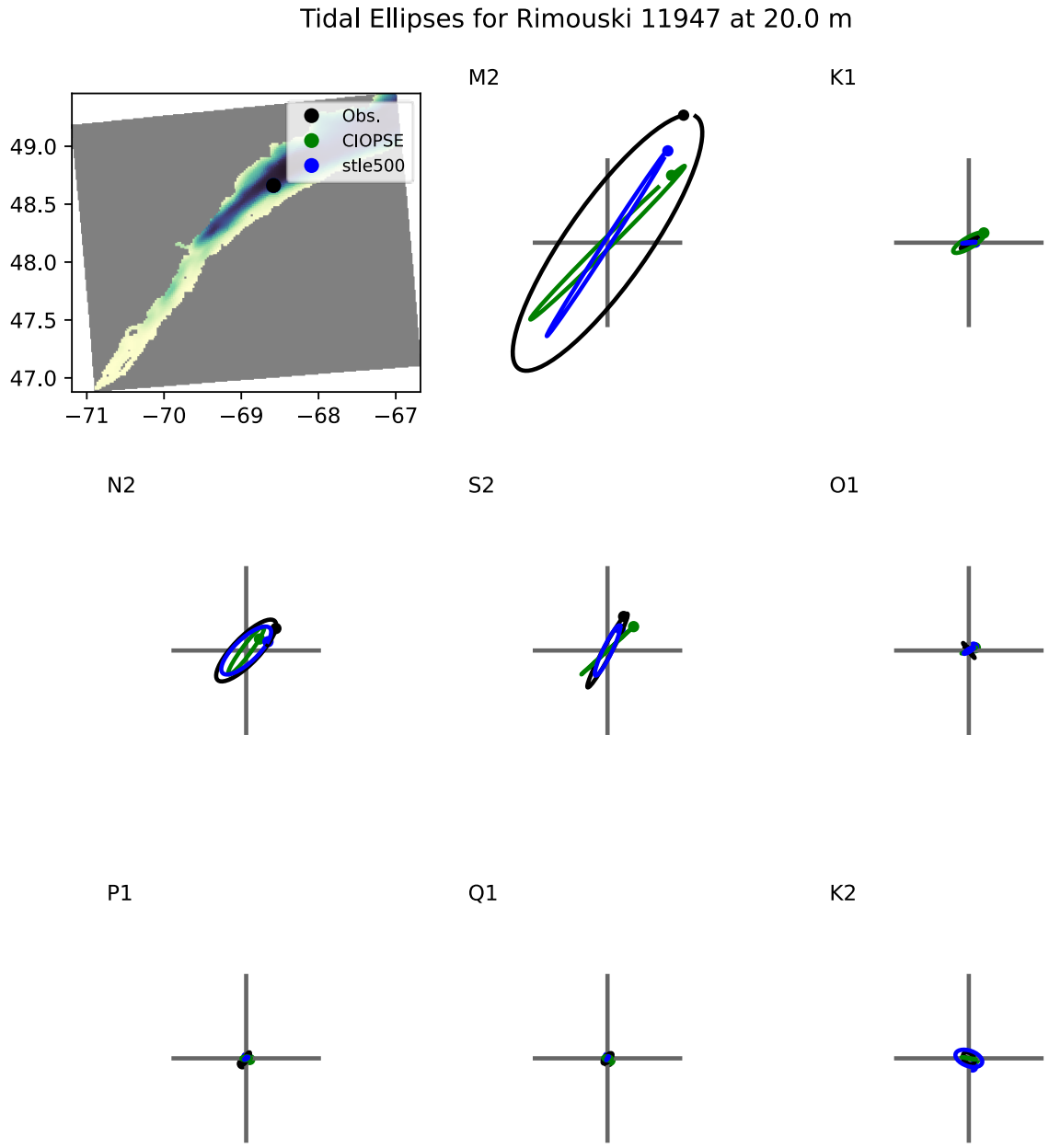

Figure 45. Tidal ellipses from ADCP at buoy IML-4 and for the 2 coarser models (CIOPS-E and STLE500) for tidal constituents M2, K1, N2, S2, O1, P1, Q1, and K2, at 20-meter depth.

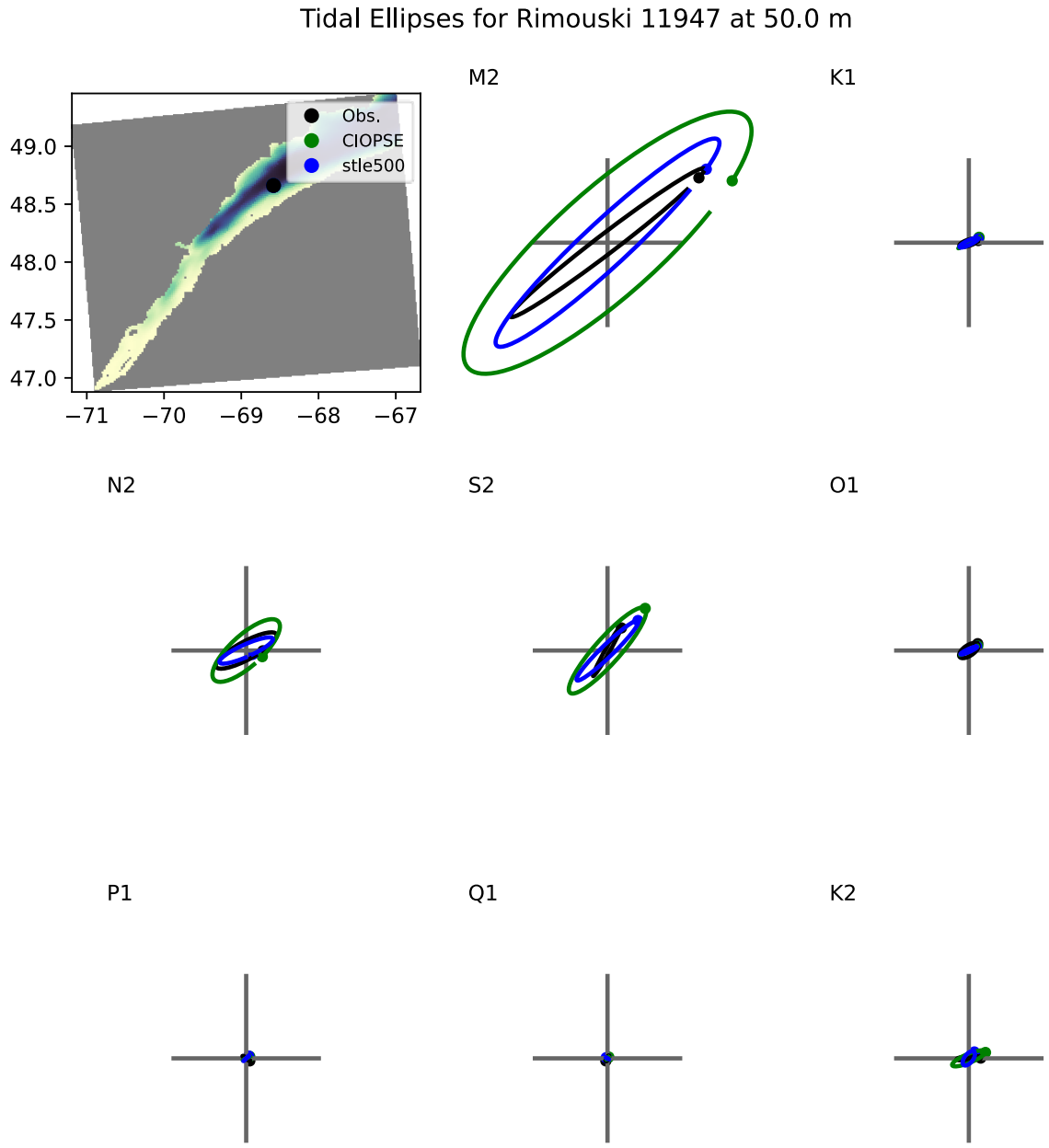

Figure 46. Tidal ellipses from ADCP at buoy IML-4 and for the 2 coarser models (CIOPS-E and STLE500) for tidal constituents M2, K1, N2, S2, O1, P1, Q1, and K2, at 50-meter depth.

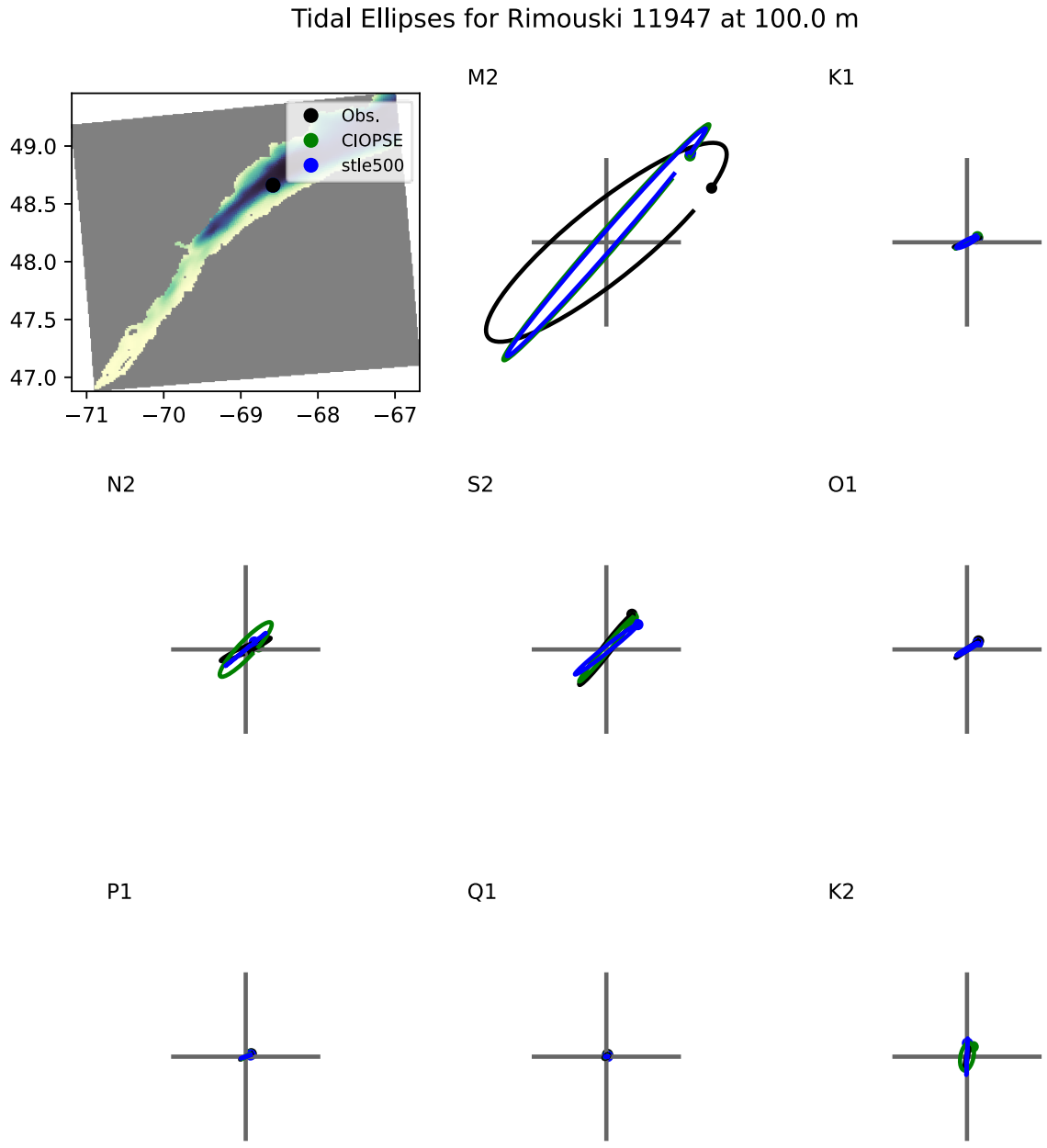

Figure 47. Tidal ellipses from ADCP at buoy IML-4 and for the 2 coarser models (CIOPS-E and STLE500) for tidal constituents M2, K1, N2, S2, O1, P1, Q1, and K2, at 100-meter depth.

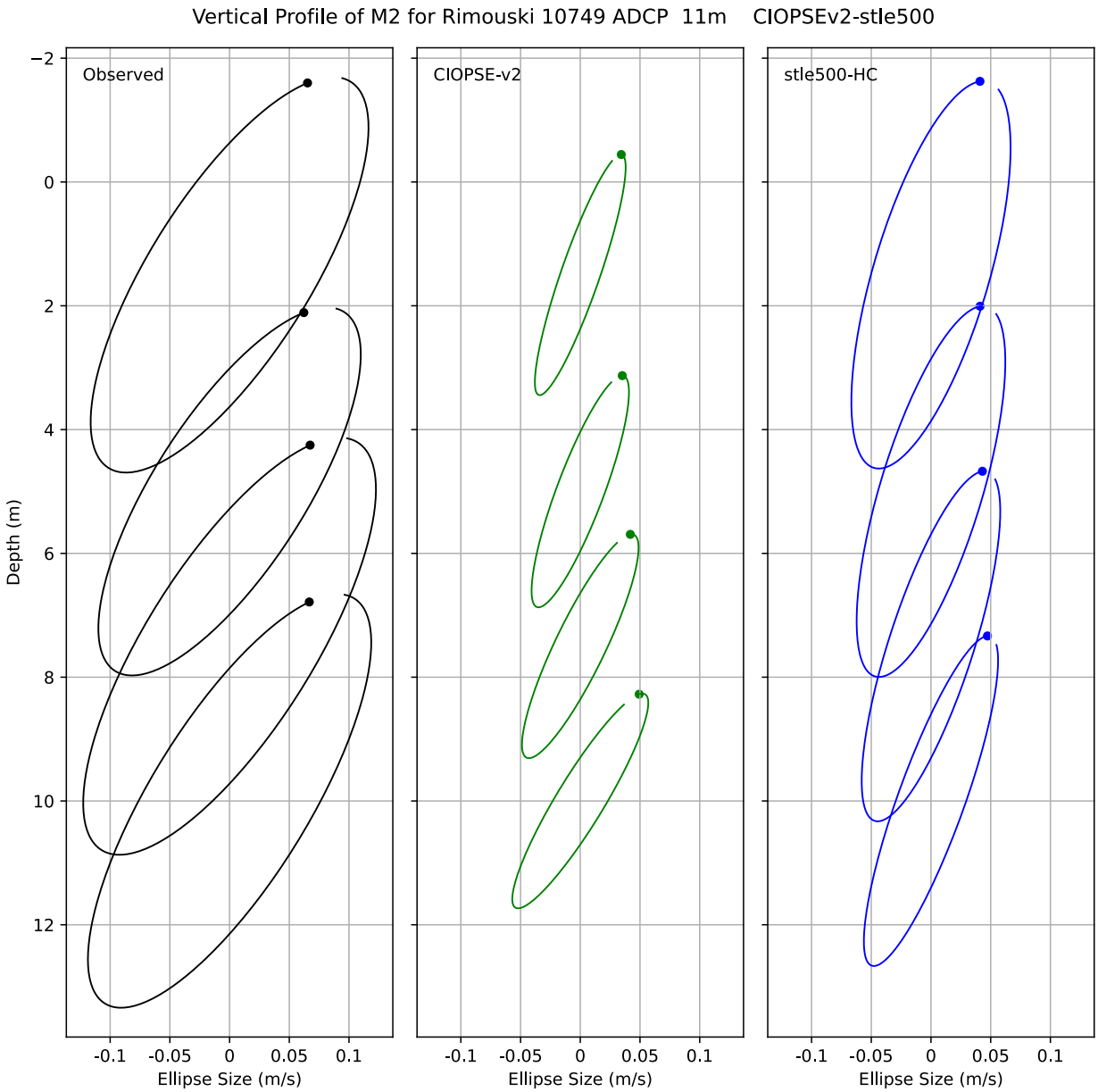

Figure 48. Tidal ellipses from surface water ADCP at buoy IML-4 in 2016 and for the 2 coarser models (CIOPS-E and STLE500) for tidal constituents M2.

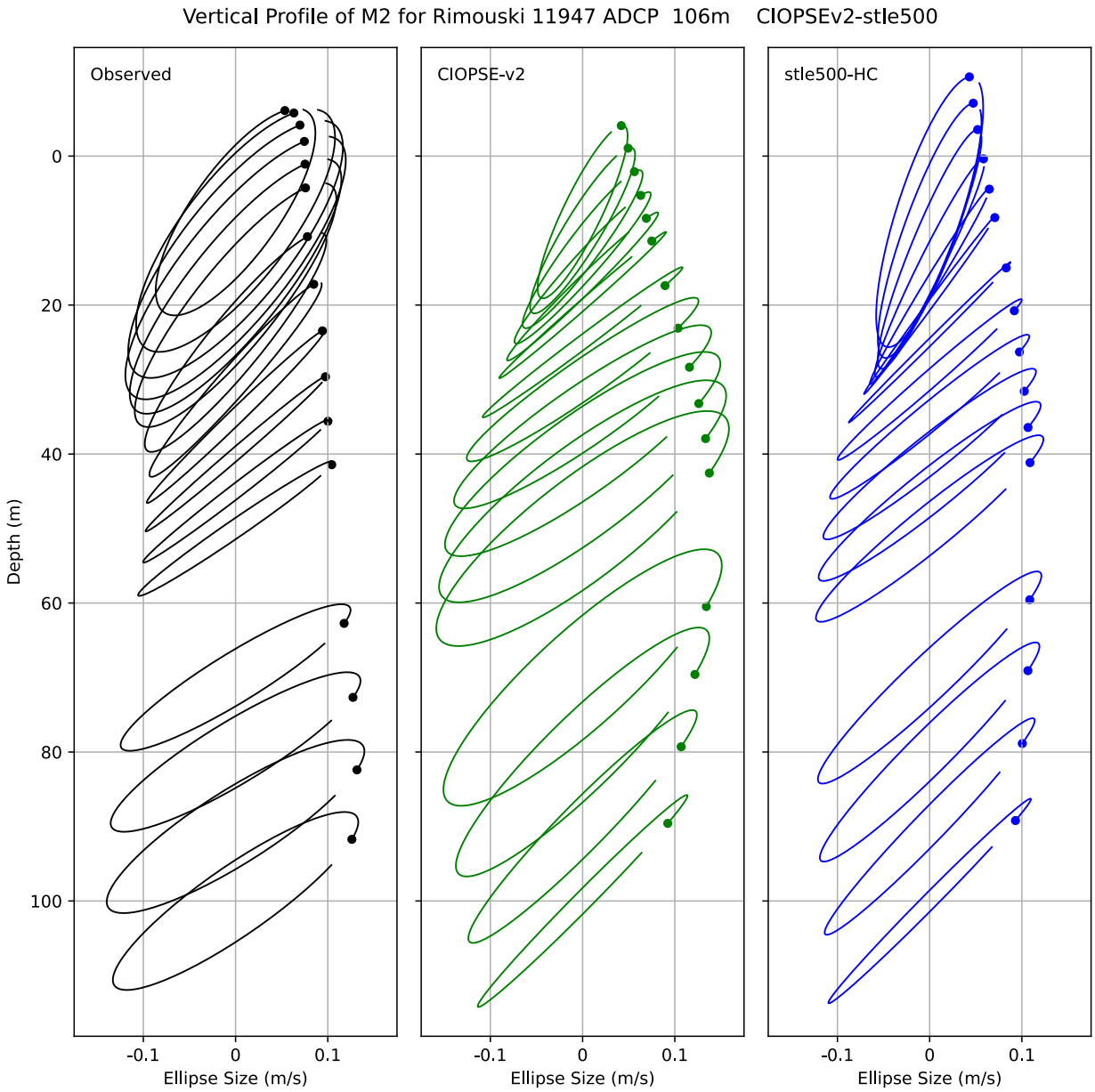

Figure 49. Tidal ellipses from ADCP at buoy IML-4 in 2016 and for the 2 coarser models (CIOPS-E and STLE500) for tidal constituents M2.

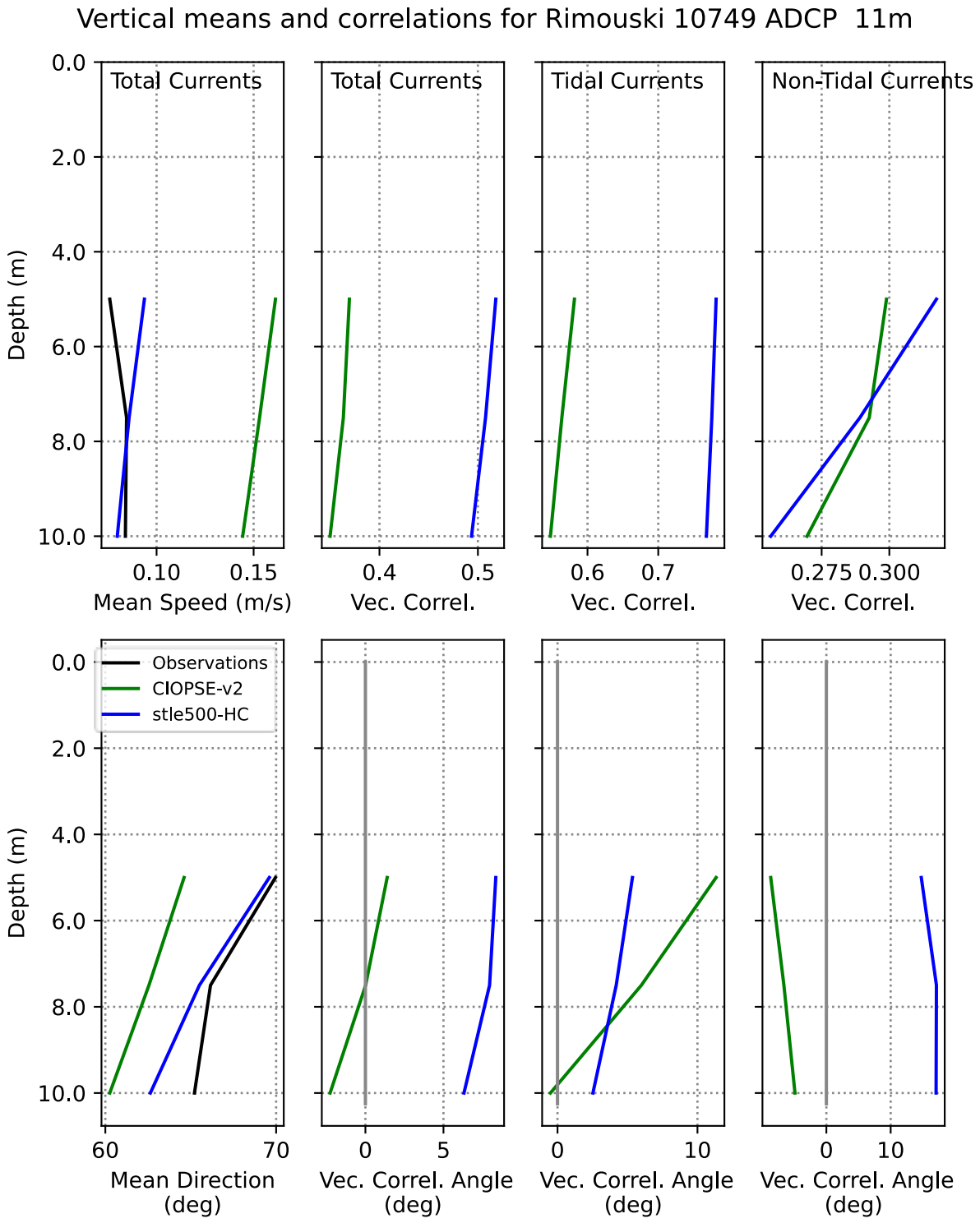

Figure 50. Mean total speed and direction (column 1), vector correlation magnitude and angle for total currents (column 2), tidal currents (column 3) and non-tidal currents (column 4), from the higher frequency ADCP at buoy IML-4 in 2016 and for the 2 coarser models (CIOPS-E and STLE500).

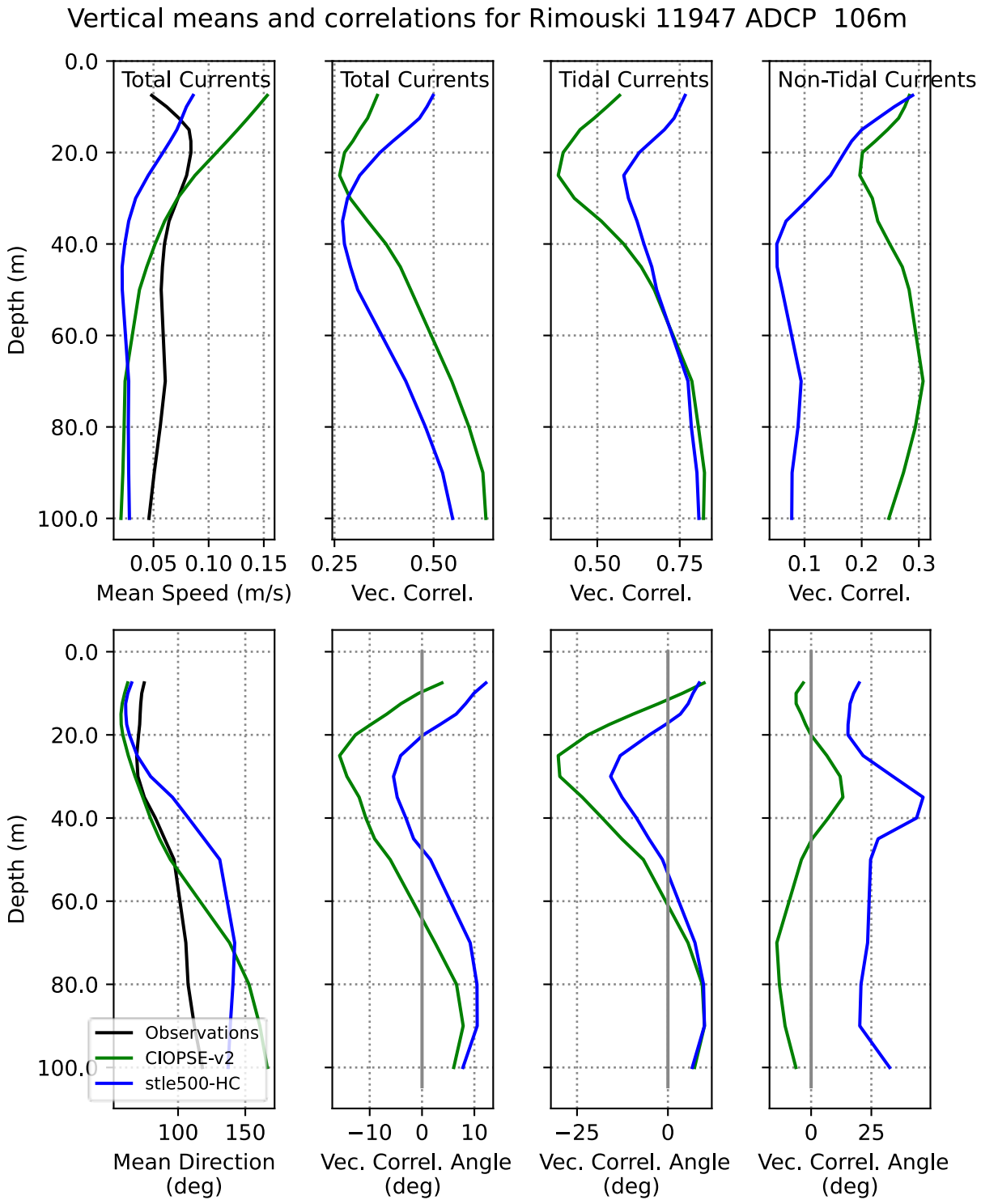

Figure 51. Mean total speed and direction (column 1), vector correlation magnitude and angle for total currents (column 2), tidal currents (column 3) and non-tidal currents (column 4), from the lower frequency ADCP at buoy IML-4 in 2016 and for the 2 coarser models (CIOPS-E and STLE500).

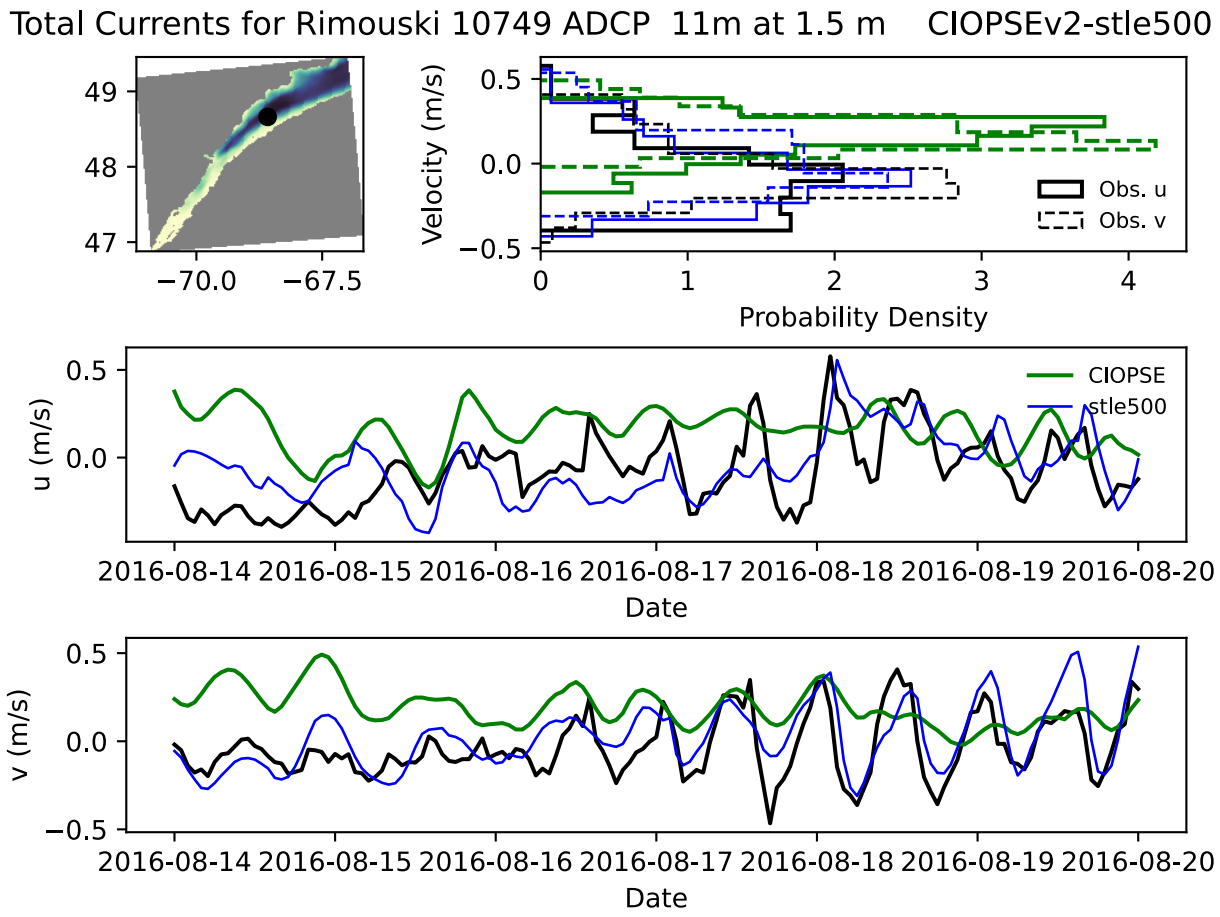

Figure 52. Short time series (1 week) of total currents u and v at 1.5-meter depth from the higher frequency ADCP at buoy IML-4 in 2016 for the 2 coarser models (CIOPS-E and STLE500).

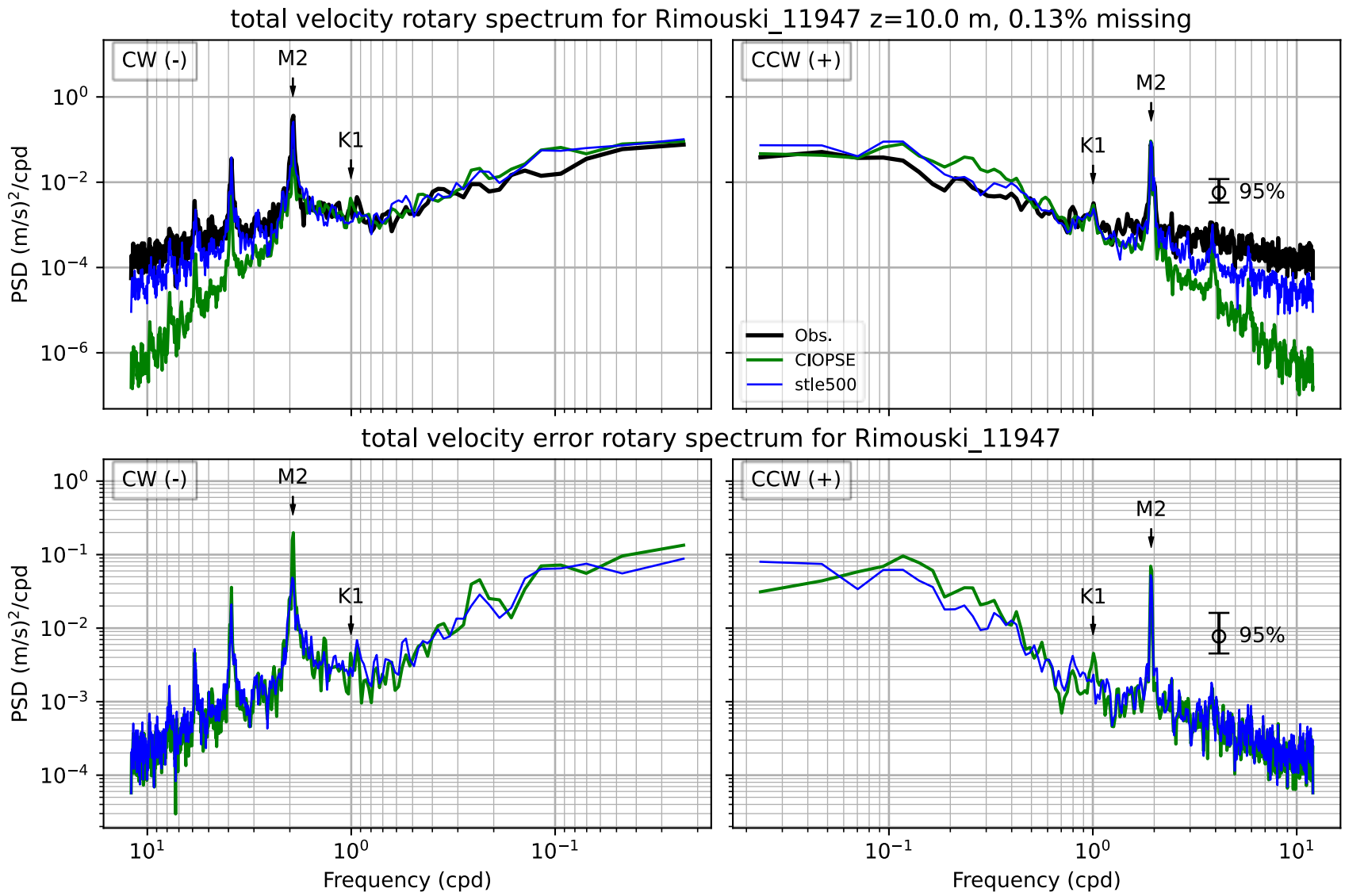

Figure 53. Total velocity (up) and velocity error (bottom) rotary spectrum for ADCP 11947 at 10 m. Clockwise (CW) rotation on left panels and counterclockwise (CCW) rotation on right panels.

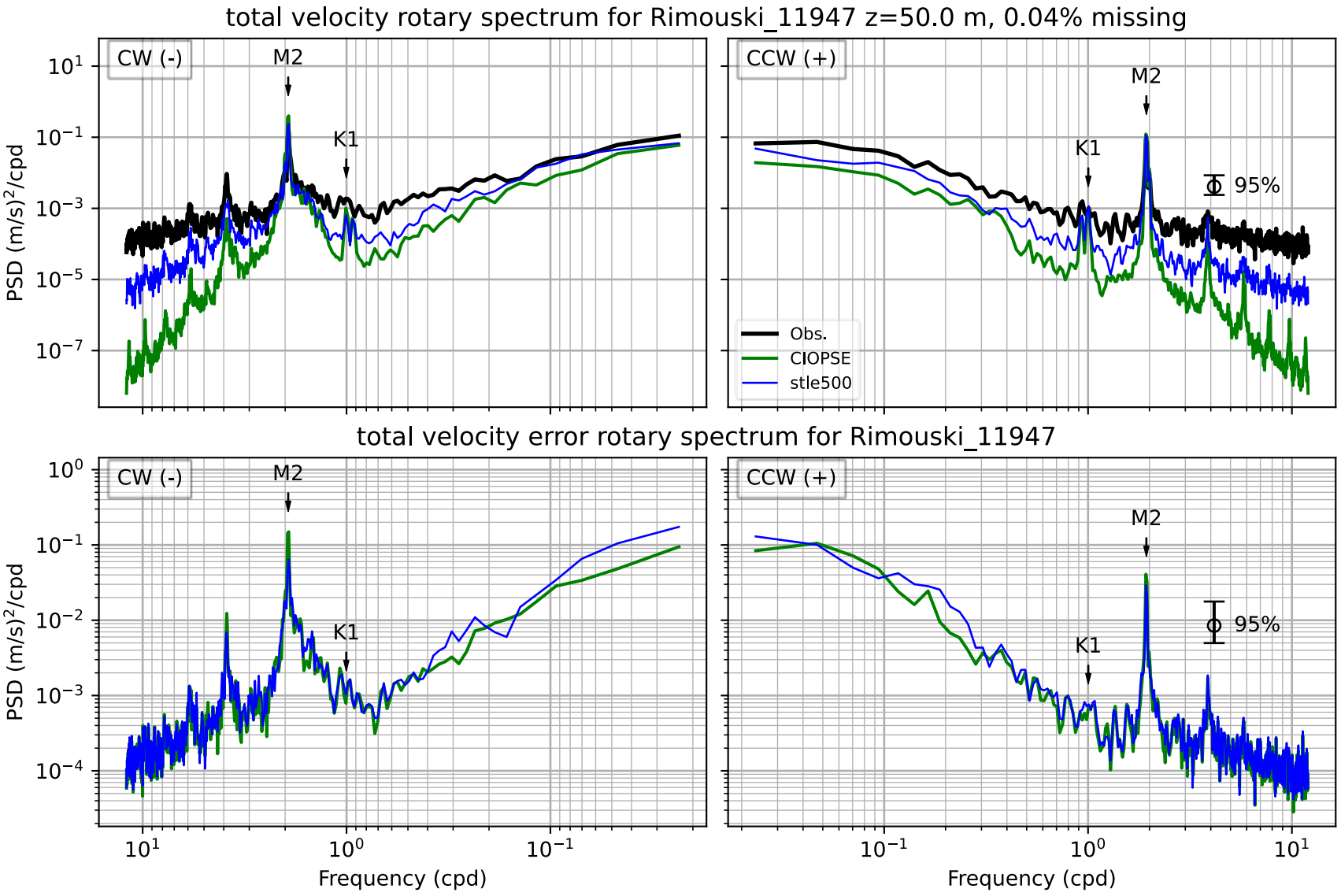

Figure 54. Total velocity (up) and velocity error (bottom) rotary spectrum for ADCP 11947 at 50 m. Clockwise (CW) rotation on left panels and counterclockwise (CCW) rotation on right panels.

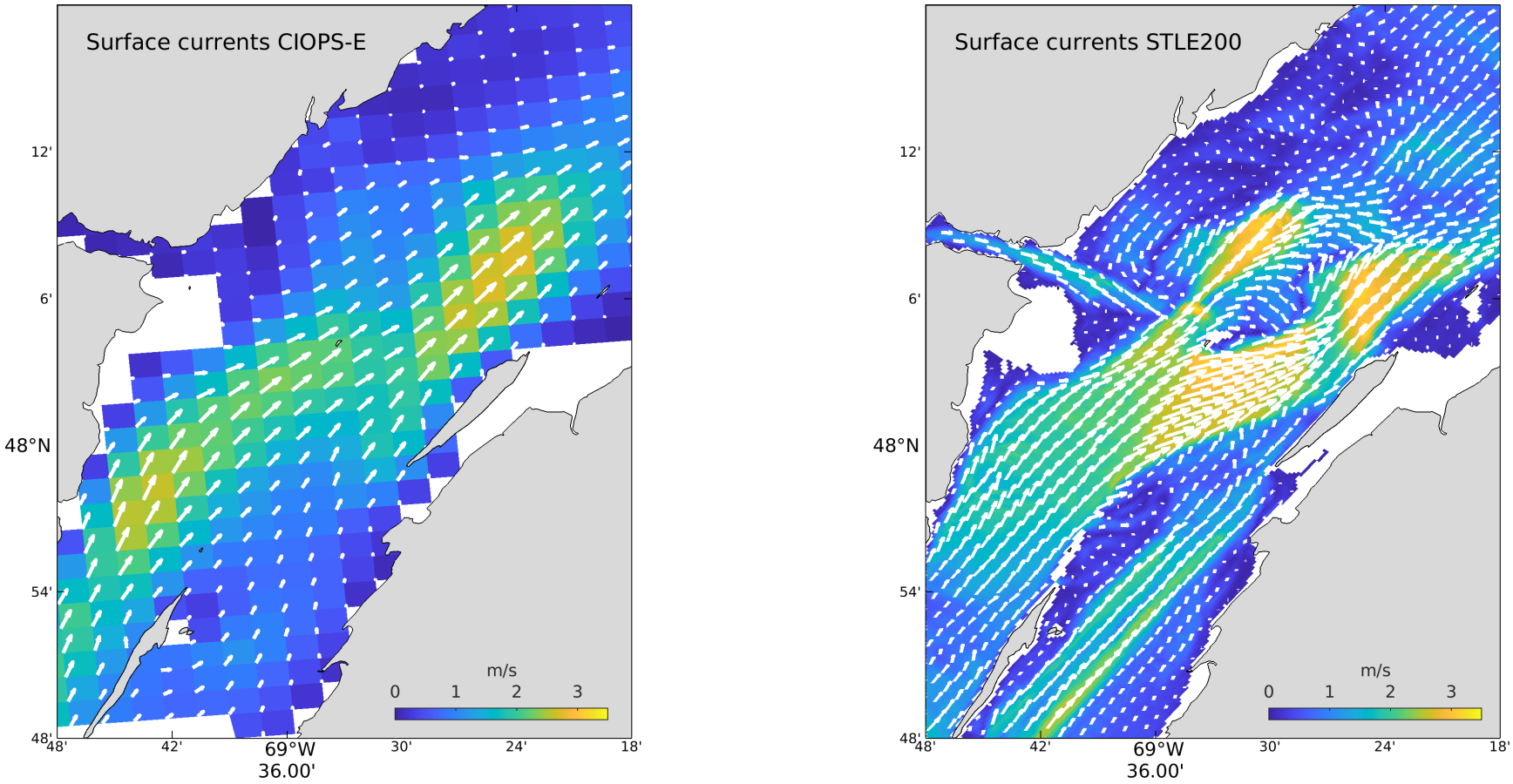

Figure 55. Snapshot of surface currents for CIOPS-E (left panel) and STLE200 (right panel) for date 2017-06-08, 13H00 (UTC), corresponding to ebb tide and low water. Surface current amplitude is represented by the color scale on the background of the white arrows. All cells of CIOPS-E are displayed, but only 1 cell out of 25 are displayed for STLE200 arrows (for clarity). All cells are shown for surface current magnitude (color scale).

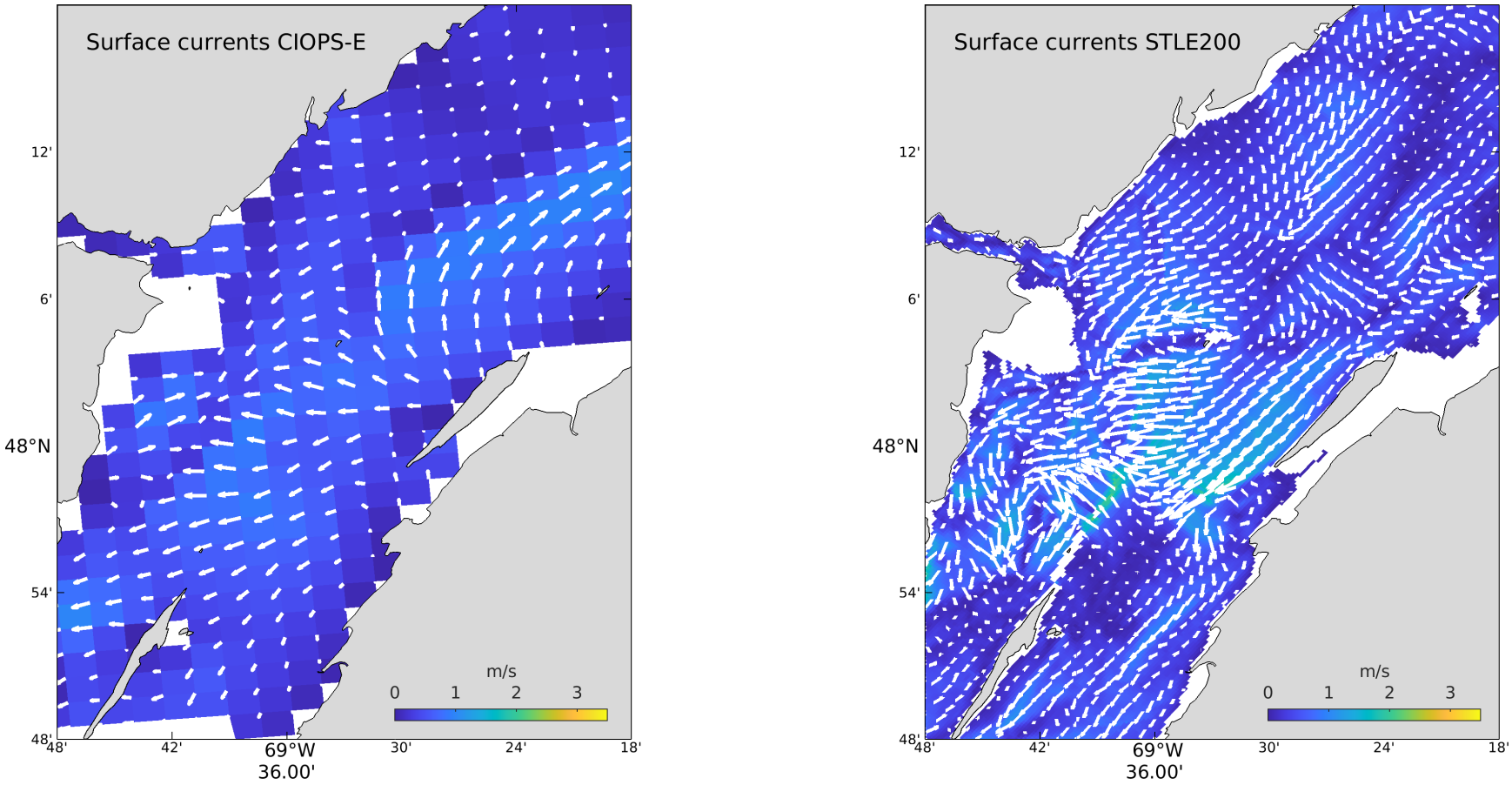

Figure 56. Snapshot of surface currents for CIOPS-E (left panel) and STLE200 (right panel) for date 2017-06-08, 19H00 (UTC), corresponding to flood tide and high water. Surface current amplitude is represented by the color scale on the background of the white arrows. All cells of CIOPS-E are displayed, but only 1 cell out of 25 are displayed for STLE200 arrows (for clarity). All cells are shown for surface current magnitude (color scale).

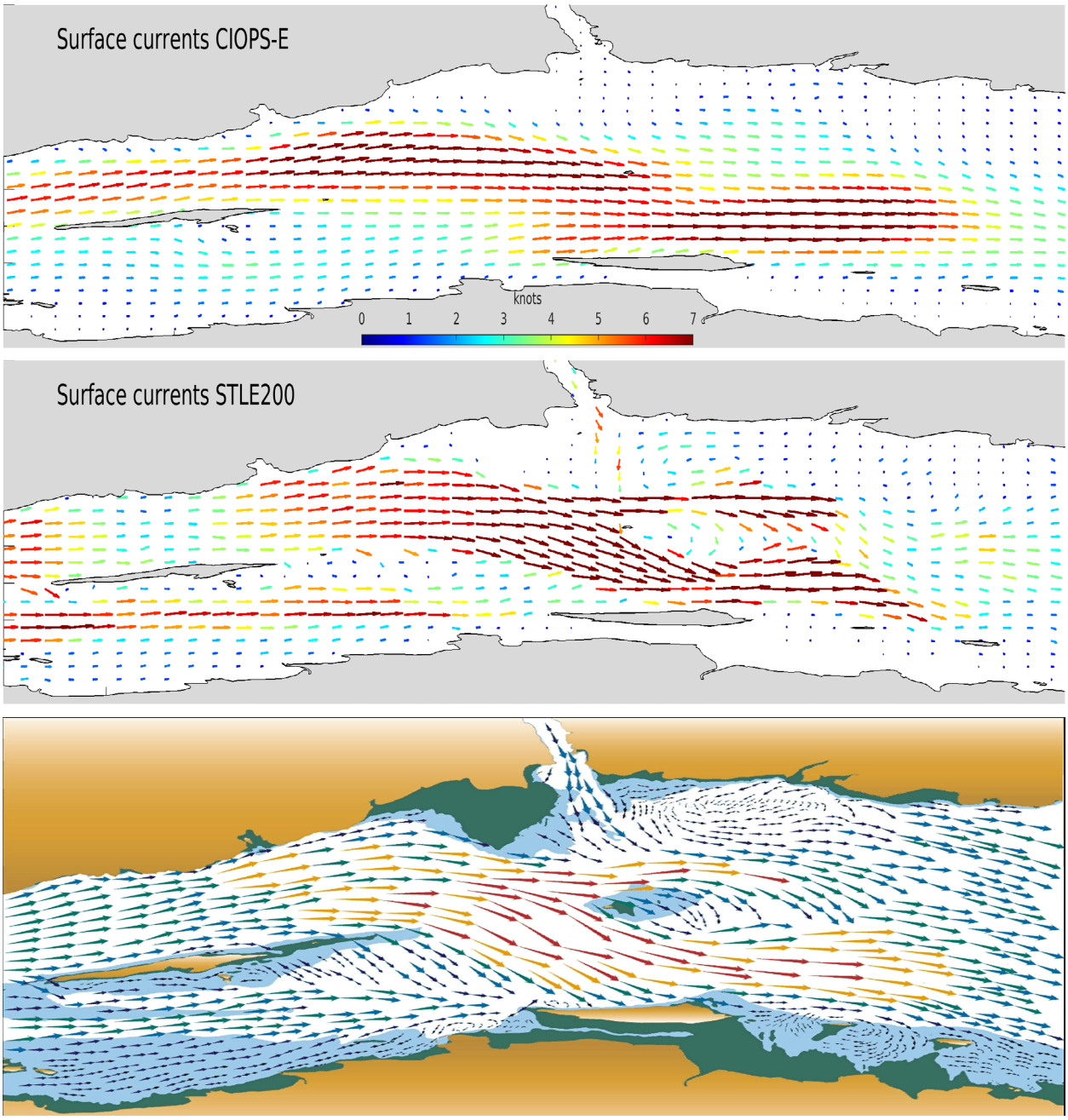

Figure 57. Snapshot of surface currents for CIOPS-E (top panel) and STLE200 (second panel) for date 2017-06-08, 13H00 (UTC), corresponding to ebb tide and low water for STLE200 and CIOPS-E. Surface current amplitude is represented by the length of the arrows and by the color scale of the arrows. CIOPS-E surface currents are interpolated on STLE200's grid, and one cell out of 49 is shown on the figure (for clarity). The bottom panel is the surface currents from the Atlas of Tidal Currents, for the period to 0 to 1 hour after low water. The color scale is common to the 3 panels, and knots are used instead of m/s to fit the color scale of the tidal atlas.

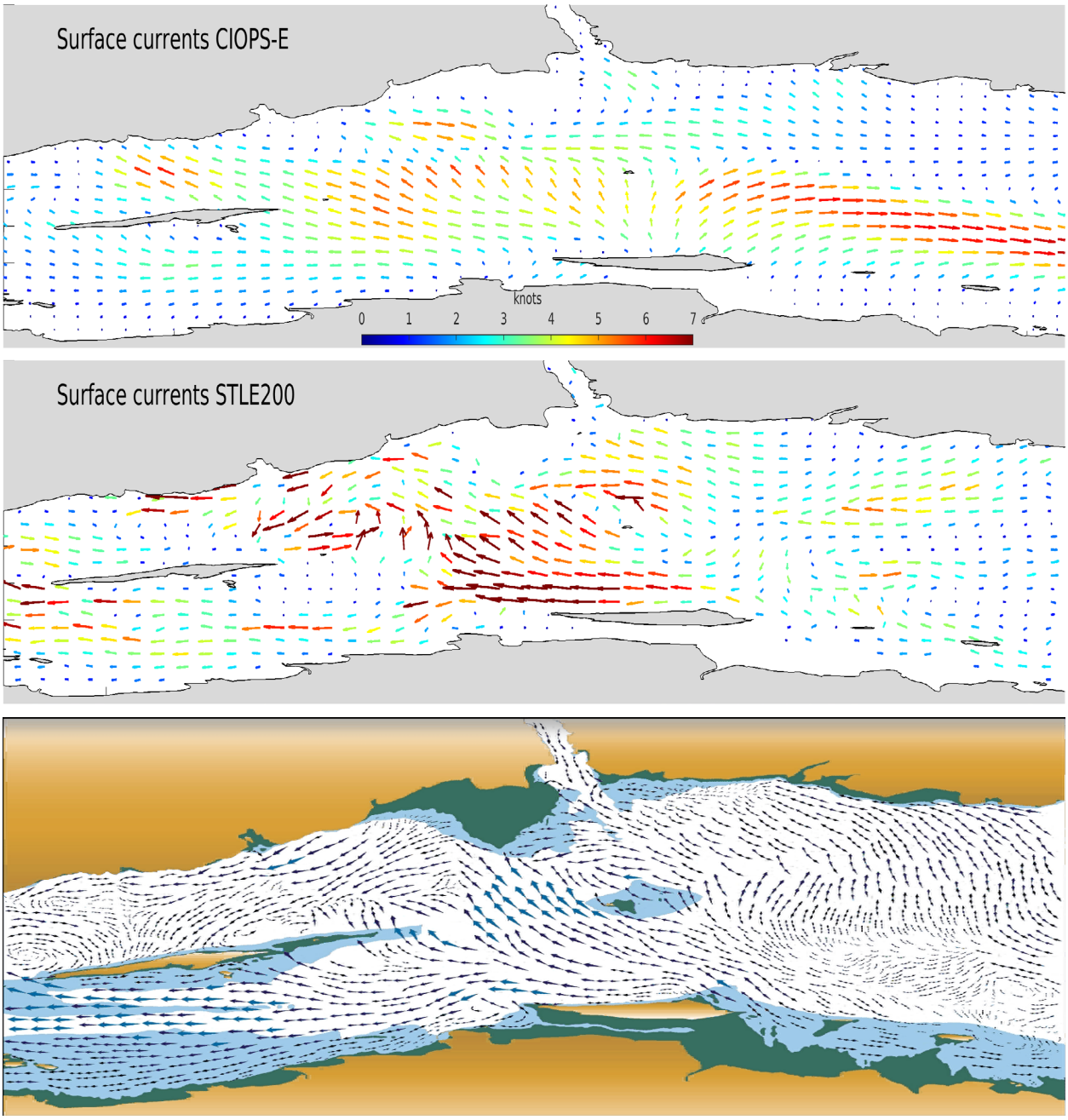

Figure 58. Snapshot of surface currents for CIOPS-E (top panel) and STLE200 (second panel) for date 2017-06-08, 19H00 (UTC), corresponding to flood tide and high water for STLE200 and CIOPS-E. Surface current amplitude is represented by the length of the arrows and by the color scale of the arrows. CIOPS-E surface currents are interpolated on STLE200's grid, and one cell out of 49 is shown on the figure (for clarity). The bottom panel is the surface currents from the Atlas of Tidal Currents, for the period to 0 to 1 hour after low water. The color scale is common to the 3 panels, and knots are used instead of m/s to fit the color scale of the tidal atlas.

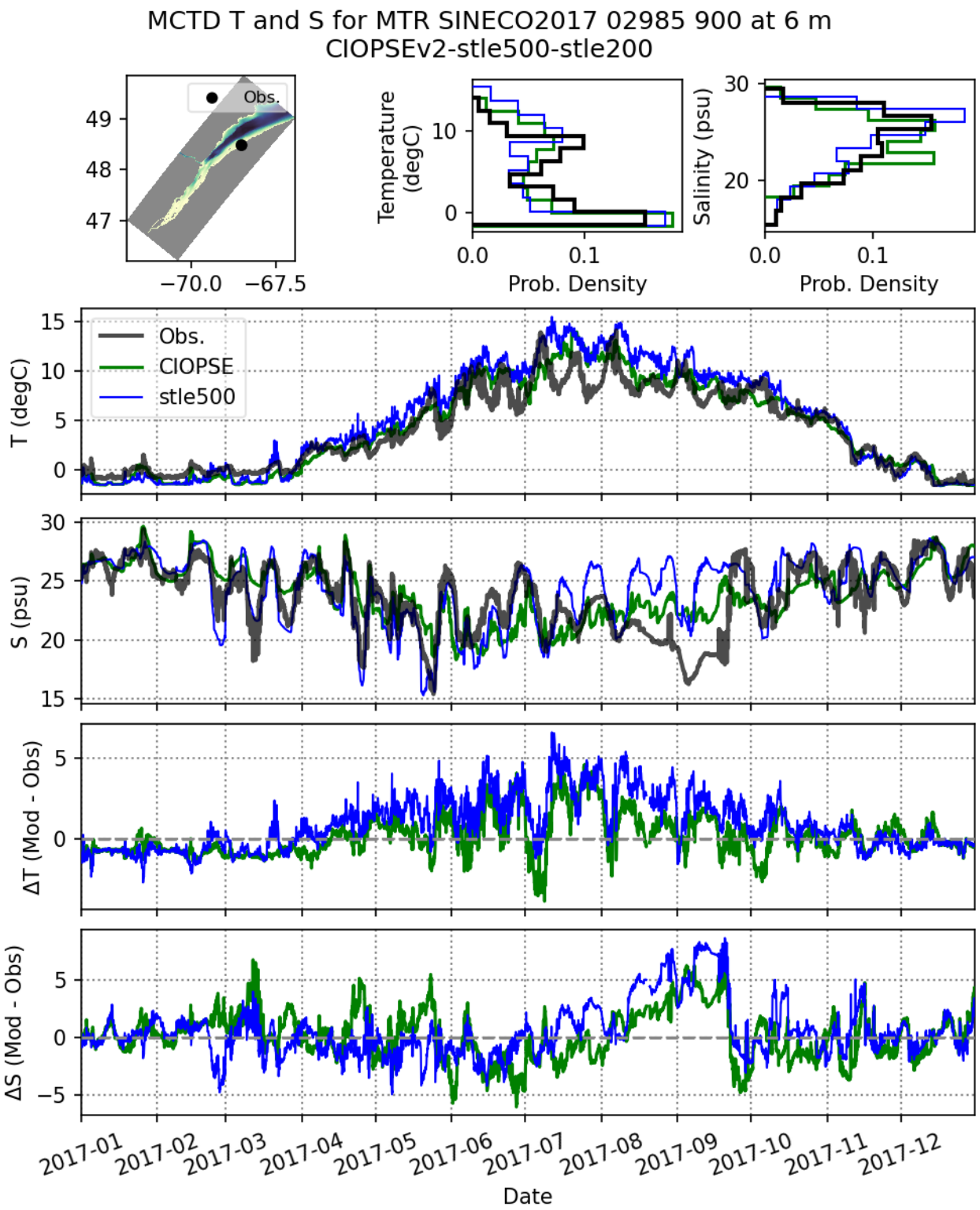

Figure 59. Near surface temperature and salinity for the 3 models and observations coming from MCTD fixed on tide gauges stations for years 2017, for station 2985 (see Figure 5 and Figure 6 for a map of tide gauge stations).

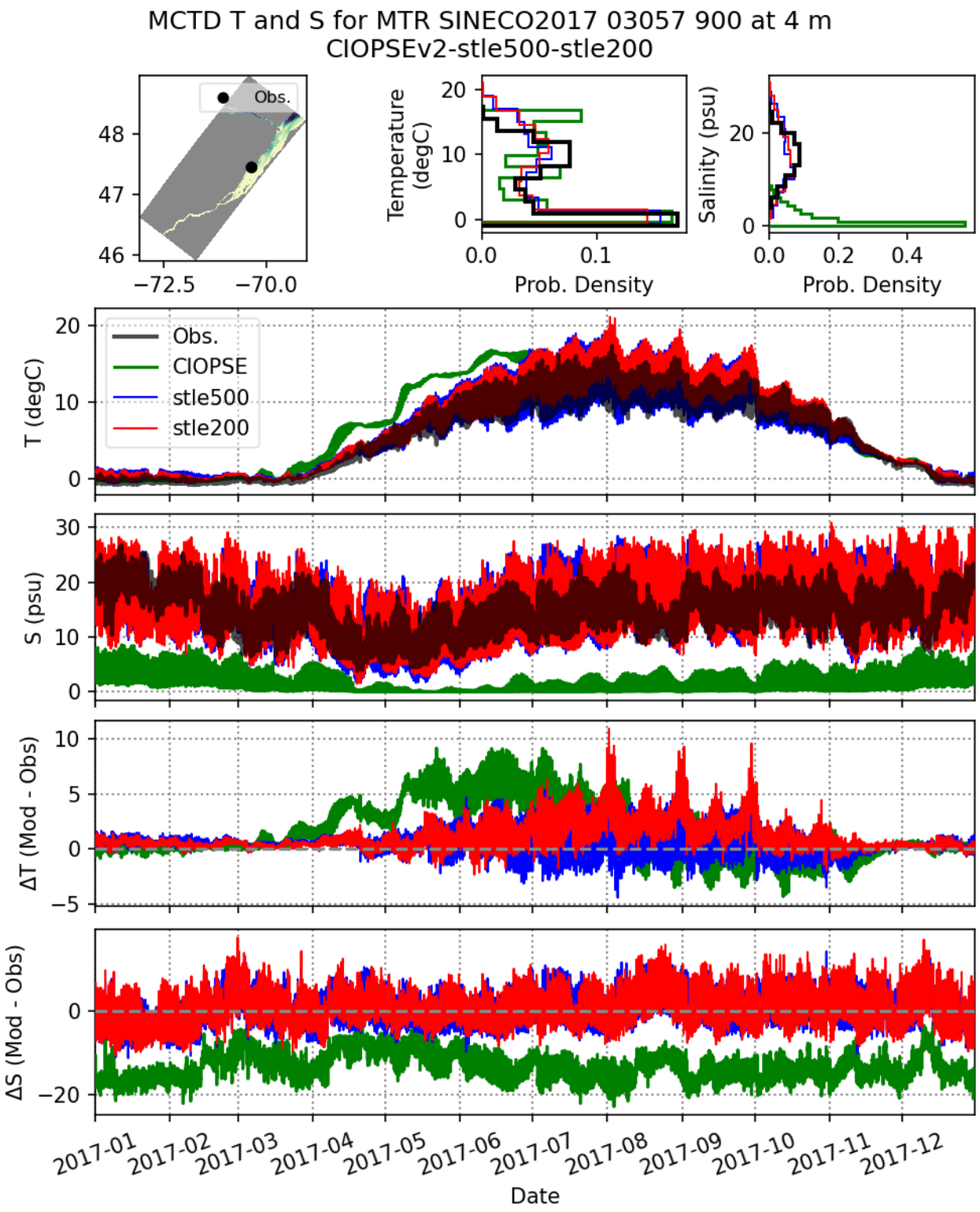

Figure 60. Near surface temperature and salinity for the 3 models and observations coming from MCTD fixed on tide gauges stations for years 2017, for station 3057 (see Figure 5 and Figure 6 for a map of tide gauge stations).

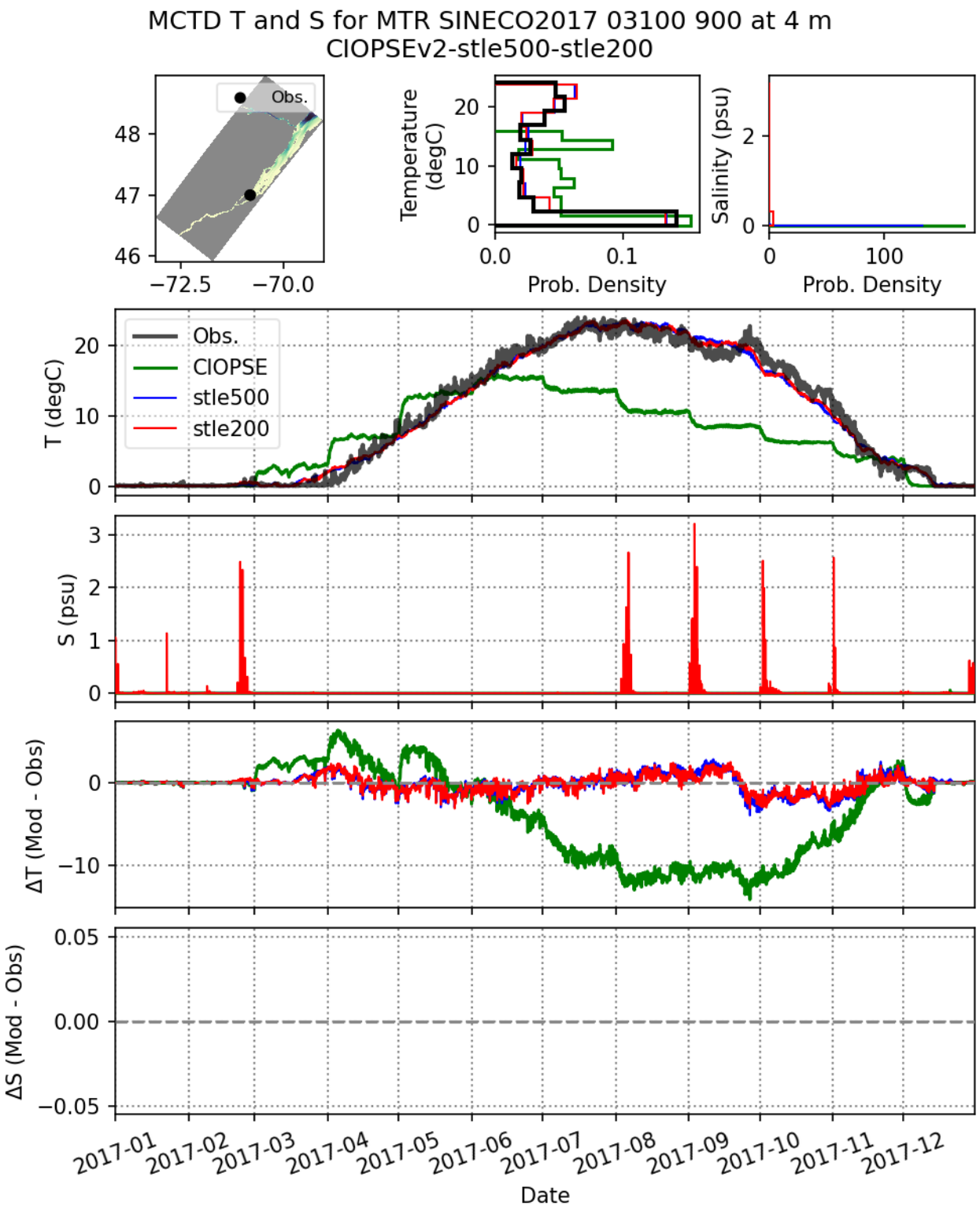

Figure 61. Near surface temperature and salinity for the 3 models and observations coming from MCTD fixed on tide gauges stations for years 2017, for station 3100 (see Figure 5 and Figure 6 for a map of tide gauge stations).

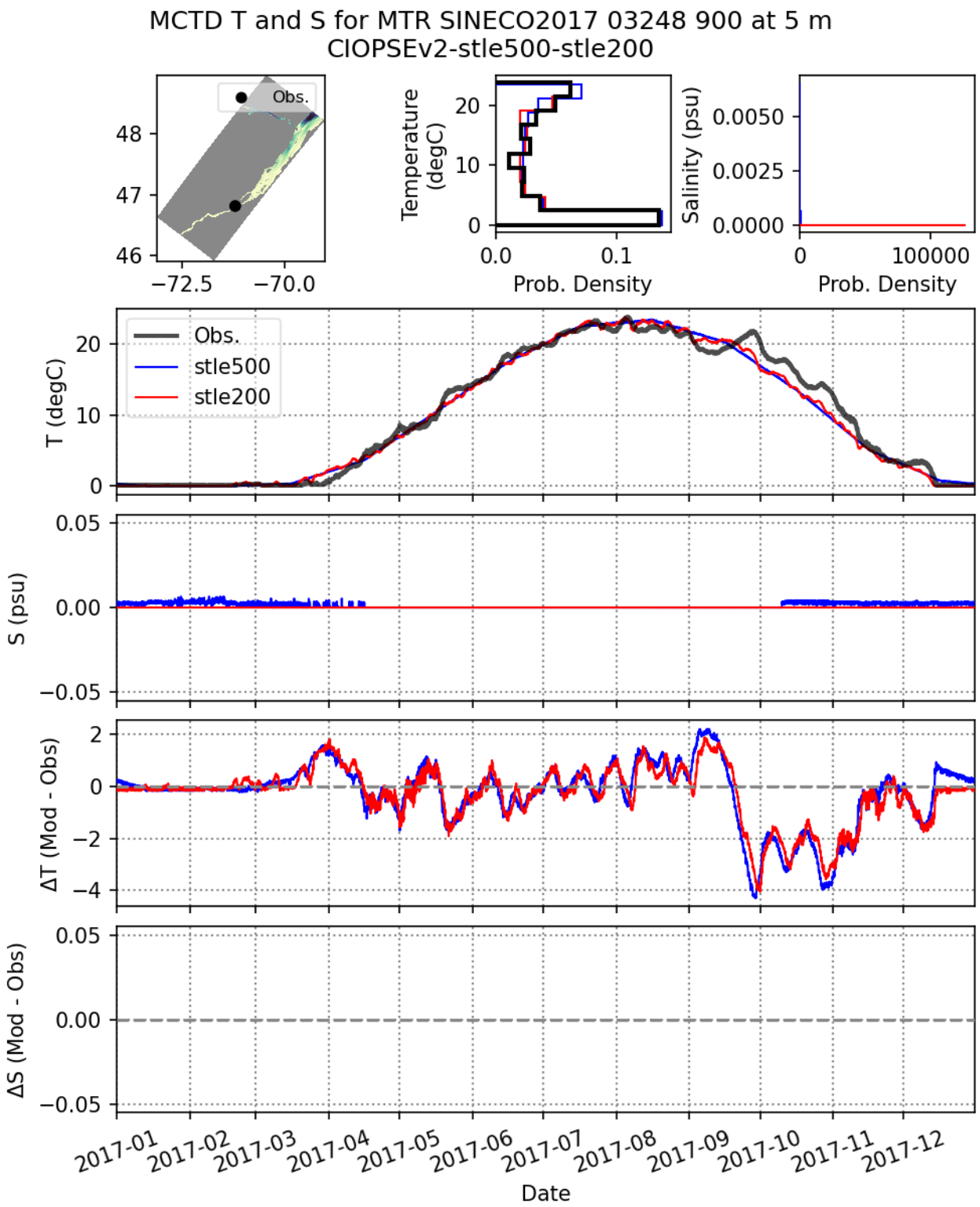

Figure 62. Near surface temperature and salinity for the 3 models and observations coming from MCTD fixed on tide gauges stations for years 2017, for station 3248 (see Figure 5 and Figure 6 for a map of tide gauge stations).

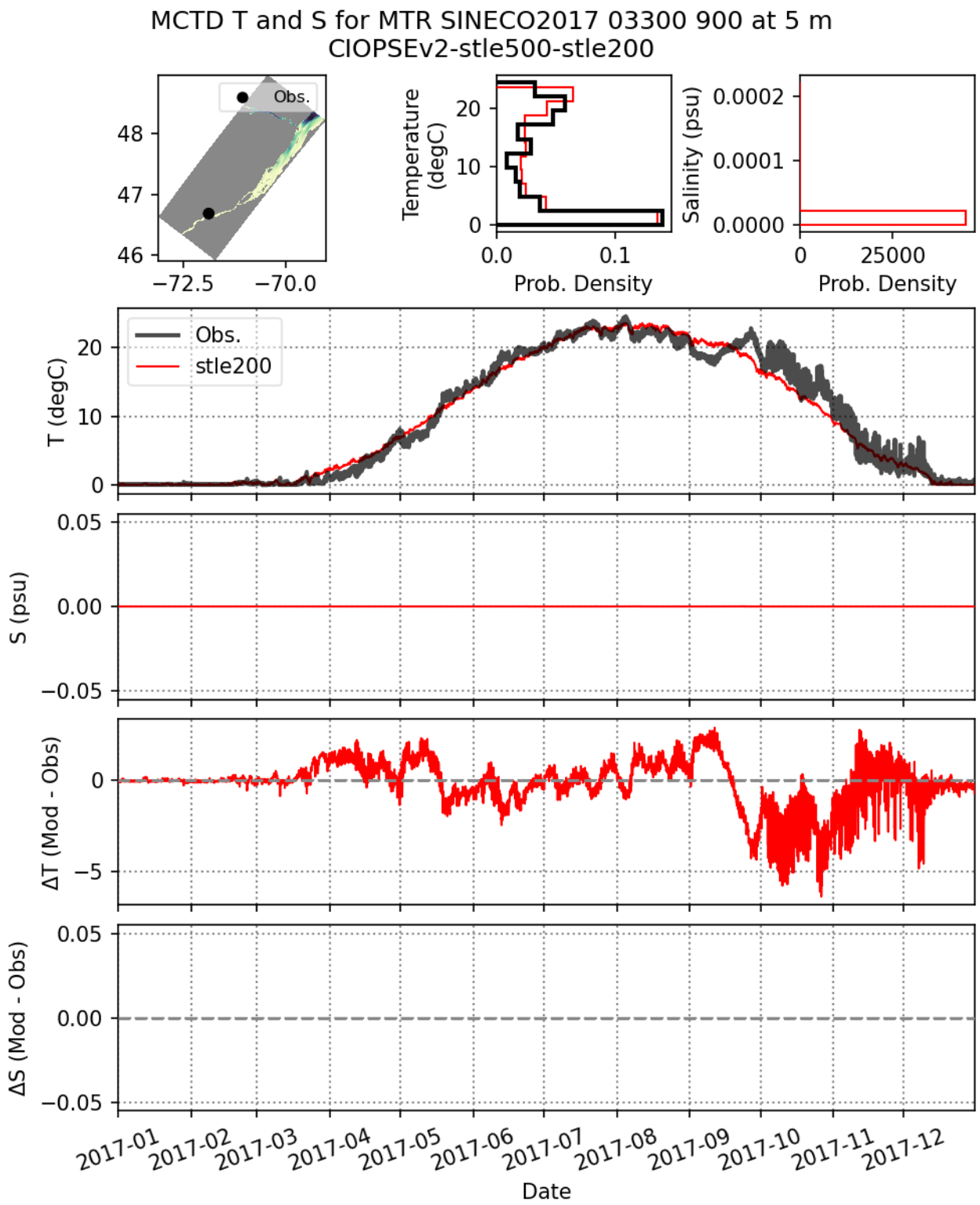

Figure 63. Near surface temperature and salinity for the 3 models and observations coming from MCTD fixed on tide gauges stations for years 2017, for station 3300 (see Figure 5 and Figure 6 for a map of tide gauge stations).

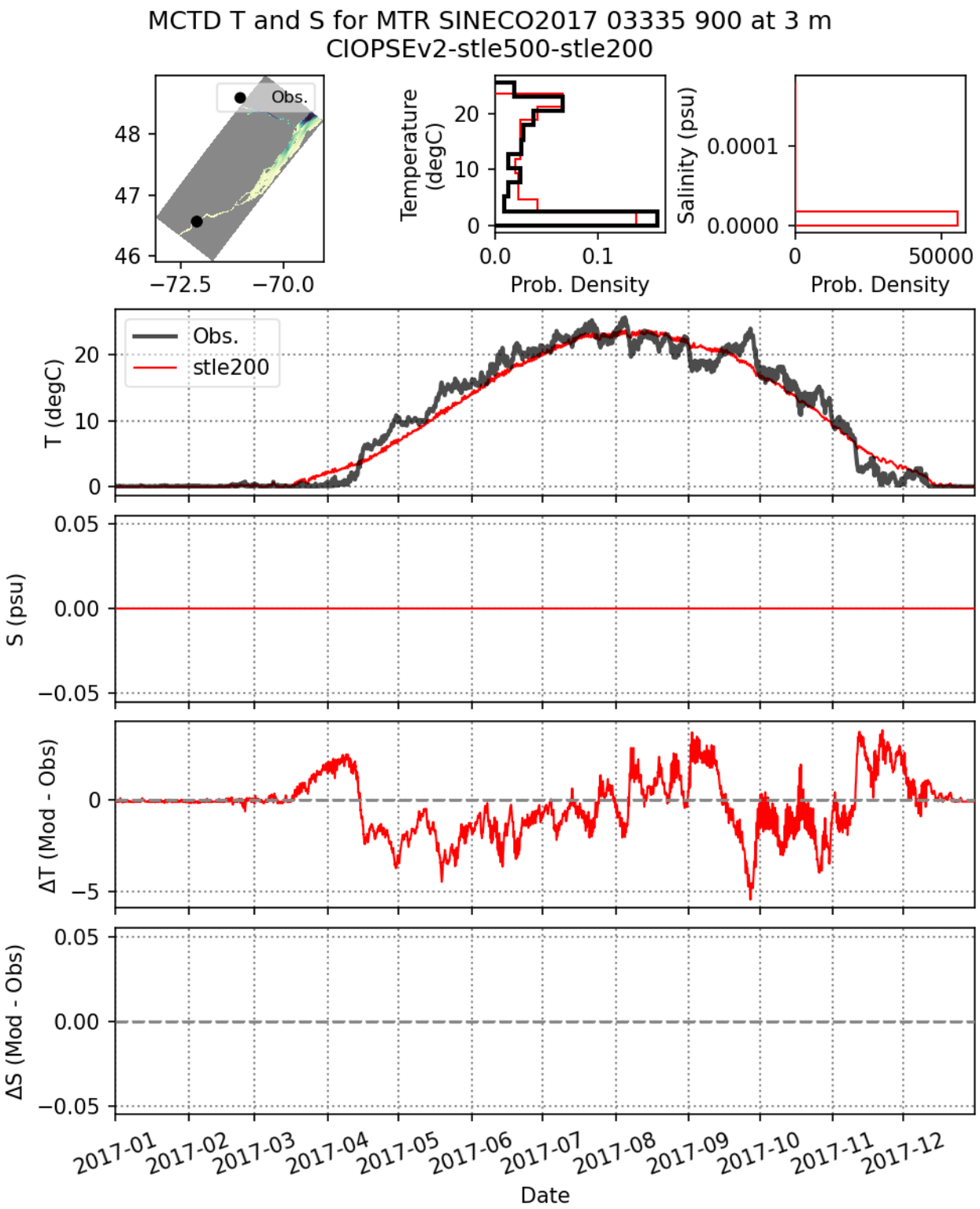

Figure 64. Near surface temperature and salinity for the 3 models and observations coming from MCTD fixed on tide gauges stations for years 2017, for station 3335 (see Figure 5 and Figure 6 for a map of tide gauge stations).

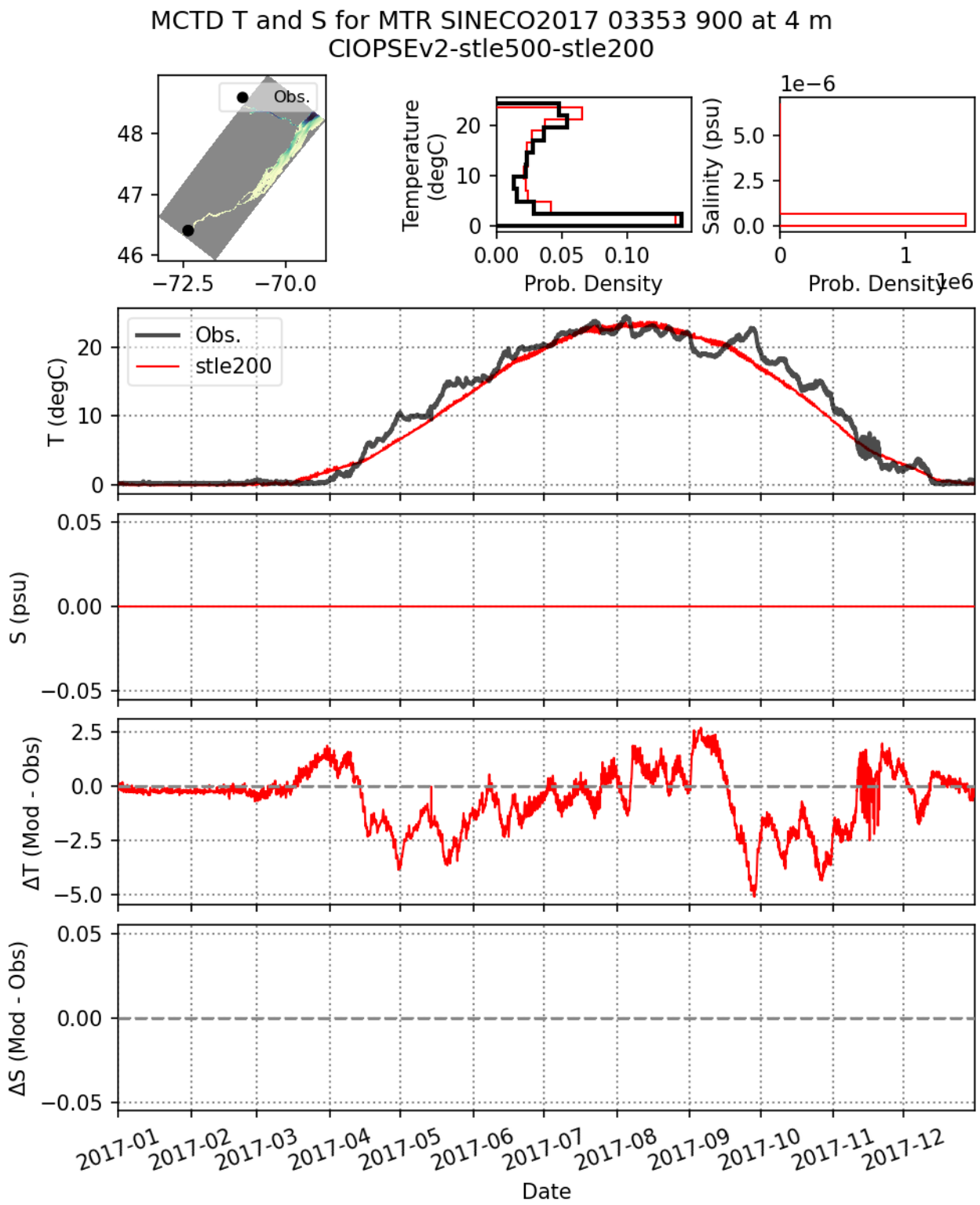

Figure 65. Near surface temperature and salinity for the 3 models and observations coming from MCTD fixed on tide gauges stations for years 2017, for station 3353 (see Figure 5 and Figure 6 for a map of tide gauge stations).

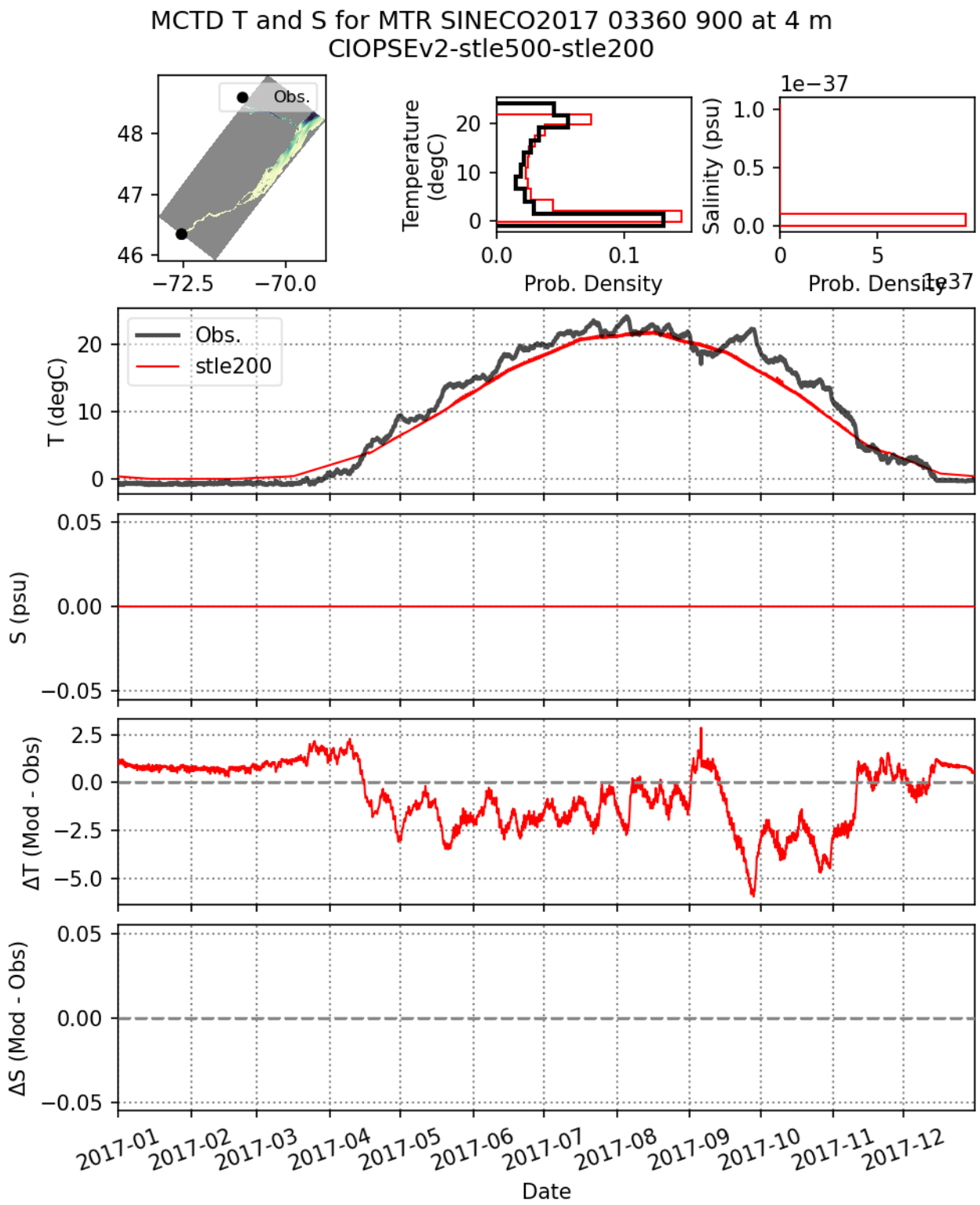

Figure 66. Near surface temperature and salinity for the 3 models and observations coming from MCTD fixed on tide gauges stations for years 2017, for station 3360 (see Figure 5 and Figure 6 for a map of tide gauge stations).

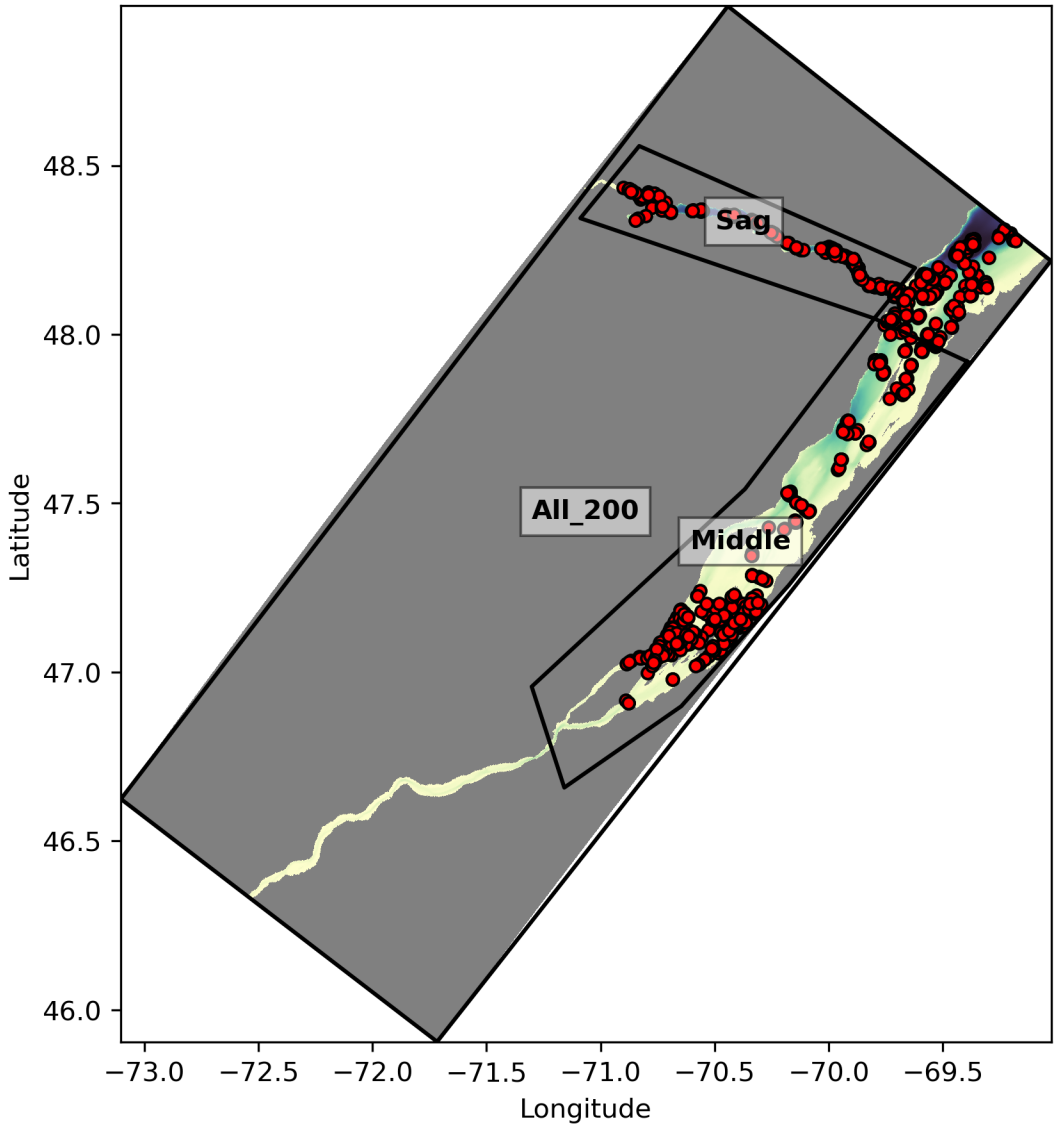

Figure 67. CTD cast and definition of the polygons over the 200m config domain.

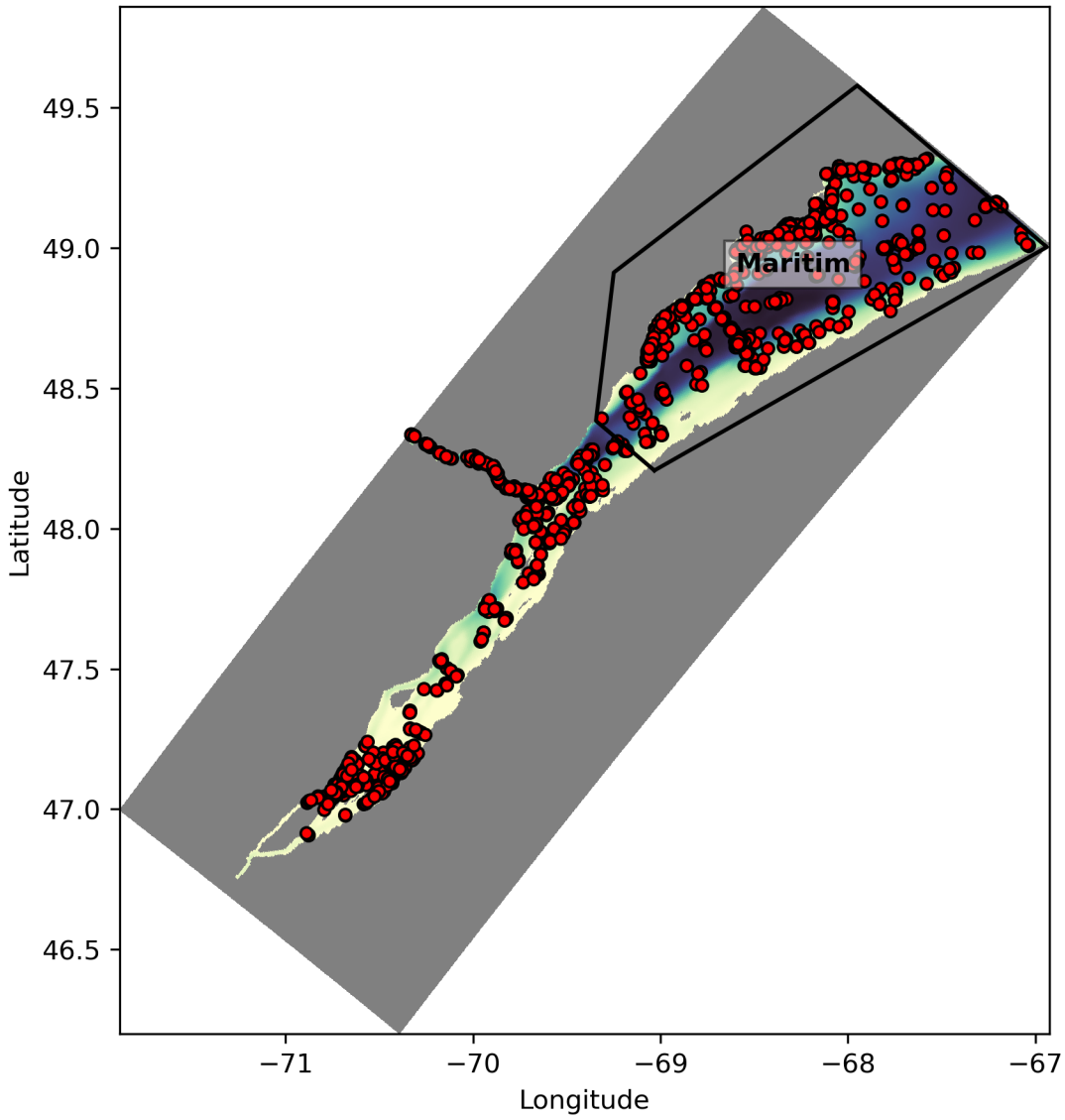

Figure 68. CTD cast and definition of the polygons over the 500m config domain not covered by the 200m domain.

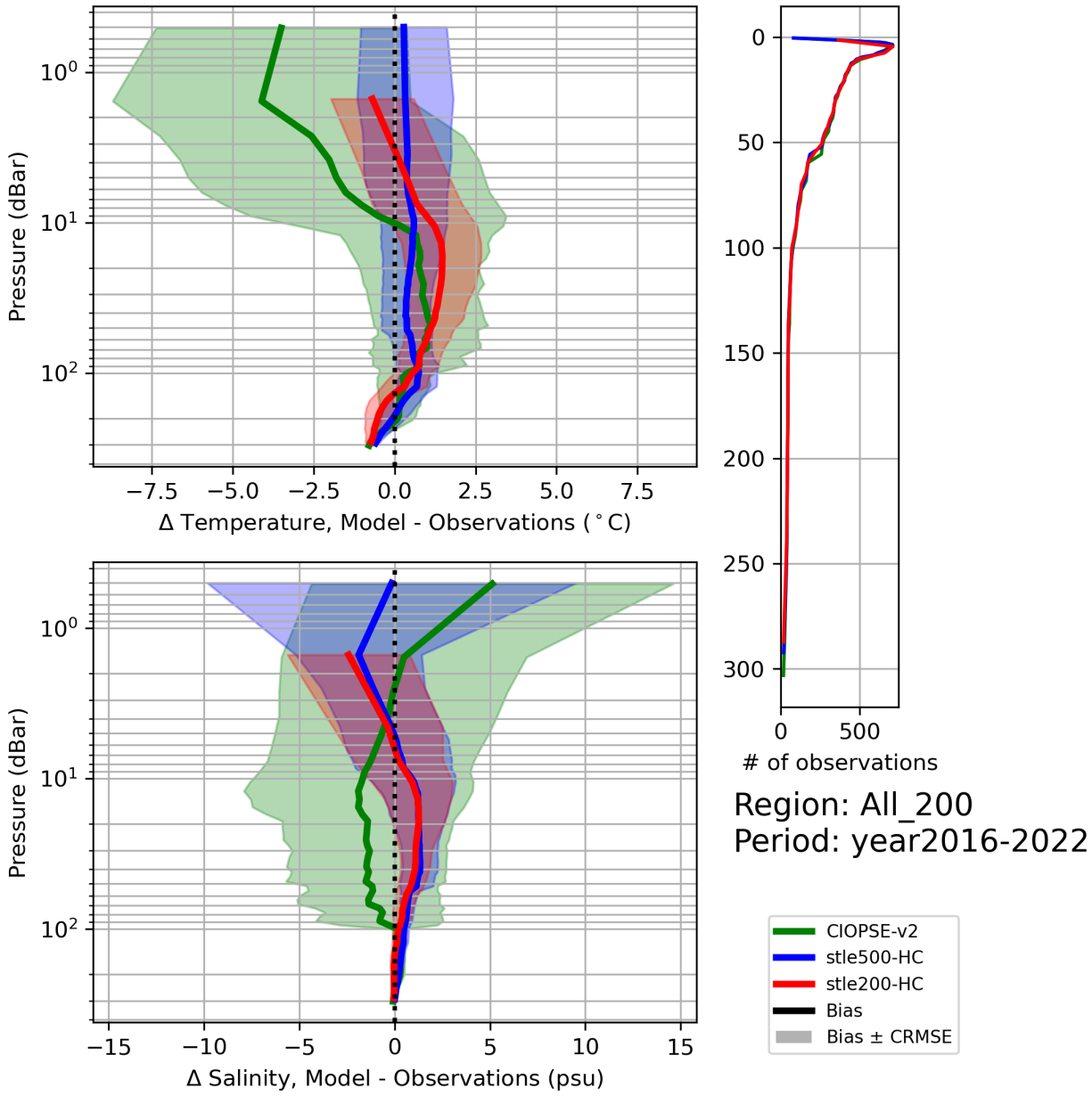

Figure 69. CTD cast comparison for the whole 200m domain. See Figure 67 for the definition of All_200 region. Note the log y-axes to show the differences in the first 10 meters.

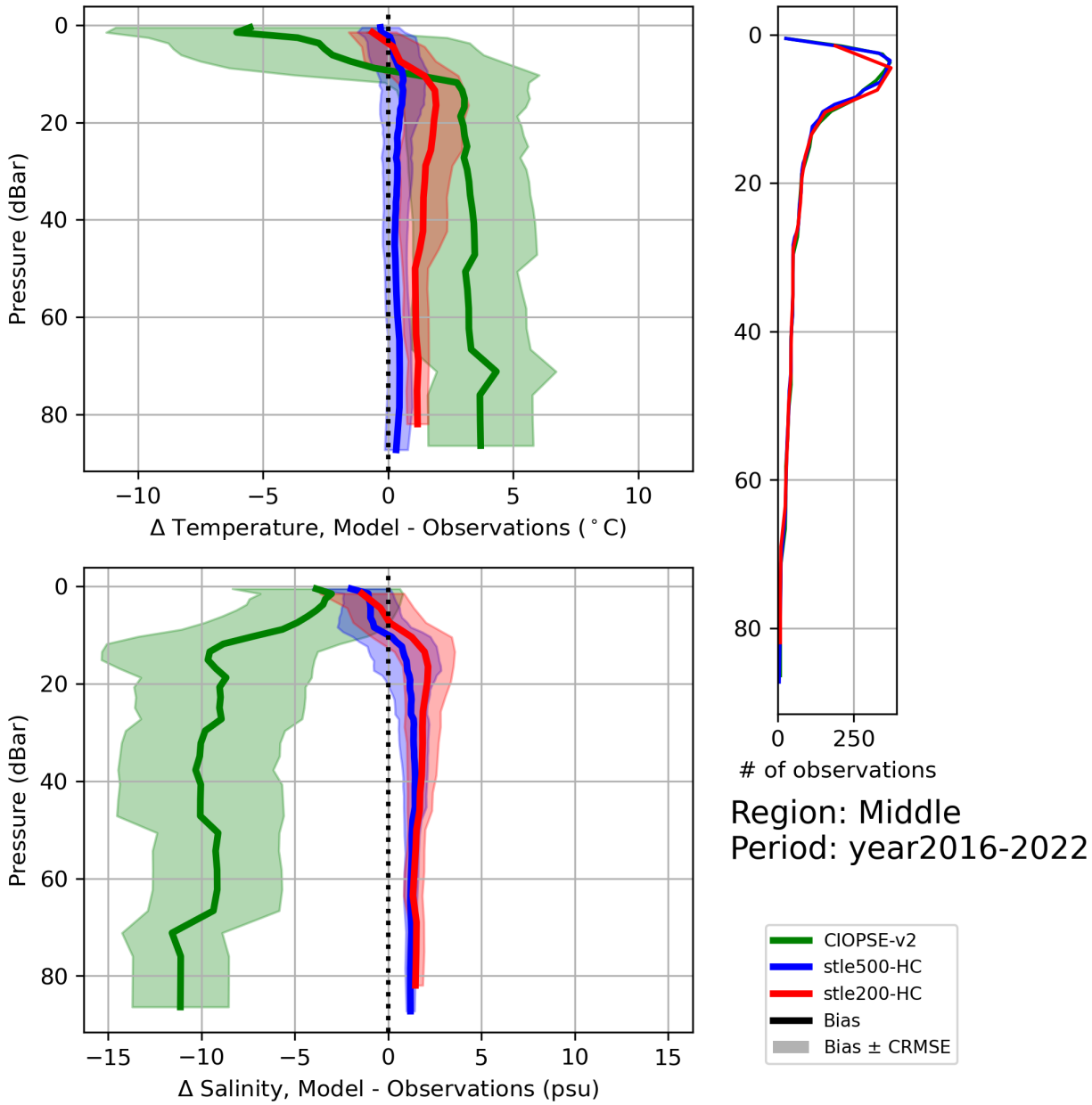

Figure 70. CTD cast comparison for the Middle Estuary region. See Figure 30 for the definition of Middle region.

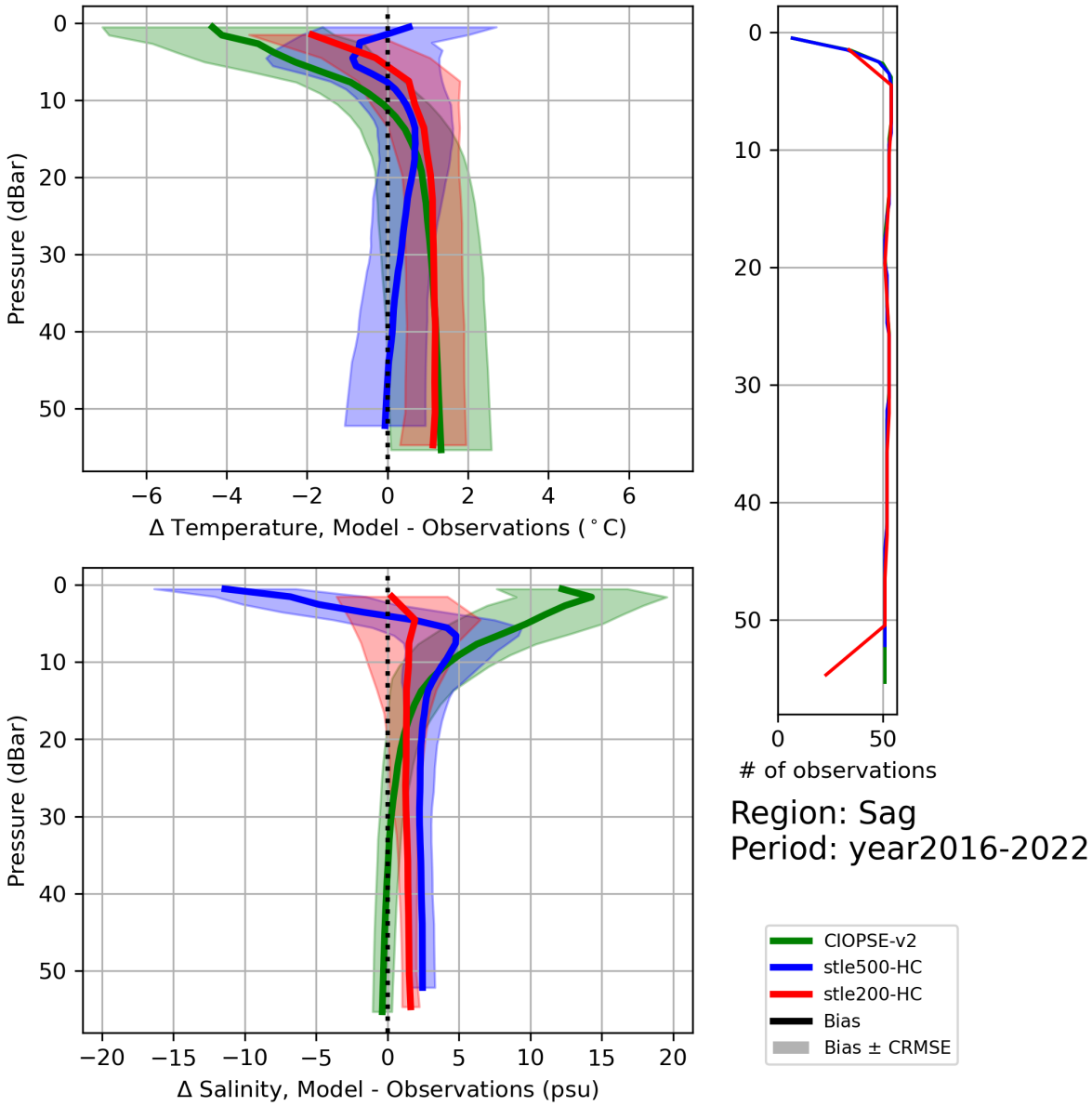

Figure 71. CTD cast comparison for the Saguenay Fjord region. See Figure 30 for the definition of Sag region.

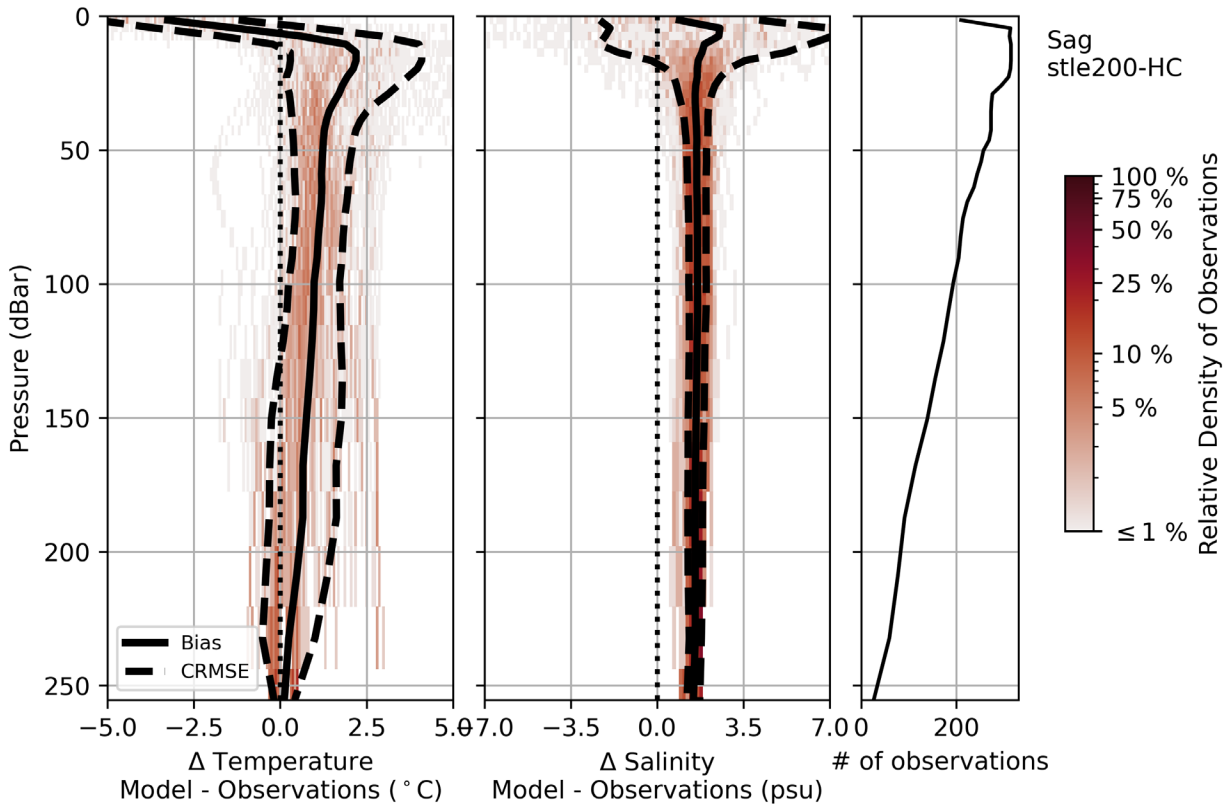

Figure 72. CTD cast for the Saguenay Fjord region, just for STLE200. See Figure 30 for the definition of Sag region.

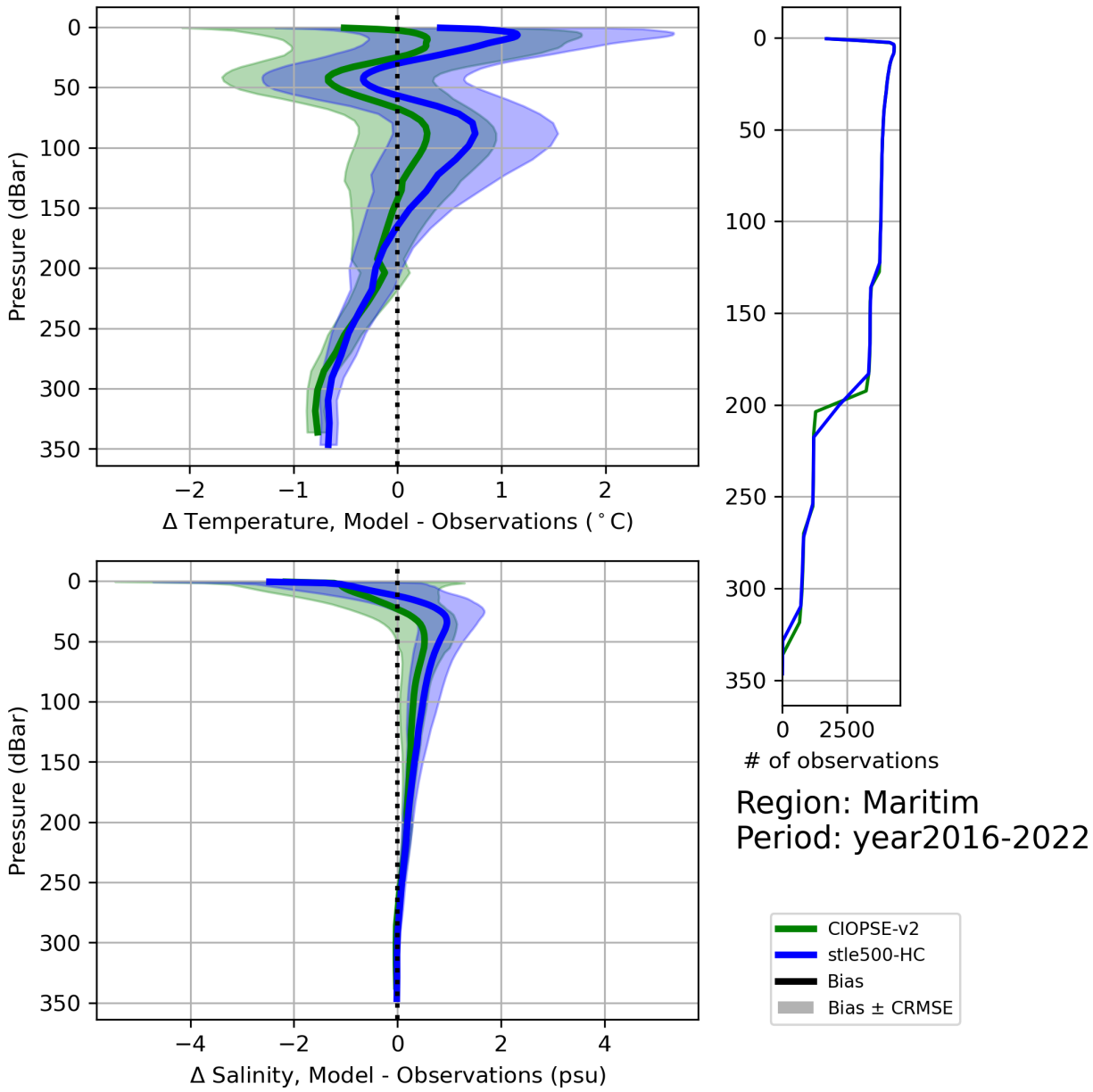

Figure 73. CTD cast comparison for the Maritime Estuary region. See Figure 30 for the definition of Maritim region.

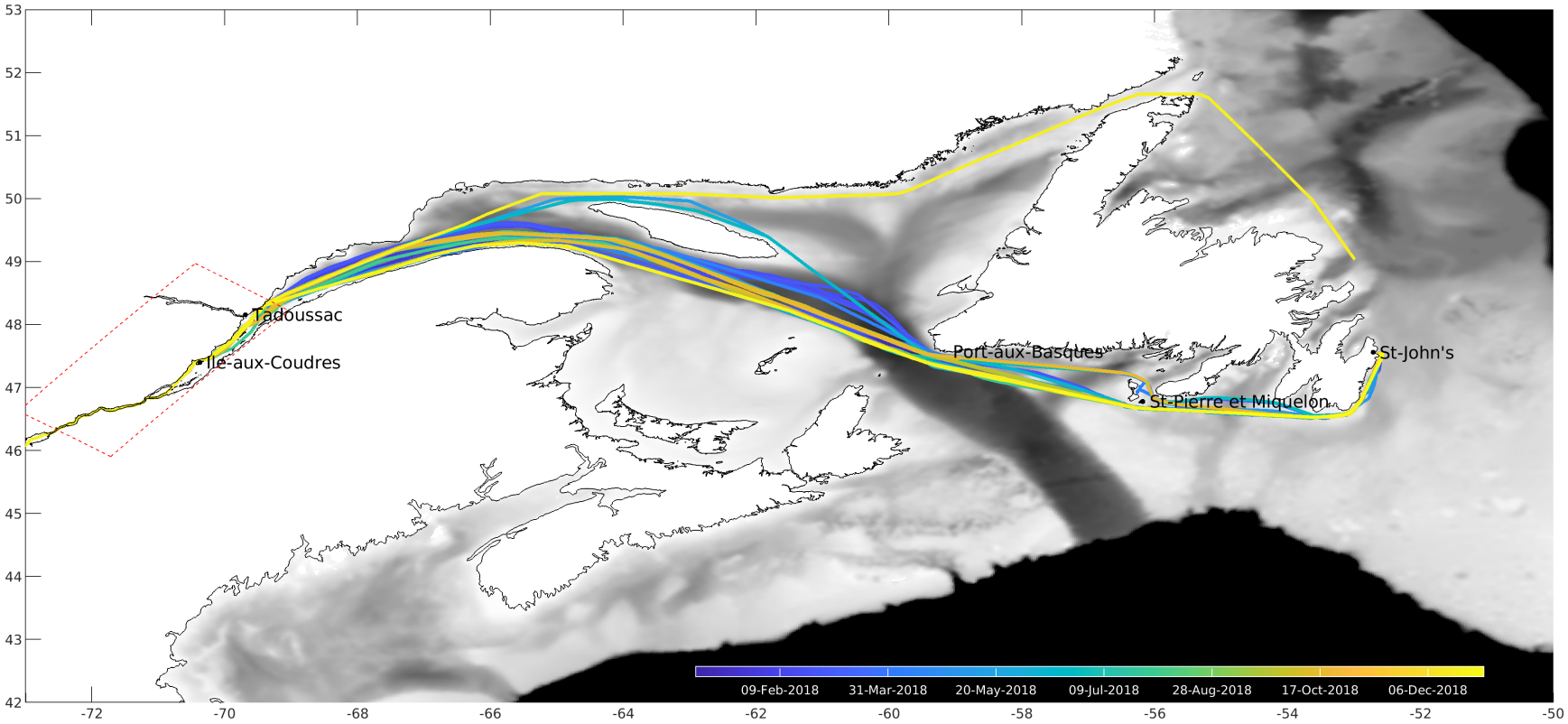

Figure 74. Ship tracks of the Oceanex Connaigra for year 2018. Timing of the ship position is represented by the color scale. Red dotted rectangle represents the limits of STLE200 domain.

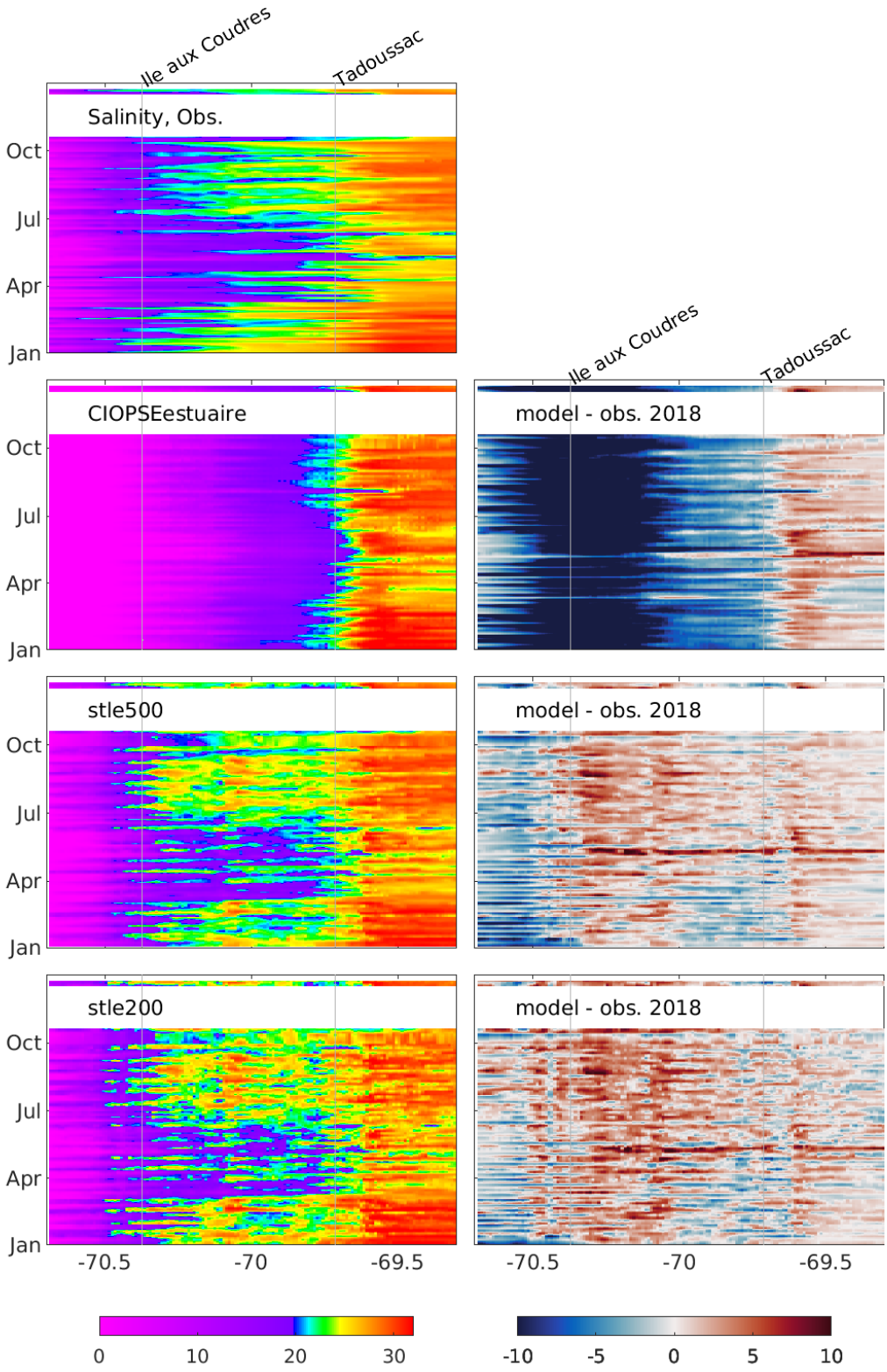

Figure 75. 8m salinity as collected by the ferry over the common section to the 3 models in the Middle Estuary. The horizontal axis is longitude with Ile-aux-Coudres and the city of Tadoussac marked as a landmark (see Figure 74). Vertical axis is the month of the year 2018. Row 1 are observations, row 2 to 4 are model results in column1, and differences with observations are in column 2.

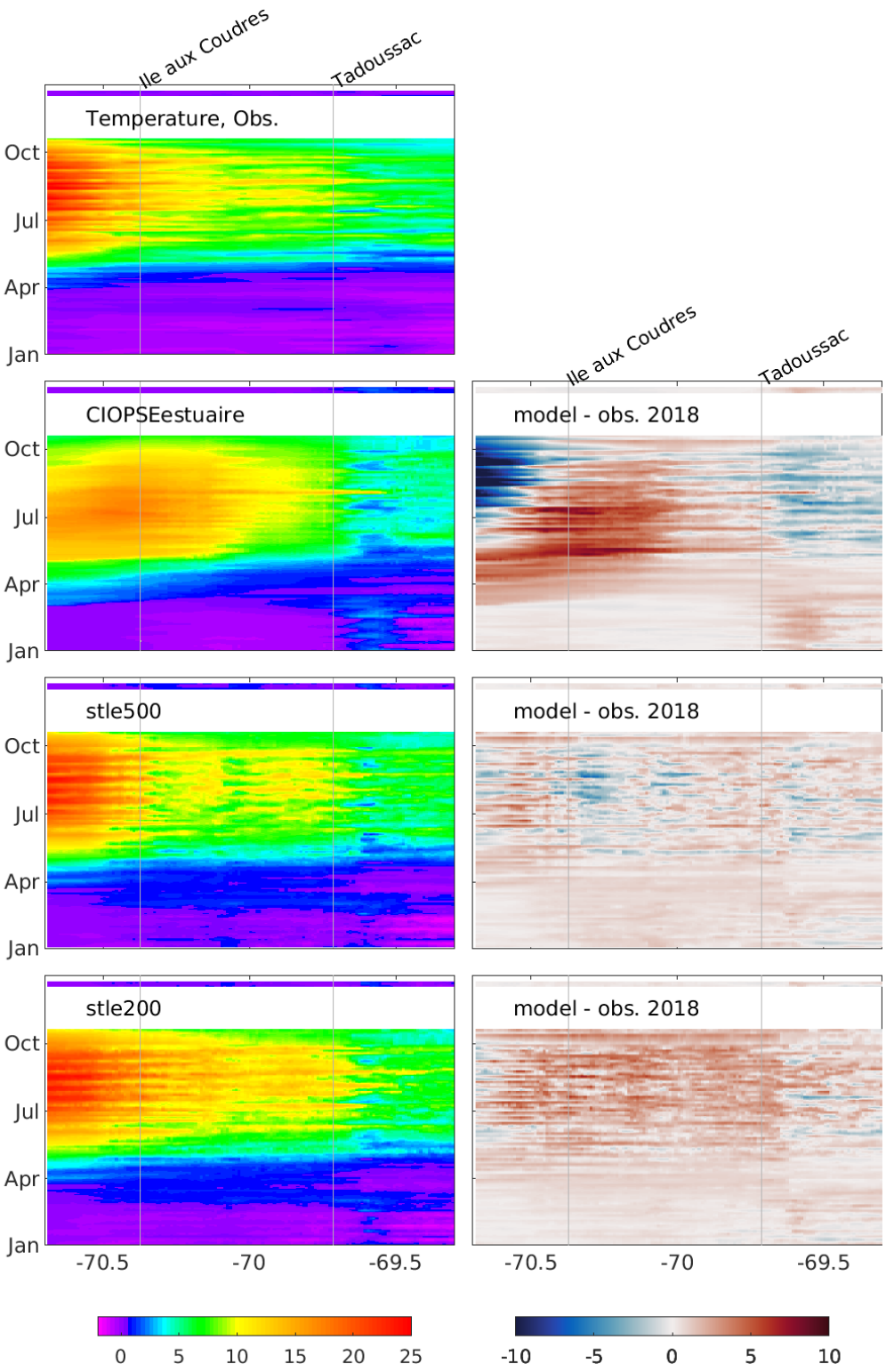

Figure 76. 8m temperature as collected by the ferry over the common section to the 3 models in the Middle Estuary. The horizontal axis is longitude with Ile-aux-Coudres and the city of Tadoussac marked as a landmark (see Figure 74). Vertical axis is the month of the year 2018. Row 1 are observations, row 2 to 4 are model results in column1, and differences with o observations are in column 2.

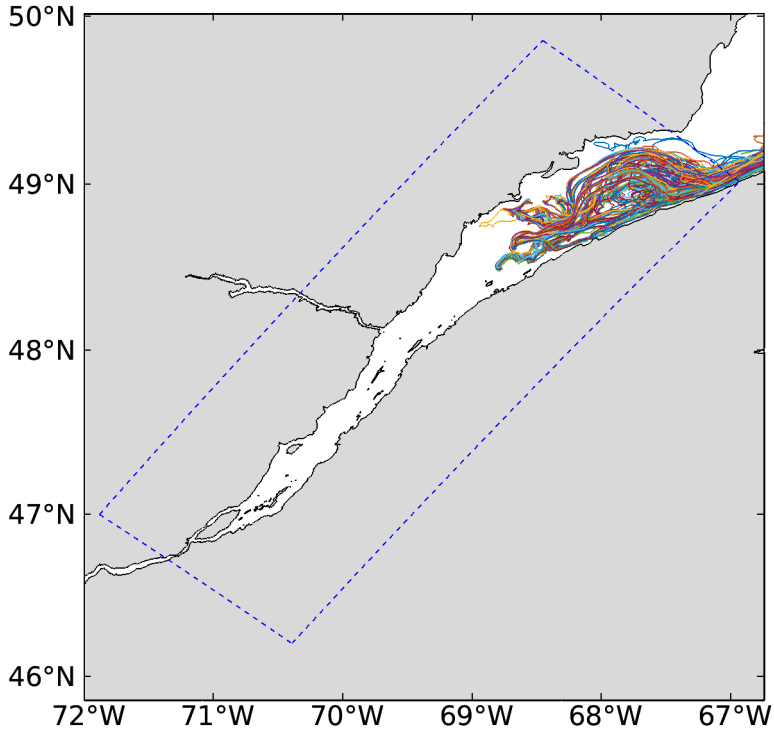

Figure 77. Map of the drifter's path for the TReX experiment, 2020. Blue dotted rectangle is STLE500 domain.

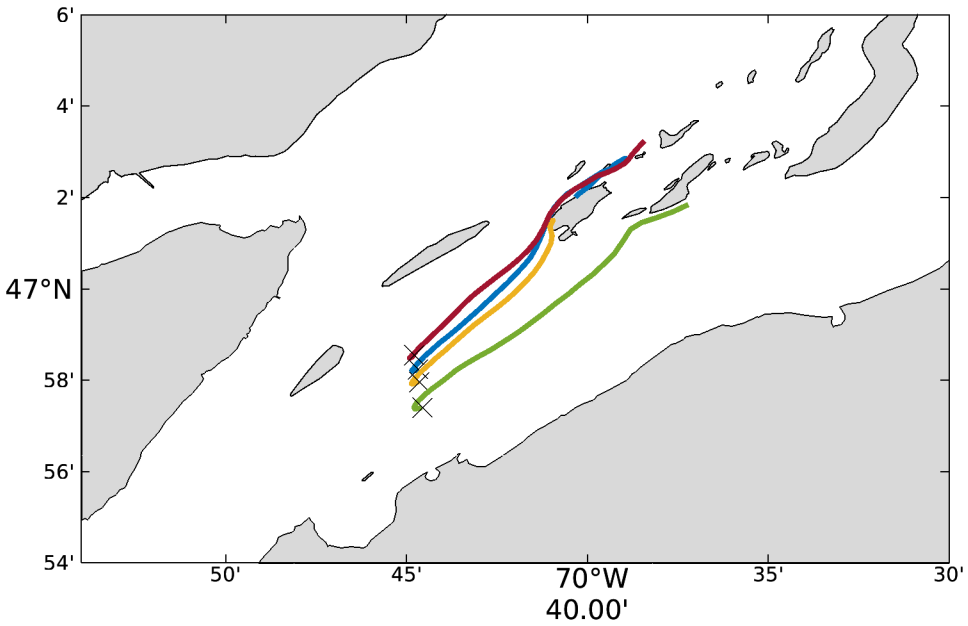

Figure 78. Map of the drifter's path near Saint-François, Ile d'Orléans. Deployment is marked by a black cross.

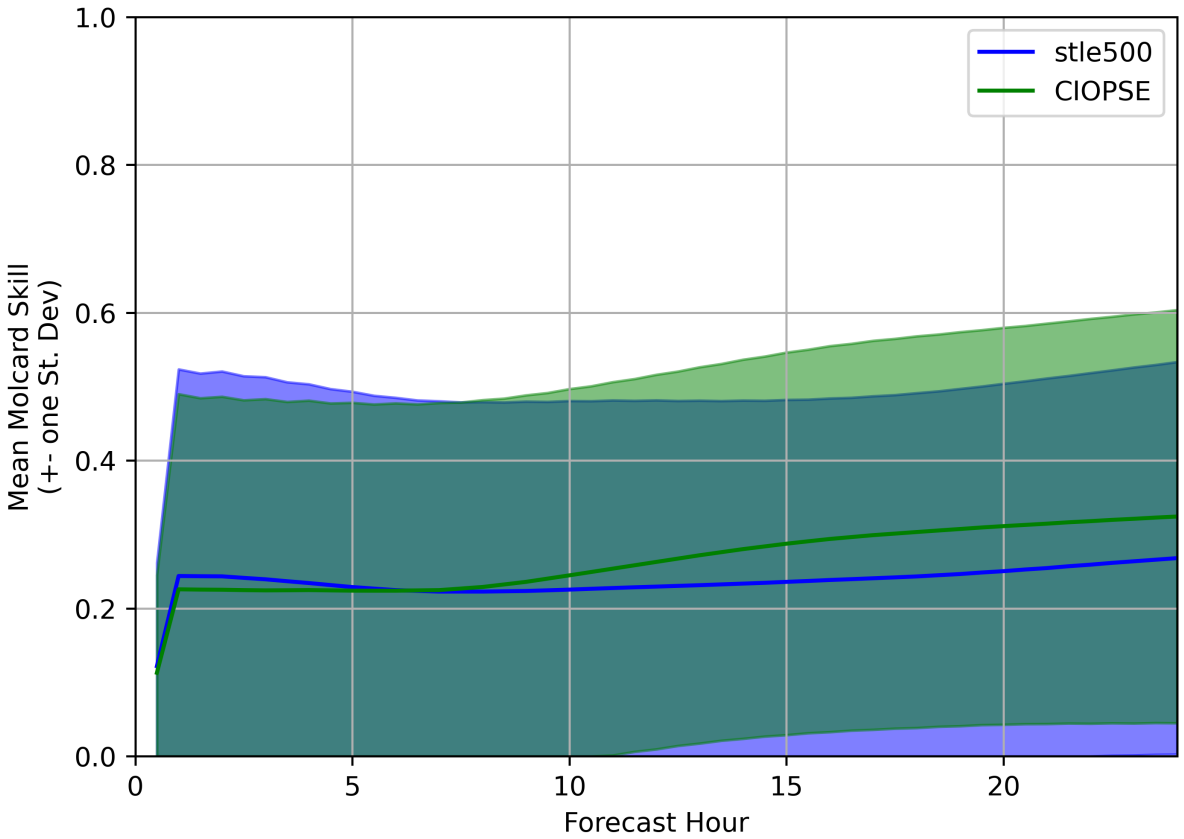

Figure 79. Mean Molcard skill for TReX experiment drifter's database in 2020.

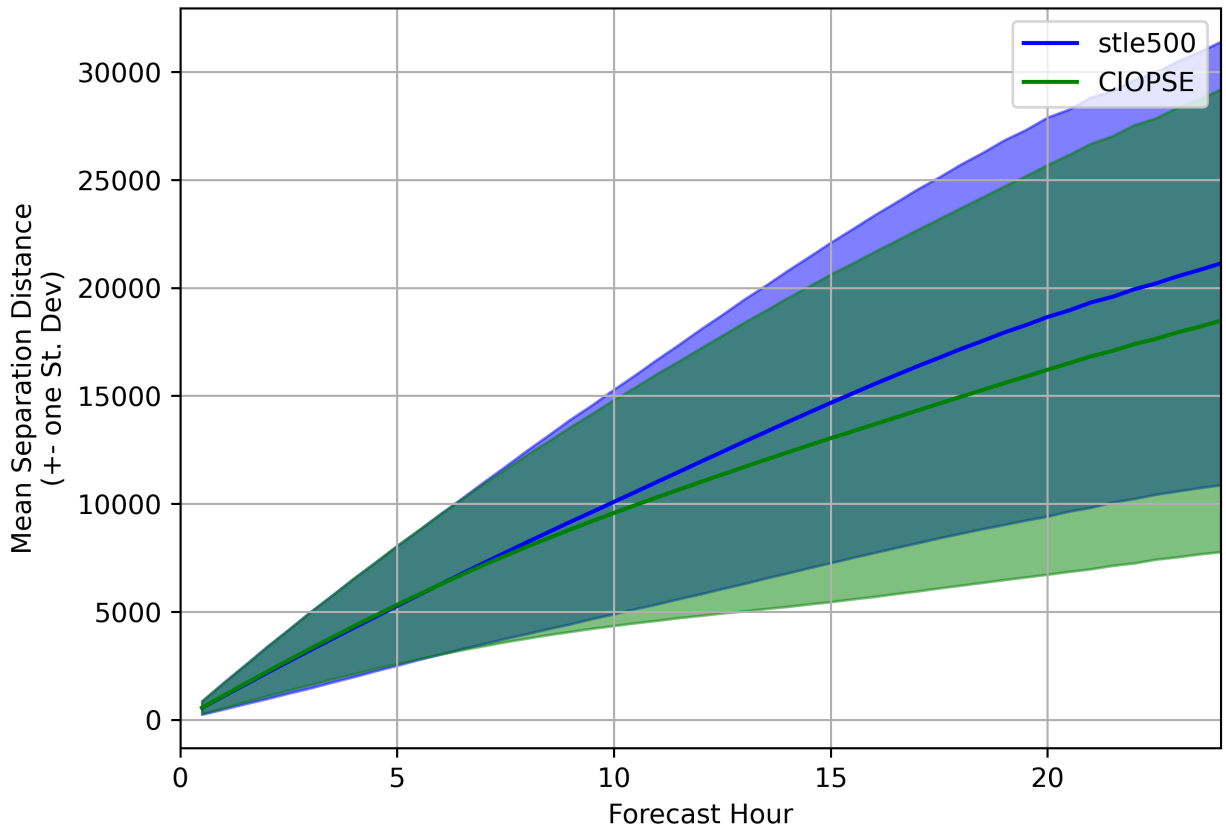

Figure 80. Mean separation distance for TReX experiment drifter's database in 2020.

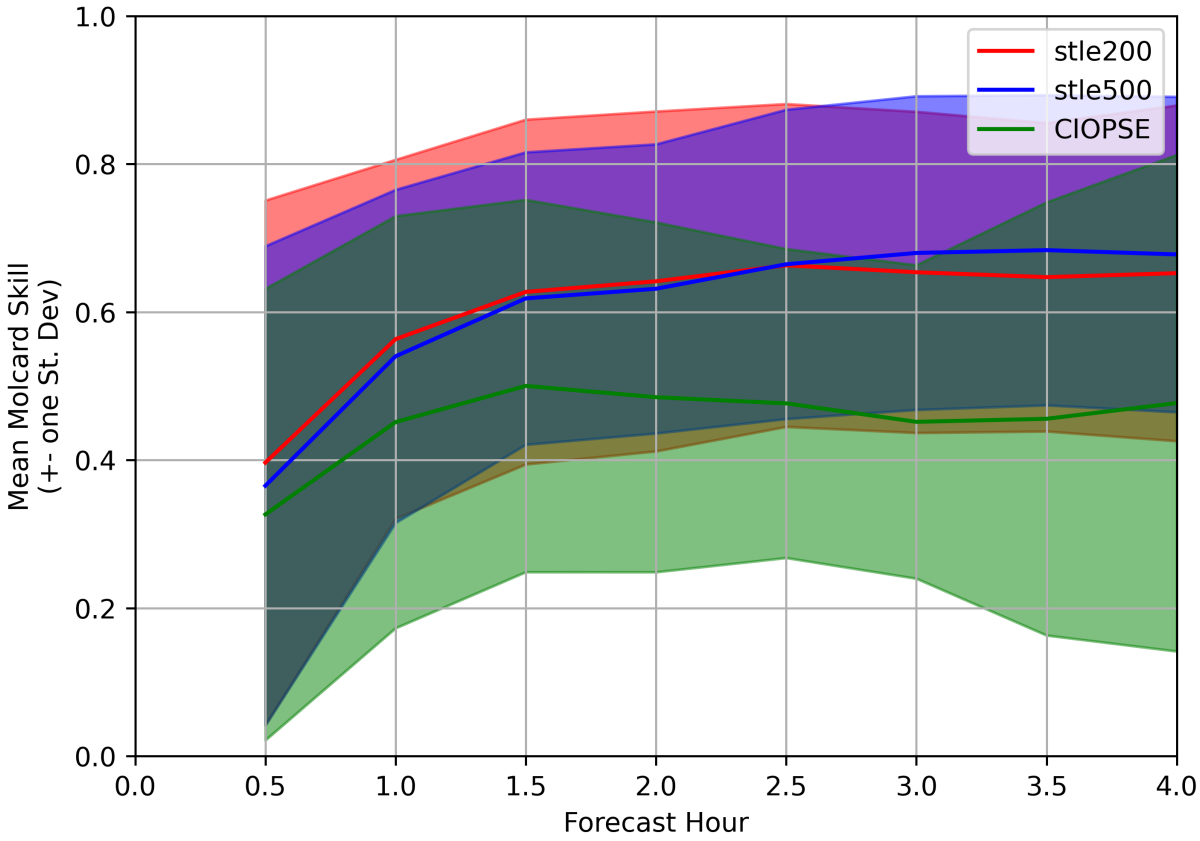

Figure 81. Mean Molcard skill for drifters deployed in the area of Saint-François, Ile d'Orléans, in July 2019.

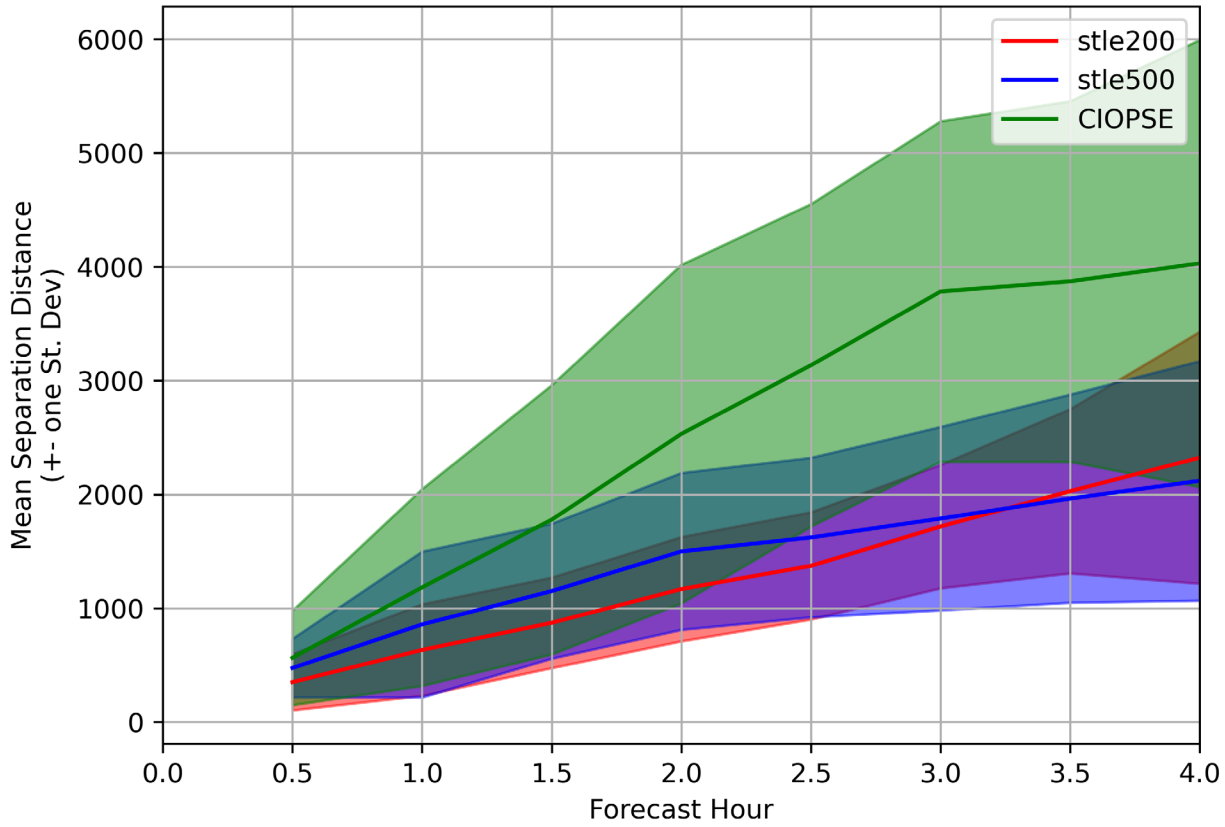

Figure 82. Mean separation distances for drifters deployed in the area of Saint-François, Ile d'Orléans, in July 2019.

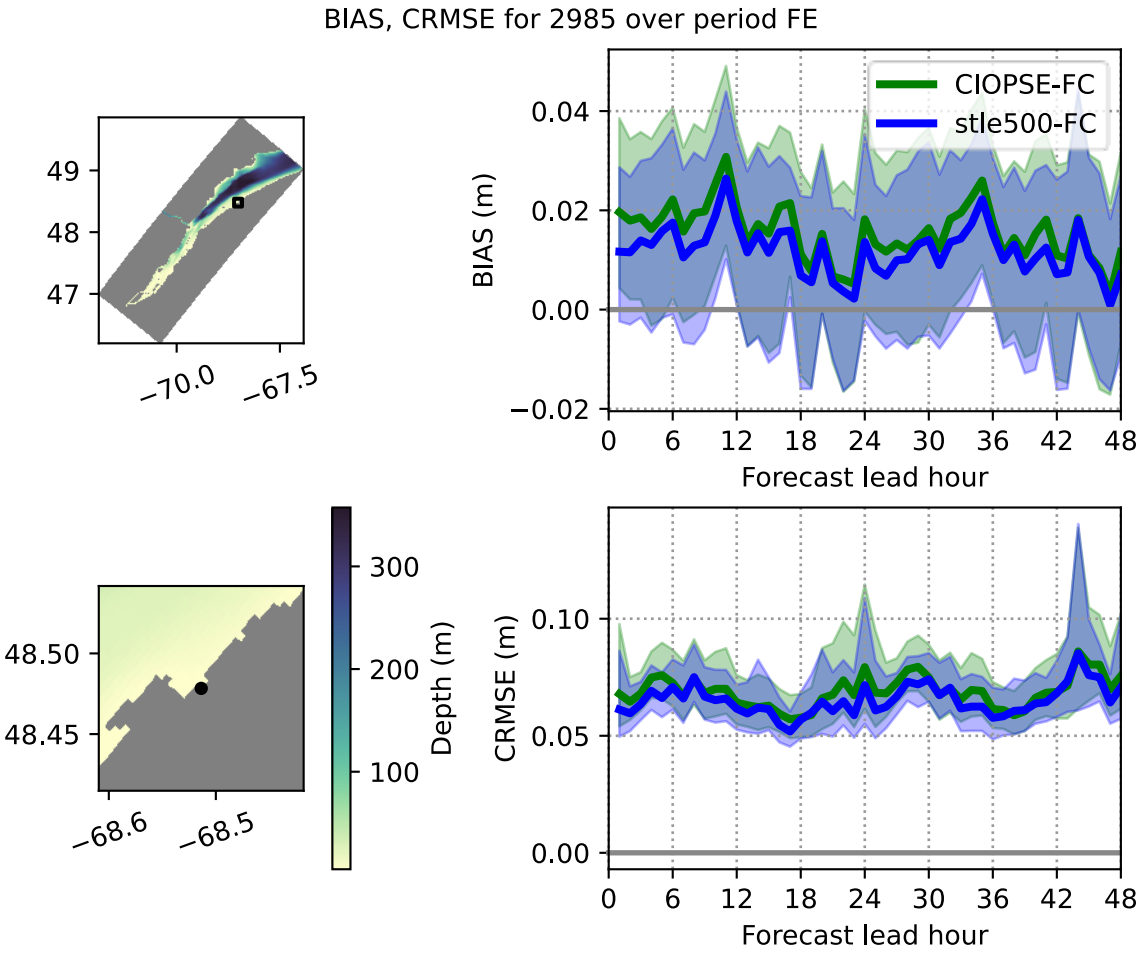

Figure 83. Non-tidal water level bias and CRMSE for station 2985.

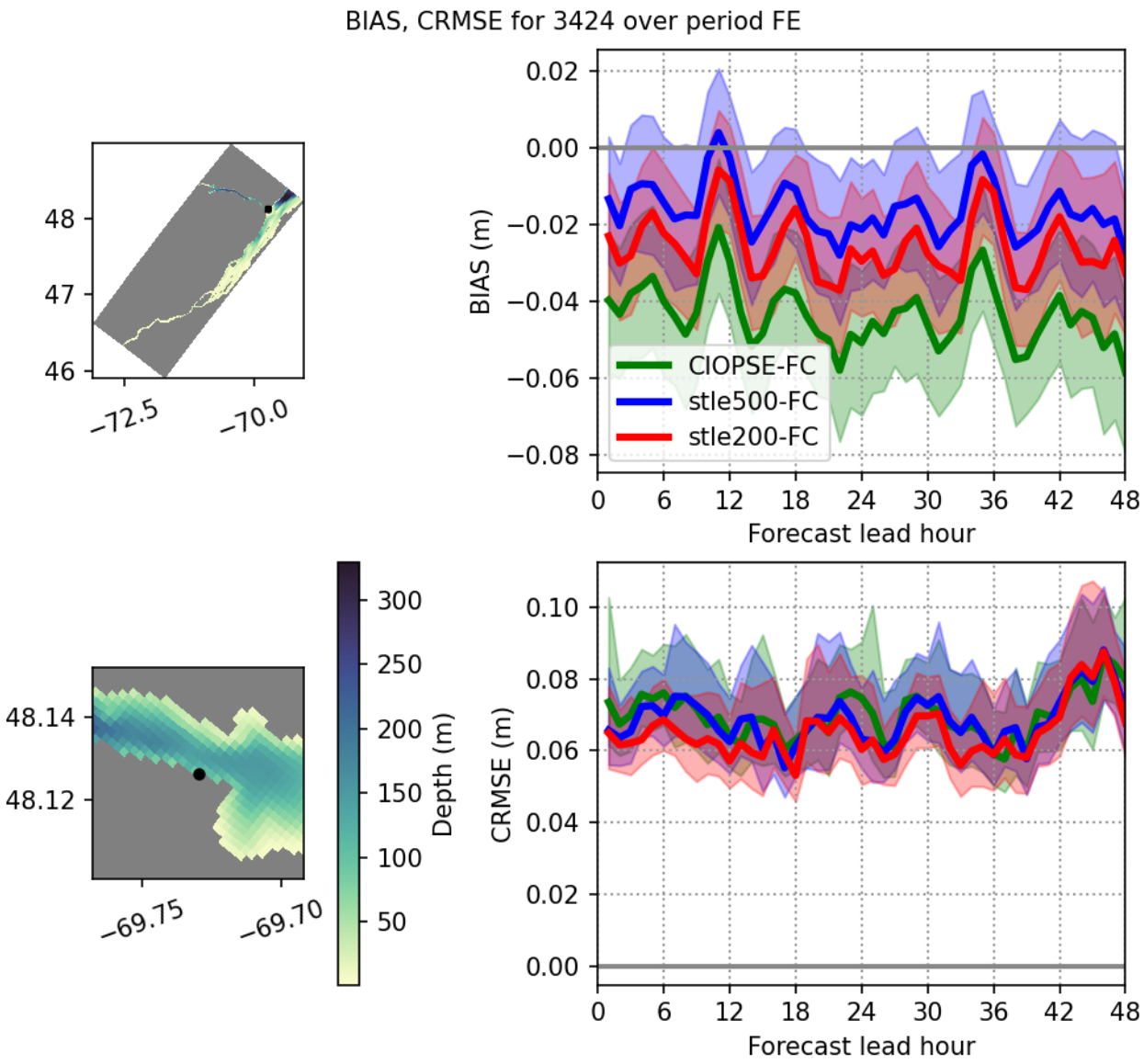

Figure 84. Non-tidal water level bias and CRMSE for station 3424.

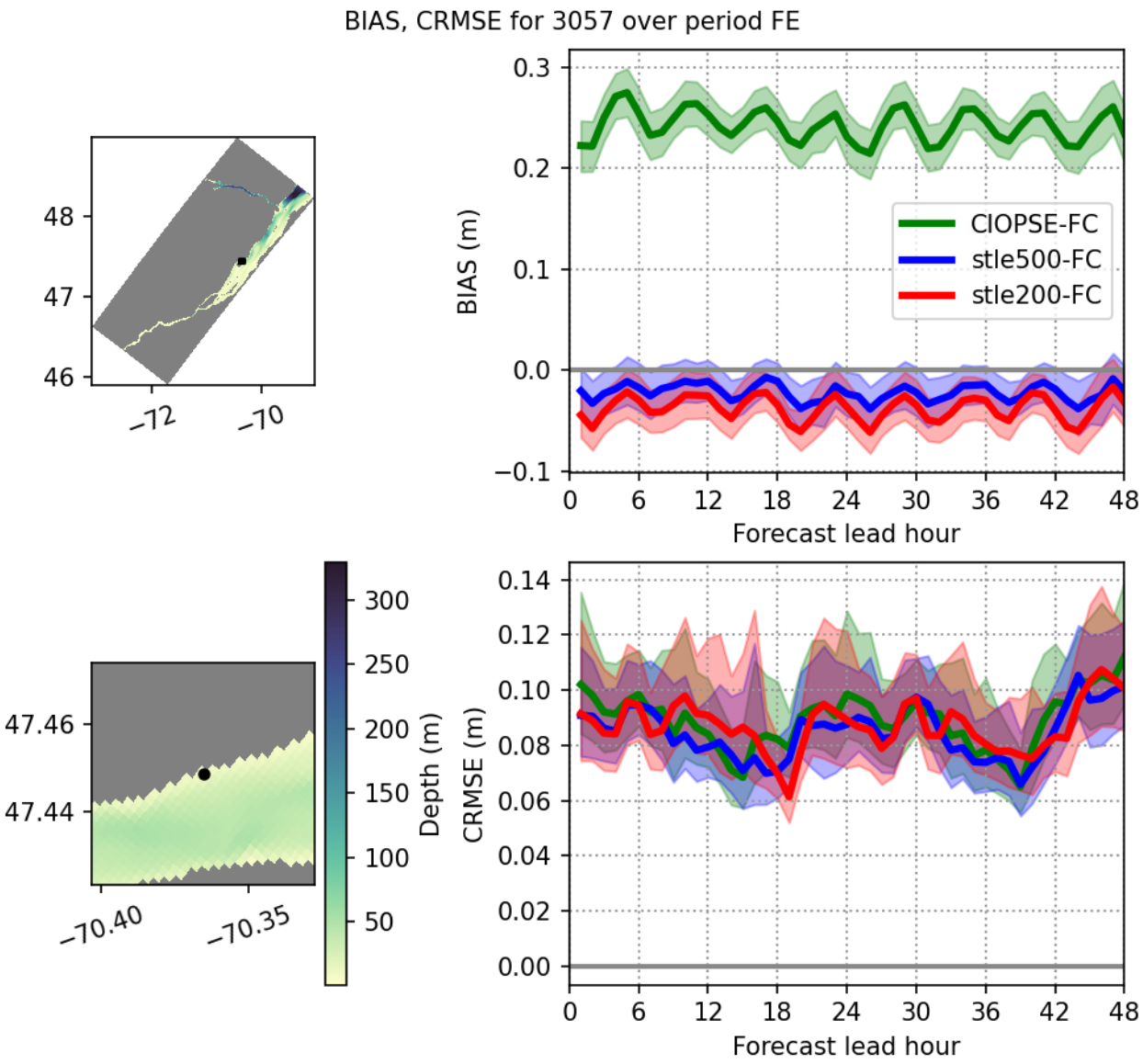

Figure 85. Non-tidal water level bias and CRMSE for station 3057.

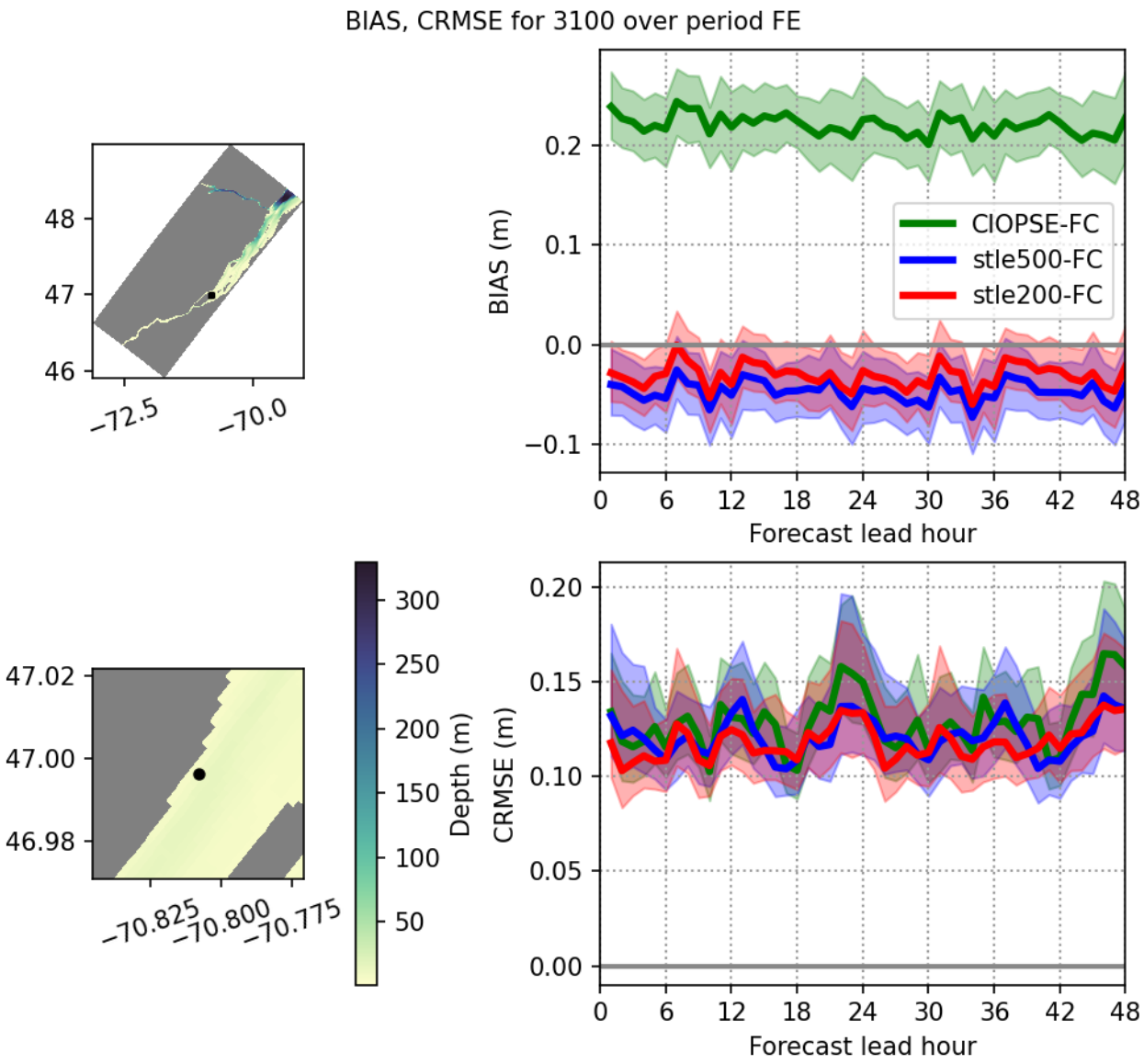

Figure 86. Non-tidal water level bias and CRMSE for station 3100.

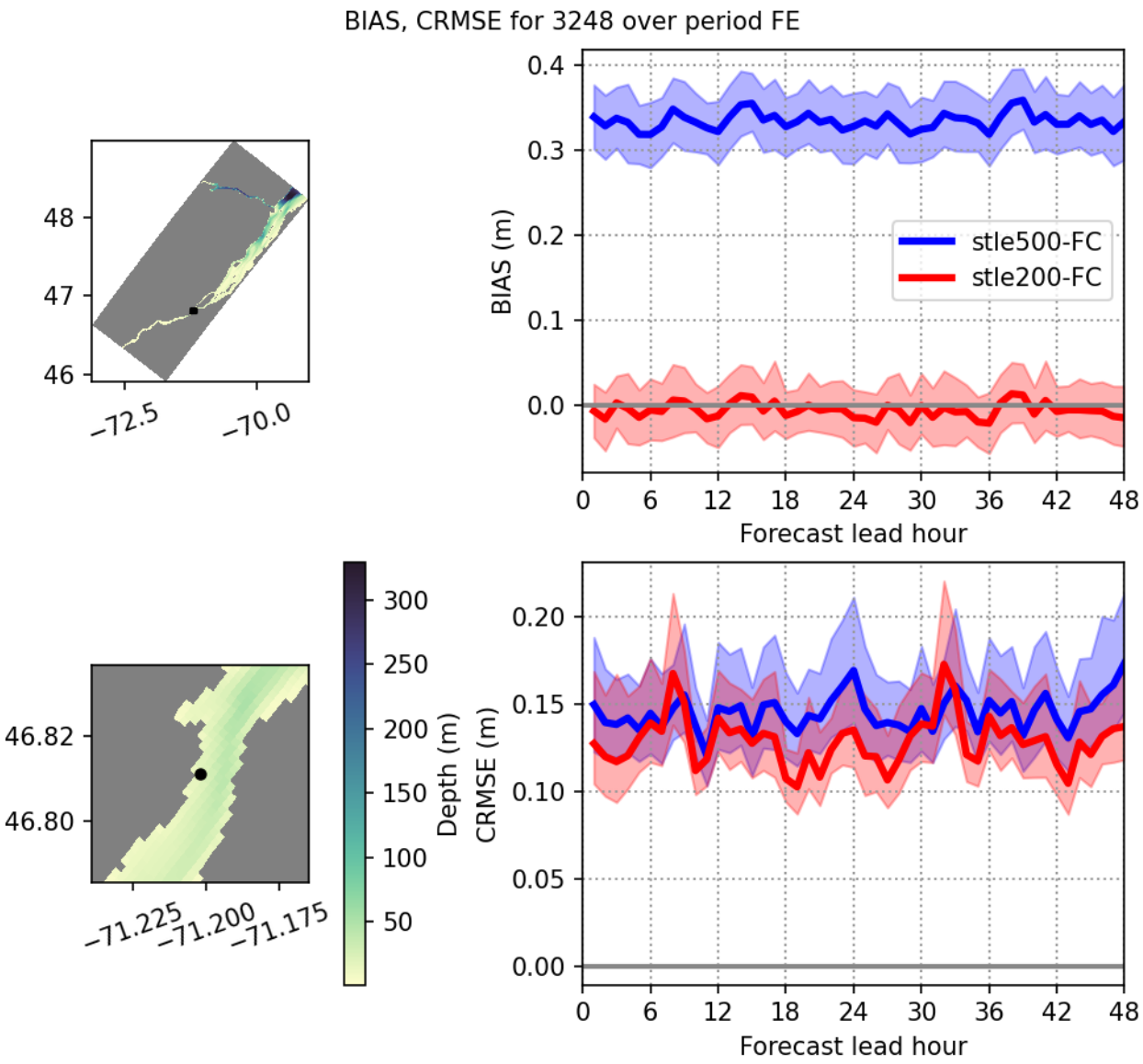

Figure 87. Non-tidal water level bias and CRMSE for station 3248.